Dust mitigation strategies for photovoltaic modules:

Vertical mounting of bifacial modules and anti-soiling coatings

Submitted in partial fulfilment of the requirements for the degree of

DOCTOR OF PHILOSOPHY

By

Sonali Bhaduri

(Roll no. 174366002)

under the guidance of

Prof. Sudhanshu Mallick

Prof. Anil Kottantharayil

Centre for Research in Nanotechnology and Sciences

INDIAN INSTITUTE OF TECHNOLOGY BOMBAY

2023

Thesis Approval

This thesis entitled

Dust mitigation strategies for photovoltaic modules: Vertical mounting of bifacial modules and anti-soiling coatings

by

SONALI BHADURI

(Roll No. 174366002)

Is approved for the degree of

Doctor of Philosophy

Prof.
(Examiner)

Prof.
(Examiner)

Prof. Sudhanshu Mallick

(Supervisor)

Prof. Anil Kottantharayil

(Co-Supervisor)

Prof.

(Chairman)

Place : IIT Bombay
Date : 05th February 2023

Dedicated to

my Family and Friends

DECLARATION

I declare that this written submission represents my ideas in my own words and where others ideas or words have been included, I have adequately cited and referenced the original source. I also declare that Chapter 3 of this thesis contains the work we have published in IEEE Journal of Photovoltaics, vol. 9, No. 1, pp. 240-244, January 2019 (DOI: 10.1109/JPHOTOV.2018.2872555). Chapter 4 contains work published in the proceedings of 47th IEEE Photovoltaic Specialists Conference (PVSC), January 2021 (DOI**:** 10.1109/PVSC45281.2020.9300697). Chapter 5 contains the work published in the Journal of Renewable and Sustainable Energy, vol. 13, no. 2, pp. 023702, March 2021 (DOI: https://doi.org/10.1063/5.0039255). Chapter 6 contains work published in IEEE Journal of Photovoltaics, vol. 10, no. 1, pp. 166-172, January 2020 (DOI: 10.1109/JPHOTOV.2019.2946709), and in the proceedings of *47th IEEE Photovoltaic Specialists Conference (PVSC),* pp. 1098-1101, January 2021 (DOI**:** 10.1109/PVSC45281.2020.9300414). Chapter 7 and 8 contains work submitted for publication in Progress in Photovoltaics, IEEE J. Photovoltaics, Materials Today Communications. I also declare that I have adhered to all principles of academic honesty and integrity and have not misrepresented or fabricated, or falsified any idea/data/fact/source in my submission. I understand that any violation of the above will be cause for disciplinary action by the Institute and can also evoke penal action from the sources which have thus not been properly cited or from whom proper permission has not been taken when needed.

Sonali Bhaduri

Roll No. 174366002

IIT Bombay

Date – 05th February 2023

ABSTRACT

Making renewable energy economical and accessible to everyone is an urgent need of this century. Sunbelt countries like India and the Middle East have high atmospheric PM counts, resulting in soiling (accumulation of dust on PV modules) losses of up to 1%/day, for which the financial loss is estimated to be 1 billion euros/annum in the year 2023. This creates an urgent need for a cost-effective dust mitigation strategy. Our work investigated 2 dust mitigation strategies; (1) dust mitigation via vertically mounted bifacial modules and (2) Anti-soiling coatings. Our study reveals that vertically mounting the bifacial modules gives zero soiling loss and zero soiling rate in warm and humid climate zones like Mumbai, India. Tracker systems can use this dust mitigation approach, where the user can extend the tilt range to 90˚ after sunset hours to achieve a 50% reduction in soiling rates. Commercially available fixed-tilt monofacial modules (mounted at latitude tilt angle) show higher soiling loss than bifacial modules at latitude and vertical tilt angles. The energy yield of vertically mounted bifacial modules with 90% bifaciality can exceed that of bifacial modules mounted at a latitude angle after three weeks if the modules are left to soil without cleaning. Vertically mounted bifacial modules also show 15°C lower temperature than bifacial modules mounted at latitude angle, implying potential benefits in long-term reliability and performance ratio.

Another cost-effective and universal dust mitigation strategy is via anti-soiling (AS) coatings. AS-coatings are nano or microlayer coatings which reduce the settlement of dust on the surface of the PV module and are extensively investigated as a dust mitigation strategy. As the AS-coating is applied on the outer surface of the PV module, the durability of these coatings is essential. This creates a need for a standard test procedure to evaluate the reliability of AS-coatings relevant to PV applications. A standard test procedure would act as a baseline to quantify the reliability of the commercially available coatings and facilitate the development of new durable AS-coatings. Most AS-coatings available in the commercial market are hydrophobic because it does not allow the water to wet the surface and the dust particle adhere to the droplet rolling off the surface, thus acting as a cleaning mechanism. Similar findings were seen in our study, where all coated samples (commercially hydrophobic AS-coatings A, B, C and D) show higher cleaning efficacy than not-coated (hydrophilic) samples under controlled environments and outdoor field exposure. This

indicates that hydrophobic AS-coatings could mitigate soiling. However, durability remains a challenge.

Thus, we studied the reliability of commercial hydrophobic AS-coating under warm and humid climate zone. This was achieved by performing various outdoor durability tests followed by numerous accelerated stress tests. The findings of the correlation study between the outdoor and indoor accelerated stress tests were then used to model the life of AS-coatings considering UV radiation and rainfall as a stressor. Two accelerated testbeds named the cleaning cycle simulator, and the rainfall simulator, were developed to simulate the damage caused by outdoor abrasion and rain. The complete study was conducted on 4 commercial hydrophobic AS-coatings named A, B, C and D. The not-coated sample was referred to as U. Coatings A, B, and D were fluoropolymer-based coatings, and coating C was a Phenylsilicone based coating. A new non-destructive characterization method was established to estimate the surface coverage of the coated area via phase imaging using tapping mode atomic force microscopy. The reliability evaluation of AS-coatings is distributed into 4 parts; (1) Cleaning efficacy, (2) Outdoor durability, (3) Indoor accelerated stress tests and (4) Lifetime prediction of AS-coatings.

1. **Cleaning efficacy** - All coated samples (hydrophobic) show higher cleaning efficacy than not-coated samples (hydrophilic) under both controlled environment and field exposure tests.
2. **Outdoor durability** – Coating life decreased by 21 X (average of coating A, B, C and D) when exposed to the rainy season compared to those being exposed to the non-rainy season, implying rain as the most significant stressor.
3. **Accelerated stress tests -** In this section, we did a detailed analysis on the effect of isolated stressors like rainfall, abrasion, UV radiation and a combination of various stressors that degrade AS-coatings.

    a. **Rainfall –** All coated samples exposed to the impact of raindrops with pH 7 water samples show 33 X lower coating life than those exposed to water immersion/water contact with pH 7 water samples. Similar findings were observed with acidic water, which indicates that during a rain event, the impact of raindrops causes greater damage than water immersion/water contact.

b. **Abrasion -** The presence of dust during cleaning cycles decreases the coating life by 82 X, compared to only-clean cycles, thus acting as the most significant stressor that abrades the coated samples.

c. **UV radiation –** When exposed to only UV radiation, coating C becomes completely hydrophilic at a very high UV dose of 366 kWh/m^2. The transition from hydrophobic to hydrophilic happened at a much lower dose when combination of UV (at 32 kWh/m^2) and condensation (441 h) was present. All coated samples show lower coating life when exposed to a combination of 4 stressors (Impact of raindrops + acidic water + UV exposure + abrasion), followed by a combination of 3 stressors (Impact of raindrops + acidic water + UV exposure) and 2 stressors (Impact of raindrops + acidic water).

4 **Lifetime prediction of AS-coatings** – Based on the understanding from the outdoor and indoor accelerated stress tests, we predicted the coating life considering UV and rainfall as a stressor.

a. **Considering rain (pH of water) as the stressor** - The activation energy and pH dependence (N) factor were calculated based on the Arrhenius-Modified Peck model. The activation energy of the coating A, B, C and D were calculated to be 0.09 eV, 0.43 eV, 0.09 eV and 0.56 eV, respectively, assuming Weibull distribution. Positive activation energy indicated that the coating life decreases with increased temperature. When exposed to a location with annual precipitation of 5213 mm with water pH 6, coatings A, B, C, and D exhibit a coating life of 0.8, 8, 0.3 and 21 months, respectively (when the tilt angle of the coated PV module is lower than the roll-off angle). Fluoropolymer based coatings (A, B and D) showed higher dependence on water pH than phenylsilicone based coating (C). All coatings showed lower coating life under varying pH when exposed at a tilt angle lower than their respective roll-off angle.

b. **Considering UV radiation as the stressor -** The activation energy was calculated based on the Arrhenius model. The activation energy of coating A, B, C and D was estimated to be 0.34 eV, 0.09 eV, 0.41 eV and 0.09 eV, respectively, assuming Weibull distribution. When exposed to a location with an annual UV dose of 131 kWh/m^2, coating A, B, C, and D exhibit a coating life of 10, 7, 11 and 9 years, respectively. Coatings with higher organic content (B and D) showed lower

activation energy and coating life (considering UV as a stressor). This indicates that the durability of the AS-coatings is a weather-dependent parameter. Thus, no coating would work for all locations.

This lifetime prediction methodology can be the basis for estimating the coating life at different locations, which can help the PV community in mapping locations/climatic conditions best suited for a specific coating type. This work can also be used as a starting point for modelling the effect of combination of stressors.

ACKNOWLEDGEMENTS

The preparation of this work entitled " *Dust mitigation strategies for photovoltaic modules: Vertical mounting of bifacial modules and anti-soiling coatings*" would not have been possible without the valuable and wholehearted guidance of many experienced people. I take this opportunity to express my sincere gratitude to my guides Prof. Sudhanshu Mallick and Prof. Anil Kottantharayil, for their continuous support of my PhD work, for their patience, exemplary guidance, monitoring and constant encouragement throughout the course of this work. I could not have imagined to have better mentors for my PhD study.

I wish to express my sincere thanks to my research progress review committee: Prof. Narendra Shiradkar, Prof. Parag Bhargava and Prof. Balasubramaniam Kavaipatti for providing directions for my PhD. I would also like to thank my department, "Centre for Research in Nanotechnology and Sciences", and the "National Centre for Photovoltaic Research and Education," and all faculty members for their hard questions, which motivated me to widen my research. I want to express my gratitude toward Prof. Juzer Vasi (EE Dept., IIT-B, India) and Prof. L. Kazmerski (NREL, USA) for their insightful comments and encouragement. I thank my fellow lab mates, Sachin Zachariah, Rajiv Dubey, Shashwata Chattopadhyay, Ajeesh Alath, Makrand Farkade, Lloyd Fernandes, Rohan Rajesh Bajhal, Shivam Vishwanath, Golive Yogeswara Rao, Shoubhik De, Pavan Fuke, Rambabu Sugguna, and the other members of the NCPRE research team for many stimulating discussions and for all the fun we have had in the last five years.

This work was supported by the National Centre for Photovoltaic Research and Education (NCPRE) at IIT Bombay, funded by Ministry of New and Renewable Energy of the Government of India through the Project No. 31/09/2015-16/PVSE-R&D dated 15th June 2016. I acknowledge IIT Bombay Nano Fabrication Facility for contact angle, AFM and XPS measurements, Department of Metallurgical Engineering & Materials Science for QUV accelerated weather tester, Department of Chemical Engineering for pH meter, Sophisticated Analytical Instrument Facility for ICP-AES, and *Central Facilities, IIT Bombay* for AFM measurements.

And last but not least, I am greatly indebted to my family and family for their tremendous amount of love and support.

Sonali Bhaduri

CONTENTS

List Of Figures

List Of Tables

List of Abbreviations

AFM	Atomic Force Microscopy
ARC	Anti-Reflective Coating
ASC	Anti-Soiling Coating
Avg	Average
BF	Bifaciality Factor (%)
BiPV	Building Integrated Photovoltaics
BSk	Tropical, and Subtropical
Bwh	Tropical, and Subtropical Desert Climate
BWk	Arid Cold Desert
CA	Contact Angle (^{o})
C-AS	Central Asia
CF	Capacity Factors (%)
COVID-19	Coronavirus Disease
CSP	Concentrated Solar Power
Dfb	Warm Summer Continental or Hemiboreal Climate
DH	Damp Heat
DI	Deionized Water
E & SE-AS	East and Southeast Asia
EDX	Energy-Dispersive X-Ray Spectroscopy
EU	Europe
E-W	East-West Directions
ICP-AES	Inductively Coupled Plasma Atomic Emission Spectroscopy
IEC	International Electrotechnical Commission
IIT	Indian Institutes of Technology
I-V	Current Voltage Characteristics
LB	Latitude Mounted Bifacial Modules
LED	Light-Emitting Diode
LM	Latitude Mounted Monofacial Modules
M & E-AF	Middle and East Africa
ME	Middle East
N & W-AF	North And West Africa
NA	North America
OA	Oceania
PDF	Probability Density Function
PM	Particulate Matter
PM10	Particulate Matter of 10 µm and less suspended in air ($\mu g/m^3$)
PR	Performance Ratio
PV	Photovoltaic

RH	Relative Humidity (%)
RoA	Roll-Off Angle (º)
SA	South America
S-AF	Southern Africa
S-AS	South Asia
SEM	Scanning Electron Microscope/ Scanning Electron Micrograph
S-N	South-North Direction
TM-AFM	Tapping Mode Atomic Force Microscopy
UAE	United Arab Emirates
UK	United Kingdom
US	United States
UV	Ultraviolet
VB	Vertically Mounted Bifacial Modules
WAT	AM1.5G Weighted Average Transmittance (%)
WCA	Water Contact Angle (º)
XPS	X-Ray Photoelectron Spectroscopy

List of Symbols

E_a	Activation Energy (eV)
Adj R^2	Adjusted R^2
θ^*	Apparent contact angle on a rough surface (º)
At%	Atomic Percentage (%)
K_b	Boltzmann Constant (m^2 kg s^{-2} K^{-1})
B	Breadth of the sample (mm)
$\Delta\tau_{d,rsw}$	Change in Transmittance (%)
Cl	Chlorine
θ_E	Contact angle of an ideal flat surface (º)
τ_d	Direct Transmittance, without Integrating Sphere (%)
F1s	Fluorine
G_{rear}	Global Horizontal Irradiance Received on the Back Side of the Bifacial Module (W/m^2)
G_{STC}	Global Horizontal Radiation Measured at Standard Test Condition (W/m^2)
L	Length of the sample (mm)
P_{max}	Maximum Power (W)
G_{POA}	Measured Irradiance at the Plane of Array (W/m^2)
P_{mpp}	Measured Power at the Maximum Power Point (W/m^2)
µ	Micron
T_{STC}	Module Temperature at Standard Test Condition (℃)
P_{STC}	Module's Power Output at Standard Test Condition (℃)
L	Monthly Soiling Loss (%)
N	The exponential factor which indicates the pH dependence
N_{1s}	Nitrogen
O_{1s}	Oxygen
$\emptyset_S$	Percentage of Solid (%)
N	pH dependence factor
K	Potassium
r	Radius (mm)
Y	Rate of Rainfall (mm/h)
rpm	Revolutions per minute (min^{-1})
h_s	Scratch depth (nm)
W_s	Scratch width (µm)
β	Shape parameter of Weibull Distribution
I_{sc}	Short circuit current (A)
J_{sc}	Short-circuit density (mA/cm^2)
Si_{2p}	Silicon

Na	Sodium
NaCl	Sodium Chloride
y_{LV}	Surface Energy between liquid and vapour/Air (N/m)
y_{SV}	Surface Energy Between solid and liquid (N/m)
Ra	Surface roughness (nm)
T	Temperature (℃)
α	Time scale parameter of Weibull Distribution
Ti	Titanium
N_{drop}	Total number of droplets required to wet the top surface of the sample in 1 h
N_c	Total number of raindrops in a column in each sample
N_r	Total number of raindrops in a row in each sample
YI	Yellowness Index

Chapter 1 – Introduction

1.1 Background – Effect of Soiling

Accumulation of dust on photovoltaic modules (also referred to as soiling) is one of the most commonly reported problems in the photovoltaic (PV) sector in India. Countries with high particulate matter (PM) counts, like India, China and the Middle East, show high soiling losses that go up to 1%/day (shown in Fig. 1), estimating a financial loss of 1 billion euros/annum in the year 2023 [1]. Soiling loss is measured via soiling measurement stations (shown in Fig. 1), which typically have a pair of identical PV modules; one of them is cleaned daily, and the other is allowed to soil at a natural rate [2]. Soiling loss is calculated via equation 1. Daily energy generated on any day is calculated by integrating the peak power as a function of time. The slope of soiling loss versus the number of days gives the soiling rate. Soiling rates of approx 0.45 %/day (cumulative energy loss rate) was reported in Mumbai, India, as shown in Fig. 1. This poses a severe challenge to the economic viability of PV deployment in sunbelt countries like India. Soiling loss is calculated based on P_{max} in the case of non-uniform soiling and I_{sc}(short circuit current) is used as a parameter when the soiling patterns are uniform [3].

$$Soiling\ loss\ =\ 1 - \frac{\frac{P_{max}}{Daily\ Energy}}{\frac{I_{sc}\ (Soiled\ Module)}{\frac{P_{max}}{Daily\ Energy}}} \quad (1)$$

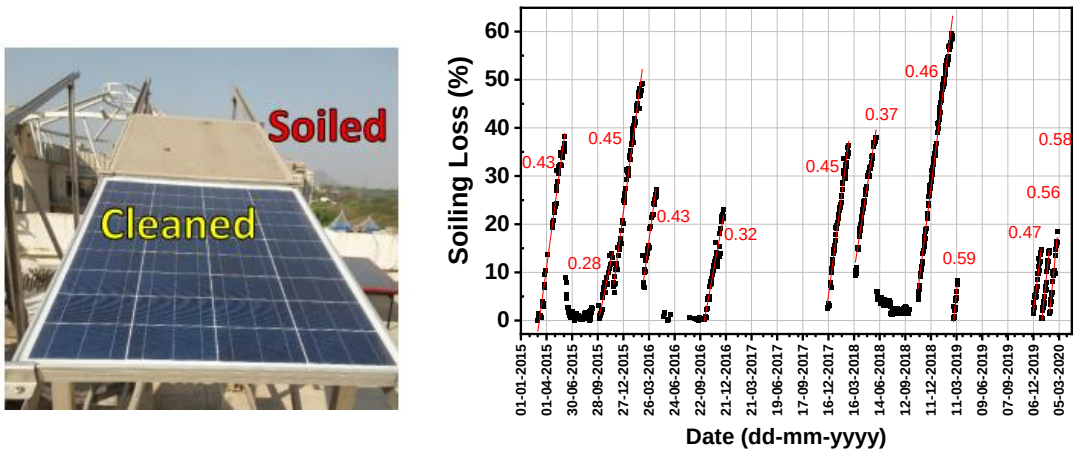

Fig. 1: Five-year soiling loss data for IIT Bombay, Mumbai, India. Soiling loss of the modules was calculated based on energy generation.

Soiling measurements can also be done via optical devices like Atonometrics, Mars Optical Soiling Sensor [4] and Kipp & Zonen's, DustIQ [5]. Such optical devices detect soiling loss based on transmission/reflection losses (for various soil types). They are calibrated against the conventional soiling measurement method (shown in Fig. 1). The optical sensors hold multiple advantages over the traditional soiling measurement setups, such as zero water requirement, no moving parts, no maintenance, compact design and low cost.

Soiling is a location-dependent phenomenon which depends upon various environmental factors like particle size, humidity, wind speed, chemical composition of dust, etc [6]. Short-term effect of soiling is observed as a decrease in the power output, whereas the long-term impact causes the formation of a cement-like coating on the surface of the PV module [7]. The cemented coating gets strongly bonded to the surface of the PV modules [10]. Three significant factors that influence dust deposition on PV modules are; (1) Environmental factors – wind direction, wind speed, dew, temperature, air pollution, humidity, dust storm, volcano and snow (2) Dust types – soil/sand, clay, bacteria, carbonaceous materials, etc. (3) location, module design and installation factors – glass material/top coatings, orientation, tilt angle, sandy area, industrial area, height, latitude (shown in Fig. 2) [8].

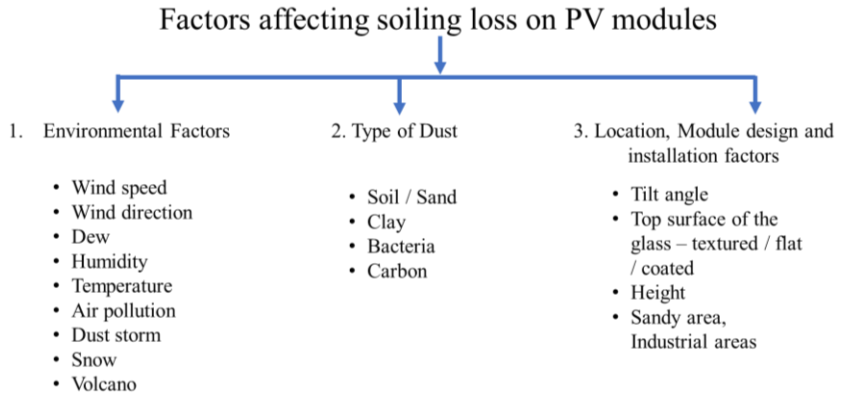

Fig. 2: Factors affecting soiling loss on PV modules.

Various PV developers and researchers use the external factor (3rd parameter - Location and installation factors) to develop new dust mitigation strategies. Dust mitigation technologies like robotic cleaning, electrostatic cleaning, tracker system, site adaptation techniques, etc., have been developed to reduce dust settlement [1]. However, these highly energy-intensive mitigation techniques increase maintenance costs [1]. This thesis discusses two cost-effective, universal, and

less energy-intensive dust mitigation strategies (1) dust mitigation via vertically mounted bifacial modules and (2) anti-soiling coatings.

1.2 Motivation and Objective

1.2.1 Dust Mitigation via Vertically Mounted Bifacial Modules

The angle of installation of solar panels is an important parameter that determines soiling of the module surface [8], [9]. A higher angle of installation leads to lower soiling [9]. However, fixed PV modules are to be installed at the Optimum tilt angle for the location, which has to be determined [10], [11]. Guo et al. theoretically analysed the energy generated by vertically mounted bifacial modules and compared it with monofacial modules mounted at latitude angle (fixed tilt) and predicted that the energy yield in the former case could be higher at many locations in the world [12]. Our objective was to evaluate the vertical mounting of bifacial modules to reduce losses due to soiling. We extend the nomenclature used by Guo et al. as follows: (i) Bifacial modules mounted at 90°, are hereafter referred to as vertically mounted bifacial modules (VB), (ii) bifacial modules mounted at the latitude angle (19° in Mumbai) are referred to as latitude mounted bifacial modules (LB), and monofacial modules mounted at the latitude angle are referred to as latitude mounted monofacial modules (LM). Bifacial modules with 90% bifaciality factor were used in the experiment, and all the relevant performance parameters are compared as a function of bifaciality. We also combined the energy produced by LB and VB for an extended generation profile. Experimental data from individual experiments on LB and VB are combined to evaluate this technique.

1.2.2 Dust Mitigation via Application of Anti-Soiling Coatings

Anti-Soiling (AS) coatings are nano or microlayer coatings, which reduce the settlement of dust on the surface of the PV module, and are extensively investigated as a mitigation strategy [1]. AS-coatings are economical and easy to maintain [1]. Even though AS-coatings may require water or air to clean the surface, the amount of water required and the frequency of cleaning runs may be significantly reduced. Anti-soiling coatings are classified into 4 types; (1) Superhydrophilic – contact angle $< 5^{\circ}$, (2) Hydrophilic – contact angle $< 90^{\circ}$, (3) Hydrophobic – contact angle is between 90° to 150°, and (4) Superhydrophobic – contact angle is between 150° to 180° [13]. Work on the development of various anti-soiling coatings has been widely reported [14]–[16]. However,

there are few reports on the detailed analysis of the performance and durability of these coatings for PV applications. As the AS-coating is applied to the outer surface of the PV module, degradation of the coating in harsh operating conditions is a concern [17]–[23]. This creates a need for a standardized test procedure to evaluate the reliability of AS-coatings relevant to PV applications. Most AS-coatings available in the commercial market are hydrophobic because it does not allow the water to wet the surface, and the dust particle adheres to the droplet rolling off the surface, thus acting as a cleaning mechanism. Illya Nayshevsky et al. also showed that hydrophobic surfaces show better cleaning efficacy of dust than hydrophilic surfaces [23]. Our work focuses on hydrophobic (water contact angle > 90^0) anti-soiling coatings. First, we identified the significant stressors that reduce the performance of 4 commercial hydrophobic AS-coatings during outdoor durability tests, conducted on solar glass samples and PV modules. Further, the effect of individual stressors like abrasion, rain, and UV radiation were studied on coated solar glass samples. The findings of the correlation study between outdoor and indoor accelerated stress tests were then used to compute a model for lifetime prediction of AS-coatings considering UV radiation and rain as a stressor.

1.4 Outline

As explained in the previous sections, soiling loss leads to enormous financial losses, and thus a cost-effective dust mitigation strategy is an urgent need in the PV sector. This work discusses two cost-effective and universal dust mitigation strategies (1) dust mitigation via vertically mounted bifacial modules and (2) anti-soiling coatings. In the 1^{st} chapter, we discussed the severity and the scale of the problem. We also discussed the factors that affect the rate and type of dust deposition on PV modules and how these parameters can be used to identify cost-effective dust mitigation strategies. The motivation and objective of the thesis are also mentioned in chapter 1.

A brief literature review on how soiling affects power generation, impact of soiling on energy costs in PV systems, and the current dust mitigation strategies available in the PV market are discussed in chapter 2. A literature review on vertically mounted bifacial modules and degradation of AS-coatings is discussed in chapter 2. Chapter 2 also states the research gaps in the current literature and explains how this thesis plans to address these research gaps.

In chapter 3, we established a dust mitigation approach via vertically mounted bifacial modules, which gave zero soiling loss and soiling rates. Chapter 4 compares the dust mitigation efficacy of

4 different commercial hydrophobic anti-soiling coatings (on solar glass and PV modules) with a not-coated (hydrophilic) sample under a controlled environment and outdoor field exposure. This is the first primary test the user can do to analyse the performance of any AS-coating.

Chapter 5 discusses a unique characterization technique developed to quantify the percentage of coating area using TM-AFM phase imaging. Phase imaging via Tapping Mode Atomic Force Microscopy (TM-AFM) is a non-destructive characterization method which shows high material contrast of fine structures that cannot be seen in topographical imaging (via AFM). With this method, we can also analyse samples under in-situ or controlled environments without any sample preparation.

As AS-coatings are applied on the outer surface of the PV module, it has to withstand harsh climatic conditions, making its durability a major concern. Thus, going forward in chapter 6, we identified the significant stressors that reduce the performance of AS coatings during outdoor field exposure. In this chapter, we also studied the effect of individual seasons that degrade AS-coatings.

In chapter 7, we investigate the individual factors that influence the effect of abrasion damage, rainfall, UV radiation and combination of various stressors on 4 different commercial hydrophobic anti-soiling coatings. This complete study was conducted on accelerated testbeds. Two accelerated testbeds, named the cleaning cycle simulator and the rainfall simulator, were developed to simulate the damage caused by outdoor abrasion and rain. A comparison of the performance of coated samples based on the IEC 61215 standard and our accelerated stress tests is also shown in this chapter.

The learnings from the correlation study between outdoor and indoor accelerated stress tests, shown in chapters 4, 6, and 7, were used to compute a model for the lifetime prediction of AS-coatings (shown in chapter 8), considering UV radiation and rain as a stressor. Chapter 9 summarises the findings of this thesis, and future directions of this research area are also discussed in this chapter.

The complete study helped us to develop a standard test procedure that the PV industry can use to test the reliability of anti-soiling coatings under warm and humid climates (shown in Appendix II).

Chapter 2 – Literature Review

2.1 Effect of Soiling on PV Power Production and Energy Costs

Soiling reduces power generation, often making PV installations economically unviable, making dust mitigation an urgent need [1]. However, the current dust mitigation strategies like robotic cleaning can significantly increase the price of the electricity generated by PV power plants. Klemens Ilse et al. have shown that even with optimised cleaning scenarios, soiling is estimated to have reduced global solar power production by at least 3% – 4% in 2018, causing global revenue losses of at least 3–5 billion euros/annum, this could rise to 4%–7%, and more than 4–7 billion euros/annum loss, in 2023, as shown in Fig. 3 [1]. Fig. 3 was estimated for the top 20 PV markets (about 90% of global installed PV capacity in 2018) and the global CSP market. The increase in soiling losses is majorly due to the increased deployment in high-insolation and highly soiling-affected countries such as China and India. Other factors that increase soiling losses are increased rooftop installation in PV and an increase in PV module efficiencies. However, these factors are not considered in the calculation shown in Fig. 3. Change in air quality may considerably impact soiling; however, air-quality policies generally operate over longer time scales. Effects of climate change, like increased temperature, droughts, higher PM counts, wildfires, and irregular rainfall, negatively impact soiling patterns and soiling rates [24].

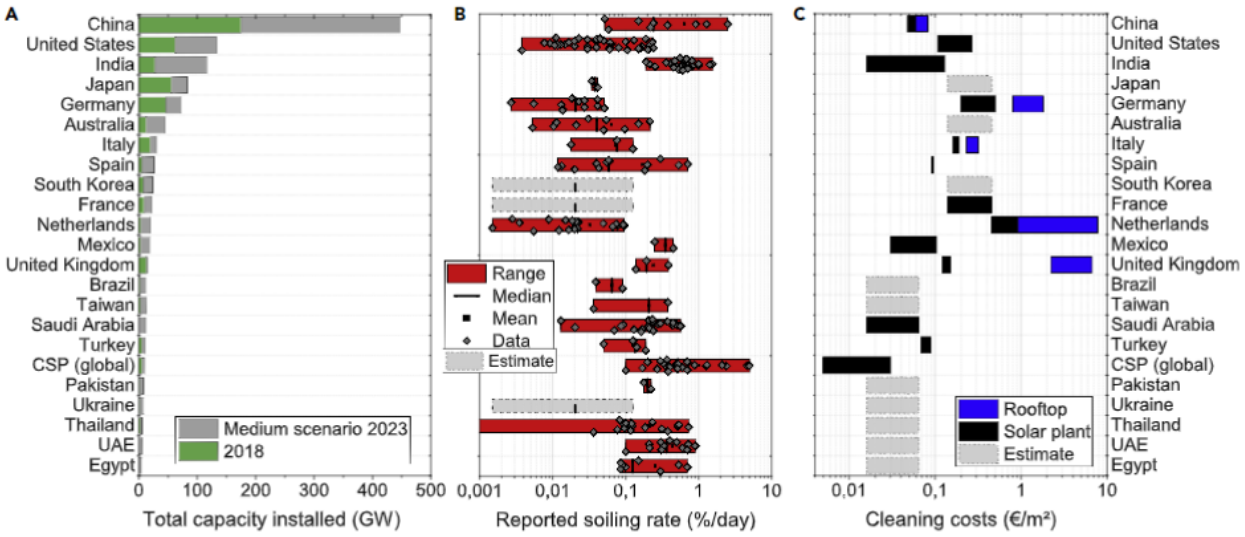

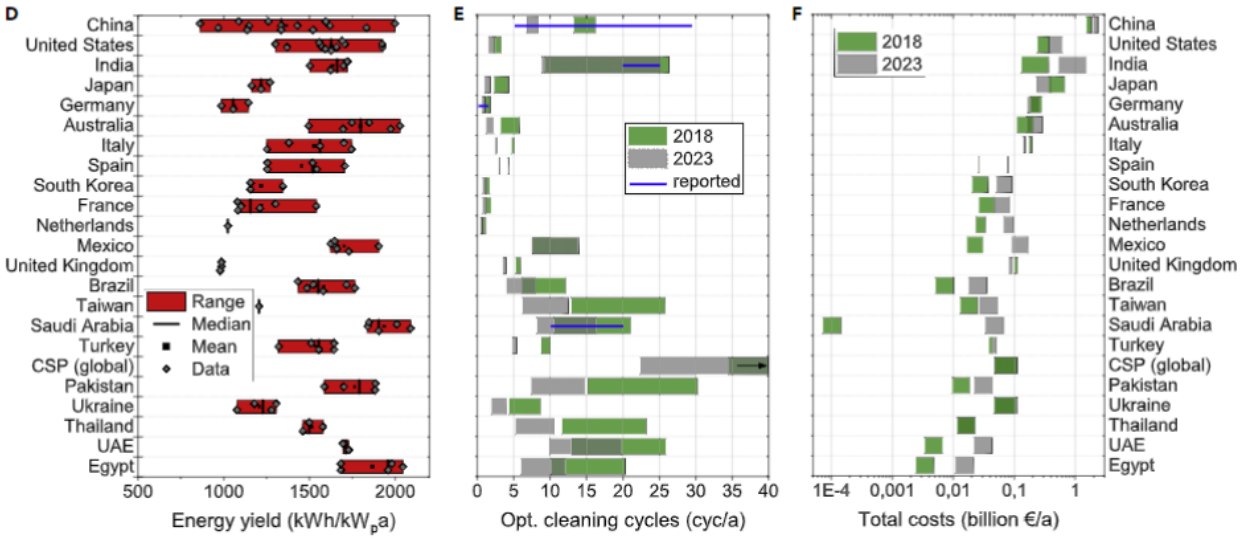

Fig. 3: "Impact of dust deposition on PV power generation and energy costs. (A) Installed PV capacity by 2018 and medium estimate for 2023, sorted by country. (B) Corresponding soiling rates reported (C) Reported cleaning costs per cleaning and square meter. (D) Typical energy yield in kWh/kWp. (E) Optimal number of yearly cleaning cycles (bars) and actual range of typical yearly cleaning cycles reported in literature (blue lines, modelled calculations are shown in box plots), and (F) Minimum expected financial losses due to soiling calculated from optimum cleaning cycles" [1].

Zhe Song et al. state that PV capacity factors reduce between 2% to 68% due to atmospheric aerosol attenuation (shown in Fig. 4) [24]. Besides dust deposition, air pollution reduces PV power generation by attenuating solar radiation through reflection, absorption, and scattering. COVID-19 lockdown restrictions reduced the levels of air pollution in many countries, improving atmospheric transparency, which increased PV power generation [25].

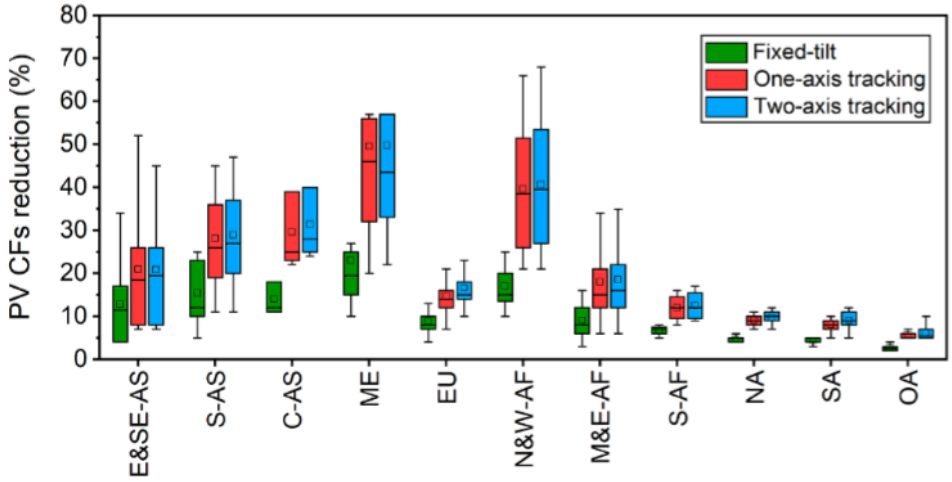

Fig. 4: "Reduction of PV capacity factors (CFs) due to atmospheric aerosols during 2003-2015. Note: East and Southeast Asia (E&SE-AS), South Asia (S-AS), Central Asia (C-AS), Middle East (ME), Europe (EU), North and West Africa (N&W-AF), Middle and East Africa (M&E-AF), Southern Africa (S-AF), North America (NA), South America (SA), Oceania (OA)" [24].

2.2 Dust Mitigation Strategies

As soiling is a location-dependent phenomenon, there is no universally recommended cleaning method as the economics, resource availability, and cleaning efficacy would change with local conditions. Broadly there are three types of dust mitigation strategies; (1) Cleaning of panels (PV modules), (2) Panel Mounting, and (3) Anti-soiling coatings [1]. Cleaning of PV modules is further subdivided into (1) Manual, (2) Semi-automatic and (3) Fully automatic [1]. Manual cleaning has a low capital cost and high labour cost and is prevalent in India. Semi-automatic cleaning can be divided into two sections: truck-mounted and portable robots/motorized brushes. Semi-automatic cleaning technologies have intermediate capital and labour costs and are common in US and Germany. Fully automatic systems have high capital and low/zero labour costs and are only common in extreme soiling locations. The factors influencing the optimal cleaning technology and optimal cleaning frequency are (1) Soiling type and deposition rates, (2) Water availability, (3) Accessibility of the site, (4) Labour cost, (5) Equipment required, (6) other financial factors and (7) System configurations (e.g., tracking versus fixed tilt angle, roof version ground-mounted) [1].

Other dust mitigation strategies are electrodynamic screens, tracking with inverted modules, site adaptations and Anti-soiling coatings (ASC) [1]. AS-Coatings are further classified into hydrophobic and hydrophilic surfaces [13]. Due to the recent developments in robotic cleaning technology, which can be integrated into the installed plant designs, fully automated cleaning/robotic cleaning, which represents 0.13% of the current global capacity, is expected to grow from 1.9 GW to 6.1 GW in 2022 [1]. Various types of robots/waterless cleaning systems have entered the PV market. The robotic cleaning industry has come up with new designs such as (1) On Truck type – BP Metalmeccanica, (2) Low water based – SunPower robots, (3) On Module type – Miraikikai, Raybot, (4) On Module frame – Exosun, Solar ASC and (5) On Specially Made Rails – Ecoppia, NOMADD. The major challenge in the robotic cleaning industry is power management, weight balance, integration issues and economic impact [26], [27]. Table 1 shows the dust mitigation potential, cost, and limitations of various dust mitigation strategies. In this thesis, we will discuss 2 dust mitigation strategies (tracking and anti-soiling coating) that are cost-effective and less energy intensive.

Table 1: "Optimum reduction of soiling rates, costs, limitations, and application scenario" for different dust mitigation strategies [1].

Sl. No	Mitigation Technology	Potential Optimum Reduction of Soiling Rates	Costs	Potential Limitations	Most Reasonable Application Scenario
1	Fully automated cleaning	> 95%	3–10 USD/m^2	Integration in plant design, research needed	PV utility-scale, ground mounted
2	Electrodynamic screen/shield (EDS)	<< 98% (laboratory), 32% - reported for 2-year study in Saudi Arabia	< 35 USD/m^2	expensive, large-scale application needs to be proven	BiPV, island systems, street lighting, rooftop, CSP
3	Tracking with inverted stowing	< 40%–60%	NA	Integration in plant planning, additional costs	utility-scale, ground mounted
4	Site adaption	Unknown, site-specific	NA	little experience, research needed	utility-scale PV
5	Anti-soiling coatings – Applied by glass manufacturer	<< 80% (literature review), < 20%–50% (authors estimate), 32% reported for commercial coating	< 2 USD/m^2	Performance dependent on location and season, degradation by cleaning and environmental stresses	utility-scale, residential, ground-mounted and rooftop, BiPV, CSP + extra benefit from AR property

2.2.1 Mounting Configuration of Modules

2.2.1.1 Effect of Tilt Angle

Studies show that the soiling loss decreases with the increase in tilt angle, as shown in Fig. 5 [9]. However, fixed PV modules are to be installed at the Optimum tilt angle for the location, which has to be determined [10], [11]. Ilse et al. showed that due to high humidity and low winds during the night and early mornings, dust accumulation during night time is higher than during sunshine hours [28]. During the night/non-sunshine hours, the module's temperature is lower than the ambient conditions, which enables the airborne particles to settle on the PV module's surface (also referred to as Thermophoresis) [29]. These principles were tested in our location, and we observed

that by inverting a monofacial module in a downward direction in the non-sunshine hour (as soiling is governed by gravity), we could reduce the soiling rate by 50%, as shown in Fig. 6.

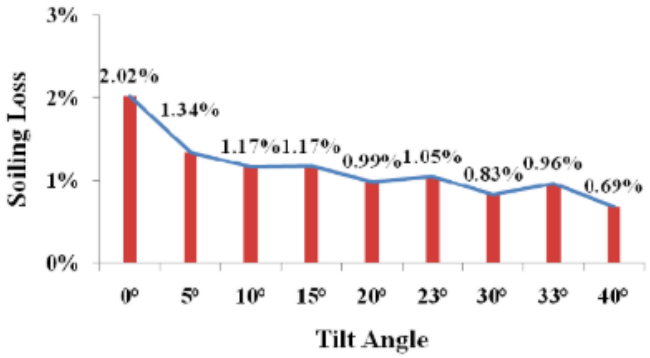

Fig. 5: Soiling loss on PV module with an increase in tilt angle [9].

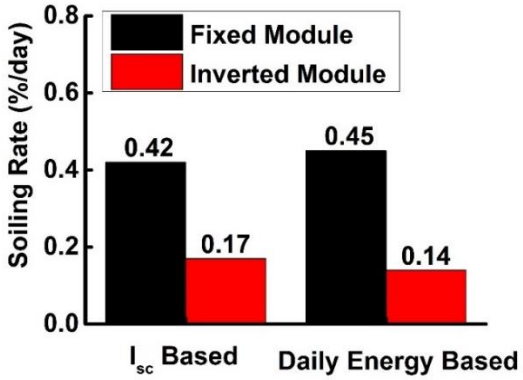

Fig. 6: Soiling rate of a fixed module and inverted module [29].

2.2.1.2 Performance of Vertically Mounted Bifacial Modules

Guo et al. analysed the energy generated by vertically mounted bifacial modules and compared that with monofacial modules mounted at latitude angle and predicted that the energy yield in the former case could be higher at many locations in the world [12]. The energy of vertically mounted bifacial modules would exceed the energy generation of monofacial modules for places with high albedo. Albedo is defined as the amount of radiation reflected from the earth's surface. Albedo value varies with different materials shown in Fig. 7 [30].

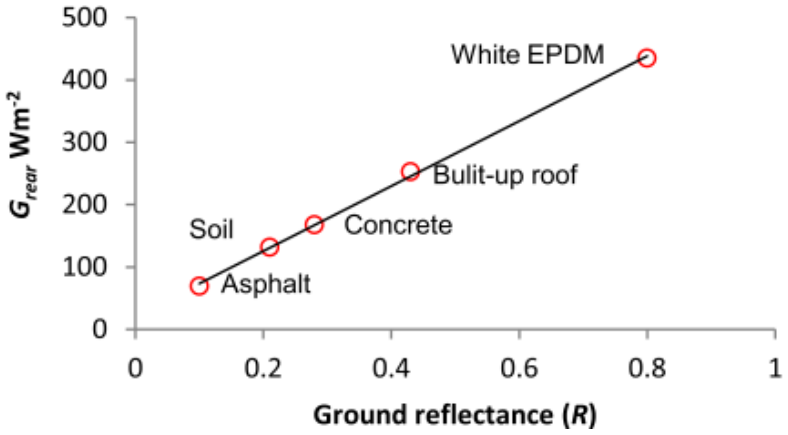

Fig. 7: Effect of material type on G_{rear} on bifacial module. G_{rear} *is the* Global Horizontal Irradiance received on the back side of the bifacial module (W/m^2) [30].

The power generation profile of a vertically mounted bifacial module has two peaks, i.e., one in the early morning and one in the afternoon, whereas the monofacial modules have only one peak in the noon time (shown in Fig. 8 [12]). Vertically mounted bifacial modules are mounted at the East-West direction, whereas the monofacial modules are mounted in the South-North direction. Guo et al. also analysed that vertically mounted bifacial modules receive 1% extra radiation than monofacial modules for places with higher diffuse fractions and low albedo values [12], shown in Fig. 9.

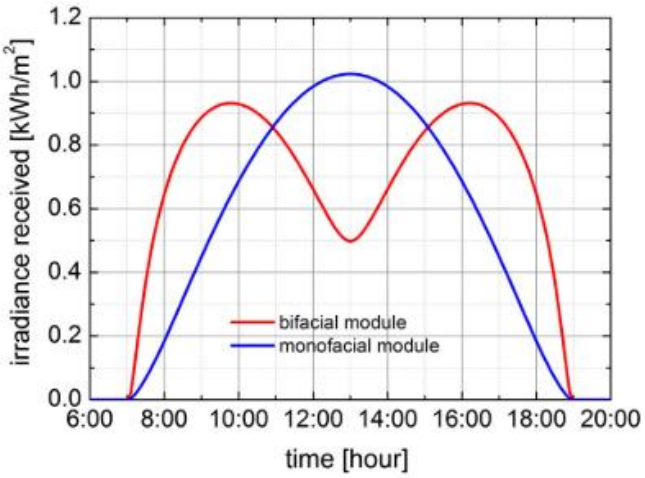

Fig. 8: Radiation profile of vertically mounted bifacial module and monofacial module throughout the day [12].

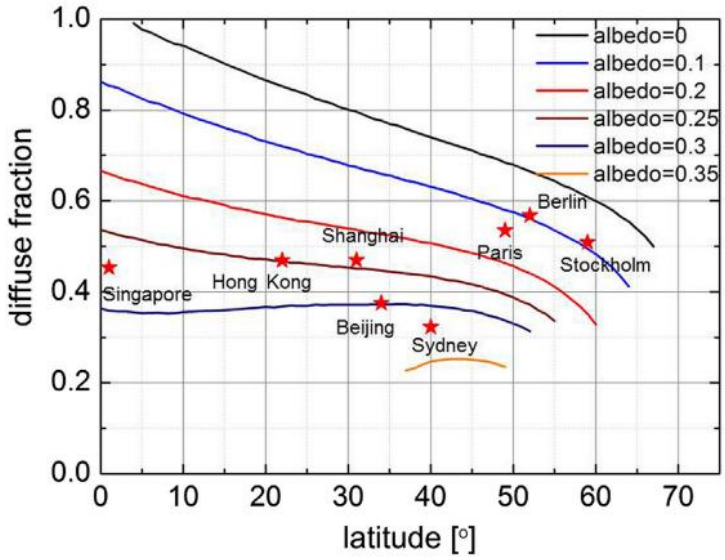

Fig. 9: Diffusion fraction and albedo values for which vertically mounted bifacial modules receive 1% extra radiation than monofacial modules [12].

2.2.2 Anti-Soiling Coatings

AS-coatings are nano/micrometer thick transparent coatings applied on the outer surface of the PV module front glass to mitigate the settlement of dust on PV modules [19]. AS-coatings are broadly grouped into 4 categories (shown in Fig. 10), viz. hydrophobic/super-hydrophobic, which repels water and has a water contact angle of more than 90º/150º, and hydrophilic/superhydrophilic, which attracts water and has a water contact angle of less than 90º/5º [13].

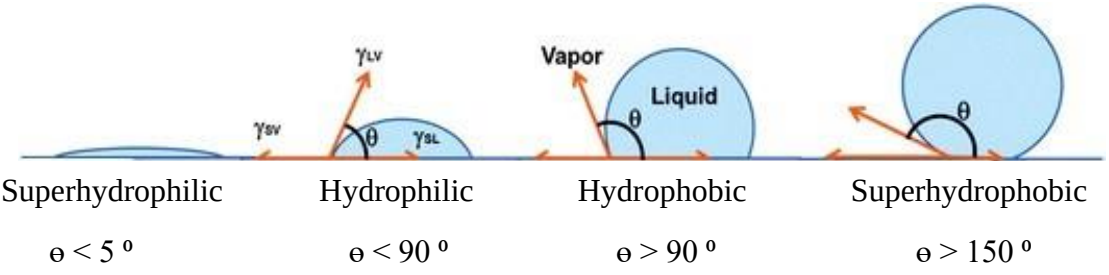

Fig. 10: Schematic diagram of superhydrophobic, hydrophobic, hydrophilic, superhydrophilic surfaces, y_{LV} is the surface energy between liquid and vapour/air, and y_{SV} is the surface energy between solid and liquid [13].

According to Cassie – Baxter and Wenzel's theory, the hydrophobicity of a substrate can be increased by increasing the roughness of the coated surface [31]. This indicated that roughness and contact angle are critical parameters for characterising anti-soiling coatings. In hydrophobic surfaces, the roll-off angle (the angle at which the water droplet would start to roll-off the coated surface [32]) is also an essential characteristic property.

2.2.2.1 Surface Characteristics of Hydrophobic and Hydrophilic Substrates

Hydrophilicity and hydrophobicity depend on mainly three factors given below

1) Contact angle
2) Surface roughness
3) Surface energy

The surface chemistry of a material determines low or high surface energy. Materials with low surface energy, like fluorinated materials or the addition of silicone compounds, are super-hydrophobic [33]. However, perfectly clean Ti surfaces with unsaturated chemical bonds represent a high-energy surface and show hydrophilic properties [34]. Higher surface energy represents hydrophilic property, and lower surface energy represents hydrophobic property.

According to Cassie – Baxter's theory, in a hydrophobic substrate, water droplets sit on the tiny air bubbles formed between the rough surfaces, as shown in Fig. 11 (a). Thus, hydrophobicity is enhanced as the droplet sits partially on the air [35]; in this state, water rolls off and takes the dirt away (shown in Fig. 11, b). Cassie – Baxter state occurs on very rough surfaces. According to Wenzel's model, a hydrophilic substrate's surface roughness increases the solid's wetted area, which increases the hydrophilicity of the surface [36].

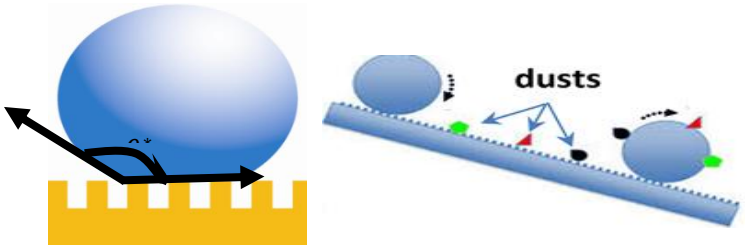

(a) (b)

Fig. 11: (a) Cassie – Baxter theory of water droplets sitting on hydrophobic rough surface, θ^* is the apparent contact angle on a rough surface [35]. (b) Schematic diagram of self-cleaning action of hydrophobic surface [33].

This particular form of the Cassie – Baxter equation is given as in equation 2 [37].

$$Cos\theta^* = -1 + \emptyset_S(Cos\theta_E + 1) \quad (2)$$

In equation 2, $\emptyset_S$ denotes the percentage of solid, θ_E is the contact angle of an ideal flat surface and θ^* is the apparent contact angle on a rough surface. From the equation, we may infer that θ^* is dependent on the percentage of solid that is in contact with the surface. Thus, as the value of $\emptyset_S$

approaches 0, $Cos\theta^*$ approaches -1, leading to θ^*=180º and making the surface super-hydrophobic.

Wenzel's equation for hydrophilic surfaces is written in equation 3.

$$Cos\theta^* = \frac{\gamma_{SV} - \gamma_{SL}}{\gamma_{VL}} = \text{r. } Cos\theta_E \qquad (3)$$

$$\text{r} = \frac{Real\ Surface\ Area}{Projected\ Suface\ Area}$$

Where γ_{SV} is the surface energy between solid and vapour/air (N/m) and γ_{SL} is the surface energy between solid and liquid (N/m). As all real surfaces are uneven at the molecular level. We assume r = 1.

$$Cos\theta^* > \text{r. } Cos\theta_E \qquad (4)$$

Where θ_E is the contact angle of an ideal flat surface and θ^* is the apparent contact angle on rough surface. An example of equation 4 is given in Table 2.

Table 2: Increase in hydrophobicity/hydrophilicity.

Hydrophilic	**Hydrophobic**
$\boldsymbol{\theta_E} <$ 90º	$\theta_E >$ 90º
Assuming, $\boldsymbol{\theta_E}$ = 45º	Assuming, θ_E = 135º
r = 1.2	r = 1.2
$\boldsymbol{\theta^*}$ = 32º	θ^* = 148º

An interesting example of this is the Namib Desert beetle shell which lives in an arid area called Namib desert in Africa [38]. The surface of the Namib Desert beetle shell is covered with bumps. The peak of each bump is hydrophilic, and the slopes of each bump and the troughs in between are hydrophobic [38]. During the morning fog, the water sticks to the peaks of Namib Desert beetle bumps, eventually forming droplets. When the droplets become large and heavy enough, they roll down (hydrophobic nature) from the top of the peaks and are channelled to a spot on the beetle's back that leads straight to its mouth.

2.2.2.2 Performance and Durability of AS-coatings – Outdoor Tests

Study conducted in Nottingham, UK (Climate zone – Cfb, Oceanic climate) – Kenan Isbilir et al. reported after 6 months of outdoor exposure that the water contact angle of the coated surface

showed ~31% (shown in Fig. 12) degradation [39]. The roll-off angle was increased by ~64º and measured to be 84º. In this study, the authors have tested a commercially available hydrophobic coating that is used on lenses and displays. This study was done in Nottingham, UK, from July to February at a tilt angle of 45º. The temperature range during this period was 21.3ºC to -0.5ºC. Rainfall varied from 85.1 to 46.2 mm each month. Sunshine duration per month ranged from 178.5 to 54.9 hours.

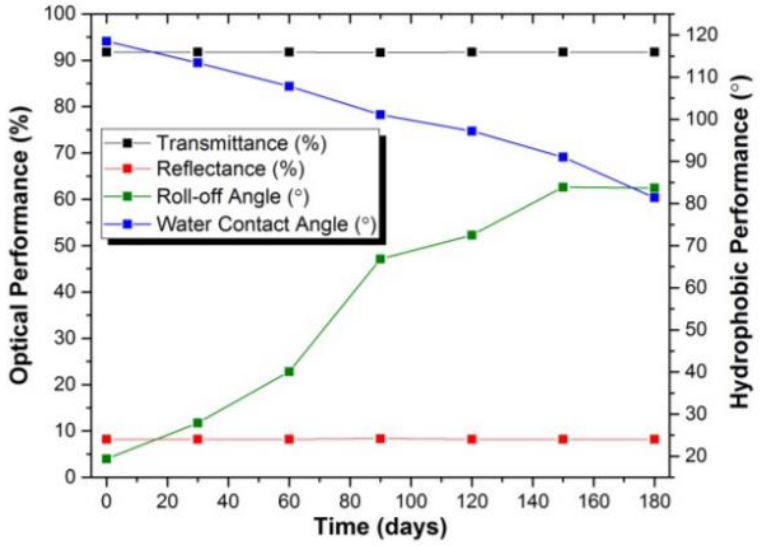

Fig. 12: "Optical and hydrophobic performance of outdoor sample" [39].

From a study conducted in Denmark (Climate zone – Dfb, Warm summer continental or hemiboreal climate) and Colorado (Climate zone – BSk, Tropical, and Subtropical), Gizelle C. Oehler et al. reported the performance of 2 transparent hydrophobic AS-coatings (Coating A and B) exposed to the outdoor environment of coastal Denmark for 24 weeks [32]. Coating A degraded after a few weeks of field exposure. Surface defects such as small pits were found in coating A at its initial stage. These resulted in blister formation at an early stage for coating A, whereas coating B did not have any surface defects at its initial stage (shown in Fig. 13).

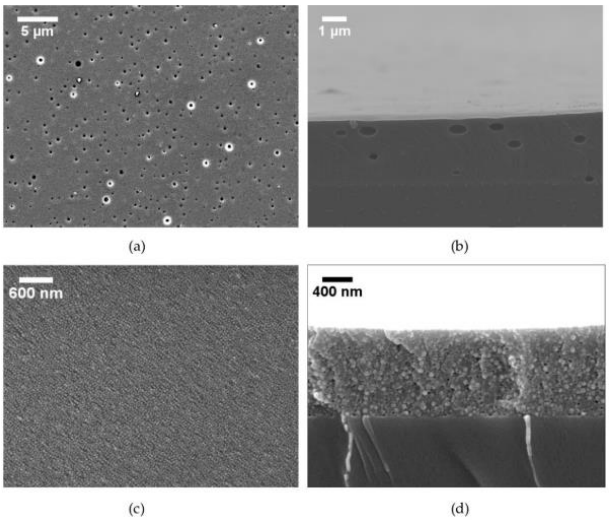

Fig. 13: "SEM (Scanning Electron Microscope) images of the as-received (initial stage, without any exposure) sample with coating A in (a) planar view, which shows surface defects and (b) cross-sectional view showing the presence of voids, and coating B in (c) planar view and (d) cross-sectional view showing no defects" [32].

Contact angle reduction measured during outdoor exposure time is shown in Fig. 14. High rate of initial degradation of contact angle was observed for both coatings A and B in the first two weeks of exposure, dropping by 7.4° (6.9%) and 12.4° (13.8%), respectively.

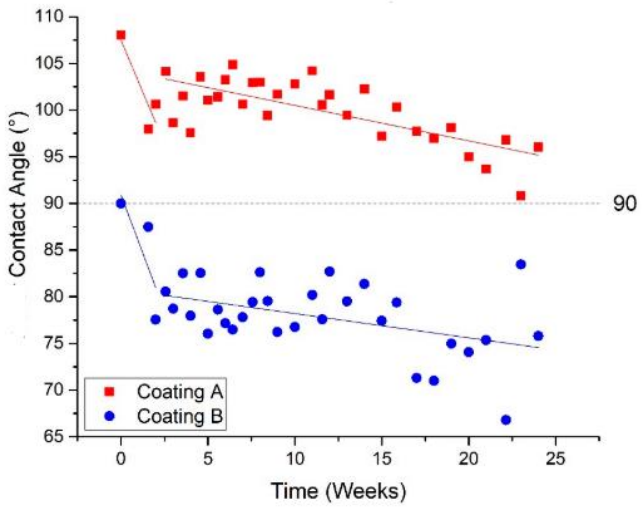

Fig. 14: Contact angle measurements for coated samples under field exposure. The data points below the black dashed line are hydrophilic (which indicates that the coating has degraded) [32].

The samples began exposure during the winter month of February when temperatures often went below 0°C. The samples were exposed to sub-zero temperatures, rainfall, and high humidity in the first two weeks. Due to the presence of rain and high humidity, surface defects like holes and blistering of the coated area were exposed to water condensation (shown in Fig. 15).

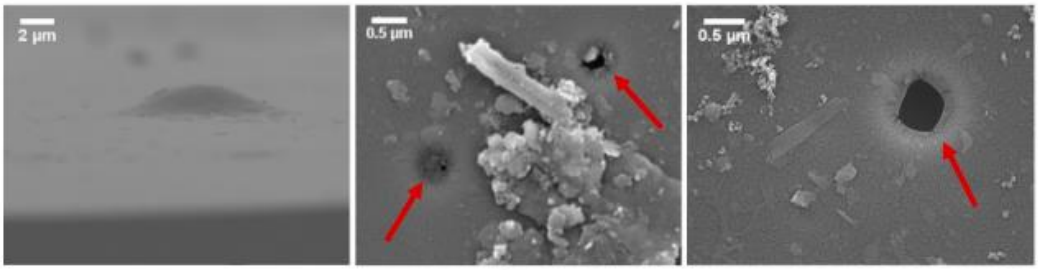

Fig. 15: "SEM images of coating A (a) cleaned sample after 4 weeks, (b) cleaned sample after 12 weeks, and (c) not cleaned sample after 15.3 weeks. The arrows points to partially and newly exposed pits" [32].

When the temperature dropped below 0°C, the water within these surface defects froze and expanded, causing stresses within the coating. In the surface analysis done via XPS (X-ray photoelectron spectroscopy), the authors found that the drop in contact angle for coating A correlated well with the reduction in fluorine content, which was reduced by 43.2% relative to the initial value (Table 3).

Table 3: "X-ray photoelectron spectroscopy (XPS) of cleaned coating A showing changes in elemental composition before and after 4 and 24 weeks of exposure" [32].

Week	Composition of Cleaned A (at%)							F reduction
	F1s	O1s	C1s	Si2p	N1s	Cl2p	K2p	
0	28.2	22.9	36.4	10.8	1.7	-	-	
4	23.1	23.4	38.5	11.2	1.9	1.1	0.9	18.1%
24	16.0	27.2	41.0	13.0	2.0	0.8	-	43.2%

Abrasion damage was evident in coating B from the first cleaning cycle conducted after 4 weeks of exposure (shown in Fig. 16). Coating A also showed abrasion damage, but at a much later stage, after 15.3 weeks of exposure.

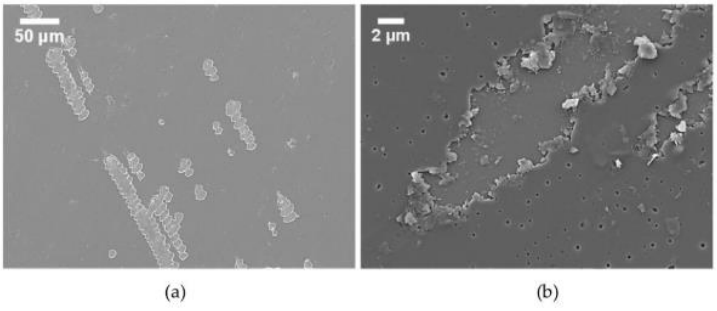

Fig. 16: "Signatures of abrasion damage caused by cleaning of (a) coating B after 4 weeks and (b) coating A after 15.3 weeks" [32].

Cl (Chlorine) on coating B (shown in Fig. 17) indicates that Cl is a surface contaminant, likely deposited by the wind from the nearby ocean. Cleaning the samples could not remove all traces of Cl. It was also observed that cycles of light rainfall and evaporation combined with humidity and

salty environmental conditions led to cementation on all samples (shown in Fig. 17). The SEM micrographs revealed that NaCl acts as the bridge between the dust and the coating surface.

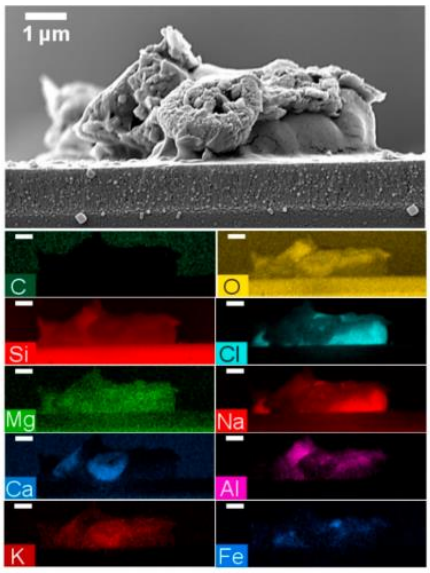

Fig. 17: "SEM and energy-dispersive X-ray spectroscopy (EDX) (coloured elemental images) of cementation on a not-cleaned coating B after 8 weeks of exposure. The white scale bar represents 1 µm in each image" [32].

The potential of AS-coating (named 'Coating-A') was confirmed in an outdoor PV test bed at Colorado State University in Fort Collins, Colorado (shown in Fig. 18). The coated module was fully operational after the snowfall, while the not-coated module retained snow coverage and thus produced no power (Fig. 18, a). After the snowmelt, the self-cleaning property of the coating was also evident; we may observe residues of dust visible on the not-coated module (Fig. 18, b), which was not present in the case of coated modules. These results confirmed the potential of hydrophobic AS-coatings in outdoor field conditions.

Fig. 18: (a) The black module (which is not covered with snow) was coated with a hydrophobic coating (coating A). "(b) Following the snowmelt, dust residues were deposited on the not-coated module (left), while the coated module (right) remained clean" [32].

DSM AS-coating tested in China (Climate – BWk, arid cold desert) [40] – P. Tummers reported testing of the DSM AS-coating that exhibits both anti-reflective and anti-soiling properties [40]. The wind speed in this location is usually low (1-5 m/s), and when there is a dust storm, the maximum wind speed can go up to 20 m/s. Three types of modules were tested – not coated modules, modules coated with AS-coating, and modules coated with anti-reflective coating. Each type of module had 10 pieces. The study shows that the increase in energy production due to the use of AS-coating was 1.1% (average), and it varied depending on environmental conditions and soiling rates (shown in Fig. 19). The formula used for calculating performance ratio (PR) is given in equation 5.

$$\mathrm{PR} = \frac{\mathrm{G_{STC}} \times \mathrm{P_{mpp}}}{\mathrm{G_{POA}} \times P_{STC} \times \left[1 + \frac{\gamma}{100}(T_{mod} - T_{STC}\right]} \quad (5)$$

In equation 5, G_{STC} refers to global horizontal radiation measured at STC (Standard test conditions, 25 ^{0}C and 1000 W/m^2), P_{mpp} refers to measured power at the maximum power point, G_{POA} refers to measured irradiance at the plane of array, P_{STC} refers to the module's power output at STC, γ refers to the module temperature coefficient of power. Throughout the experiment, the coated module (both anti-soiling and anti-reflecting coatings) showed better performance than the not coated module (Not coated module is denoted as BL in Fig. 19, (a)). During the high soiling month (November 2016), the coated modules showed a lower soiling rate (the soiling rate of the AS-coated module was 0.15 %/day, and the anti-reflective coated module was 0.22 %/day). The soiling rate of the not-coated module was 0.24 %/day (Not coated module is denoted Bare glass in Fig. 19, b).

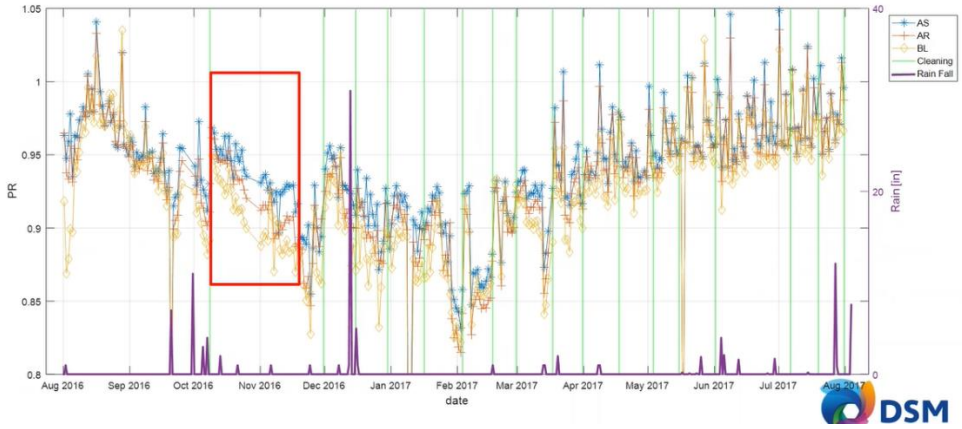

(a)

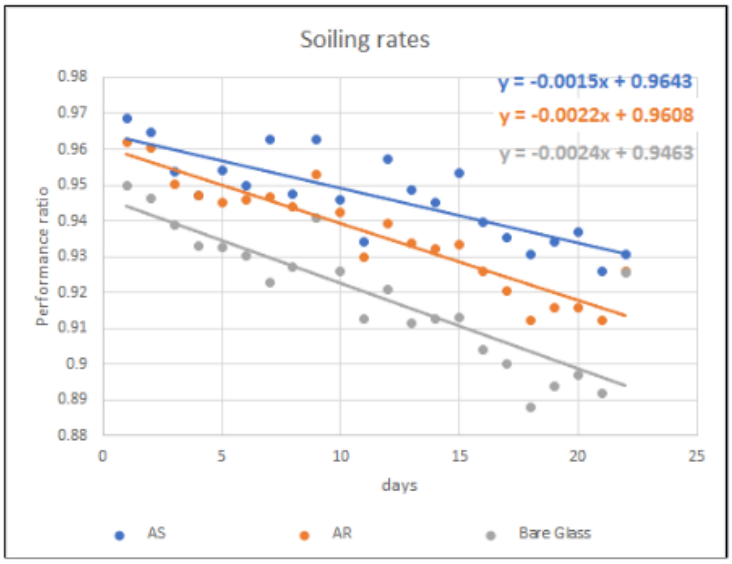

(b)

Fig. 19: a) Performance ratio of coated and not-coated modules under outdoor exposure in China (cold arid desert) for 1 year. b) Soiling rates of coated and not coated modules during November 2016 (indicated as a red box in Fig 19 (a). Here, the legend AS refers to the module coated with anti-soiling coating, AR refers to the module coated with anti-reflective coating, and BL and Bare Glass refers to the not coated modules. Green lines refer to manual cleaning intervals [40].

Study conducted in Saudi Arabia (Climate zone – Bwh, Tropical, and Subtropical Desert Climate) showed that the occurrence of dew has a higher correlation with soiling rates than other investigated factors, such as dust concentration and precipitation frequency as shown in Fig. 20 [41]. In Fig. 20, we may observe that the performance of a hydrophilic coating (ASC-III) was significantly better in humid areas like Al-Khafji, while the hydrophobic coating (ASC-II) performed better in dry conditions like Solar Village (shown in Fig. 20, Fig. 21 and Fig. 22).

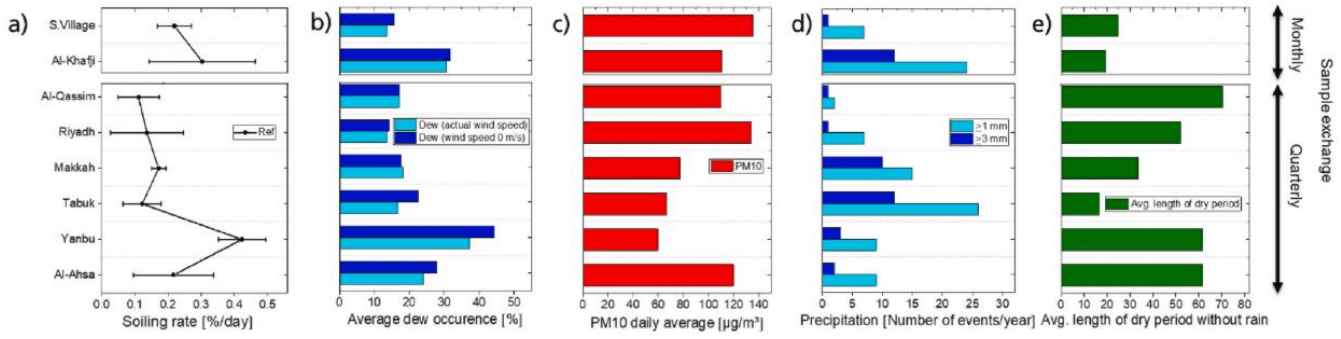

Fig. 20: "Soiling rate and weather parameters comparison based on daily average values for 2019–2020. a) soiling rate, b) average dew occurrence at actual wind speed and 0 m/s, c) PM10, d) number of events of precipitation in a year, e) Average length of the dry period" [41].

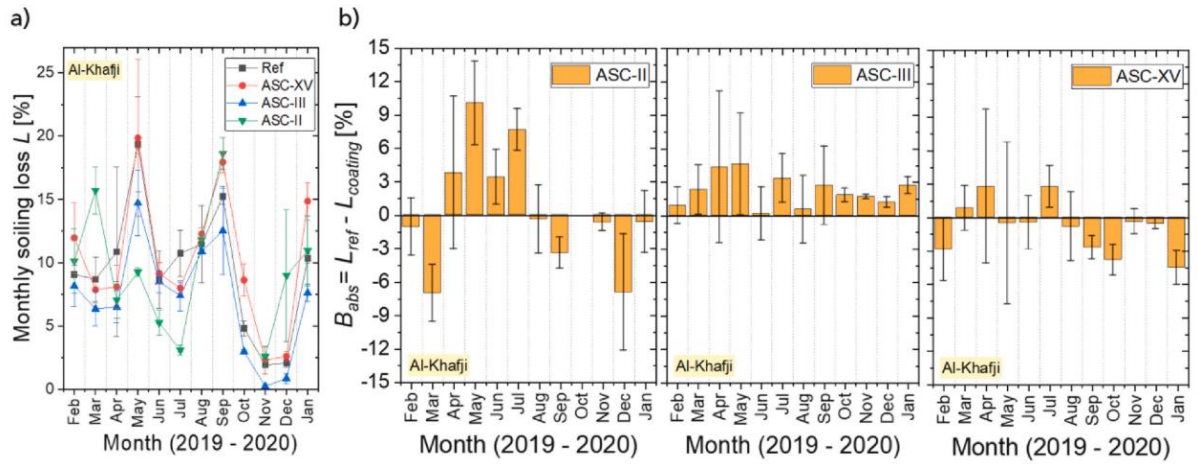

Fig. 21: "Performance of anti-soiling coatings at Al-Khafji site a) soiling trends b) absolute soiling benefits" [41].

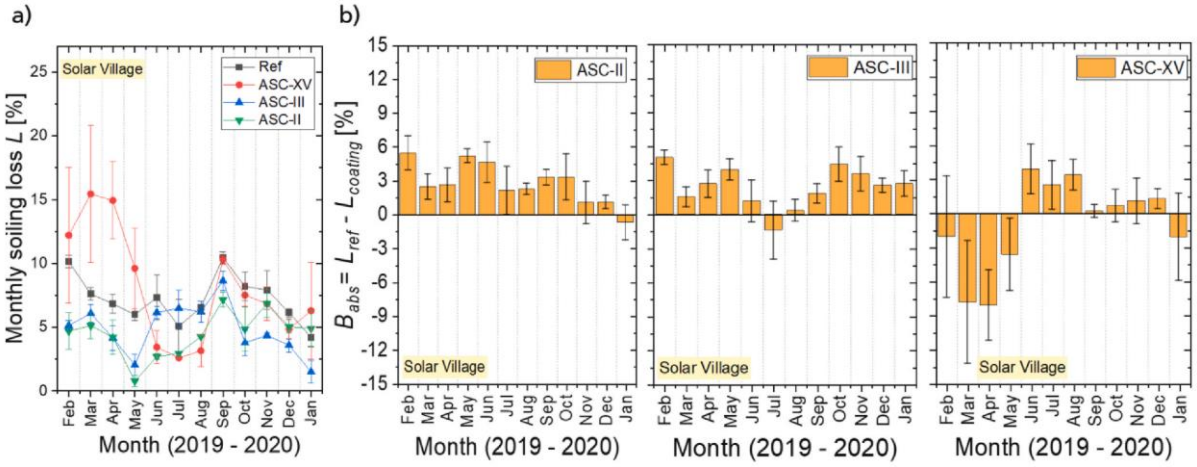

Fig. 22: "Performance of anti-soiling coatings at Solar Village site a) soiling trends, b) absolute soiling benefits" [41].

2.2.2.3 Performance Testing under Accelerated Stress and under a Controlled Environment

2.2.2.3.1 Dust Deposition

D. Goossens reported the effect of dust deposition on coated (DSM AS-coating and DSM anti-reflective coating) and uncoated (not-coated) surfaces [42]. Belgian Brabantian loess was used as test dust [42]. Dust cloud (median diameter = 37µm) was generated by a wind tunnel using a constant dust supply and airflow to ensure uniform dust deposition. It was concluded that for 0° tilt angle, the AS-coating and anti-reflective coatings showed no dust-attractive nor any dust-repellent benefits compared to not-coated (denoted as "uncoated" in Fig. 23) glass during low wind speed conditions. Dust deposition mainly affected the transmittance in the long-wavelength part of the spectrum (shown in Fig. 24).

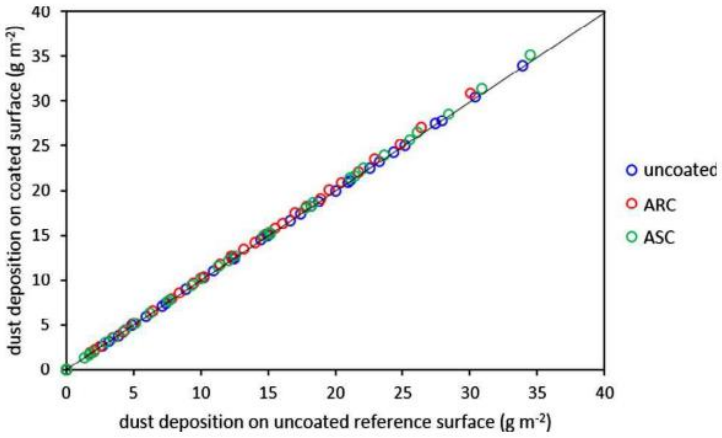

Fig. 23: Dust deposition on the coated surfaces of ARC (DSM anti-reflective coating) and ASC (DSM AS-coating) compared to the uncoated surface (not-coated surface). The tilt angle was kept at 0˚ for all 3 cases [42].

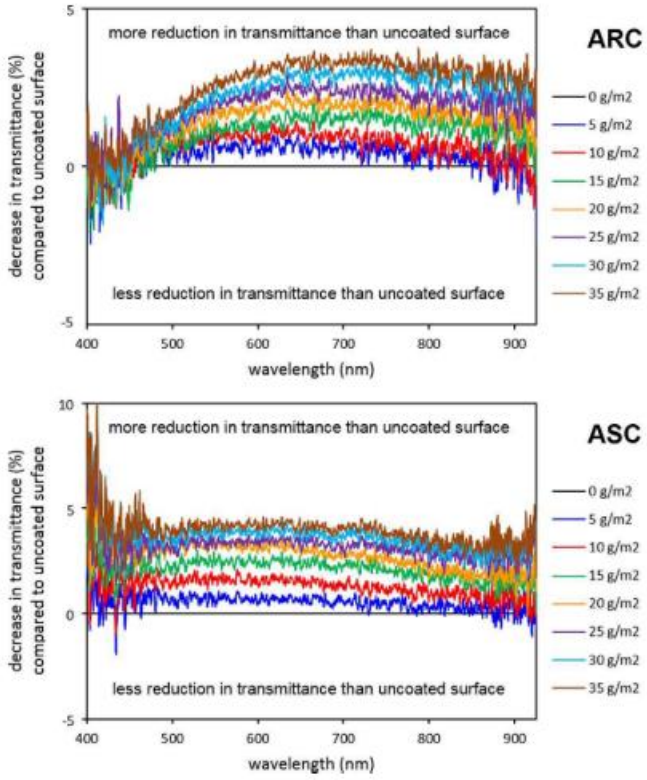

Fig. 24: Transmittance of coated surfaces with an increase in dust density (ARC refers to the samples coated with DSM anti-reflective coating, and ASC – refers to the samples coated with DSM anti-soiling coating) relative to the not-coated surface [42].

Illya Nayshevsky et al. showed that in a uniform artificial dust deposition chamber, soiling rates are lower for dust that is unreactive with water (Arizona Test Dust) and dust that contains NaCl (Aramco Test Dust), which is highly soluble in water [43]. In contrast, calcium carbonate ($CaCO_3$)

and Portland cement, which can chemically react with water, show higher soiling rates than silicate-based dust (shown in Fig. 25). The higher soiling rates are observed on the deposition of reactive dust on bare (not coated) glass substrates than a glass coated with hydrophobic or hybrid AS-coating (Fig. 25).

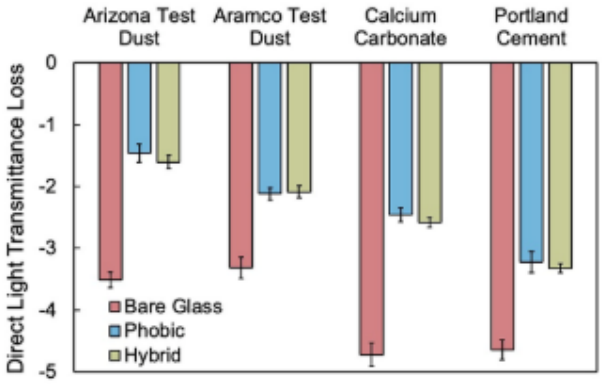

Fig. 25: Change in transmittance with respect to the dust type and surface coating for Bare Glass, Phobic, and Hybrid coatings after three dew-dust-bake soil deposition cycles. Bare glass refers to the not coated glass, Phobic glass refers to the glass coated with a hydrophobic anti-soiling coating, and Hybrid glass refers to glass coated with hydrophobic and hydrophilic AS-coating [43].

2.2.2.3.2 Dust Removal

The DSM AS-coating showed higher dust removal at lower wind speeds (shown in Fig. 26) and also cleaned the surface more rapidly than the DSM anti-reflective coating. However, at the end of the tests, the cleaning rate was identical for both anti-soiling and anti-reflective coatings (88%) [42]. The coatings (DSM AS-coating and anti-reflective coating) performed much better than the uncoated surface (not-coated glass), for which dust removal started at a considerably higher wind speed and the cleaning rate at the end of the tests was only 71%.

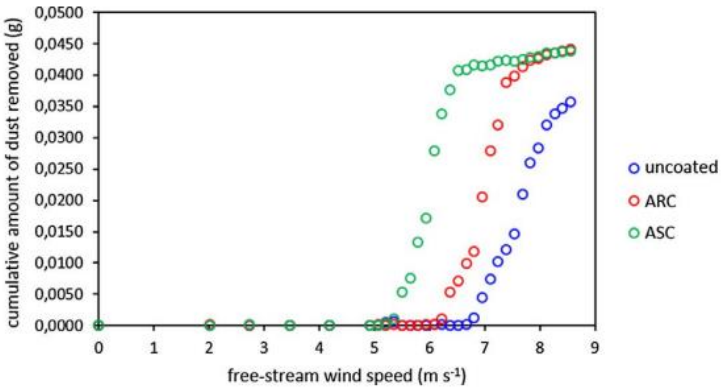

Fig. 26: Cumulative dust removal curves for the coated surfaces (DSM AS-coating and DSM anti-reflective coating) and the uncoated (not-coated) surface[42].

Illya Nayshevsky et al. [43] stated that a glass coated with hydrophobic or a hybrid (hydrophobic and hydrophilic) AS-coating shows anti-soiling behaviour compared to a not-coated glass for four types of dust samples (shown in Fig. 27). In this study, self-cleaning of the artificial dust was observed by simulating natural dew. For not-coated glass samples, water condenses in a film-wise manner. Dust particles become suspended within the liquid water film and are redistributed during drying. For samples coated with hydrophobic AS-coating, water suspends in a dropwise manner and evaporates by leaving the dust at the central point [44]. Anti-soiling effectiveness was also compared qualitatively by visual comparison of not-coated glass, glass coated with hydrophobic and hybrid (hydrophobic and hydrophilic) AS-coating after three dew–dust–bake cycles (Fig. 28). Hybrid and hydrophobic samples exhibit the same dust deposition as expected because both the coatings were prepared using the same method.

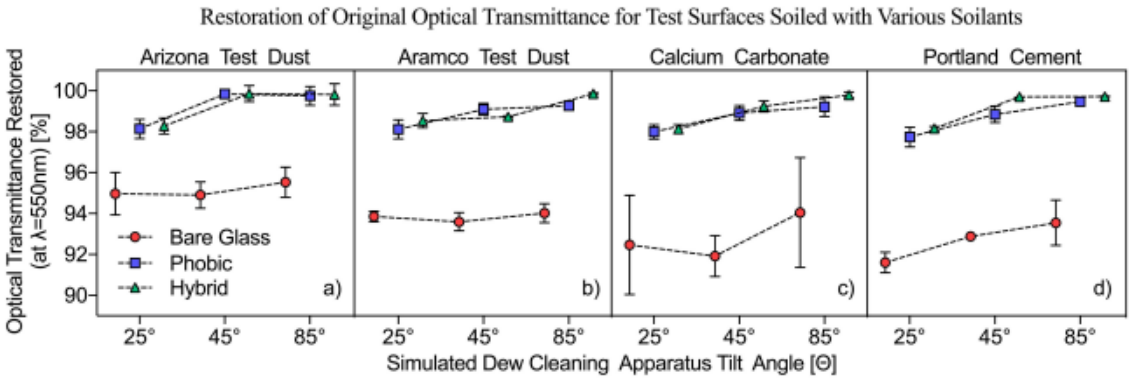

Fig. 27: "Restoration of original transmittance as a function of simulated dew cleaning tilt angle on Bare Glass, Phobic and Hybrid coatings after three dew-dust-bake soil deposition cycles; utilizing a) Arizona Test Dust, b) Aramco Test Dust, c) calcium carbonate, and d) Portland cement." Bare glass refers to the not coated glass, Phobic glass refers to the glass coated with hydrophobic AS-coating, and Hybrid glass refers to the glass coated with hydrophobic and hydrophilic AS-coating [43].

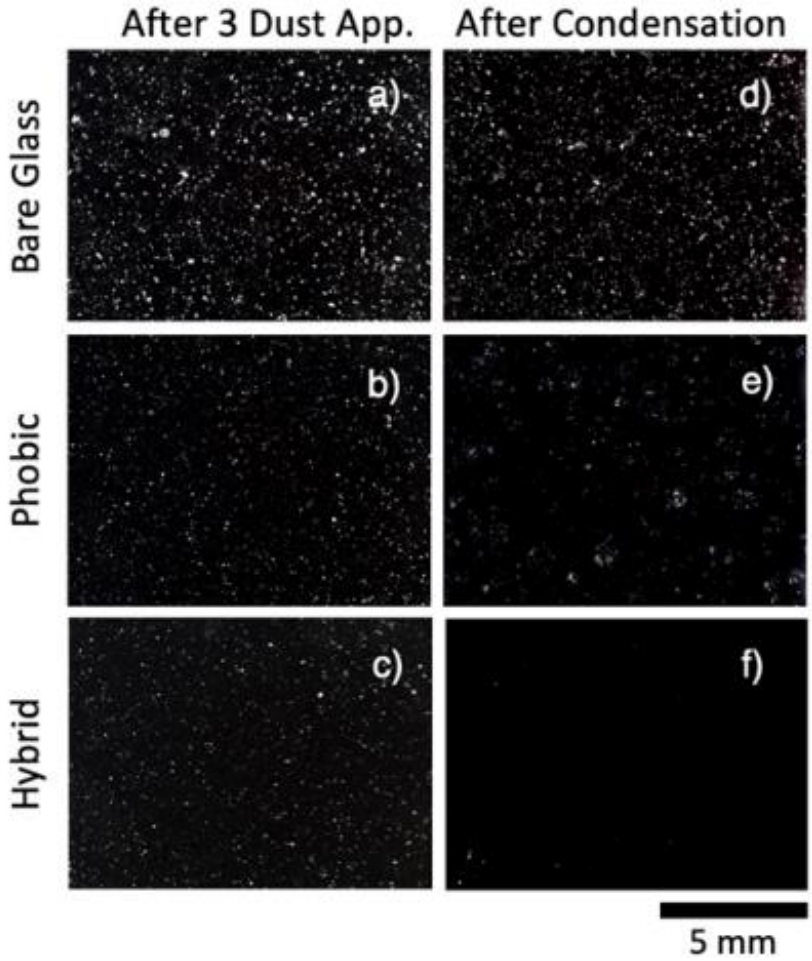

Fig. 28: "Microscopy images of Bare Glass, Phobic and Hybrid surfaces after 3 dew-dust-bake cycles (a, b, c respectively) and after simulated dew cleaning (d, e, f respectively), soiled with Portland cement test dust". Bare glass refers to the not-coated glass, Phobic glass refers to the glass coated with hydrophobic anti-soiling coating, and Hybrid glass refers to glass coated with hydrophobic and hydrophilic AS-coating [43].

2.2.2.3.3 Accelerated Stress Tests

(A) UV Exposure and Damp Heat Test

Kenan Isbilir et al. [39] reported that hydrophobic AS-coatings show no significant degradation after accelerated humidity freeze and thermal cycling test based on the IEC 61215-2:2016. The coating was also able to withstand damp heat exposure of 85 ºC/85 % relative humidity (RH) for 1000 h and 4000 h of DI water immersion with no significant degradation. However, after the UV exposure tests, water contact angle (WCA) lowered to 87º (Fig. 29), and the Roll off-angle (RoA) increased to 60.5º. The coating was severely affected by UV exposure as it was not designed for solar application, and resistance to the sun was not part of its specification.

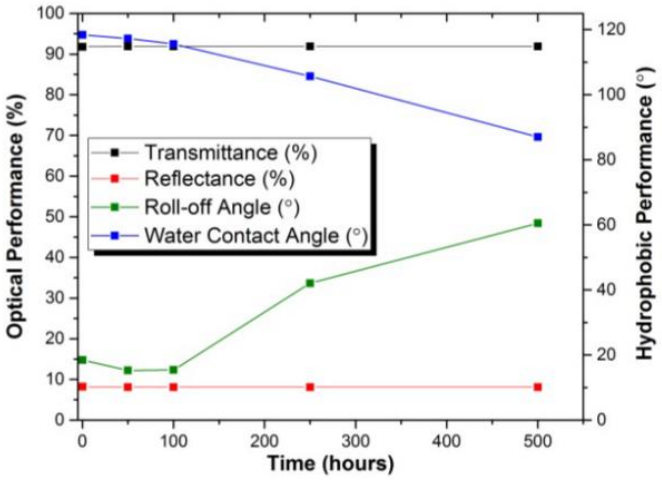

Fig. 29: "Optical and hydrophobic performance during UV exposure" [39].

After the UV exposure, a reduction in fluorine concentration (by X-ray photoelectron spectroscopy) was detected, from ~40 to ~26 At% (shown in Fig. 30). The reduction of fluorine in the chemistry of the surface correlated to the decrease in contact angle. The UV Exposure test was conducted as per the IEC 61215-2:2016 standard, where the samples were exposed for 500 h, equivalent to 15 kWh/m^2 of UV light.

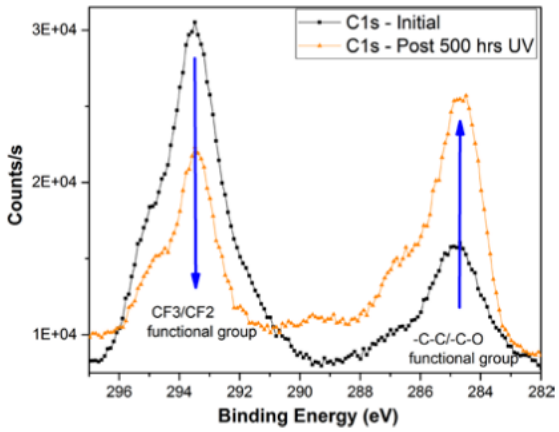

Fig. 30: "XPS spectra of the hydrophobic surface before and after 500 hours of UV exposure" [39].

Syeda Farwah Bukhari et al. [45] showed that the contact angle remains constant even after 1000 h of UV exposure test based on IEC16215-17 (no significant degradation). However, Damp heat testing indicated a reduction of water contact angle after 500 h of exposure (shown in Fig. 31, a) because of the solvent/moisture entrapment.

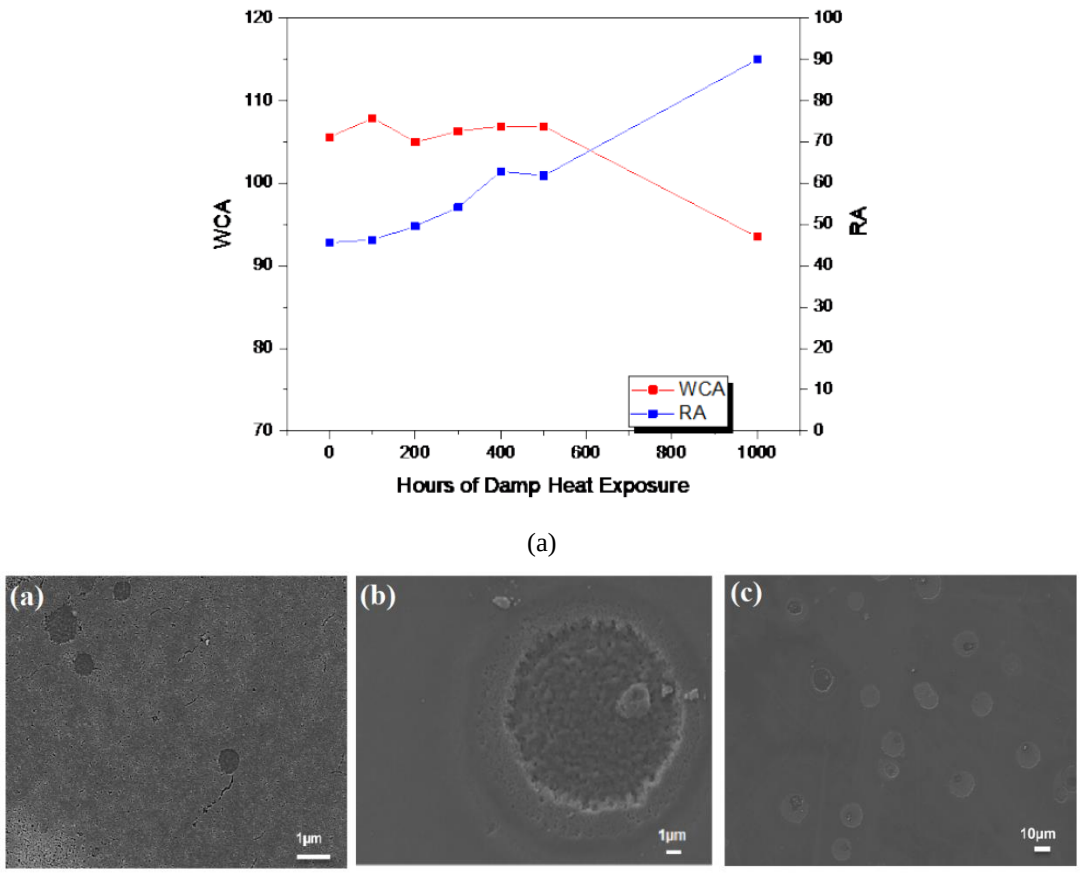

Fig. 31: "(a)Water Contact Angle (WCA) and Roll-off Angle (RA) of the hydrophobic coating after damp heat(b) SEM images of 100 h (a) and 1000 hours (b and c) of DH exposure" [45].

After 100 h of damp heat test, we may observe the formation of circular features (shown in Fig. 31, b). After 500 h of damp heat, these defects start to impact the contact angle and the roll-off angle. These defect patterns are seen due to moisture/water ingress within the coated layer. In this study, a sol-gel coating consisting of trimethylsilylated silica and a siloxane adhesion-promoting agent was deposited onto glass substrates using the dip-coating method. The coating thickness was approx. 2 μm, and the refractive index was 1.38. Curing was done for 72 h, at 65˚C at 85 % relative humidity. The authors suggest that such defects can be avoided by optimizing the curing parameters.

(B) Abrasion Test

The abrasion test [39] showed no significant abrasion caused by soft material, e.g., felt pad. However, using industry-standard abrasive materials such as CS10 significantly damaged the

coating (shown in Fig. 32). CS-10 is an abrasive wheel used in Taber testers. CS-10 wheels offer a mild to medium abrasive effect, simulating the impact of cleaning and polishing.

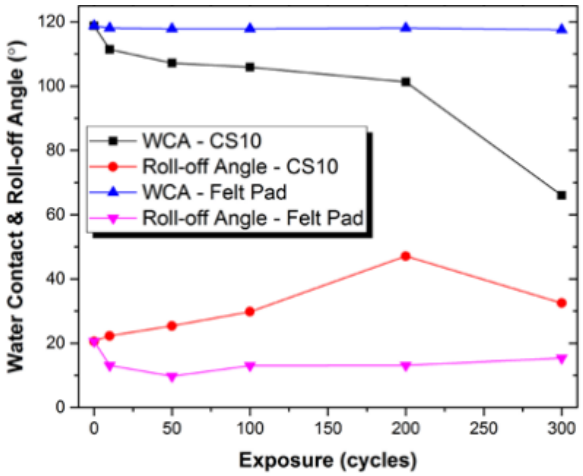

Fig. 32: "Performance before and after abrasion with CS10 and Felt Pad" [39].

The effect of linear artificial brush abrasion on anti-soiling and anti-reflective coatings used in the PV industry was reported by Jimmy M. Newkirk et al. [46]. The authors stated that "the change in characteristics is consistent with the processes of damage initiation, damage accumulation, followed by the destruction of the film, with the eventual convergence of τd (Direct transmittance), YI (Yellowness Index), CA (contact angle), and Ra (Surface Roughness) to those values observed for the glass (shown in Fig. 33) substrate (not-coated sample)" [46]. The authors also show that damage initiation started from localized damage [46]. The localized damage initiated from the edges of dust and brush bristles, indicating the types of brush bristles and dust are significant stressors. The brushes used in this study were similar to the commercially available PV cleaning brushes. The minimum and average W_s (scratch width) in Table 4 are typically in the order of micrometres, whereas the average and maximum h_s (scratch depth) are in the order of tens of nanometers.

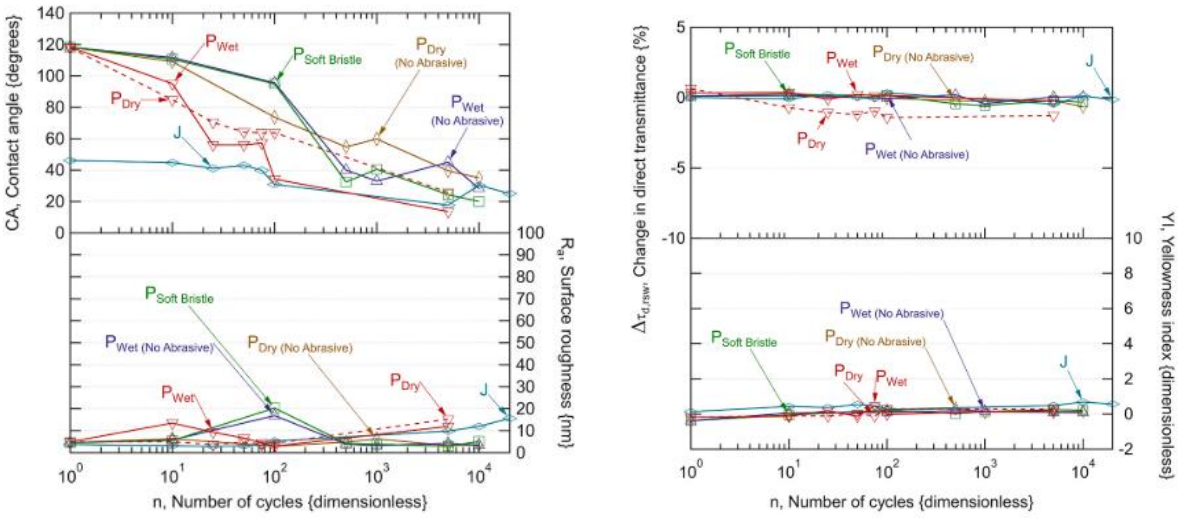

Fig. 33: "Effect of abrasion test type on coating P: comparison of the change in surface energy, surface roughness, direct transmittance and Yellowness Index with the brush-cycle count (n ≤ 20000) for select experiments. J refers to the not-coated sample" [46].

Table 4: "Measured scratch geometry for select specimens after 10 cycles in the linear abrasion experiments. Minimum, average, and maximum values are given as well as the nominal coating thickness" [46].

		w_s, SCRATCH WIDTH {μm}			h_s, SCRATCH DEPTH {nm}			
COATING	TEST CONDITION	MINIMUM	**AVERAGE**	MAXIMUM	MINIMUM	**AVERAGE**	MAXIMUM	h_n, NOMINAL COATING THICKNESS {nm}
B	SLURRY	1.2	**2.0**	4.0	128	**136**	142	125
	DRY DUST	0.6	**1.7**	4.8	1.5	**76**	136	125
E	SLURRY	0.6	**1.8**	7.1	3.3	**42**	121	130
	DRY DUST	0.6	**1.2**	2.2	8.8	**43**	121	130
L	SLURRY	0.6	**1.0**	3.7	8.8	**34**	84	0
	DRY DUST	0.6	**2.7**	22	19	**46**	88	0
P	SLURRY	1.0	**3.3**	17	28	**38**	50	40
	DRY DUST	1.0	**4.3**	13	17	**24**	33	40
	WET BRUSH	0.6	**2.9**	8.5	12	**25**	62	40
	DRY BRUSH	0.6	**4.2**	11.9	20	**36**	58	40
	SOFT BRUSH (SLURRY)	0.6	**1.7**	3.7	13	**30**	55	40
J	SLURRY	0.8	**0.9**	1.2	5.1	**13**	24	0
	DRY	0.4	**0.8**	1.2	5.2	**20**	69	0

2.3 Identified Research Gaps and Organization of the thesis

The literature review shows that in places with high PM count, like India, UAE and China, soiling rates go as high as 1 %/day. Such high soiling rates lead to enormous financial loss and indicate an urgent need for a dust mitigation strategy.

The available literature has pointed out the following research gaps with respect to vertically mounted bifacial modules and anti-soiling coatings, which we have tried to address in our study.

- Previous studies have shown that soiling loss decreases with an increase in the tilt angle. It was also reported that the energy generated by vertically mounted bifacial modules is comparable with the conventionally mounted modules, and the energy yield in the former case could be higher at many locations/conditions with high albedo. The effect of soiling on vertically mounted bifacial modules and how it compares to conventionally mounted monofacial and bifacial modules is not reported in previous work. This motivated us to explore vertically mounted structures as a dust mitigation strategy explained in chapter 3.
- Another cost-effective dust mitigation strategy is AS-coating (explored in chapter 4).
- Electron microscopy has been frequently used to characterize the surface properties during various stages of coating development and reliability evaluation of anti-soiling coatings. However, electron microscopy requires specific sample preparation due to the nonconducting nature of the substrate (glass), thus can only be used via destructive sample analysis. In chapter 5, we establish TM-AFM phase imaging (a nondestructive characterization method) as a promising approach to characterize anti-soiling coatings subjected to environmental stress. While the analysis of the phase angle distribution can resolve the removal of the coating, contact angle and surface roughness cannot do so unambiguously.
- As the AS-coatings are applied on the outer surface of the PV module, the durability of these coatings is essential. There are few reports on the outdoor durability of AS-coating in some climatic conditions. A detailed analysis of the outdoor durability tests, which shows clear signatures of stressors that degraded the coatings in the field, is still missing in work reported until now. In chapter 6, we explored the durability of AS-coatings during field exposure tests, and further, the effect of different seasons was studied to segregate the stressors that degrade AS-soiling coatings during field exposure tests.
- Literature reviews on the impact of various accelerated stress tests are also reported in previous work. However, most reported studies are based on the IEC 61215 standard, which is not relevant to coatings or the IEC 62788-7-3, which only talks about abrasion testing techniques and does not talk about any pass/fail criteria specific to AS-coating applied on PV modules. In our work, we have explored the impact of multiple stressors

like abrasion, rain, UV radiation and combination of various stressors, which are relevant to the reliability evaluation of AS-coating for PV application, as shown in chapter 7.

- The understanding from the correlation study between outdoor and indoor accelerated stress tests was then used to compute a model for lifetime prediction of AS-coatings considering UV radiation and rain as stressors, discussed in chapter 8. Such lifetime prediction study is not reported in previous work. This lifetime prediction study will generate a good database that the PV plant developers can use to predict the coating life at different locations. It will also be helpful in mapping different coating types that work for specific weather conditions.
- In chapter 9, we discussed the key takeaways and future directions of this research area are also discussed in this chapter. This complete study was used to formulate a standard test procedure for performance evaluation of AS-coating under warm and humid climate zone, discussed in Appendix II. A standard test procedure that accounts for all the stressors seen in India is not shown in any reports published until now.

Chapter 3 – Mitigation of soiling via vertically mounted bifacial modules

In this chapter, we evaluate the vertical mounting of bifacial modules to reduce losses due to soiling. We extend the nomenclature used by Guo et al.[12] as follows: (i) Bifacial modules mounted at 90°, are hereafter referred to as vertically mounted bifacial modules (VB), (ii) bifacial modules mounted at the latitude angle (19° in Mumbai) are referred to as latitude mounted bifacial modules (LB), and monofacial modules mounted at the latitude angle are referred to as latitude mounted monofacial modules (LM). Bifacial modules with two different bifaciality factors were used in the experiments, and all the relevant performance parameters are compared as a function of bifaciality. This chapter also shows the impact of combining energy produced by LB and VB for an extended generation profile. Experimental data from individual experiments on LB and VB are combined to evaluate this proposal.

3.1 Experimental Details

In this study, two separate sets of modules with different bifaciality factors (BF), defined as the ratio of the backside I_{sc} to the front side I_{sc} (both measured under standard test conditions with only one side illuminated), were used. The 1st set of the bifacial modules had a BF of 55.7%, and the 2nd set had a BF of 90%. The average cell efficiency was estimated by considering only the area covered by the cells in the modules. All the performance parameters listed in Table 5 were measured using SPIRE–Sun Simulator 5600SPL at the standard test conditions. The active area in the module is taken as the area covered by all the cells in the module.

Two sets of experiments were conducted, and identical experiment plans were used in both cases. In each set, one pair each of LM, LB, and VB was rack mounted on a rooftop in Mumbai (19.1334° N, 72.9133° E) which falls in the Warm & Humid climatic zone [47]. In each pair, one module was cleaned every day in the evening, and the other module was left for natural soiling. In the case of bifacial modules, cleaning was performed on both (front and back) sides of the modules. LB and LM were kept in S-N direction, 19º tilt- South facing, and VB was kept in E-W direction, 90º tilt (vertical) [12]. The modules were connected to a multi-channel I-V curve tracer (Daystar MT5

3200) to measure the I-V curves once every 10 minutes. Irradiation was measured at the plane of array using a pyranometer (Kipp and Zonen). Module operating temperature and ambient temperature were measured using thermocouples, and all the data was logged by the Daystar data logger at 1 min intervals.

Table 5: Performance parameters of modules used in the experiments. Power and efficiency values were measured at 1000 W/m^2 and 25ºC.

	1st set of experiment		**2nd set of experiment**	
Period of the experiment	**28th March to 15th May 2017 (48 days)**		**12th December 2017 to 30th April 2018 (120 days).**	
Parameters	**4 Bifacial modules with BF = 55.7%**	**2 Mono-facial Modules**	**4 Bifacial modules with BF = 90%**	**2 Monofacial Modules**
Average Module Power (W)	Front = 262 Back = 150	84	Front = 229 Back = 209	84
Average Cell Efficiency, η	Front = 18 Back = 11	16	Front = 19 Back = 18	16
Average Module Efficiency, η	Front = 16 Back = 9	14	Front = 14 Back = 13	14
Active Area to Module Area Ratio	0.86	0.91	0.69	0.71

3.2 Results and Discussion

3.2.1 Effect of Soiling

The soiling loss of the modules was calculated based on energy generation (shown in equation 6).

$$Soiling\ Loss\ (\%) = \left(1 - \frac{Energy_{\_soiled}}{Energy_{\_cleaned}}\right) \times 100 \quad (6)$$

Energy generated on any day is calculated by integrating the peak power as a function of time. The soiling rate is calculated as the slope of soiling loss with respect to the number of days. For the 2nd set of experiments, there was shadowing due to a nearby construction from December 2017 to April 2018, so modules with BF = 90% showed lower energy generation. We didn't have such issues in the 1st set of experiments as it was done from March 2017 to May 2017, when there were

no shadow issues due to external structures. To compare both the bifacialities, for LM and LB modules with BF = 55.7% and 90%, we have taken the integration of power from 10 am to 7 pm, and for VB modules for both bifacialities, we have taken a time slot from 8 am to 4 pm, to avoid the effect of shadows on the modules on energy calculations.

In the case of bifacial modules, the soiling loss would include contributions from both sides of the modules, which could be asymmetric depending on the bifaciality, mounting configuration, etc. The slope of soiling loss versus the number of days gives the soiling rate. The soiling loss as a function of the days of experiment are shown in Fig. 34. The soiling rates of the VB with BF = 55.7% is estimated as 0.02 %/day, and for BF = 90%, it is 0.01 %/day. For modules with BF=55.7%, soiling rate of LB is 0.39 %/day, and LM is 0.40 %/day. Soiling losses in the back side of the module is less than the front side in the latitude mounted bifacial module; thus, the soiling loss of LB is less than the LM. Soiling rate of LB is lower than LM due to the light received by the back side of the LB, where chances of soiling are low [29]. The difference in soiling rates is significant with higher bifaciality factor, as can be seen in Fig. 34. The LM in the 2nd set of experiment shows a slightly higher soiling rate than in the 1st set of experiments because of ongoing construction work near the location of the experiment from December 2017 to April 2018.

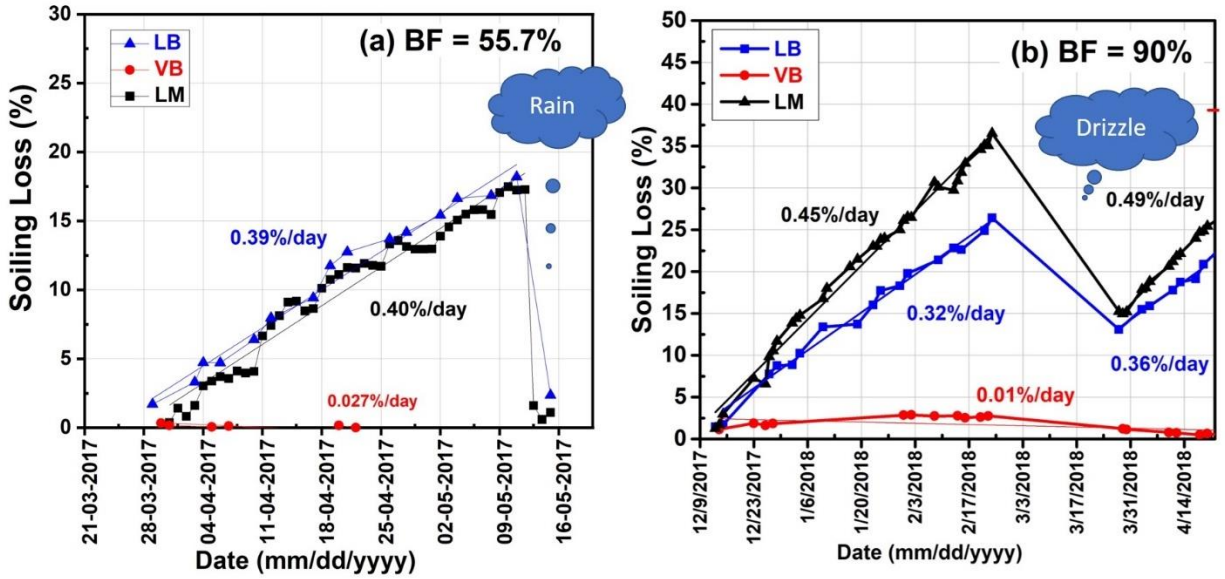

Fig. 34: (a) Soiling loss data for the 1st set of experiments. (b) Soiling loss data for the 2nd set of experiments. The straight lines indicate linear fits to the measured data. Soiling rates are slopes of these lines.

3.2.2 Effect of Bifaciality Factor on Energy Generation

Fig. 35 shows the energy generated by the modules in the two sets of experiments. The energy versus days for the soiled LB and VB are fitted with straight lines. Energy in y-axis in Fig. 35 (a)

and (b) correspond to cumulative energy generated in kWh. It is seen that for bifacial modules with BF = 55.7%, these lines would cross over after 10 weeks of exposure. This indicates that the energy generated by the vertically mounted bifacial module would be higher than that of the latitude mounted bifacial module after 10 weeks, if not cleaned. There was rainfall after the 6th week, so we could not record the crossover data point. For modules with BF = 90%, it would take approximately 3 weeks of exposure for cross-over, as can be seen in Fig. 35, (b). The difference between the crossover points for modules with BF = 90% and 55.7% is seven weeks. The number of days for the crossover points may be overestimated due to data correction because of shadowing issues, but the difference in the crossover points between the modules with two BF values is significant.

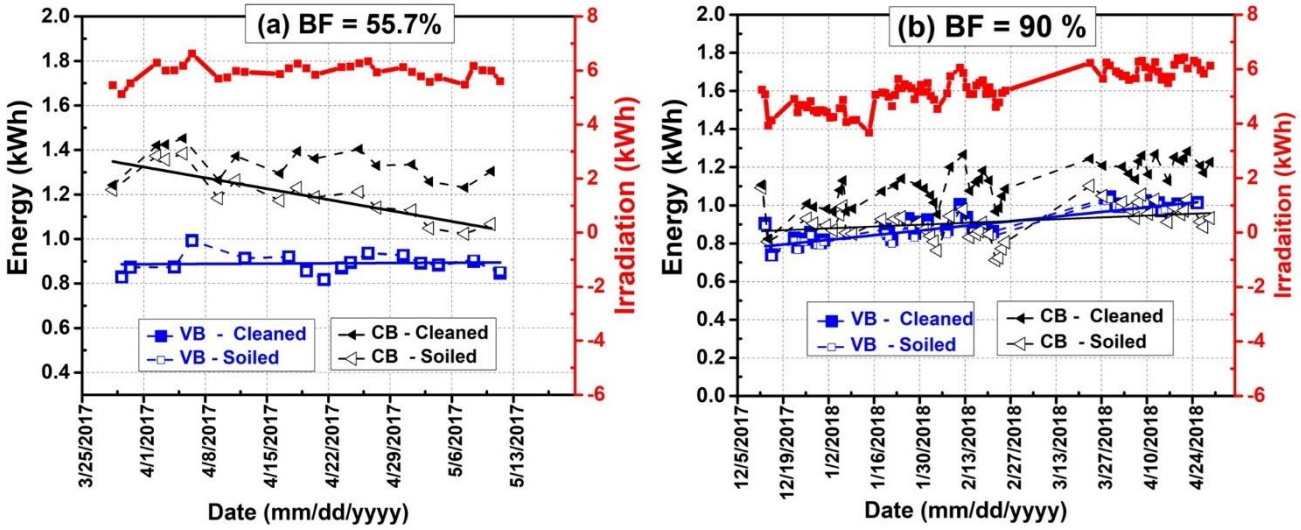

Fig. 35: (a) Energy generated by the modules in the 1st set of experiments. (b) Energy generated by modules in the 2nd set of experiments. The data for VB – cleaned and VB – soiled overlap in both the cases.

3.2.3 Operating Temperature of the Modules

It is observed that for modules with BF = 90%, LB and LM run at 15°C higher temperature than VB (Fig. 36). In the case of latitude mounted modules, the radiation and ambient temperature peaks at the same time, at solar noon. On the other hand, the vertically mounted modules receive the maximum in-plane radiation in the morning and afternoon hours when the ambient temperature is lower than at noon. It is observed that for modules with BF = 90% and 55.7%, LB and LM ran at similar operating temperatures (Fig. 36). VB with BF = 55.7 % ran at significantly higher operating temperatures in the early morning than VB with BF = 90 %. This can be due to two factors: (i) VB with BF = 55.7% has a higher active area to module ratio than the module with BF = 90%, see

Table 5. The high active area to module ratio enables a higher fraction of the light to be incident on the solar cells. The inactive areas let light pass through in the case of bifacial modules. (ii) The cell efficiency of the modules with BF = 55.7% is lower than that of the module with BF = 90%. This implies that a larger fraction of the energy incident on the module with BF = 55.7% is converted to heat. The small dip in temperature at 200 W/m^2 during the evening time for VB with BF = 90% is because of human interference while cleaning the module.

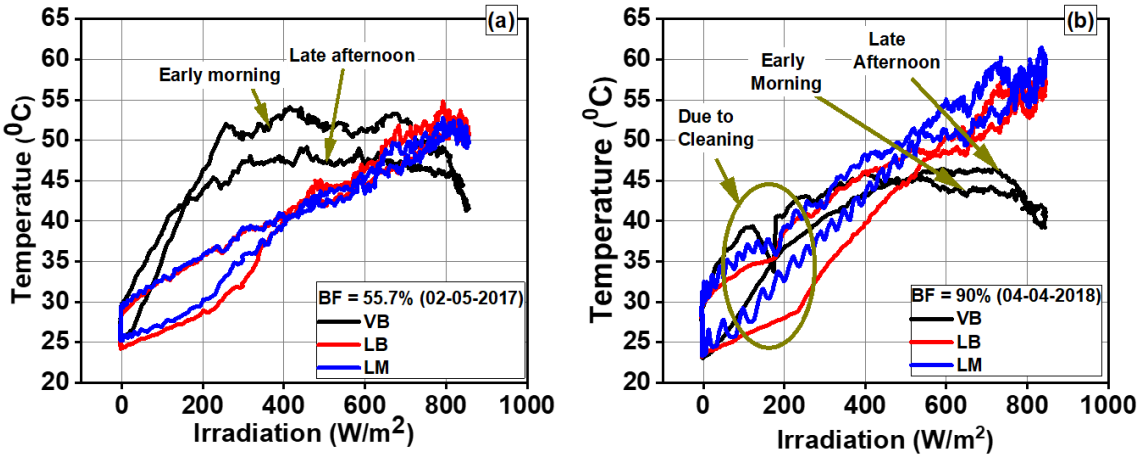

Fig. 36: (a) Operating temperature of modules for the 1st set of experiments. (b) Operating temperature of modules for the 2nd set of experiments.

3.2.4 Combination of Latitude Mounted Bifacial Module and Vertically Mounted Bifacial Module

Fig. 37 shows the power generation profiles of the VB and LB for bifaciality of 90%. The VB power peaks twice during the day, and the peaks are much before and after the solar noon. At solar noon, VB produces only about 35% of the power produced by LB. By combining VB and LB, the power generation profile is seen to broaden and also become flatter. Let us consider the peak power generation time as the time period during which the system generates 84% or more of the maximum power obtained on the day. By this definition, the peak power generation time for a combination of LB and VB is 7.5 h (approx.), whereas for LB and VB individually, it is 4.5 h (approx.). Hence, using a design with a combination of LB and VB, a longer duration of peak power generation is possible.

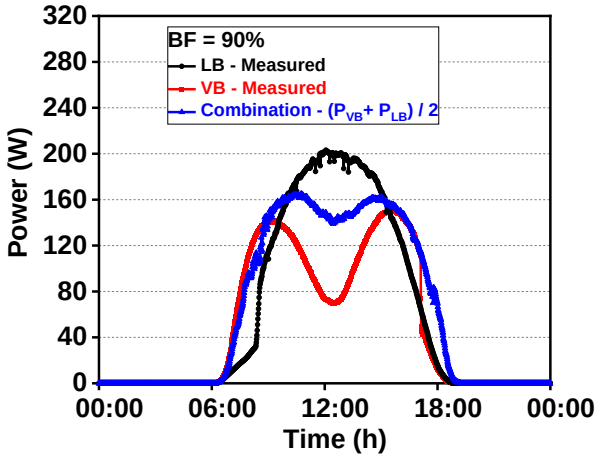

Fig. 37: Energy generation profile for modules with BF=90% for LB, VB, and LB + VB.

3.3 Conclusions

Based on our experiments, it can be concluded that (i) Vertical mounting of bifacial modules mitigates soiling losses, and hence cleaning of panels can be avoided (ii) bifacial modules mounted at the latitude angle have lower soiling loss compared to monofacial modules mounted at the latitude angle and hence may require less frequent cleaning (iii) For BF = 90%, vertically mounted bifacial modules produce lower energy compared to latitude mounted bifacial modules to begin with, in the high soiling conditions prevailing in Mumbai, the latitude mounted bifacial panels would produce lower energy after 3 weeks, if they are not cleaned in the meanwhile (iv) vertically mounted modules with high bifaciality runs at lower temperature than latitude mounted modules, with potential improvements in the performance ratio and long term reliability (v) by combing vertically mounted bifacial modules and modules mounted at latitude angle, increase in the duration of peak power generation is approximately by 80%. These results were obtained in Mumbai. We anticipate that several of these conclusions would apply to many other geographical locations with high irradiance and soiling rates. The tracker systems could also use this dust mitigation approach, where the user can extend the tilt angle to 90˚ after sunset hours, which will result in a 50% reduction in soiling rates [29]. Vertical mounting of PV modules may require care in the design of the power plant layout to minimize the effect of shadowing between adjacent modules.

Chapter 4 – Cleaning efficacy of anti-soiling coatings

Another cost-effective dust mitigation strategy discussed in chapter 2 was the AS-coatings. AS-coatings are nano or microlayer coatings and are broadly categorized into (i) hydrophobic (contact angle > 90°) and (ii) hydrophilic (contact angle < 90°) [13] surfaces. AS-coatings offer a cost-effective solution and are extensively investigated as a dust mitigation strategy [1]. This chapter focuses on the measurement of the cleaning efficacy of hydrophobic AS-coatings. Most commercial AS-coatings are hydrophobic in nature, as it does not allow the water to wet the surface [48]. When the coated surface is tilted at an angle greater than its roll-off angle (the angle at which the droplet starts to roll-off [49], [50]), the dust particle adheres to the droplet rolling off the surface, thereby cleaning the PV modules [48]. This allows the hydrophobic AS-coatings to clean the surface with the help of dew or water. Roll-off angle also depends on droplet volume and the properties of the glass surface [49], [50]. Development [44] and degradation [39] of AS-coatings have been discussed in previous studies, but no reports are available on the efficiency of cleaning of AS-coatings under a controlled environment and how they correlate with field exposure. Such a correlation is essential for the development of accelerated testing methodologies for AS-coatings. In this chapter, we compare the cleaning efficacy of 4 types of commercial hydrophobic anti-soiling coatings with a not-coated glass sample, under field exposure, and in indoor controlled experiments.

4.1 Experimental details

4.1.1 Sample Preparation

Four different commercial hydrophobic AS-coatings were applied on solar glass samples (one type of coating solution applied on one solar glass) by manual spray coating as per the instructions in the respective product manuals. The commercial coatings used in this thesis were marketed for solar application. After 20 min. of application, the excess coating was removed, and the samples were left for curing at room temperature for 24 h. Dust deposition was done in a dry dust deposition chamber [51] on all coated and not-coated glass samples. Fig. 38 shows the XPS (X-ray photoelectron spectroscopy) scan of the coated and not-coated samples at their initial state. Coatings A, B, and D show F-C_2 peaks in F_{1s} and C_{1s} narrow and survey scans, indicating that they

are fluoropolymer-based coatings. Coating C shows phenylsilicone peaks in Si_{2p} and O_{1s} narrow spectra (shown in Fig. 38), indicating coating C to be a phenylsilicone based coating. Fig. 39 shows the scanning electron micrographs (SEM) of the coating A, B, C, and D. In Fig. 39; we may observe that the average nanoparticle size of the coated samples (A, B, C, and D) was approximately 100 nm. Coating A and Coating D show spherical-type nanostructures, coating B, shows triangular nanostructures, and coating C shows fibre-like features. The thickness of the coatings was not measured due to charging issues faced during SEM cross-section imaging.

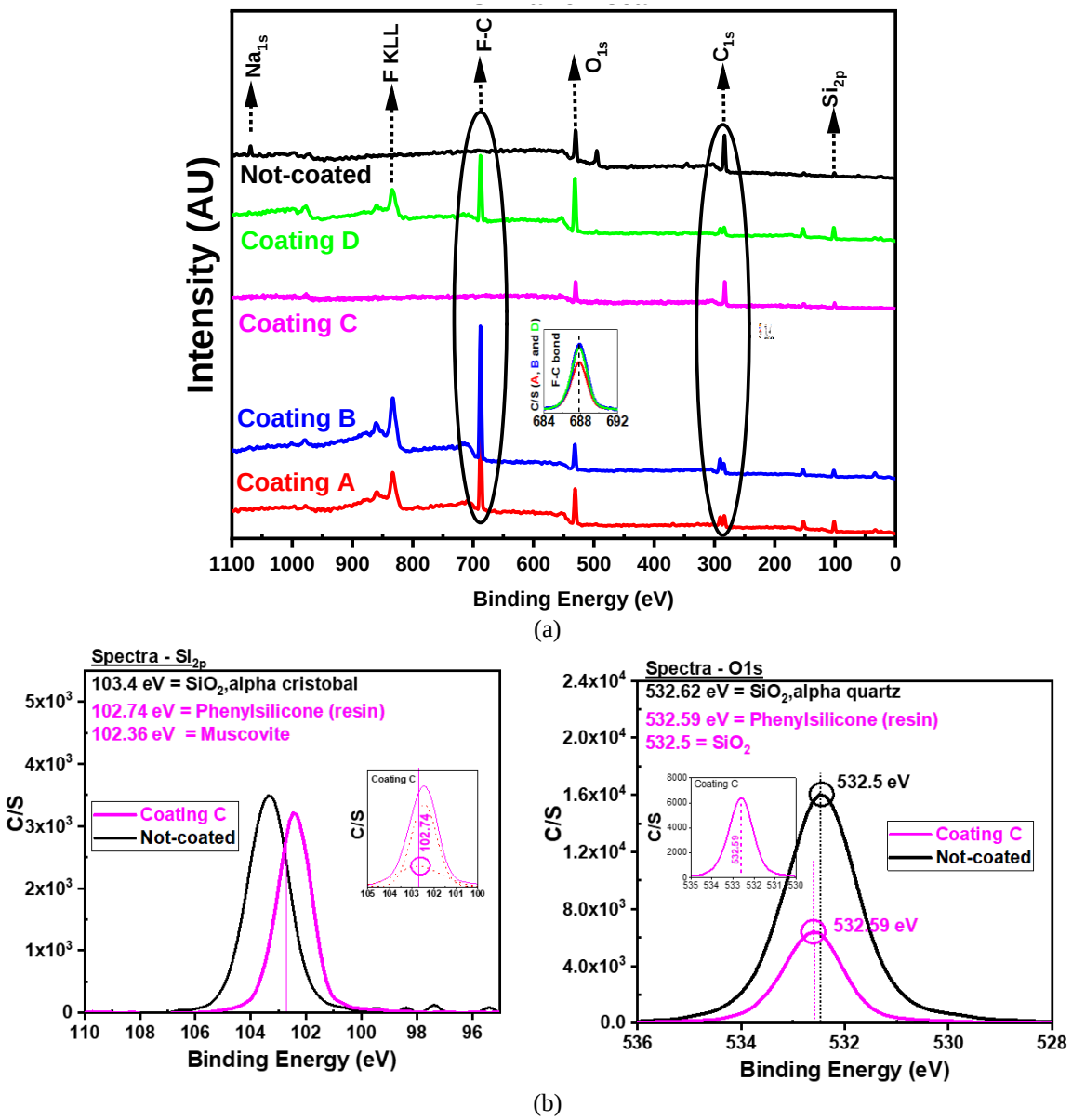

(a)

(b)

Fig. 38: (a) XPS survey scan of coatings A, B, C and D, (b) XPS, Si_{2p} and O_{1s} narrow scan of coating C.

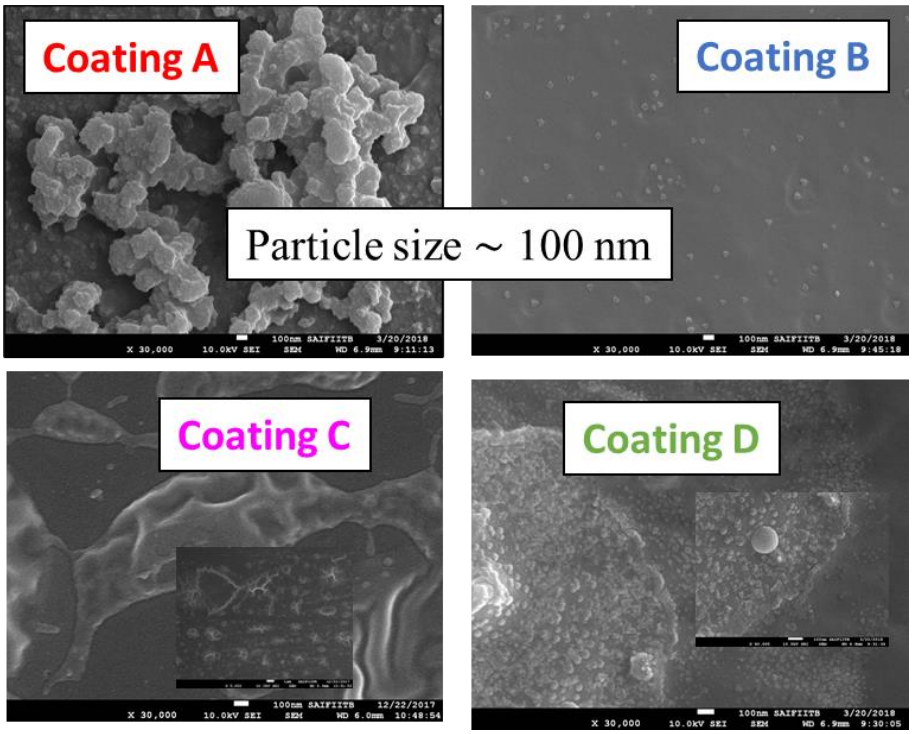

Fig. 39: SEM (scanning electron micrograph) of coating A, B, C and D.

4.1.2 Characterization

A roll-off angle set-up was developed to study the cleaning efficacy of AS-coatings. Roll-off angle was measured by keeping a water droplet at 0° and then allowing the glass substrate to incline at a speed of 1°/s. The angle at which the water droplet starts to roll off was measured as the roll–off angle. The soiled coated and not-coated glass samples were cleaned with 45 µl of deionized water droplets at their respective roll-off angle (measured after depositing dust, as described in section 4.2.1). Soiling loss on the glass samples was calculated based on equation 7.

$$Soiling\ Loss\ (\%) = \left(1 - \frac{Energy\ or\ J_{sc\_soiled}}{Energy\ or\ J_{sc\_cleaned}}\right) \times 100 \quad (7)$$

The outdoor study on PV modules (100 Wp) was carried out from 14th Nov. 2019 to 23rd Jan. 2020 (total of 71 days) at IIT Bombay, Mumbai, India, which falls under warm and humid climate zone. Four sets of modules were used for this study. Each set corresponds to one type of coating (B, C, and D), and one of the sets was not-coated (U). Each set has two modules – one was cleaned daily (named as cleaned in the equation), and the other was left for natural soiling (named as soiled in the equation). The modules were kept in the S-N direction, 19° tilt (latitude angle). Soiling loss of the modules was calculated based on daily energy generation or J_{sc}. Manual cleaning was done by water using a squeegee sponge wiper.

The contact angle was measured using Data-Physics Instruments, model OCA 15SEC and J_{sc} was measured over a slit width of 1.5 mm × 5 mm using a Quantum Efficiency measurement system (Bentham – PVE 300). Multi-crystalline silicon solar cell was used as a reference for J_{sc} measurement, over which different types of samples were placed. All solar glass samples used in the experiment were from Borosil Glass Works Limited, India. All measurements of contact angle (droplet volume = 2µl) and roll-off angle (droplet volume = 45µl) were done using deionized water. For outdoor study, PV modules were connected to a multichannel I–V curve tracer (Daystar MT5 3200) to log data on power (P_{max}) at 1 min interval. Irradiation was measured at plane of array of the latitude mounted module, i.e., with 19° tilt, using a pyranometer (Kipp and Zonen). Contact angle and roll-off angle were measured at 10 points on each sample (denoted at N =10). In the box plots (shown in this thesis), the extreme lower end and upper ends of the box refer to the 25th percentile (first quartile), and the 75th percentile (third quartile) of the data sets, the horizontal line inside the box refers to the 50th percentile (Median) of the data sets and the two horizontal lines that cap the vertical lines at the bottom and the top refer to the 5th percentile and 95th percentile of the data sets. Wilcoxon's signed rank test [52] was used to identify if the difference between samples before and after the experiment is statistically significant. P values obtained by Wilcoxon's signed rank test < 0.05, were considered statistically significant, considering a confidence interval of 95%.

4.2 Results and Discussions

4.2.1 Roll-Off Angle - With and Without Dust Deposition

Roll-off angle was measured for both cleaned, and dust deposited glass samples to simulate on-the field scenarios. Dust with density of 0.2 mg/cm^2 was deposited on all glass samples (A, B, C, D and U). For clean coated glass samples (A, B, C and D), the contact angle and roll-off angle decreased with an increase in the droplet volume, which further gets stabilized after 45 µl. Thus, 45µl of deionized water was taken for all roll-off angle measurements.

The roll-off angle of glass samples coated with A, C and D increases by a factor of 2 upon dust deposition (Fig. 40). The factor of increase was 1.4 for the not-coated sample. Coating B showed high roll-off angle without any dust deposition, which decreased by a factor of 0.7 after dust deposition. The roll-off angle of the not-coated glass sample, with and without dust deposition, was also found to be statistically significant, as verified by Wilcoxon signed-rank test [52]. This

shows that roll-off angle depends on the surface of the solar glass, which will vary upon dust deposition (under field condition).

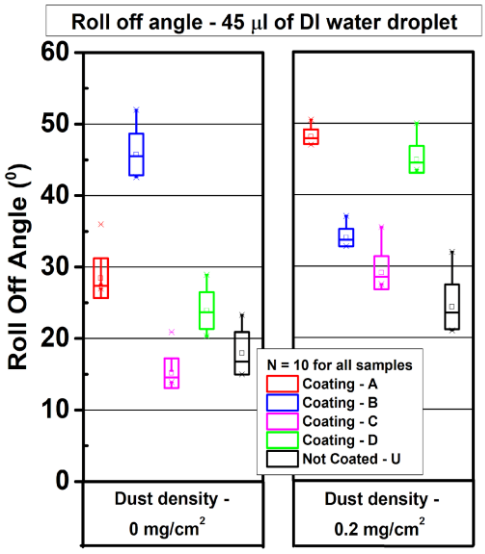

Fig. 40: Roll-off angle of coated (A, B, C, D) and not-coated (U) glass samples with and without dust. Each box plot is based on 10 measurements taken in each glass sample to account for non-uniformity of coating within the sample.

4.2.2 Cleaning Efficacy of Anti-Soiling Coating - on Solar Glass under Controlled Environment

To compare the cleaning efficacy of coated and not-coated samples, 0.2 mg/cm^2 of dust was deposited on all samples, which were then cleaned by 45 ul water droplet. The water droplet was kept on the sample at the respective roll-off angle with dust (shown in Fig. 41 (a)), allowing the droplet to roll off and clean the sample. Soiling loss based on J_{sc} along the cleaned area was measured to study the cleaning efficacy of AS-coating. Before soiling, the newly cleaned, coated samples do not show a significant difference (of J_{sc}) in comparison to the not-coated sample.

All coated samples (A, B, C and D) show higher cleaning efficacy (lower soiling loss) than the not-coated sample (Fig. 41 (b)). However, cleaning efficacy of all coated glass samples reduces (soiling loss increases) by a factor of 6 (average) as the rolling water droplet travels from top to bottom (covering a total distance of 3.6 cm). In contrast, the cleaning efficacy of the not-coated sample reduces by a factor of 30. It was also seen that at 0.9 cm (top position), coating A and C show higher soiling loss than the not-coated sample (U). The rate of increase in soiling loss per distance travelled by the droplet cannot be extrapolated for a full-size module, as capillary force and the adhesion between dust and the substrate will vary with substrate conditions. It was also seen that soiling loss of samples A and U increases the most between 1.8 cm to 2.7 cm; this is because the speed at which the water droplet rolls off decreases significantly as the water droplets

collect more dust. This increase in soiling loss for coating B, C, and D happens between 2.7 cm to 3.6 cm. Due to the significant slowing of the water droplet roll-off, the time required for the water droplet to roll off also varied significantly (shown in Table 6).

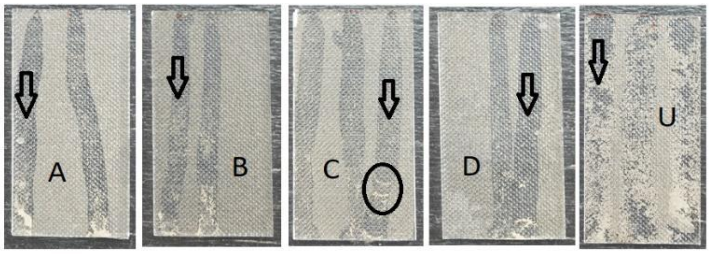

(a)

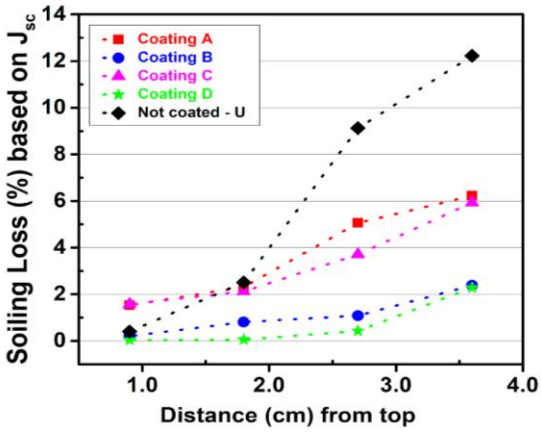

(b)

Fig. 41: (a) Dust deposited samples (A, B, C, D and U) of 0.2mg/cm^2 after a 45µl of water droplet has rolled off in order to clean the dust. The arrow represents the roll-off line along which J_{SC} values were measured. (b) Soiling loss of coated (A, B, C, D) and not-coated (U) glass samples along the cleaned area after 45µl of water droplet has cleaned the sample.

Coating C took the highest time for the water droplet to roll off and thus indicates the highest decrease in speed of water droplet to roll-off. Imprints of the dusty water droplets (encircled) can also be seen in Fig. 41 (a). Based on the uniformity of cleaning, the cleaning efficacy between the glass samples was ranked as D > B > C > A > U.

Table 6: Time taken for the water droplet to roll-off the dust deposited samples. Here, the samples were kept at their respective roll-off angle with dust (shown in Fig. 41).

Sample Name	Time (min:sec)
Coating A	0:25
Coating B	4:15
Coating C	9:20
Coating D	1:00
U (not-coated)	2.50

4.2.3 Cleaning Efficacy of Anti-Soiling Coating – on PV modules under Field Exposure

Coatings B and C show higher cleaning efficacy (lower soiling loss) than the not-coated module U throughout the experiment (Fig. 42). Coating D also shows higher cleaning efficacy (lower soiling) than not-coated sample until the 2nd manual cleaning run, after which the difference in cleaning efficacy/soiling loss between coating D and not-coated module U reduces significantly. The reduction in cleaning efficacy of coating D shows signature of abrasion caused by the manual cleaning runs. It was observed that after every manual cleaning run, soiled modules produced higher energy than daily cleaned modules. This is due to less abrasion caused by less cleaning runs (in soiled modules), thus showing negative soiling loss after manual cleaning runs.

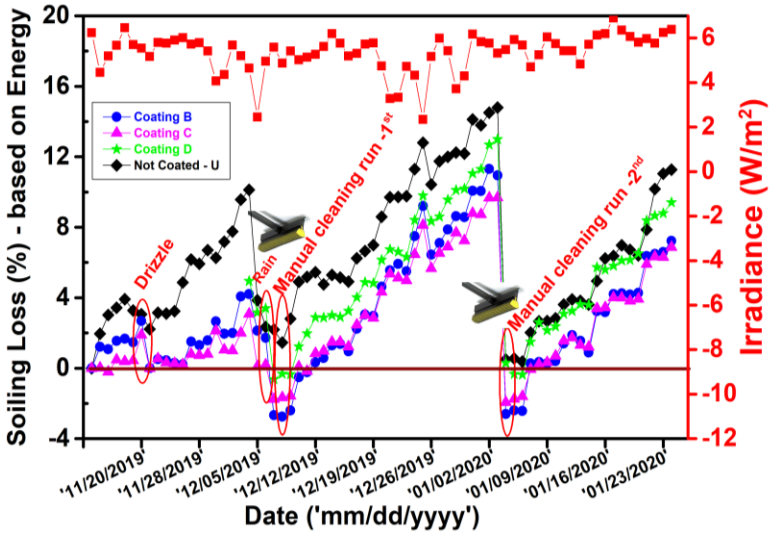

Fig. 42: Soiling loss of coated (B, C, D) and not-coated (U) modules upon field exposure.

The ranking in cleaning efficacy based on soiling loss for coated samples B, C, and D correlate well with the roll-off angle of the samples with dust deposition (shown in Fig. 40). Coating C and B show low roll-off angle after dust deposition, followed by D. Coating C and B also show higher cleaning efficacy in the field, followed by D, indicating roll-off angle as an important measure for evaluation of AS-coating.

4.3 Conclusions

A comparative study on the cleaning efficacy of 4 different commercial hydrophobic anti-soiling coatings with not-coated sample (solar glass and PV modules) is reported in this chapter. Coated samples show higher cleaning efficacy than not-coated samples (in both controlled environment and field exposure). This indicates that hydrophobic AS-coating can mitigate soiling. However,

cleaning efficacy of coated sample reduces (soiling loss increases) by a factor of 6 (average) as the rolling water droplet travels from top to bottom (covering a total distance of 3.6 cm). In contrast, the cleaning efficacy of the not-coated sample reduces by a factor of 30. We also observed that roll-off angle depends on the surface of the solar glass, which vary upon dust deposition (under field condition). During field exposure study, we saw a significant decrease in cleaning efficacy (for coating D) after 2^{nd} manual cleaning, indicating abrasion caused by the cleaning tool. The ranking in cleaning efficacy for coated samples B, C, and D during field exposure correlate well with the ranking of roll-off angle measurements with dust deposition, implying roll-off angle as an important measure for the evaluation of anti-soiling coatings.

Chapter 5 – Quantification of the percentage coated area using TM-AFM Phase Imaging

Compared to other dust mitigation strategies, anti-soiling coating could provide an economical and universal solution. This has generated an increased interest in the development of durable anti-soiling coatings. Electron microscopy has been frequently used for the characterization of surface properties during various stages of coating development and reliability evaluation of anti-soiling coatings [53]. However, electron microscopy requires specific sample preparation due to the non-conducting nature of the substrate (glass), thus can only be used via destructive sample analysis. Phase imaging via Tapping Mode Atomic Force Microscopy (TM-AFM) is a non-destructive characterization method which shows high material contrast of fine structures that we cannot see in topographical imaging (via AFM). With this method, we can also analyze samples under in-situ environments or in controlled environments without any sample preparation.

TM-AFM phase imaging has been adopted for investigating the surface properties in many scientific fields. However, most of the studies discuss the surface morphology based on TM-AFM height images; little information is reported on the phase image/phase angle analysis [54]–[57]. TM-AFM phase images are generated due to the phase lag between the oscillation frequency of the cantilever and the driver when the scanning tip interacts with different surface materials [58]. The inherent roughness of the sample also masks the phase contrast. Surfaces with high roughness show phase contrast at a high tapping mode, and for samples with medium roughness, phase contrast is seen at a low tapping mode [57]. The phase lag shows the interactions between the scanning tip and the surface of the sample, and the phase images have the advantage of demonstrating the surface material properties of coated and the not coated area. Apart from the instrument settings (like amplitude modulation feedback, driving frequency, the tip's sharpness, and spring constant) which impact the phase lag of an oscillating cantilever, the chemical and physical properties of the surface like friction, adhesion, viscoelasticity, etc. also impacts the phase contrast [57], [59]–[64]. Any boundaries with material discontinuity caused by the difference in surface properties are reflected by TM-AFM phase images [56]. Therefore, AFM phase imaging is a useful tool in visualizing and analyzing the coating material changes on the surface by revealing the features of damage, non-uniformity, breakage, and fragmentations.

In this chapter, we investigate the application of TM-AFM phase imaging as a tool to investigate the degradation of anti-soiling coatings, when the coatings are subjected to field exposure and different accelerated stress tests. For a direct comparison of phase images of samples exposed to different environmental stressors, all the samples were scanned with the same instrument settings. All phase and height images taken via AFM were normalized. We observed a significant difference in adhesive force (tip-sample interaction) and phase angle (creating a significant phase contrast) between the coated and not-coated areas of the glass surface. We also performed a quantitative analysis by plotting the probability density function of the phase images taken over a large area.

5.1 Experimental Details

5.1.1 Sample Preparation

Four different commercial hydrophobic anti-soiling coatings (A, B, C, and D) were applied on solar glass samples (one type of coating solution applied on one solar glass) by manual spray coating method as per the instructions given in the respective product manuals. Details of samples preparation and coatings are given in section 4.1.1.

5.1.2 Experimental Setup

Both outdoor field exposure and indoor accelerated stress tests were studied on solar glass samples (5 cm × 2.5 cm). For outdoor studies, the samples were kept at 19^0 tilt (latitude angle). To study the effect of rain, outdoor field exposure study was done during the rainy season for 40 days from 30^{th} Sept. to 8^{th} Nov. 2019. The total precipitation during this period was 180 mm [65], and the total solar irradiance was 196 kWh/m^2. The outdoor field exposure study during the non-rainy season was done for 63 days from 24^{th} Dec. 2019 to 24^{th} Feb. 2020. Total precipitation during this time was 0 mm, and the total solar irradiance was 375 kWh/m^2. All accelerated tests (experimental details are mentioned in sections 7.1 and 7.2) were conducted under controlled environments in the laboratory to isolate the stressors.

5.1.3 Characterization

For evaluating the performance of coatings on solar glass, contact angle and roughness measurements were done. Contact angle and roughness were measured at ten locations (denoted as N=10) on each sample. Water contact angle was measured using DataPhysics Instruments,

model OCA 15SEC. Roughness was measured using an atomic force microscope (AFM) from Asylum/Oxford Instruments, model MFP3D. Irradiation was measured at plane of array of the latitude mounted structure, i.e., with 19° tilt, using a pyranometer (Kipp and Zonen). Wilcoxon signed-rank test [52] was used to identify if the difference between samples before and after the experiment is statistically significant (statistical significance of 5 % was considered).

The MFP3D Origin AFM (Asylum/Oxford Instruments) in tapping mode was used to image (topography and phase image) the coated and not-coated samples. For taking phase images, appropriate scan rate and set point ratio were considered based on the roughness of the samples. For measuring the adhesive force (tip-sample interaction) via AFM, we used a silicon probe (Model no. – Econo-FESP-Au) along with a silicon tip with no coating (from Asylum Research). The adhesive force was measured via contact mode in atomic force microscopy. The measured spring constant (k) of the tip was 1.44 N/m, and the resonant frequency was about 75 kHz. The relative humidity of the chamber was maintained to be dry (relative humidity = 19 %) during the measurement of adhesive force. All other instrumental parameters, like amplitude modulation feedback, driving frequency and the tip's sharpness were kept constant for all samples. All topographical and phase images (via AFM) were taken over a 50 µm × 50 µm area at 5 different locations within each sample. The adhesive force between the tip and the sample was obtained over a selected area of 2 µm × 2 µm. The adhesive force stated in the thesis is the average adhesive force measured at 5 different locations for each sample.

5.2 Results and Discussions

5.2.1 Phase Image Analysis of Coated and Not-Coated Samples

Fig. 43 (a) and (c), shows the two-dimensional height image and phase image of coating D and the not-coated sample. Fig. 43 (b) and (d) show the phase angle and height corresponding to the black line across the phase image and height image for coating D and the not-coated sample. Fig. 43 (c) and (d) shows that the not-coated glass surface is smooth, and the phase angle is zero through out the surface.

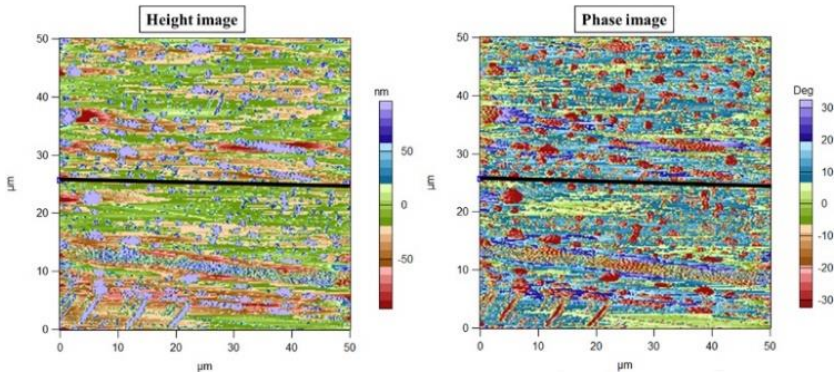
Height image
Phase image
nm
Deg
µm
µm

(a)

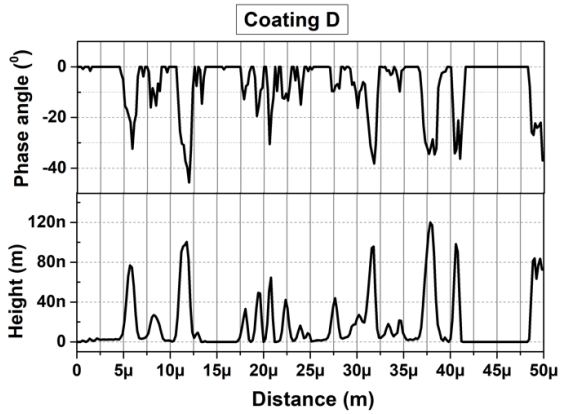
Coating D
Phase angle (°)
Height (m)
Distance (m)

(b)

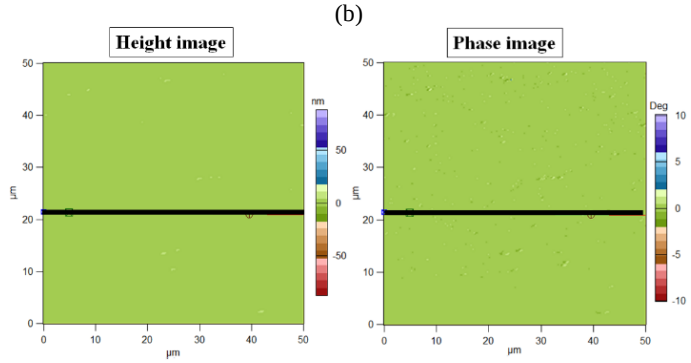
Height image
Phase image
nm
Deg
µm
µm

(c)

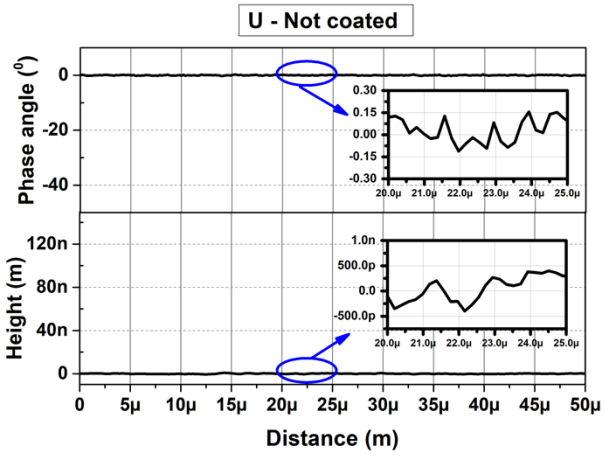
U - Not coated
Phase angle (°)
Height (m)
Distance (m)

(d)

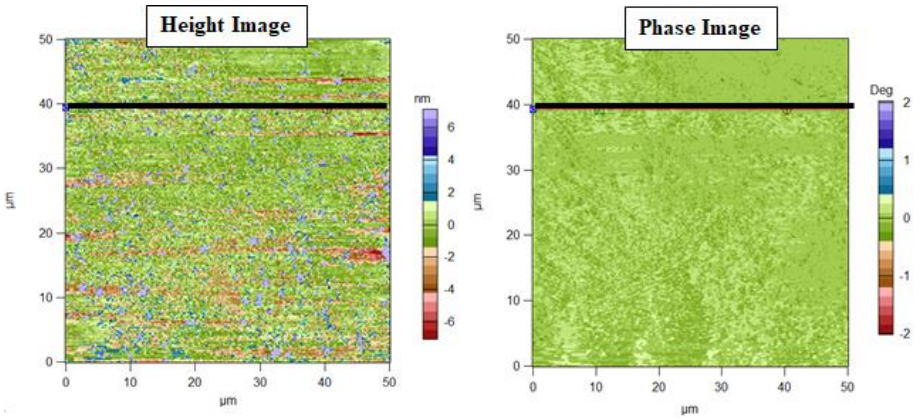

(e)

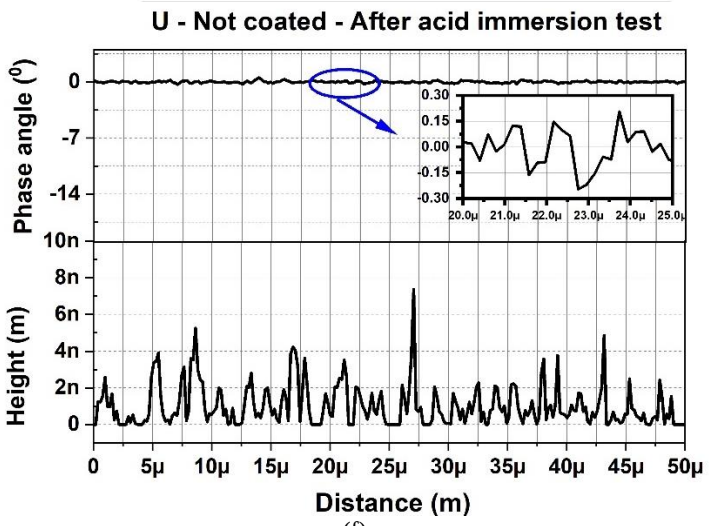

(f)

Fig. 43: (a) Height and TM-AFM phase images of coating D, as-deposited (initial stage without environmental exposure). (b) TM-AFM phase angle and height corresponding to the black line across the TM-AFM phase image and height image shown in Fig. 43(a). (c) Height and TM-AFM phase image of not-coated sample, initial stage without environmental exposure. (d) TM-AFM phase angle and height (nm) corresponding to the black line across the TM-AFM phase image and height image shown in Fig. 43(c). (e) Height and TM-AFM phase images of the not-coated sample, after undergoing 60 days of acid immersion test with pH 6 water sample. (f). TM-AFM phase angle and height (nm) corresponding to the black line across the TM-AFM phase image and height image shown in Fig. 43(e).

Fig. 43 (b) shows that the phase zero regions have a height of zero. By comparing this with the observation for the not-coated glass, we may conclude that the phase angle of zero is indicative of the fact that the coating has not formed a closed film on the surface of the glass. The regions with phase angle of zero do not have any coating, while those with nonzero phase angle have coating. This can also be seen in Fig. 43 (e) and (f), where we observe a change in topography (in the height image) on the top surface of the not-coated sample after the acid immersion test, likely caused by the etching of Na from the glass surface [66]. However, it does not demonstrate any change in the

material of the not-coated glass (shown in the phase angle image, Fig. 43 (e) and (f)). This confirms the ability to detect changes in surface material via TM-AFM phase imaging.

5.2.2 Adhesive Force of Coated and Not-Coated Samples:

Fig. 44 shows the average adhesive force (average of 5 locations) between the scanning tip and the coated and not-coated surface at the initial stage (when samples are not exposed to any stressors). In Fig. 44, we may observe that the not-coated sample (U) shows 3 X times (at least) higher adhesive force than coated samples (A, B, C and D). Due to this significant difference in adhesive force between the coated and not-coated samples, we observe a change in phase angle (which creates phase-contrast in phase images) between the coated and not coated area within a sample.

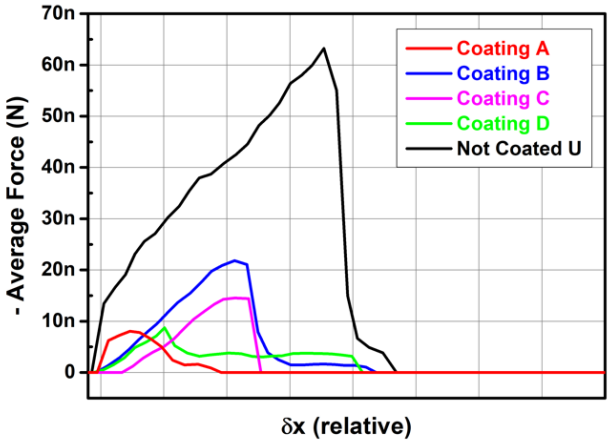

Fig. 44: Average adhesive force of coated (A, B, C and D) and not-coated sample (U) at 19 % relative humidity, at the initial stage (not exposed to any stressors). The adhesive force stated here is the average adhesive force of 5 different locations for each sample.

5.2.3 Effect of Outdoor Field Exposure:

By plotting the probability density function (PDF) of the complete phase image matrix (of 50 µm × 50 µm area), we were able to perform a quantitative analysis of the phase distribution over a larger surface area, shown in Fig. 45 - Fig. 47. Specifically, for the not-coated sample, without any exposure to environmental stress, the phase angle is tightly distributed around zero. Environmental exposure is not seen to alter the phase distribution for the not-coated sample. In contrast, during the initial stage, when the samples are not exposed to any stressors, coated samples show a high spread of the phase angle (from 0^0), indicating the presence of the coated material on the solar

glass. Coated samples, after being exposed to rainy and non-rainy seasons, show a significant decrease in the spread of the phase angle.

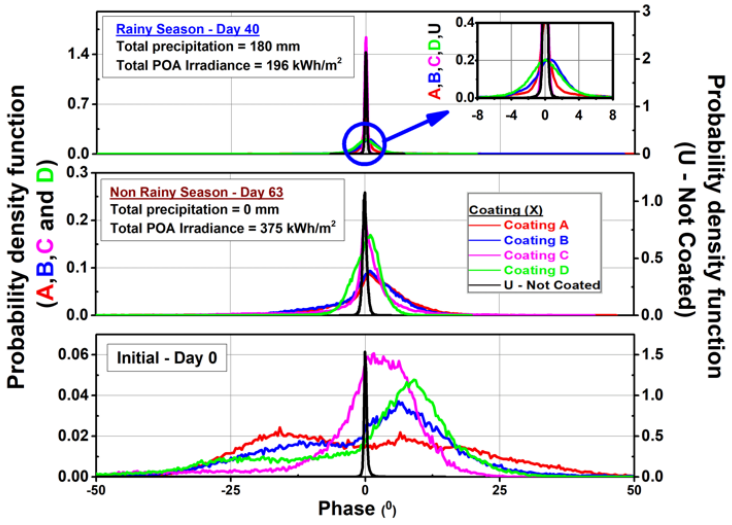

(a)

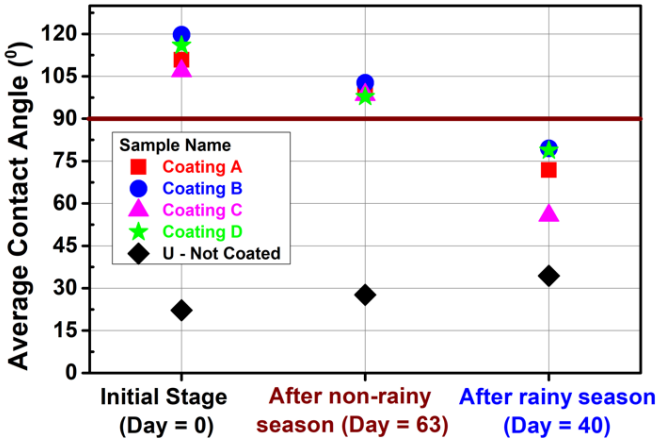

(b)

Fig. 45: (a) Probability density function of TM-AFM phase angle for coated (A, B, C and D) and not-coated sample (U), at its initial stage (as-deposited) after being exposed to rainy and non-rainy seasons. (b) Average contact angle of coated (A, B, C, D) and not-coated (U) glass samples under field exposure during rainy and non-rainy season.

Specifically, in the case of coating C, after being exposed to the rainy season, the phase angle distribution is seen to be similar to that of the not-coated sample. This correlated well with contact angle measurements, where the contact angle of coating C shows values close to the not-coated sample after being exposed to the rainy season (shown in Fig. 45 (b)). All coated samples (A, B, C, and D) show a lower spread in the phase angle (from 0^0) after the rainy season when compared to the samples exposed to the non-rainy season.

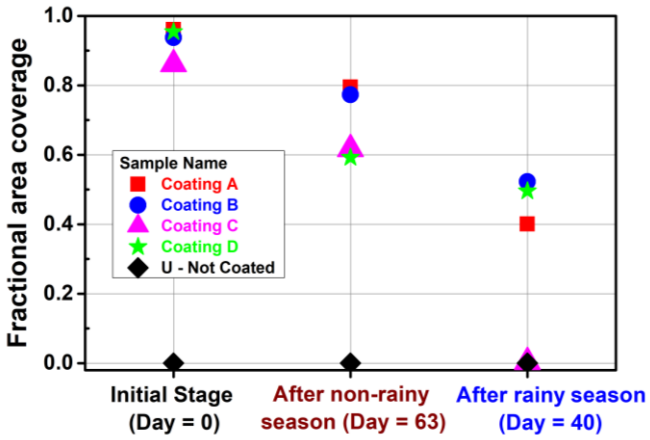

Fig. 46: Fractional area coverage of coated (A, B, C and D) and not-coated (U) samples, at its initial stage (as-deposited) after being exposed to rainy and non-rainy seasons. The area scanned is 50 µm X 50 µ in all cases.

Based on these observations, we adopted the following methodology to quantify the surface coverage of the coating. For the not-coated samples, the area under the probability distribution (Fig. 45 (a)) is determined by integration over phase angle range of +/- 1.5°. This window is selected to obtain the total fractional area (out of that scanned in TM-AFM) that is not covered by any coating. As expected, for the not-coated sample, total fractional area that is not covered is 1. Substrating this from 1 would give us the fractional area coverage. This procedure is repeated for the other samples for the initial condition and also after environmental stress. The results are shown in Fig. 46. From Fig. 46, we may conclude that the fractional area coverage for all coated samples after being exposed to the rainy season is lower compared to the samples exposed to non-rainy season. For coating C, the fractional area coverage becomes equal to the not-coated sample after being exposed to rainy season, which indicates complete removal of the coated layer. After the rainy season, coated samples also show a statistically significant decrease in roughness from its initial stage, making the surface hydrophilic.

5.2.4 Accelerated Stress Test: Acid (pH 6) Immersion Test

To emulate the composition of acidic rain in Mumbai, an acid immersion test was carried out. In this test, all samples were immersed in a pH 6, sulphuric acid solution at room temperature, for which the sulphur concentration was 60 ppm, which is a 20 X acceleration over the rainfall samples collected during field exposure test.

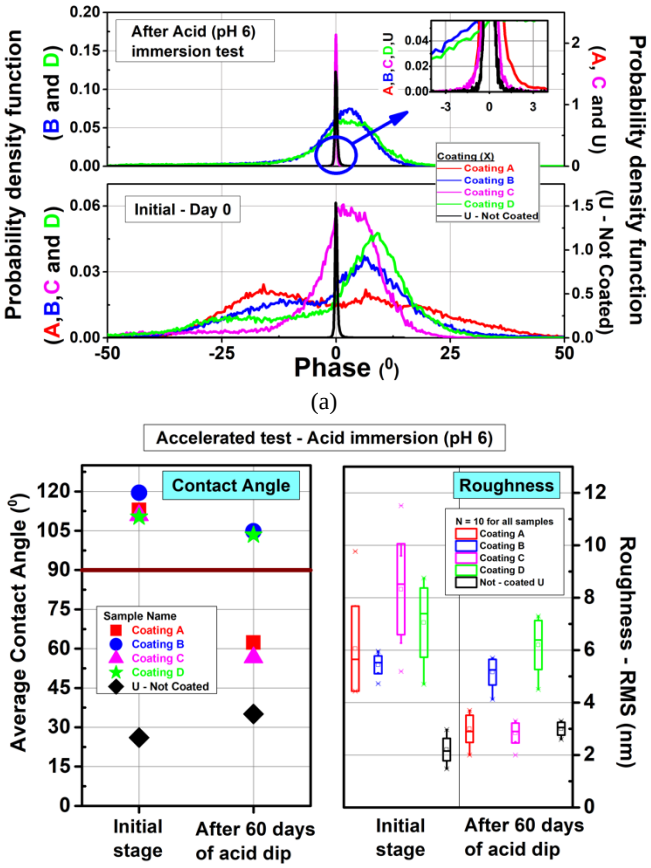

Fig. 47: (a) Probability density function of TM-AFM phase angle for coated (A, B, C and D) and not-coated sample (U), at its initial stage (as-deposited), and after being exposed to acid (pH 6) immersion test. (b) Average contact angle and roughness of coated (A, B, C, D) and not-coated (U) glass samples under acid (pH 6) immersion test.

In Fig. 47 (a) we may observe that coatings A and C show an approximately 0° phase angle after the acid immersion test, which indicates that surface coverage of the coating material decreases for A and C after acid immersion test (compared to coatings B and D). Coatings A and C also shows a statistically significant decrease in roughness after the acid immersion test (shown in Fig. 47 (b)), making the surface hydrophilic.

Not-coated sample (U) does not show any change in phase angle after the acid immersion test, which indicated that the increase in contact angle (shown in Fig. 47 (b)) is due to the increase in roughness that is likely caused by etching of Na from the glass surface [66]. After being exposed to the acid immersion test, the fractional area coverage is approximately 0% for coatings A, and C. Fractional area coverage for coatings B and D are approximately 84% and 86% (respectively) after being exposed to the acid immersion test. These correlate well with the trends in contact angles measured before and after the acid immersion test.

5.2.5 Accelerated Stress Test: Impact of Rainfall

To study the effect of the impact of rainfall, a rainfall simulator was developed, which emulates the natural rainfall.

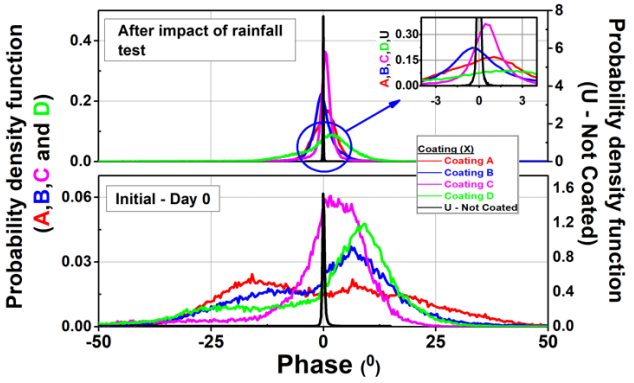

(a)

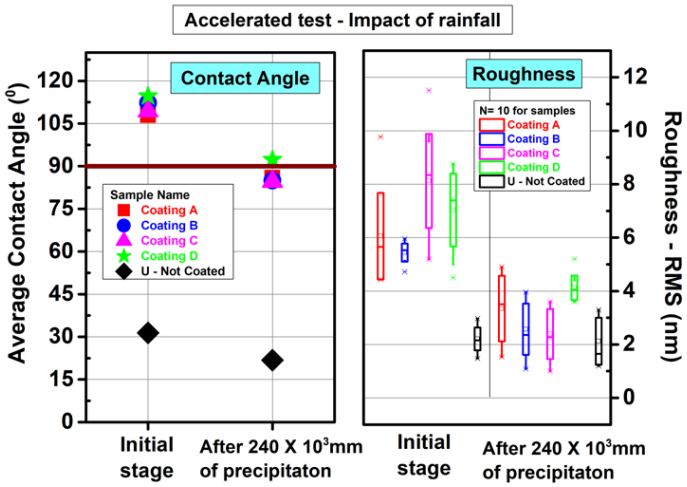

(b)

Fig. 48: (a) Probability density function of TM-AFM phase angle for coated (A, B, C and D) and not-coated sample (U), at its initial stage (as-deposited), with exposure to high impact rainfall intensity of 2000 mm/h (representing extreme case scenarios) with velocity of 2 m/s. (b) Average contact angle and roughness of coated (A, B, C, D) and not-coated (U) glass samples with exposure to high impact rainfall intensity of 2000 mm/h (representing extreme case scenario) with velocity of 2 m/s.

From the phase image analysis (shown in Fig. 48 (a)), we observe that all coated samples show a decrease in the spread of the phase angle (from 0°) after being exposed to 240×10^3 mm of precipitation via artificial rain/impact of rainfall test. Thus, we may conclude that the surface coverage of the coating material decreases (from its initial stage) for all coated samples after exposure to artificial rain. The coated samples also show a statistically significant decrease in roughness (shown in Fig. 48 (b)) after being exposed to the impact of rainfall test, making the samples hydrophilic. The fractional area coverage for coatings A, B, C and D are approx. 59%,

48%, 37% and 80%, respectively, after being exposed to artificial rainfall. We also observe a good correlation between the fractional area coverage with contact angles measured before and after exposure to artificial rain.

5.3 Conclusion

In this chapter, we establish Tapping Mode AFM as a reliable characterization technique to investigate the changes in surface coverage of AS-coatings on PV cover glass, when subjected to different environmental stressors. The not-coated glass surface shows 3 X times (at least) higher adhesive force, compared to coated glass surface, which produced a phase contrast between the coated and not-coated areas within the same sample. Compared to other characterization techniques like electron microscopy, this method offers a non-destructive characterization technique which does not require any sample preparation. By plotting the probability density function of the phase image, we were also able to perform a quantitative analysis to obtain fractional area coverage. We observed a decrease in the spread of the TM-AFM phase angle, as the coatings degraded when subjected to outdoor field exposure test, and 2 different accelerated stress tests. This indicates that the relative surface coverage of the coating material decreases when subjected to different stressors. We also demonstrated a good correlation between continuous surface changes (resulting in contact angle and roughness) with phase angle distribution.

Chapter 6 – Outdoor durability of AS-coatings

Work on the development of various AS-coating has been widely reported [14]–[16]. However, there are fewer reports on detailed analysis of the performance and durability of these coatings. Chapter 4 established that coating A, B, C and D show better cleaning efficacy than the not-coated sample (U). This showed that AS-coatings could mitigate soiling under controlled environments and outdoor field exposure. However, degradation of the coating under harsh environmental conditions is a concern [17]–[23], [45]. In this chapter, we investigate the significant stressors that reduce the performance of AS-coatings during field exposure tests. Further, the durability was tested during rainy and non-rainy seasons to segregate the impact of stressors that degrade AS-coatings in the field.

6.1 Experimental Details

Outdoor exposure test was done on solar glass (5 cm × 2.5 cm) and crystalline silicon PV modules (100 W_p). All Indoor stress tests were carried out on solar glass samples. For the outdoor exposure test on solar glass samples, we tested coated and not-coated samples with two different cleaning frequencies, i.e., weekly cleaned and cleaned once in 4 weeks, which went through a total of 10 and 2 manual cleaning runs, respectively, throughout the experiment, lasting 89 days. Cleaning runs are the time when the glass samples or PV modules were cleaned manually, excluding rain events (natural cleaning). For module-level analysis, we used three pairs (each pair containing one coated and one not coated) of PV modules. We cleaned the modules at three different cleaning frequencies: daily, weekly, and never cleaned. The solar glass sample and the PV modules were installed at a 19º angle tilt on a rooftop in Mumbai (19.1334° N, 72.9133° E), which falls in warm & humid climatic zone. The outdoor exposure study on solar glass samples was done from 19th March to 22nd May 2018 (9 weeks), followed by three weeks of heavy rainfall from 26th June to 17th July 2018 (3 weeks). PV modules were installed in the field from 13th December 2017 to 31st December 2018. A multi-channel I-V curve tracer (Daystar MT5 3200) was used to measure the power generated at an interval of 1 min. To evaluate the effect on the solar glass, contact angle, roughness, and X-ray photoelectron spectroscopy (XPS) measurements were carried out. The contact angle was measured using DataPhysics Instruments, model OCA 15SEC. Roughness was

measured using Atomic Force Microscope (AFM) from Asylum/Oxford Instruments, model MFP3D. ULVAC-PHI, PHI5000VersaProbeII was used for XPS measurements. All solar glass samples used in the experiment were from Borosil Glass Works Limited, India.

To study the effect of rainy seasons, outdoor field exposure was carried out from 30th Sept. to 8th Nov. 2019, and the total precipitation during this period was 180 mm [65]. The outdoor field exposure for the non-rainy season was carried out from 24th Dec. 2019 to 24th Feb. 2020; precipitation during this time was zero. AS-coating was applied on solar glass samples and PV modules by manual spray coating as per the instructions in product manuals. Details of sample history and sample preparation are given in section 4.1.1. The coatings were named A, B, C and D, and the not-coated glass sample was named as U. Contact angle and roughness were measured at 10 points on each sample (denoted at N =10). Wilcoxon's signed rank test [52] was used to identify if the difference between samples before and after the experiment is statistically significant. P values obtained by Wilcoxon's signed rank test < 0.05 was considered to be statistically significant, which considers a confidence interval of 95 %. When the contact angle of the coated surface went below 90˚, it was defined as failure.

6.2 Results and Discussion

6.2.1 Outdoor Durability Test on Coated and Not-Coated Solar Glass Samples

The samples A, B, C and D changed from hydrophobic to hydrophilic in 89 days (Fig. 49). Coating A was the weakest performing coating showing a decrease of 70º contact angle (after 89 days and 10 cleaning runs) from its initial values. Coating D performed comparatively better, showing a decrease of approx. 35º in contact angle. The Wilcoxon's signed rank test showed that the difference (in contact angle) between before (Day 0) and after the experiment (Day 89) for 2 and 10 cleaning runs for all the coated samples (A, B, C and D) is statically significant with a p-value of 0.002. It was also verified that the difference (in contact angle) between different cleaning runs (10 and 2 cleaning run) is statistically significant. The samples that underwent 2 and 10 cleaning runs had same environmental exposure, while the only difference between these samples was the amount of abrasion experienced by them (number of cleaning runs). This points toward the role of abrasion in the degradation of AS-coatings. Apart from manual cleaning, all samples were also exposed to 3 weeks of heavy rainfall, which added to the effect of abrasion by natural cleaning. Fig. 50 shows the variation in roughness values within the coated samples. The roughness seen on

Day 0 is due to non-uniform deposition of the coating due to manual spray. The roughness of the coated solar glass surface (A) reduces to that obtained for not-coated glass samples after exposure for 89 days and 10 cleaning runs. The difference in roughness is also seen to be statistically significant (average p-value of 0.003) for high cleaning runs. This correlates to the drop in hydrophobicity (Fig. 49). The difference in roughness between different cleaning runs was seen to be statistically significant for only coatings A and C.

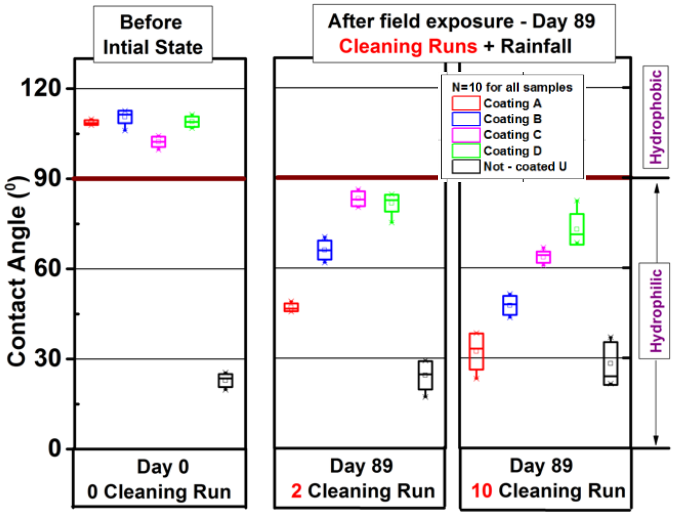

Fig. 49: Contact angle of coated (A, B, C, D) and not-coated (U) glass samples before and after the experiment for 2 different manual cleaning runs.

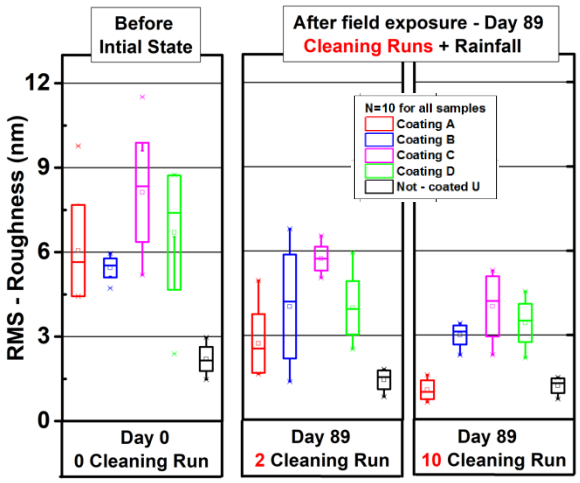

Fig. 50: Roughness of coated (A, B, C, D) and not-coated (U) glass samples before and after the experiment for 2 different manual cleaning runs.

6.2.2 Effect of Exposure on Elemental Composition

In XPS scan shown in Fig. 51, a sharp decrease in the intensity of the F-C bond was observed after 89 days of exposure for coatings A, B and D for samples with both 2 and 10 cleaning runs. The

reduction in the F-C bond may be caused by the impact of UV radiation [39]. This is accompanied by the reduction of the hydrophobicity of the coated surface (Fig. 49). For 2 cleaning runs, coatings B and D showed a small intensity peak of F-C bond. Coating D shows F-C bond after the experiment for both cleaning runs, which correlated to a comparatively higher contact angle (72º) seen in Fig. 49. Similarly, in C_{1s} spectra, we found signature of C-F_2 bond (Day 0- initial state), which shows a significant amount of reduction after exposure for both 10 and 2 cleaning runs in Coating A, B and D. Coating C shows phenylsilicone (107.24 eV - present in initial state, day 0) signature at the initial state. After exposure of 89 days, it shows a shift in the Si_{2p} peak position for both 2 and 10 cleaning runs. Si_{2p} peak for Coating C, at day 89 and 2 cleaning runs, shows signature of Mica muscovite, and at 10 cleaning runs, it shows signature of Aluminosilicate. Both of these minerals (Mica muscovite and Aluminosilicate) show elements found in the bare solar glass. For the not-coated sample (U), we may observe that Na (Sodium) present in the initial state – Day 0, is not present after Day 89 for both cleaning runs. This is a signature of acid rain as Sulphuric acid (present in acid rain for Bombay/Mumbai region) etches the Na from the glass [67]–[69].

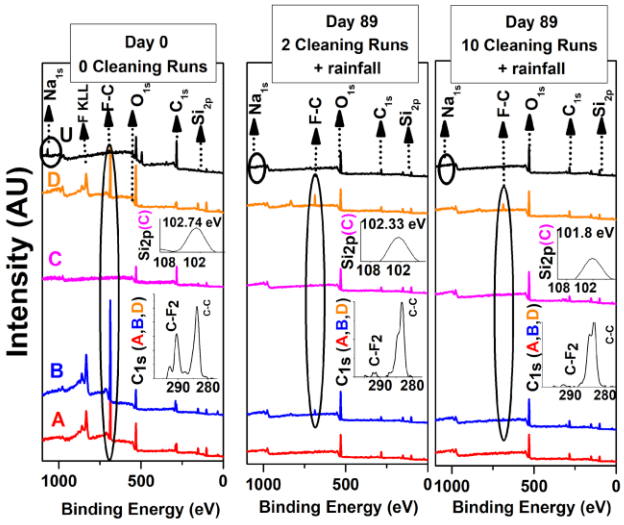

Fig. 51: XPS of coated and not-coated samples before and after exposure for different cleaning runs.

6.2.3 Performance of PV module Coated with the Worst-Performing Coating

Soiling loss for PV modules coated with coating-A was calculated based on energy generation [70]. The soiling rate of coated and not-coated PV module did not show any significant difference throughout the year. However, a difference of 2.2 % (average) in soiling loss is observed between weekly cleaned coated and not-coated modules, Fig. 52. For weekly cleaned coated module, soiling loss went back to zero after every cleaning. This trend reversed after the rainy season. This

implies that rainfall acted as a significant stressor and reduced the efficacy of the coating. For coated module after cleaning runs, weekly cleaned modules produced higher energy than daily cleaned modules due to less abrasion caused by less cleaning run (in weekly cleaned modules), thus showing negative soiling loss during the rainy season.

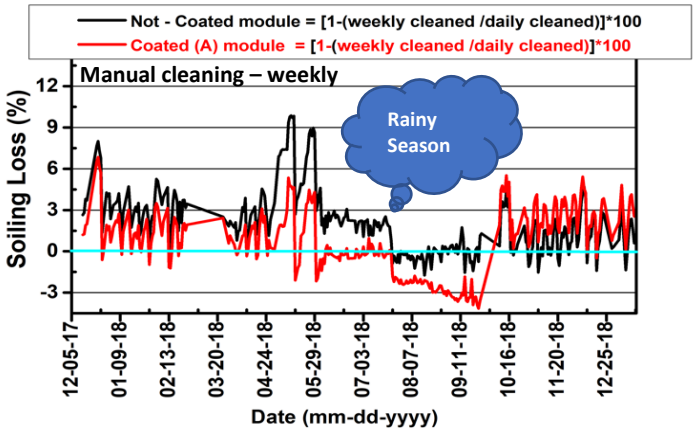

Fig. 52: Difference in soiling loss between not-coated and coated (coating A) modules. Weekly manual cleaning was done.

6.2.4 Effect of Rainy and Non-Rainy Season

In the previous section, 6.2.3, the degradation of the coated samples was due to the coupled effect of the damage caused by abrasion and rain. To segregate the effect of rain and sunny events, we studied the effect of seasonal variation (rainy and non-rainy seasons) on degradation of AS-coatings.

To investigate the effect of rainfall, all samples were exposed to the field during the rainy season, and after every rain event contact angle of all exposed samples was measured. The contact angle of coatings A, B, C, D changes from hydrophobic to hydrophilic in 40 days of field exposure during the rainy season, Fig. 53 (a). Coating C becomes hydrophilic in 5 days of field exposure during rainy season. This is because silane based materials gets easily hydrolyzed and can be removed from glass [71], [72]. Coatings B and C show high rates (^{o}/day) of initial degradation in contact angle, which reduces after the 10th day of field exposure (Fig. 53). Similar findings were observed in Denmark [32].

To evaluate the performance of AS-coating during the non-rainy season, contact angle measurements were done on field exposed samples at weekly intervals. All samples show an initial drop in contact angle, which stabilized after 7 days of field exposure. All coatings remain hydrophobic after 63 days of field exposure during the non-rainy season (shown in Fig. 53 (a)). For

both rainy and non-rainy season, all coatings show a statistically significant decrease in contact angle after 5th day (for rainy season) and 7th day (for non-rainy season) of field exposure. The roughness of coated and not-coated samples was also measured before and after field exposure. Samples exposed to rainy season showed a statistically significant difference in roughness for all coated samples before and after the complete field exposure, which was not seen for samples exposed to non-rainy season (Fig. 53 (b)). This correlates well with the decrease in contact angle in rainy and non-rainy seasons. We saw a good correlation between contact angle and fractional area coverage for all coated samples (shown in Fig. 45 and Fig. 53).

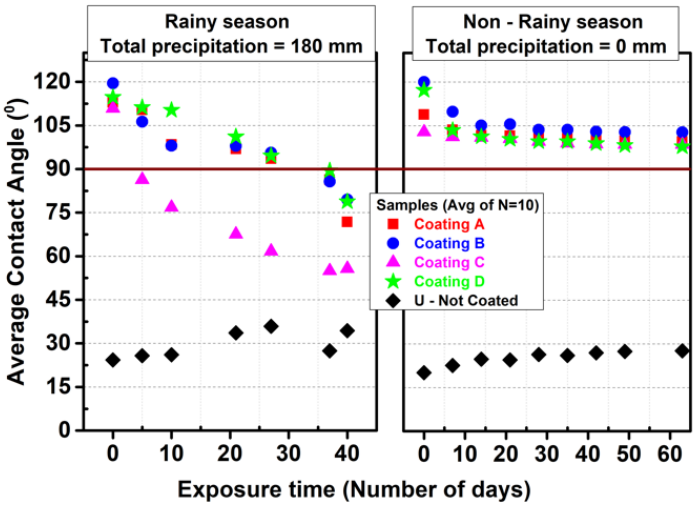

(a)

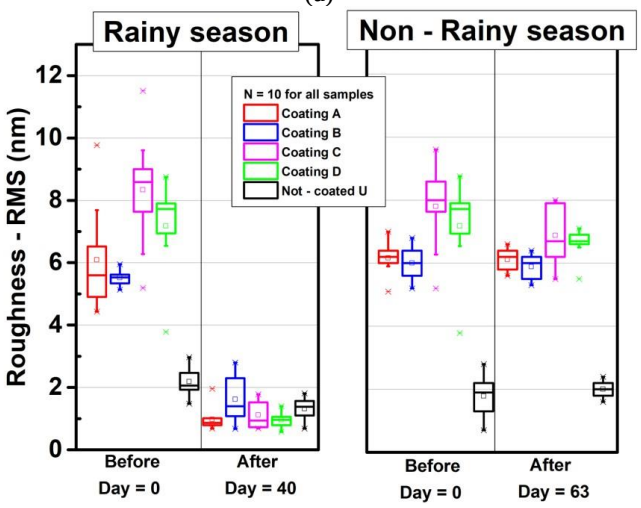

(b)

Fig. 53: (a) Contact angle and (b) Roughness of coated (A, B, C, D) and not-coated (U) glass samples under field exposure during rainy and non-rainy season.

We also quantified the impact of 2 different seasons that degrade AS-coatings during field exposure tests. Time to failure was calculated in terms of days. Time to failure was noted when

the contact angle of the coated samples went below 90˚. For datasets where we experimentally saw the failure of the coated sample, the exact time to failure data was determined by interpolation, using a polynomial fit with Adj $R^2 > 0.9$. For data sets where we experimentally did not see the failure of the coated sample, the best fit line through the last three points was used for estimating the time to failure through extrapolation. The time to failure of coated samples for rainy and non-rainy season is shown in Table 7. Equation 8 shows the acceleration factor formula.

Table 7: Time to failure for outdoor durability test.

	Coating A	Coating B	Coating C	Coating D
Outdoor test - Number of days in which the coating becomes hydrophilic (days)				
Rainy season	32	36	5	35
Non-rainy season	639	549	221	215

$$Acceleration\ factor\ (Outdoor)\ = \frac{Time\ to\ failure\ during\ non-rainy\ season}{Time\ to\ failure\ during\ rainy\ season} \quad (8)$$

In Fig. 54, we may observe that coating life decreases by 21 X (average of coating A, B, C and D) when exposed to rainy season compared to the samples exposed to the non-rainy season. During the rainy season, phenylsilicone based coating (C) shows 7 X lower coating life than fluoropolymer based coatings (average of A, B and D).

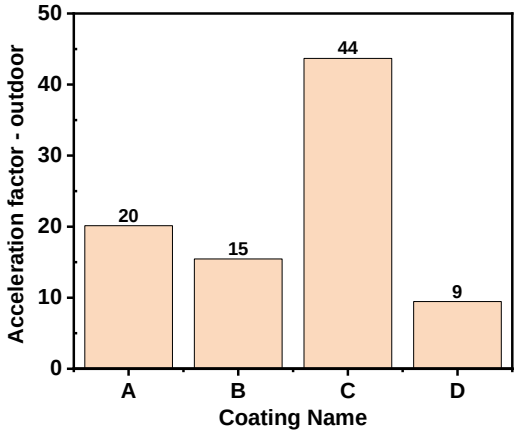

Fig. 54: Acceleration factor for outdoor durability tests.

6.3 Conclusions

We found that for Mumbai weather conditions (warm and humid), commercial hydrophobic AS-coatings lose their hydrophobicity in 89 days (9 weeks of non-rainy season and 3 weeks of heavy rainfall) of field exposure.

From the outdoor field test, the following signature of stressors were identified :

1. The difference in contact angle between two different cleaning runs (10 and 2 cleaning run) was statistically significant. The samples that underwent 2 and 10 cleaning runs had same environmental exposure, while the only difference between these samples was the amount of abrasion experienced by them (number of cleaning runs). This points toward the role of abrasion in the degradation of AS-coatings.
2. Coatings A, B and D were degrading with decrease in C-F bond. The reduction in the C-F bond may be caused due the impact of UV radiation [39], indicating UV radiation as a stressor which degraded the AS-coatings.
3. Weakest performing coating A was tested on PV modules, which showed no significant change in rate of dust deposition between coated and not-coated PV module through one year of field exposure. However, a difference of 2.2% (average) in soiling loss is observed between weekly cleaned coated and not-coated modules. For weekly cleaned coated module, soiling loss went back to zero after every cleaning run before rainfall. This trend reversed after the rainfall. This implies that rainfall acted as a significant stressor that degraded AS-coatings.
4. To segregate the effect of rainy and non-rainy events, we further tested the durability of the coated samples in 2 different seasons. Coating life decreased by 21 X when exposed to the rainy season compared to the samples being exposed to the non-rainy season. During the rainy season, phenylsilicone based coating (C) shows 7 X higher than fluoropolymer based coatings (average of A, B and D), as silane based materials gets easily hydrolyzed and can be removed from glass [71], [72]. This confirmed that rain is a significant stressor that degraded AS-coatings during field exposure.

Chapter 7 – Indoor accelerated stress tests

In chapter 6, we identified the stressors that degrade AS-coatings under field exposure tests. Three stressors were identified; (1) Rain, (2) Abrasion, and (3) UV radiation. In this chapter, we have investigated the impact of each stressor in detail to understand the factors that influence these environmental stressors. We have also studied the impact of combination of stressors and how it compares with isolated stress tests. The complete study was conducted on 4 different accelerated testbeds; (1) Abrasion tester, (2) Rainfall simulator, (3) UV 365 chamber and (4) UV and condensation chamber. Damp heat, humidity freeze, and the thermal cycling test (based on the IEC 61215 standard) were also conducted to compare the results with the other accelerated stress tests.

7.1 Experimental Details

7.1.1 Sample Preparation

Four different commercial hydrophobic anti-soiling coatings were applied on solar glass samples (size 5 cm × 2.5 cm) (one type of coating solution applied on one solar glass) by manual spray coating method as per the instructions given in the respective product manuals. Details of sample history and sample preparation are given in section 4.1.1. The coated samples (A, B, C, and D) did not show any anti-reflective properties. Thus, there was no significant difference in the AM1.5G weighted average transmittance (WAT) of the coated samples and not-coated sample ‘U’ in their initial state.

7.1.2 Accelerated Test Beds

(1) Abrasion tester - An indoor abrasion testbed (shown in Fig. 55) was built to emulate the following stressors that influence abrasion damage during outdoor field conditions, relevant for PV application - (a) thermal cycling (heating and cooling cycles), (b) formation of dew, (c) dust deposition and (d) cleaning cycles via brush.

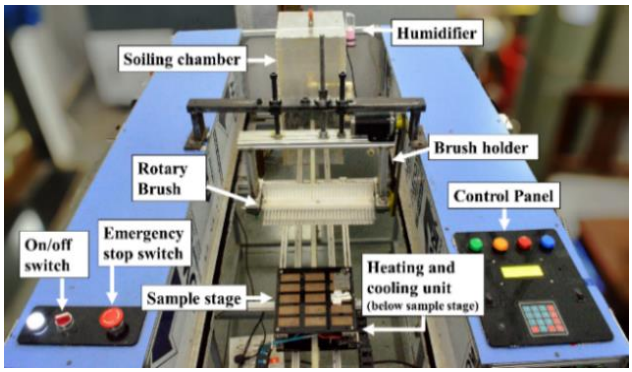

Fig. 55: Picture of the indoor abrasion testbed.

In a natural dust deposition process, accumulation of dust is coupled with cooling (at night), dew (early mornings), and heating (during noon) cycles. This process allows the dust to adhere more strongly to the surface of the PV modules [7]. To mimic this process on the indoor abrasion testbed, the substrate was cooled down to 21°C (minimum module temperature observed in Mumbai during the field exposure test), followed by a water vapour mist spray via a humidifier, which led to deposition of the mist on the samples. This was followed by dust deposition of 0.2 mg/cm^2, which is equivalent to 2 weeks of soiling measured at NCPRE, PV Module Monitoring Station (PVMMS), IIT Bombay, Mumbai, India [6]. Then, the samples were heated to 65°C (maximum module temperature observed in Mumbai during the field exposure test) to emulate the heating cycle seen during field exposure. The particle size distribution of the dust sample used in this study is shown in Table 8, and the mineral composition is shown in Fig. 56. Both the particle size distribution and mineralogy are similar, but not identical, to those reported earlier for the same location in [6].

Table 8:The dust particle size distribution used in the indoor abrasion testbed.

D (µm)	% of Total Sample (Used in the indoor abrasion testbed)	Sediment Type
0-4	6.15	Clay
4-8	12.71	Very Fine Silt
8-16	25.16	Fine Silt
16-31	41.55	Medium Silt
31-63	14.43	Course Silt
63-125	0	Very Fine Grained

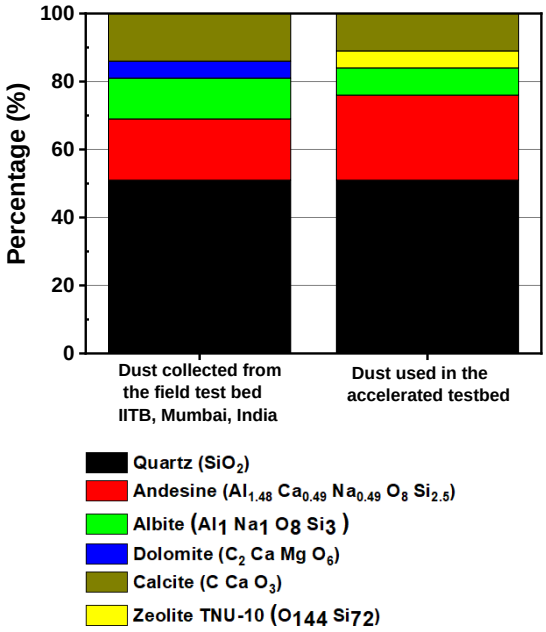

Fig. 56: Analyzed XRD data of dust samples collected from PV modules under outdoor field exposure (in the year 2020) at IIT Bombay, Mumbai, India, and the indoor abrasion testbed

To emulate different combinations of stressors, samples were subjected to different types of cycles. One run of the only-clean cycle refers to 1 cycle of forward and backward movement. One dew-dry-clean cycle refers to one cycle of cooling + heating + one run of cleaning. One dew-dust-dry-clean cycle refers to one cycle of cooling + dust deposition of 0.2 mg/cm^2 + heating + one run of cleaning. The horizontal velocity of the brush travel on the samples for cleaning was fixed at 0.4 m/sec. Linear abrasion refers to the cleaning cycles run via the linear brush, and rotary abrasion refers to the cleaning cycles run via the rotary brush. All brushes were custom-made and set to be identical in bristle length, diameter, number of tufts/rows, and number of bristles/tufts. The rotary brush and linear brush 2 had equal row spacing (distance between two rows at the outer end of brush bristles) between the brush bristles. Linear brush 1 had 3.5 times higher packing density of brush bristles than linear brush 2 and rotary brush. Photographs of the 3 brushes used in this study are shown in Fig. 57. The rotary and linear brush used in this study show equal cleaning efficacy. The spacing between the brush frame and the solar glass surface were kept identical for both linear and rotary abrasion tests.

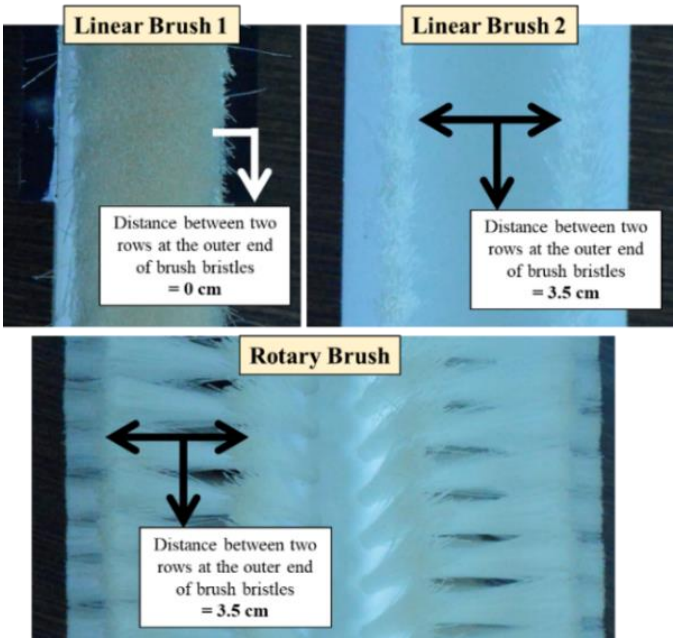

Fig. 57: Photographs of custom-made brushes used in this study - linear brush 1, linear brush 2 and rotary brush.

(2) Rainfall simulator - The rainfall simulator was built to investigate the impact of rainfall on the degradation of AS-coatings. The velocity of raindrops hitting the top surface of the sample was calculated to be 7.3 m/s which falls within the range of terminal velocities reported during an actual rain event [73]. The average raindrop diameter was 2 mm, and the rainfall intensity was fixed at 21 mm/h, which comes under the moderately heavy rainfall category [74]. The elemental contamination of the water samples used in this study, measured using ICP-AES (Make - SPECTRO Analytical Instruments GmbH, Germany and model - ARCOS, Simultaneous ICP Spectrometer), is shown in Table 9.

Table 9: Elemental contamination of water used in tests.

Name	S (ppm)	Ca (ppm)	Na (ppm)	K (ppm)	Mg (ppm)
Experimental water samples					
pH 7 water sample	0.89	16	4.7	0.4	6.1
pH 6 water sample	60	10	1.4	0.6	2.3
Rainwater samples (collected from IIT Bombay, September 2019)					
Rainwater sample (pH 7)	0.72	1.5	2.1	0.7	0.3

(3). UV chamber - The UV exposure test was done in UV 365 chamber. The chamber had a single wavelength LED source of 365 nm. The average UV intensity over a 5 cm × 2.5 cm area was 203 W/m^2, and the substrate temperature was set to 65℃. The schematic diagrams of the rainfall simulator and the UV chamber are shown in Fig. 58.

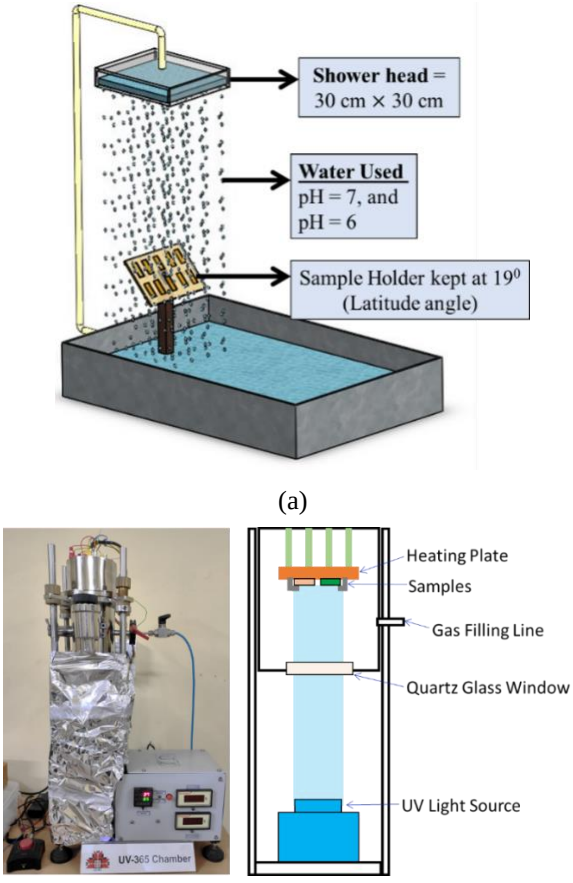

Fig. 58: Schematic diagram of the (a) Rainfall simulator and (b) UV 365 chamber. The photograph of the UV 365 chamber is also shown in (b).

(4) UV and condensation chamber - The effect of combination of UV and condensation was studied in QUV accelerated weather tester, model QUV/basic [75]. In this accelerated chamber, 1 cycle includes 8 hours of UV exposure, followed by 4 hours of only condensation (with no UV exposure). UV exposure test was done at 60℃, and condensation was performed at 50℃. This test was chosen to investigate the effect of combination of stressors (UV + condensation) on AS-coatings. A graphical representation of 1 cycle of the QUV Accelerated weather tester is shown in Fig. 59. UVA-340 lamps were used for this test which covers the complete UV part of the sun's spectrum from 300 nm to 400 nm, with a peak wavelength at 340 nm. The intensity of the UV

lamp was 37 W/m^2. The water used for this accelerated test had all elements detected in rainwater sample (for IIT-Bombay, Table 9). However, Na and K content was approximately 20 times higher than the rainwater samples.

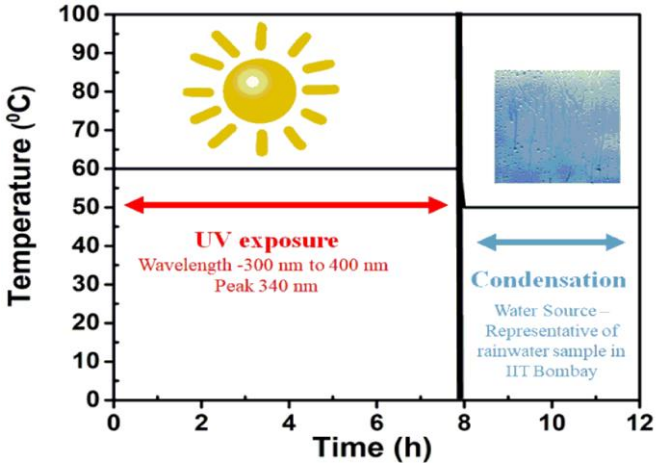

Fig. 59: Graphical representation of 1 cycle of the QUV Accelerated weather tester.

7.1.3 Characterization

All tests were conducted on 5 cm × 2.5 cm solar glass samples. The top coating was characterized via contact angle, roll-off angle, roughness, transmittance, and TM-AFM phase imaging. The contact angle measurements were performed using a 2µl water droplet. An in-house roll-off angle (RoA) meter was developed to measure RoA. A 45 µl of deionized (DI) water droplet was used to measure the RoA. The weight of the brush bristles was measured via an electronic weighing machine. Raman spectroscopy, scanning electron microscopy, and hardness measurements were done to characterize the damage caused to the brush bristles. Roughness, Raman, XPS, and SEM measurements are shown in Appendix I. Measurements of contact angle, roll-off angle, and roughness were taken at 10 locations for each sample. All box plots in this chapter are based on 10 data points taken in each glass sample to account for non-uniformity of coating within the sample. Fractional area coverage was calculated over a 50 µm × 50 µm area. Contact angle measurements were done using Data-Physics Instruments model OCA 15SEC; transmittance was measured via PerkinElmer LAMBDA 950 (wavelength range from 300 nm to 1200 nm), roughness and TM-AFM phase imaging was done via Asylum/Oxford Instruments, model MFP3D. X-ray photoelectron spectroscopy was measured via XPS - Kratos Analytical, AXIS Supra. Raman spectroscopy was done via Horiba Jobin Yvon, model HR800-UV confocal, Nanoindentation was done via TI Premier, and scanning electron microscopy was done via Hitachi S 3400N. The particle

size of the dust samples was analyzed using Malvern Mastersizer 3000, and XRD analysis was done using a PANalytical Empyrean system. The cleaning efficacy of the brush was calculated via transmittance measurements (average of 3 solar glass samples) before and after one dew-dust-dry-clean cycle. The transmittance measurements for the cleaning efficacy test were done via Jasco spectrometer (model: V-650 Series, wavelength range: 300 nm to 900 nm). Statistical analysis was done via the Wilcoxon signed-rank tests to verify if the difference between the samples is statistically significant [52]. When the contact angle of the coated surface went below 90˚, it was defined as failure.

7.2 Result and Discussion

7.2.1 Factors that Influence Abrasion Damage

7.2.1.1 Abrasive Agent

Dew-dust-dry-clean and dew-dry-clean cycles represent actual field conditions under which the samples are exposed to a combination of stressors. Nylon 6,12 brush material was used in this study. Only-clean cycles represent (cleaning runs) the effect of an isolated stressor, namely abrasion by brush bristles. In this section (7.2.1.1), Nylon 6,12 rotary brush was used for all 3 types of stress cycles. The horizontal velocity of brush travel was fixed at 0.4 m/sec. In Fig. 60, it can be seen that all coated samples that underwent dew-dust-dry-clean cycles show lower coating life than the other stress cycles, indicating that dust (abrasive agent) is the most significant stressor that abrades the coated samples, followed by dew-dry-clean cycles as the next significant stressor. All coated samples show lower coating life when exposed to a combination of stressors than an isolated stressor. All coated samples showed a statistically significant change in roll-off angle (RoA) after 120 dew-dust-dry-clean cycles, Fig. 61. The change in RoA is statistically insignificant after 120 dew-dry-clean cycles and only-clean cycles for all coated samples. The not-coated samples show signatures of surface modification (increase in RoA, contact angle, and roughness) after 120 runs of dew-dust-dry-clean and dew-dry-clean cycles. Similar observations were made by Miller et al. in a study on the effect of abrasion on PV glass [76]. Roughness measurements (shown in Appendix I, Fig. A1) indicate a reduction in the surface roughness in the case of dew-dust-dry-clean, correlating well with the contact angle and RoA data. Coating A and C show a significant decrease in the WAT after 120 dew-dust-dry-clean cycles (Fig. 62), indicating a more

significant damage for this stress cycle. Coating C was completely removed after 120 dew-dust-dry-clean cycles, as shown in the fractional area coverage measurements (Fig. 63). We may observe the signature of amide deposits on the top surface of the not-coated sample after 120 runs of all three stress cycles (Fig. 64). This deposit resulted in the surface modification (change in contact angle and RoA) on the not-coated samples after abrasion tests. We observed damage in the brush bristles, indicated by the absence of N-H, CH_2, Amide, C-C, and C-CO functional groups after 120 runs of dew-dust-dry-clean cycles (Appendix I, Fig. A2). The absence of N-H and amide functional groups was also seen after 120 dew-dry-clean cycles (Appendix I, Fig. A2).

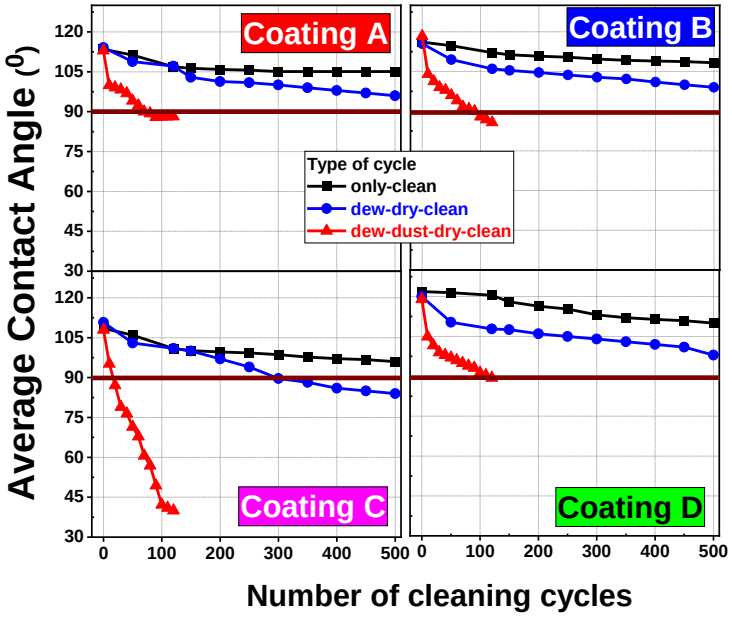

(a)

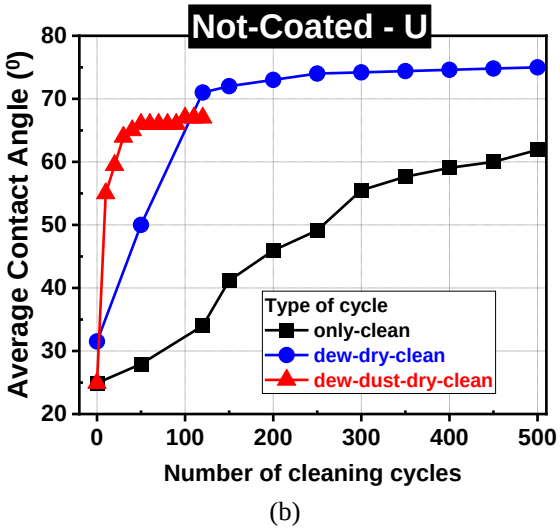

(b)

Fig. 60: Contact angle performance of (a) Coating A, B, C, D and (b) U - Not-coated sample, after being exposed to dew-dust-dry-clean cycle, dew-dry-clean cycle and only-clean cycles.

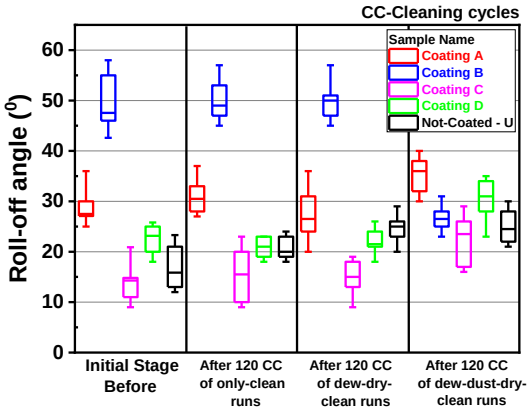

Fig. 61: Roll-off angle performance of the coated and not-coated (U) samples after being exposed to 120 dew-dry-clean cycles, dew-dry-clean cycles and only-clean cycles.

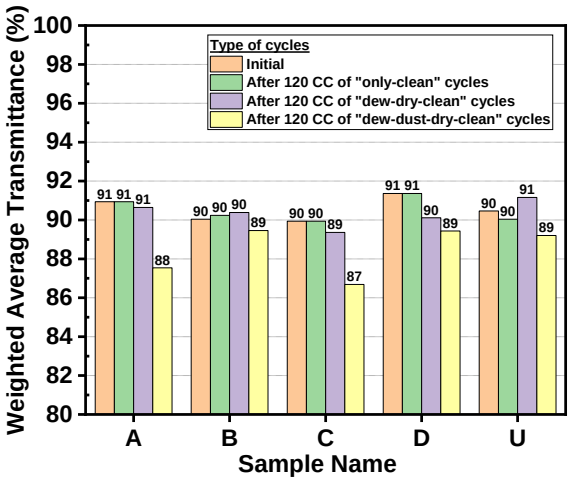

Fig. 62: WAT of the coated and not-coated (U) samples before and after being exposed to 120 dew-dust-dry-clean cycles, dew-dry-clean cycles and only-clean cycles.

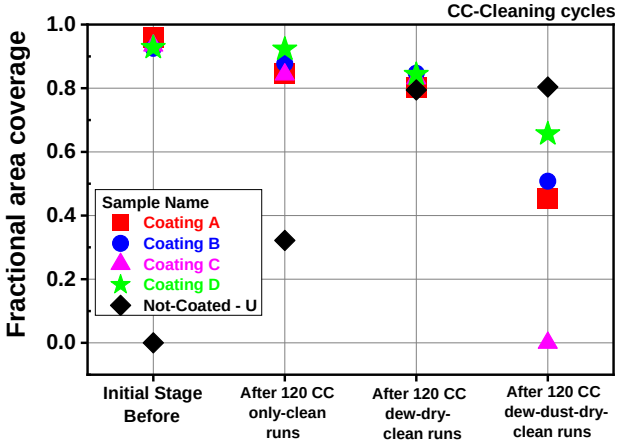

Fig. 63: Fractional area coverage of coated and not-coated (U) samples, before and after being exposed to 120 dew-dust-dry-clean cycles, dew-dry-clean cycles and only-clean cycles.

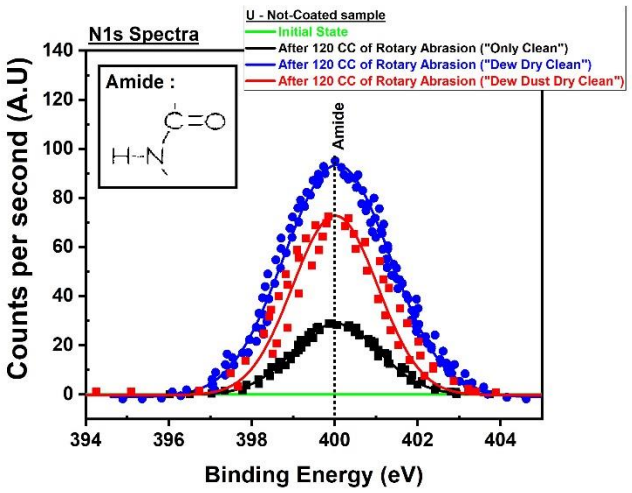

Fig. 64: N1s XPS-narrow scan of the not-coated sample before and after exposure to 120 runs of dew-dust-dry-clean, dew-dry-clean and only-clean cycle (experimental data is shown by the scatter plot; solid lines refer to the data points after smoothening using Savitzky-Golay filtering [77]).

A statistically significant decrease in the hardness of the brush bristles tips was observed after 120 dew-dry-clean cycles and dew-dust-dry-clean cycles, with a greater reduction seen in the later case (Fig. 65). The decrease in the hardness of brush bristles tips after 120 only-clean cycles (from its initial state) is statistically insignificant. This indicates that the brush bristle tips undergoing dew-dust-dry-clean cycles experienced more damage than those undergoing the other two stress cycles. The tips of the brush bristles show significant damage to their shape after 120 runs of all three stress cycles (shown in Appendix I, Fig. A3). The bristle diameter shows a decrease of 50 um after 120 dew-dust-dry-clean cycles (shown in Appendix I, Fig A3).

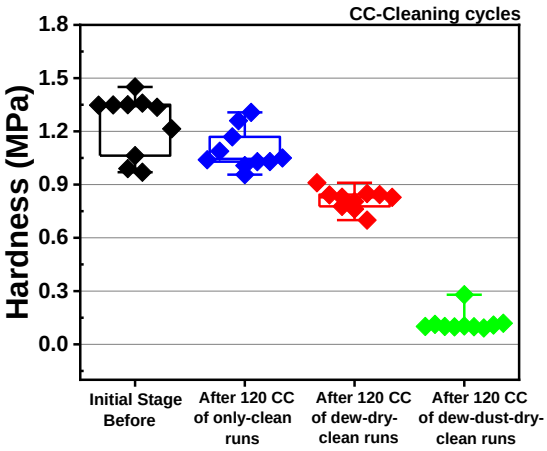

Fig. 65: Hardness of brush bristles tips before and after being exposed to 120 dew-dust-dry-clean cycles, dew-dry-clean cycles and only-clean cycles.

7.2.1.2 Packing Density

Coated samples show lower coating life when cleaned with linear brush 1 than linear brush 2 and rotary brush (Fig. 66 (a,b,c)). Degradation enhancement factor due to the packing density of the brush bristles (shown in equation 9 and Table 10) is defined as,

$$Degradation\ enhancement\ factor = \frac{Cycles\ to\ failure\ (\ Avg\ of\ Linear\ Brush\ 2\ and\ Rotary\ Brush)}{Cycles\ to\ failure\ for\ Linear\ Brush\ 1} \quad (9)$$

Cycles to failure is defined as the number of cycles at which the water contact angle drops below 90˚. The degradation enhancement factors increased from 1.2 X to 4.4 X. This is because linear brush 1 has 3.5 times higher packing density than the other two brushes. Solar glass samples come in contact with seven rows of brush bristles when cleaned with linear brush 1, whereas cleaning with a rotary brush and linear brush 2, samples come in contact with only two rows of brush bristles in each pass per cleaning cycle. We also observe that in the case of all three brushes, phenylsilicone based coating (C) shows lower coating life (varying from 2.9 X to 11.2 X) than fluoropolymer-based coatings. The high packing density of the brush bristles in linear brush 1 resulted in the application of significantly higher weight on the solar glass sample than linear brush 2 and rotary brush (shown in Fig. 67). After accelerated abrasion tests, we observed surface modifications (increase in Roughness, RoA and contact angle) on the top surface of the not-coated samples (Fig. 66 and Fig. 68). In terms of optical losses, there was no significant decrease in the solar-weighted transmittance after 3700 cycles with any of the brushes (Fig. 66 (d)). All coated samples show high initial contact angle degradation rates irrespective of the brush type. Similar trends were seen during the field exposure study in the non-rainy season.

Table 10: Number of cycles at which the samples become hydrophilic.

Cycles to failure / Number of cycles at which the sample becomes hydrophilic				
	Coating A	**Coating B**	**Coating C**	**Coating D**
Linear Brush 1	2798	3586	451	5035
Linear Brush 2	11089	5066	1750	5844
Rotary Brush	13537	5114	1578	5989
Degradation enhancement factor	4.4	1.4	3.7	1.2

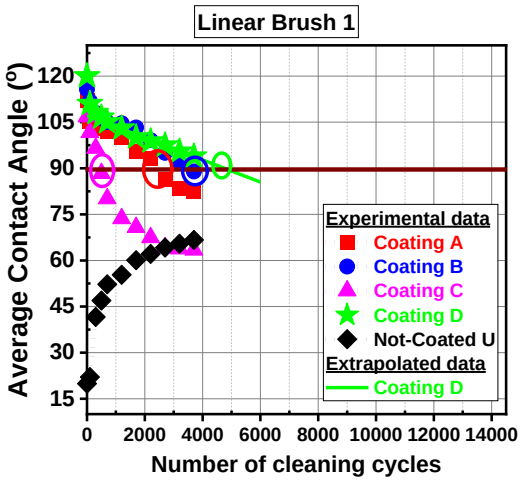
Linear Brush 1
Average Contact Angle (°)
120
105
90
75
60
45
30
15
0
2000
4000
6000
8000
10000
12000
14000
Number of cleaning cycles
Experimental data
Coating A
Coating B
Coating C
Coating D
Not-Coated U
Extrapolated data
Coating D

(a)

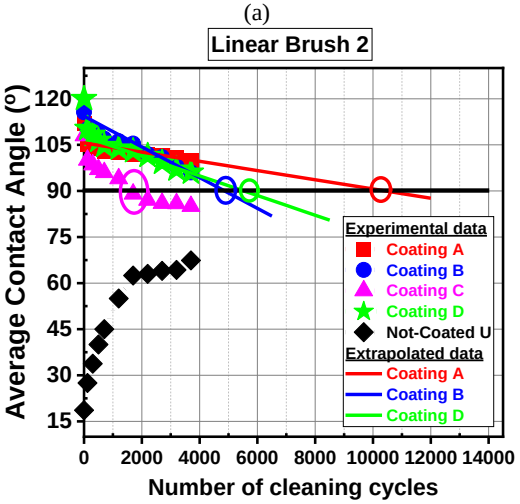
Linear Brush 2
Average Contact Angle (°)
120
105
90
75
60
45
30
15
0
2000
4000
6000
8000
10000
12000
14000
Number of cleaning cycles
Experimental data
Coating A
Coating B
Coating C
Coating D
Not-Coated U
Extrapolated data
Coating A
Coating B
Coating D

(b)

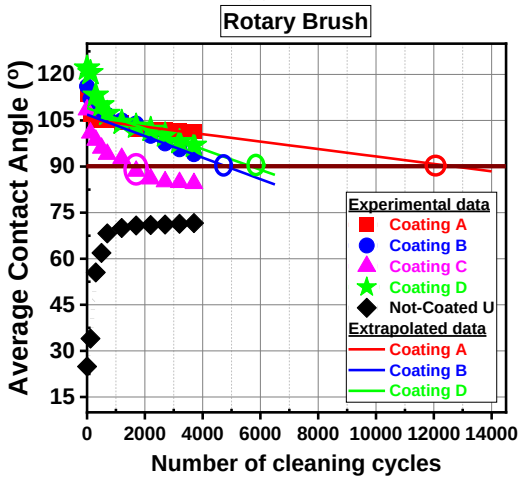
Rotary Brush
Average Contact Angle (°)
120
105
90
75
60
45
30
15
0
2000
4000
6000
8000
10000
12000
14000
Number of cleaning cycles
Experimental data
Coating A
Coating B
Coating C
Coating D
Not-Coated U
Extrapolated data
Coating A
Coating B
Coating D

(c)

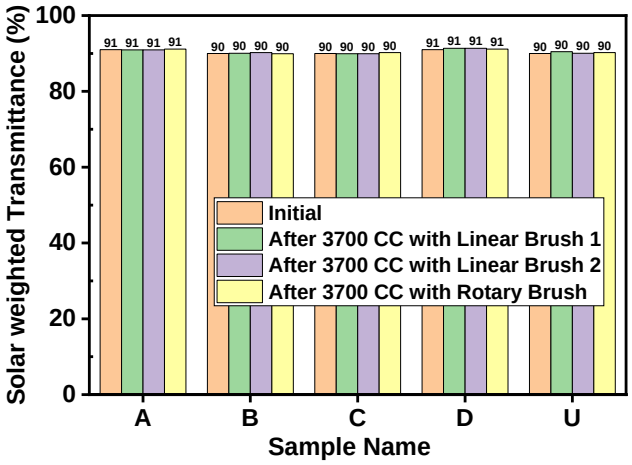

(d)

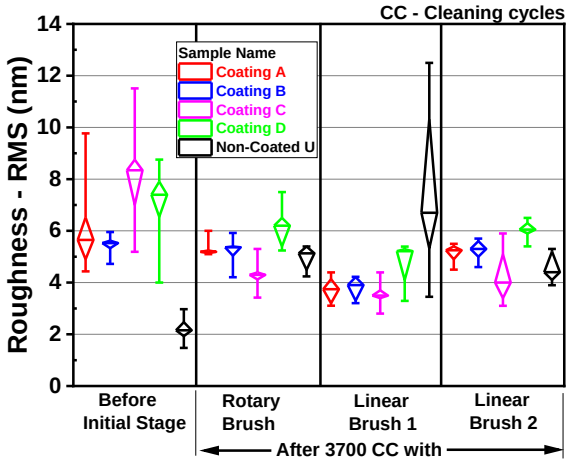

(e)

Fig. 66: Contact angle degradation when cleaned with (a) Linear brush 1, (b) Linear brush 2 and (c) Rotary brush. (d) Solar-weighted transmittance after 3700 cleaning cycles (CC) cleaned with linear brush 1, linear brush 2 and rotary brush. (e) Roughness of the coated and not-coated samples after 3700 cleaning cycles (CC) cleaned with linear brush 1, linear brush 2 and rotary brush. In Fig. 66(a), Extrapolation (via linear fit) was done by considering the slope of the last 3 data points.

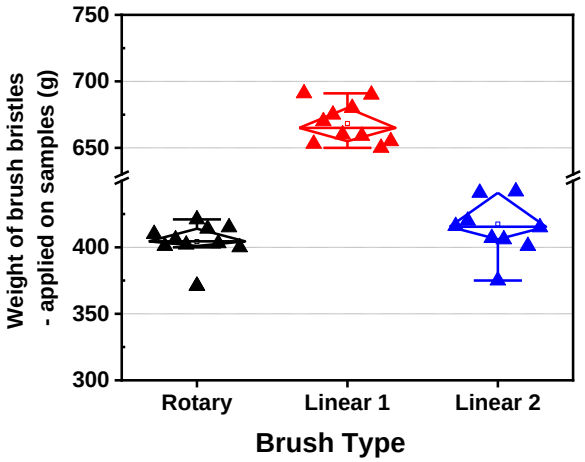

Fig. 67: Brush bristles weight on glass samples - linear brush 1, linear brush 2 and rotary brush.

In Fig. 68, we may observe a statistically significant change in roll-off angle before and after 3700 abrasion cycles with linear brush 1, linear brush 2 and rotary brush. The coatings would exhibit anti-soiling properties only when the roll-off angle of the coated samples is lower than the tilt angle of the location (19º). After 3700 abrasion cycles with linear brush 1, linear brush 2 and rotary brush, the coatings show higher roll-off angles than Mumbai, India's tilt angle. Thus, coating A, B, C, and D do not display anti-soiling properties in Mumbai, India, after 3700 abrasion cycles with linear brush 1, linear brush 2, and rotary brush.

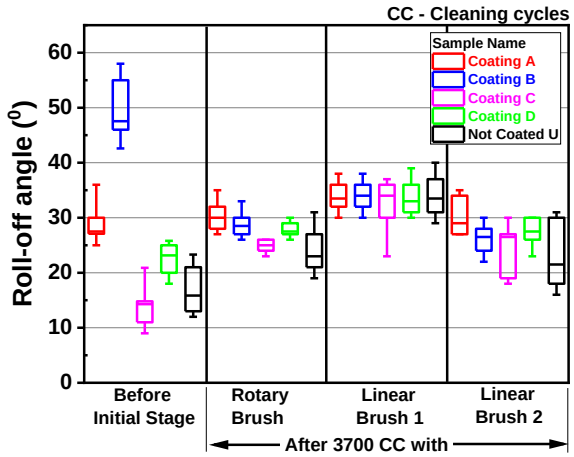

Fig. 68: Accelerated brush abrasion test when cleaned with linear brush 1, linear brush 2, and rotary brush - RoA performance of coated and not-coated samples.

The surface coverage of the coated area was calculated based on TM AFM phase imaging. Coated samples show the highest coating removal when cleaned with linear brush 1 (Fig. 69). Coating C shows the greatest damage in terms of fractional area coverage, as it shows complete removal of the coated layer when cleaned with linear brush 1 and 50% removal when cleaned with linear brush 2 and rotary brush. The damage patterns seen in RoA, and contact angle correlate well with the patterns seen in fractional area coverage.

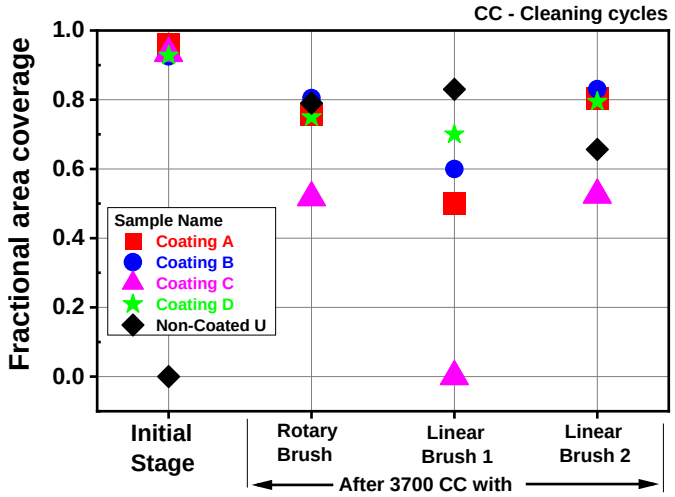

Fig. 69: Accelerated brush abrasion test when cleaned with linear brush 1, linear brush 2, and rotary brush - Fractional area coverage of coated and not-coated samples.

Nitrogen was detected on the not-coated sample (Fig. 70 (a)) after it underwent 3700 cycles with all three brushes (early signs of material deposition were indicated via TM-AFM phase imaging). The not-coated sample shows deposition of amide, and due to the deposit, we observed an increase in characteristic properties of the not-coated samples. Nylon 6,12 material was used for all 3 brushes designs. A greater change (absence of Amide, N-H stretch, C-CO, and C-C stretch) was seen in the composition of the brush bristles tips when cleaned with linear brush 1, compared to linear brush 2 and rotary brush (Fig. 70 (b)). All 3 types of brushes (linear brush 1, linear brush 2 and rotary brush) show significant wear and tear to their shape after 3700 cleaning cycles. The average diameter of the brush bristles for linear brush 1 was 0.24 mm at its initial stage, which was reduced to 0.19 mm after undergoing 3700 cleaning cycles (Fig 70 (c)). The bristle diameter of the rotary brush and linear brush 2 do not show any significant change after undergoing 3700 cycles. Few tips of the brush bristles were seen to be broken after undergoing the brush abrasion test. The brush bristles' tips of the linear brush 1, linear brush 2 and rotary brush showed a statistically significant decline (from its initial stage) in hardness after 3700 cleaning cycles (Fig. 70 (d)). A greater reduction in hardness was seen in the brush bristles tips of linear brush 1 (after 3700 cleaning cycles) than the rotary brush and linear brush 2.

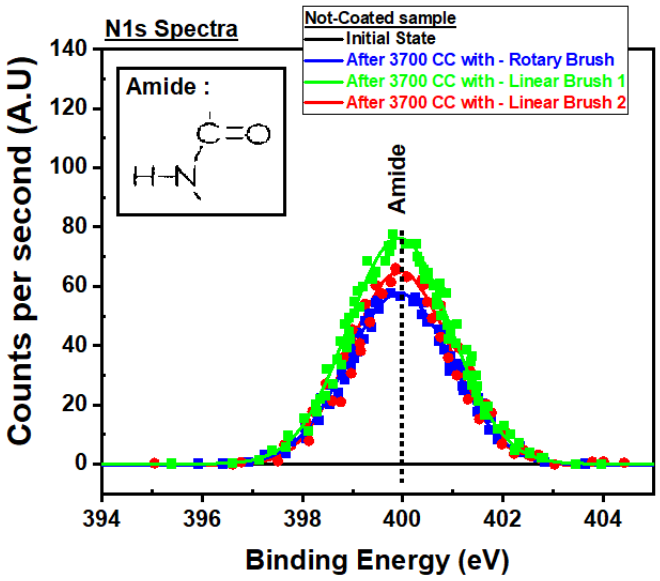
N1s Spectra
Not-Coated sample
Initial State
After 3700 CC with - Rotary Brush
After 3700 CC with - Linear Brush 1
After 3700 CC with - Linear Brush 2
Amide :
Amide
Counts per second (A.U)
Binding Energy (eV)

(a)

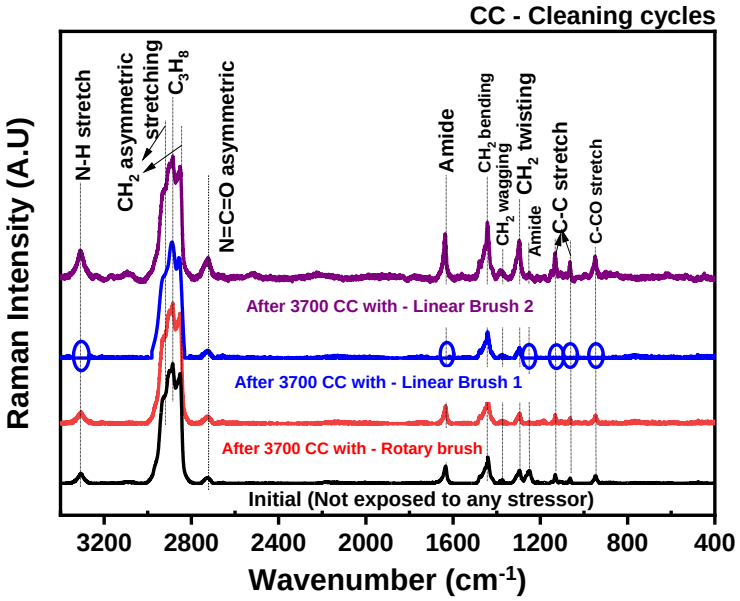
CC - Cleaning cycles
N-H stretch
CH2 asymmetric stretching
C3H8
N=C=O asymmetric
Amide
CH2 bending
CH2 wagging
CH2 twisting
Amide
C-C stretch
C-CO stretch
After 3700 CC with - Linear Brush 2
After 3700 CC with - Linear Brush 1
After 3700 CC with - Rotary brush
Initial (Not exposed to any stressor)
Raman Intensity (A.U)
Wavenumber (cm-1)

(b)

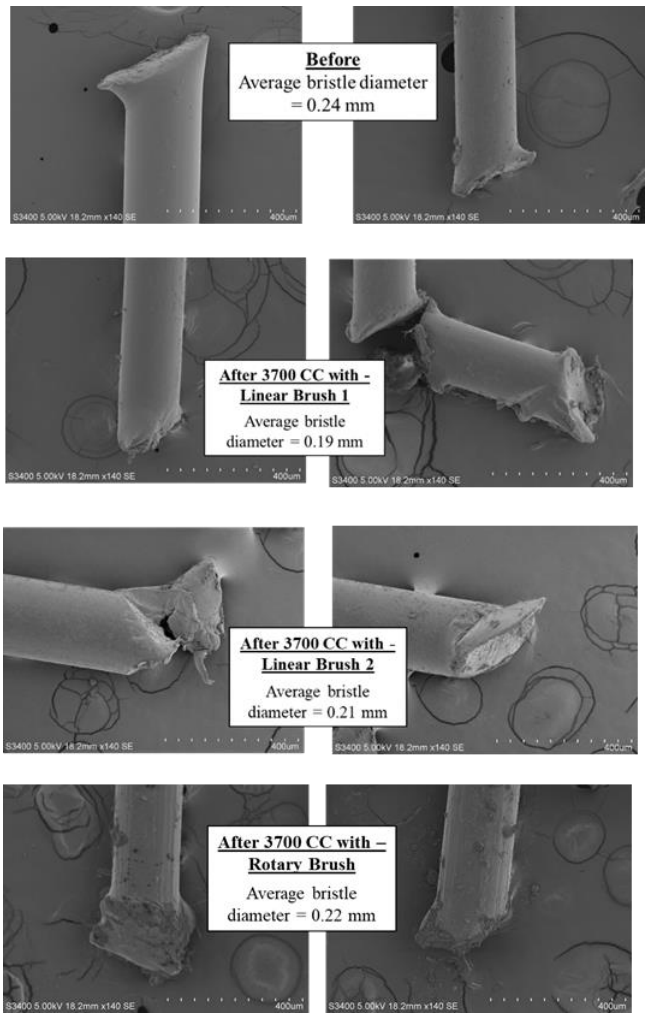

(c)

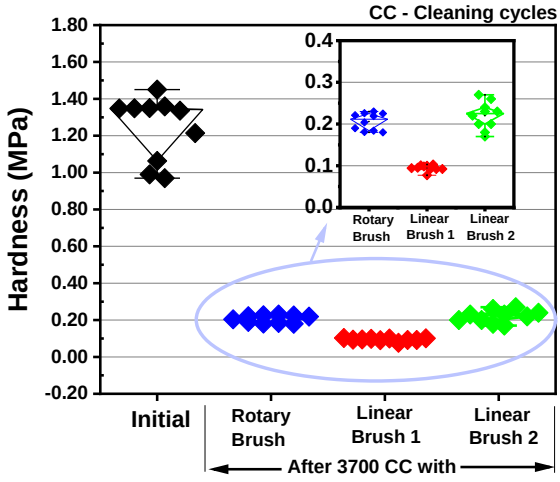

(d)

Fig. 70: (a) XPS spectroscopy of the not-coated sample after 3700 cycles with linear brush 1, linear brush 2 and rotary brush. Degradation of the brush bristles when cleaned with linear brush 1, linear brush 2, and rotary brush - (b) Raman spectroscopy of the brush bristles tips, (c) SEM of the brush bristles tips, (d) Hardness of the brush bristles tips.

7.2.1.3 The Direction of Rotation of the Brush

In this section, three scenarios were tested: (1) when the direction of rotation of the brush is towards the direction of travel, (2) when the direction of rotation of the brush is opposite to the direction of travel, and (3) when the direction of rotation of the brush is clockwise, leading to direction of rotation being same as the direction of travel in one half cycle and being opposite to the direction of travel in the other half cycle. All 3 scenarios show similar cleaning efficacy (Appendix I, Fig. A4). We used a Nylon 6,12 rotary brush in all the scenarios. In this section, one cleaning cycle refers to [(dust deposition of 0.2 mg/cm^2) + (Cleaning)]. The motor of the abrasion test-bed drives the forward and backward movement of the brush. The naming "towards the direction of travel" and "opposite to the direction of travel" was given to align with the movement of the brush in order to study the effect of brush rotation on the degradation of anti-soiling coatings. In scenario I, the brush, while rotating towards the direction of travel, the dust in front of the brush bristles get dragged along with the brush over the samples, causing severe scratches on the sample due to the combined effect of brush bristles and dust particles. In scenario II, the brush, rotating opposite to the direction of travel, tosses the dust in backward direction as it comes in contact with the dust deposited samples. A schematic diagram describing the 3 scenarios is shown in Fig. 71.

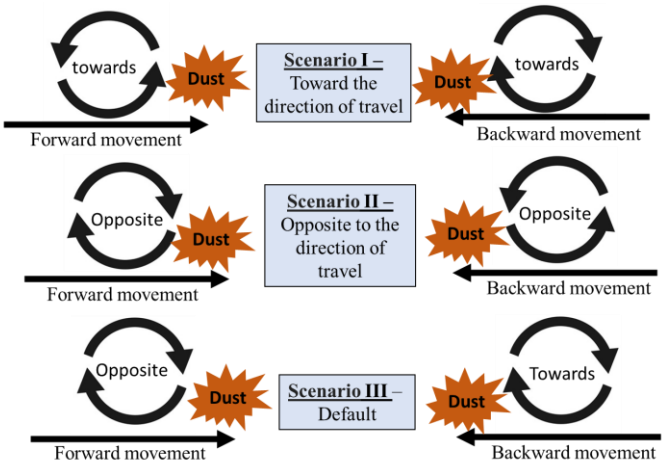

Fig. 71: Schematic diagram of 3 scenarios studied to understand the effect of direction of brush rotation on the degradation of anti-soiling coatings.

In Fig. 72, it can be seen that all coated samples that underwent rotary abrasion with the direction of rotation as "towards the direction of travel" show lower coating life compared to the other 2 scenarios. As the brush moves towards the direction of travel, the dust in front of the brush bristles gets dragged along with the brush over the samples. This causes severe scratches on the sample

due to the combined effect of brush bristles and dust particles. It was also observed that the solar glass samples show similar cleaning efficacy after one pass (forward movement) and after two passes (forward and backward movement) of the cleaning cycle. Due to this, the damage patterns for scenarios II and III are similar, Fig. 72, as most of the dust is removed during the forward movement, and the effect of abrasion damage is reduced during backward movement.

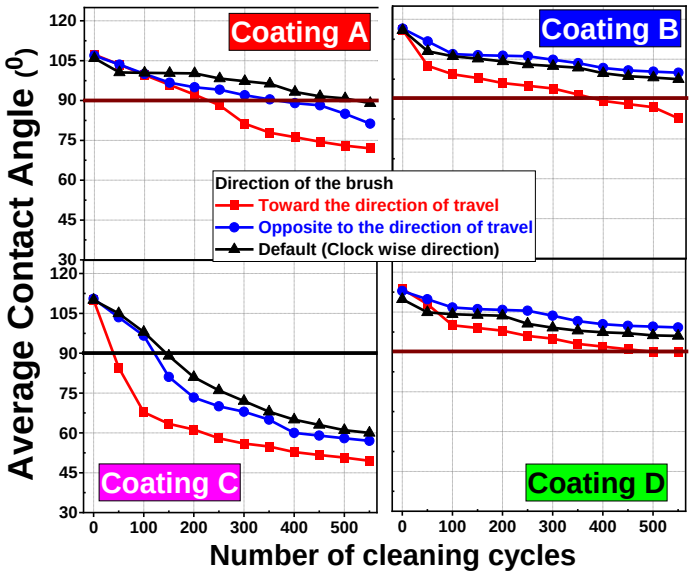

(a)

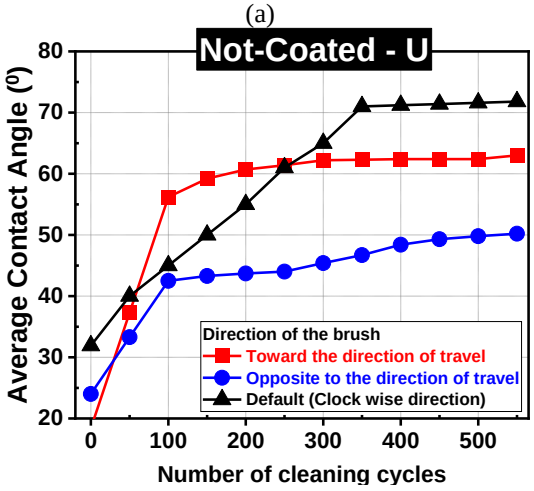

(b)

Fig. 72: Contact angle performance for (a) coated and (b) U - not-coated samples for all the 3 scenarios.

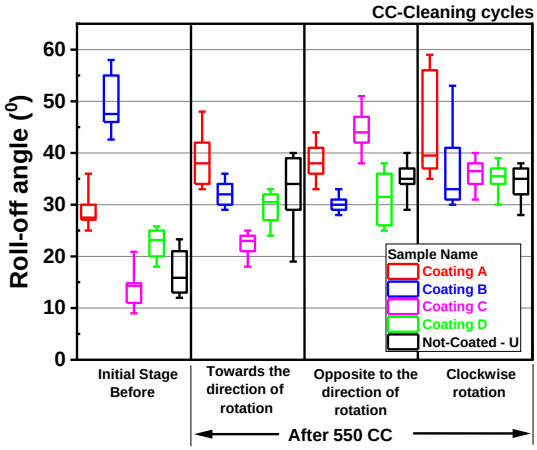

Fig. 73: Roll-off angle performance of the coated and not-coated (U) samples before and after 550 cycles of rotary abrasion for all the scenarios. Each box plot in this graph is based on 10 data points.

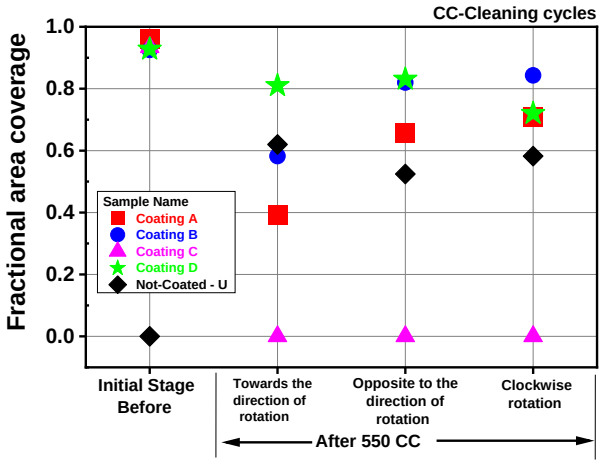

Fig. 74: Fractional area coverage of coated and not-coated (U) samples before and after 550 cycles of rotary abrasion for all the scenarios.

We observed a decline in the anti-soiling property (indicated by the change in RoA) of all coated samples after abrasion tests, irrespective of the direction of travel (Fig. 73). We observed a decline in the anti-soiling property of the not-coated samples (indicated by the increase in RoA) after 550 cycles for all the scenarios. In terms of surface coverage of the coating material, coating C displays the greatest damage, as the complete coating was removed after 550 cycles of rotary abrasion irrespective of the direction of brush travel (Fig. 74). The not-coated samples show deposition of amide (nylon) after 550 abrasion cycles for all 3 case scenarios (Appendix I, Fig. A5). A good correlation was seen between the characteristic properties (TM-AFM Phase angle (Fig. 74), contact angle (Fig. 72), RoA (Fig. 73) and roughness (Appendix I, Fig. A6)). We observed significant damage in the composition (shown via the absence of amide functional group (Appendix I, Fig. A7)), morphology (Appendix I, Fig. A8) and hardness (Fig. 75) of the brush

bristles after 550 cycles of rotary abrasion for all 3 scenarios. Greater reduction in hardness was seen for brush bristles which underwent 550 cycles of rotary abrasion with the direction of rotation as "towards the direction of travel".

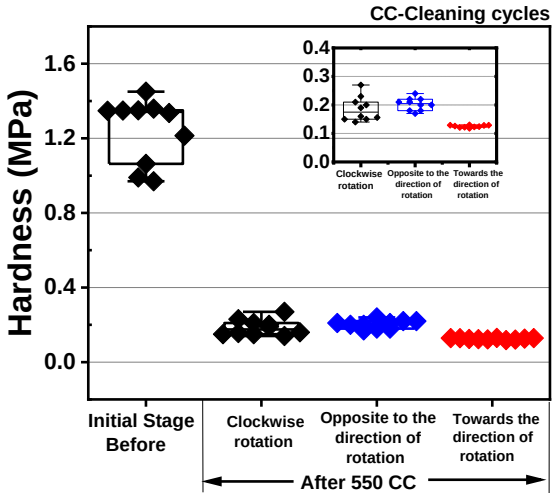

Fig. 75: Hardness of brush bristles tips before and after 550 cycles of rotary abrasion for all the 3 scenarios.

7.2.1.4 The Horizontal Velocity of Brush Travel

This section reports the effect of two different horizontal velocities (0.1 m/sec and 0.4 m/sec) of the brush travel on the solar glass samples. All brushes used in this section were of Nylon 6,12 brush material and rotary in design. In this section, one cleaning cycle refers to 1 pass of forward and backward movement. The brush's rpm (rotation per minute) was identical for both horizontal velocities. Solar glass samples show similar cleaning efficacy for both horizontal velocities of brush travel.

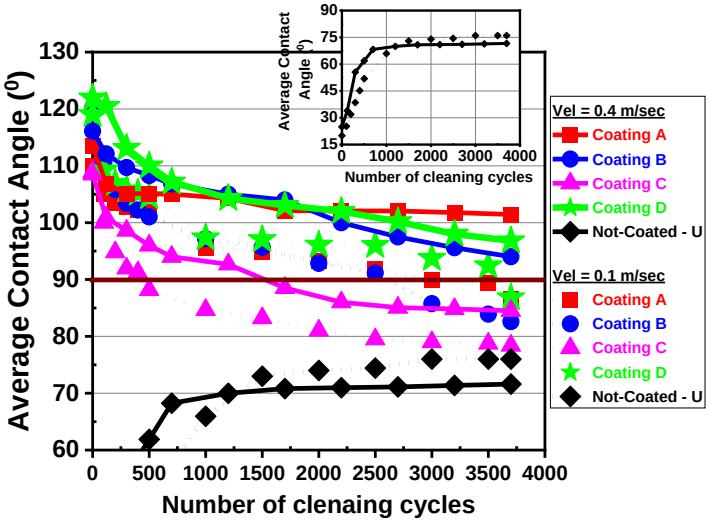

Fig. 76: Contact angle performance of the coated (A, B, C, and D) and not-coated (U) samples at two different horizontal velocities of brush travel (1) 0.4 m/sec and (2) 0.1 m/sec.

In Fig. 76, we observe that lower horizontal velocity results in lower coating life. This is because ten rows of brush bristle tufts come in contact with each sample during each pass per cleaning cycle when cleaned with a velocity of 0.1 m/sec. In contrast, at 0.4 m/sec, only four rows of bristle tuft come in contact with a solar glass sample during each pass per cleaning cycle. We may observe a decline in the anti-soiling property (indicated by the change in RoA (Fig. 77) of all coated samples after 3700 abrasion cycles when cleaned at a velocity of 0.1 m/sec. The anti-soiling property of coating B, C, and D declines (indicated by the change in RoA) after 3700 abrasion cycles when cleaned at a velocity of 0.4 m/sec.

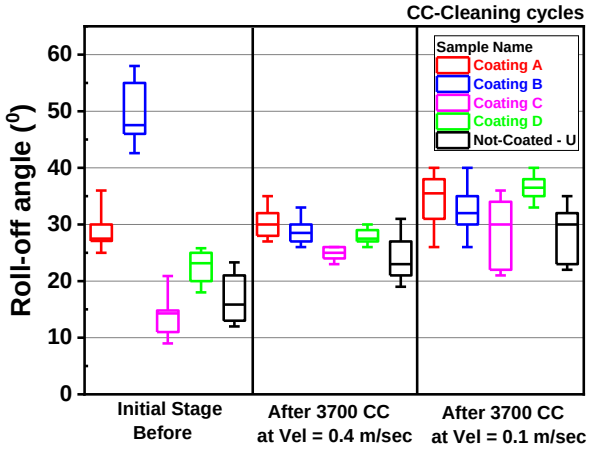

Fig. 77: Roll-off angle performance of the coated and not-coated (U) samples after 3700 cycles of rotary abrasion, cleaned at two different horizontal velocities of brush travel (1) 0.4 m/sec and (2) 0.1 m/sec.

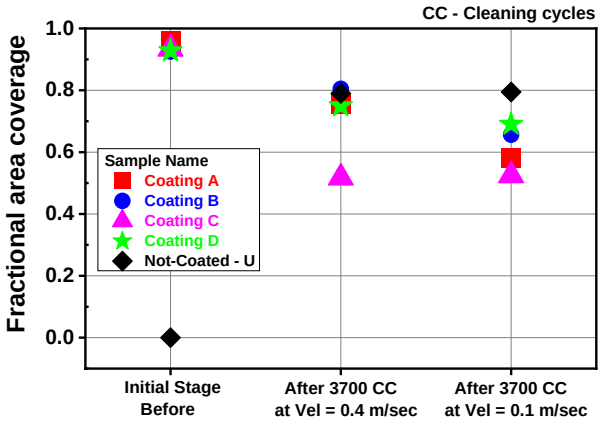

Fig. 78: Fractional area coverage of coated and not-coated (U) samples, before and after 3700 cycles of rotary abrasion, cleaned at two different horizontal velocities of brush travel (1) 0.4 m/sec and (2) 0.1 m/sec.

A good correlation was seen between the characteristic properties of the coated samples (Fractional area coverage (Fig. 78), contact angle (Fig. 76), RoA (Fig. 77), and roughness (Appendix I, Fig. A9)). In terms of the surface coverage of the coating material, coating C shows 50% removal of the coated layer after 3700 abrasion cycles when cleaned with a velocity of 0.4 at m/sec and 0.1

m/sec (Fig. 78). Deposits of amide were seen on the top surface of the not-coated samples (Appendix I, Fig. A10), which led to a significant change in the surface of the not coated samples (indicated by the increase in contact angle, roughness, and RoA) after 3700 cycles when cleaned at velocities of 0.4 m/sec and 0.1 m/sec. In Fig. 79, a statistically significant decrease in the brush bristle tip's hardness can be seen for both the horizontal velocities, with a greater reduction for velocity of 0.1 m/sec. The brush bristles show significant damage in composition (indicated by the absence of the amide functional group (Appendix I, Fig. A11) after 3700 abrasion cycles when cleaned at a velocity of 0.1 m/sec) and morphology (after 3700 abrasion cycles when cleaned at a velocity of 0.1 m/sec and 0.4 m/sec, Appendix I, Fig. A12).

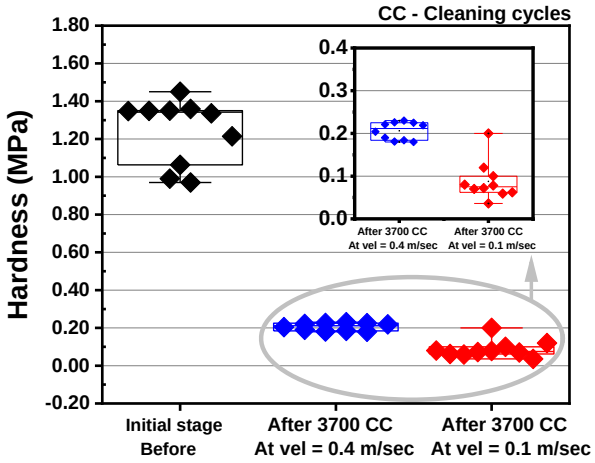

Fig. 79: Hardness of brush bristles tips before and after 3700 cycles of rotary abrasion cleaned at two different horizontal velocities of brush travel (1) 0.4 m/sec and (2) 0.1 m/sec.

7.2.1.5 Brush Materials

To understand the effect of different brush materials on the degradation of anti-soiling coatings, all samples were exposed to multiple runs of only-clean cycles, with Brush A, Nylon 6,12, Brush B (Polyester + Nylon mix), and Microfibre cloth brush. The bristles of Brush A, as per the manufacturer, were composed of different materials such as Nylon, Polyester, animal hair, etc. In this section, one cleaning cycle refers to 1 pass of forward and backward movement. All the brushes used in this section were rotary in design. The horizontal velocity of the brush travel on the solar glass sample for cleaning was fixed at 0.4 m/sec. The cleaning efficacy of all four brushes was identical (Appendix I, Fig. A13). All coated samples show lower coating life when cleaned with Brush A, followed by Nylon 6,12 and Microfiber cloth brush (Fig. 80). This is because, at the initial state, the brush bristles of Brush A exhibited higher hardness (1.3 X higher than Nylon 6,12) compared to other brush materials at their initial state (see, Fig. 81). Nylon 6,12 and Brush B

(Polyester + Nylon mix) do not follow this particular pattern. Brush B (Polyester + Nylon mix) shows low initial hardness than Nylon 6,12 brush; however, in some cases, Brush B causes more damage to the coated surface. This may be due to other parameters like brush stiffness which also affects the degree of abrasion damage. Brush A, Nylon 6,12 and microfiber brush show a clear pattern that, increase in hardness caused lower coating life when cleaned with a harder brush material. It was expected that brushes with higher hardness would cause lower coating life; however, the study aimed to quantify the degree of damage due to the hardness of brush bristles (shown in section 7.2.1.6).

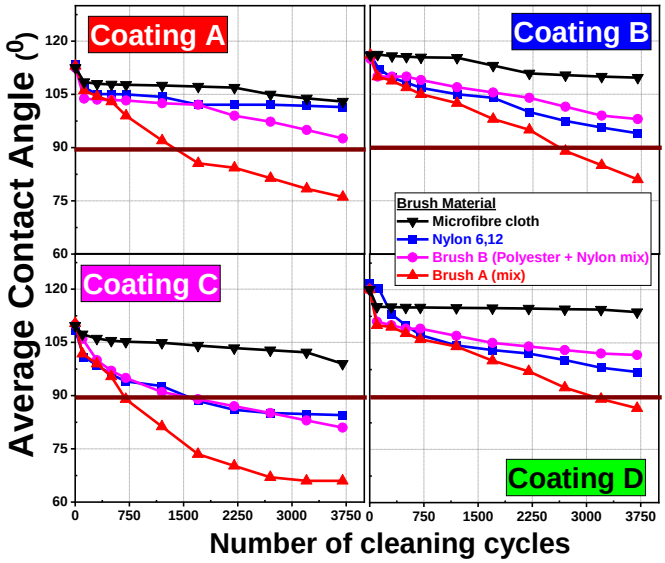

(a)

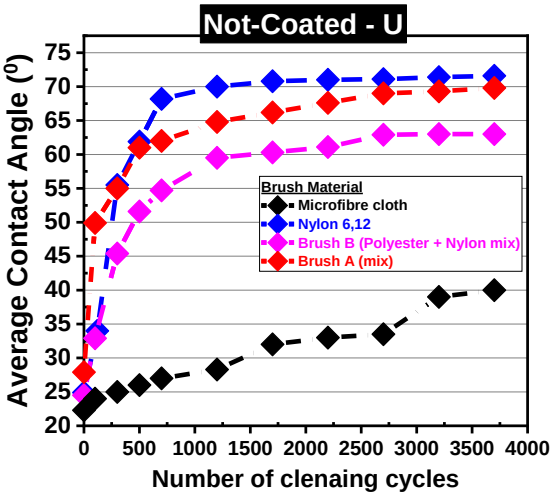

(b)

Fig. 80: Contact angle performance of (a) Coated samples and (b) U - Not-coated sample, after being cleaned via Microfibre cloth brush, Nylon 6,12 brush, Brush B (Polyester + Nylon mix), and Brush A.

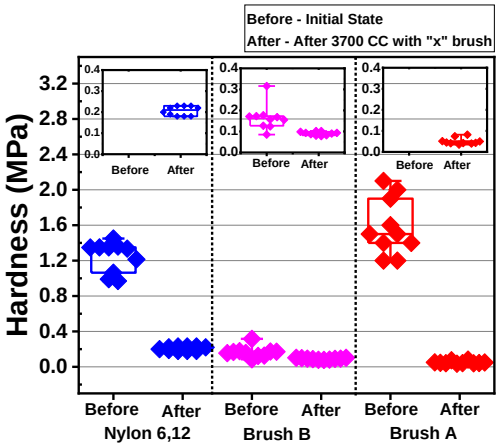

Fig. 81: Hardness of brush bristles tips before and after being exposed to 3700 cleaning cycles with Nylon 6,12 brush, Brush B (Polyester + Nylon mix) and Brush A. "CC" refers to cleaning cycles.

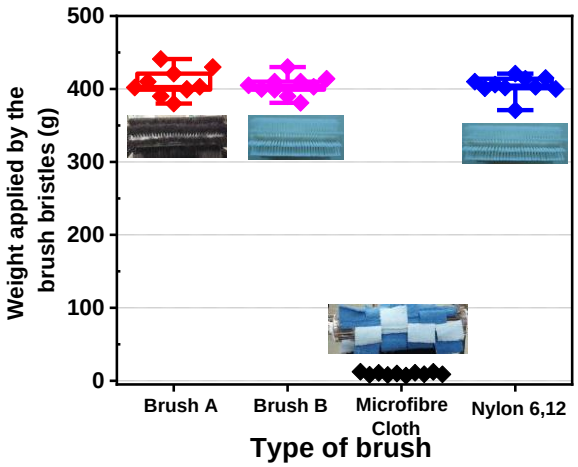

Fig. 82: Weight applied by the brush bristles of Brush A, Brush B (Polyester + Nylon mix), Microfibre cloth and Nylon 6,12 brush on the samples.

The hardness of Microfibre cloth bristles could not be measured due to the limitations (the fibre of the brush bristles (shown in Appendix I (Fig. A18)) were smaller than the instruments limits) of the instrument, but is anticipated to be lower than other brush materials. Microfibre cloth brush causes the least damage (see, Fig. 80) to the coated samples as it applies the smallest weight on the sample's surface (see, Fig. 82) compared to other brush materials. We observed a decline in the anti-soiling property (indicated by the change in RoA) of the coated samples after 3700 cycles with Brush A and Brush B (Fig. 83). Coated samples show no damage in the anti-soiling property when cleaned with a microfibre cloth. Coated samples that underwent cleaning with Brush A show greater damage than other brush materials (Fig. 80).

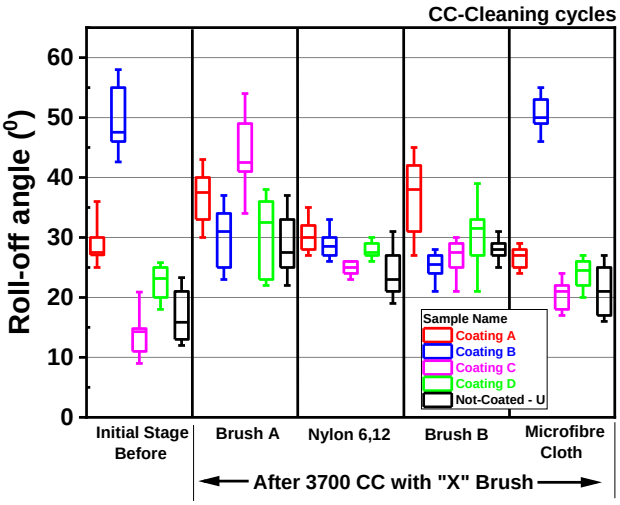

Fig. 83: Roll-off angle performance of the coated and not-coated (U) samples after exposure to 3700 cycles with all types of brush materials tested. Each box plot in this graph is based on 10 data points.

There was no significant change in the WAT before and after 3700 cycles with types of brush materials tested. Complete removal of the coated layer was seen in coating C after 3700 cycles with Brush A (Fig. 84). Deposition of amide (Appendix I, Fig. A14) resulted in the change of the top surface properties (contact angle (Fig. 80), RoA (Fig. 83) and roughness (Appendix I, Fig. A15)) of the not-coated sample after 3700 cycles with all types of brush materials tested. This indicated that the amide is part of all brush materials. The brush bristles do not show significant damage to its composition after 3700 cycles (Appendix I, Fig. A16) with Nylon 6,12 and Brush B (Polyester + Nylon mix). The morphology of the brush bristles tips shows significant damage after 3700 cycles with Brush A, Brush B, and Nylon 6,12 brushes (Appendix I, Fig. A17).

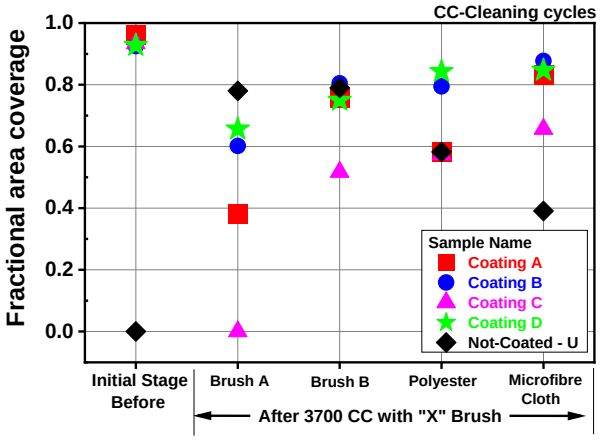

Fig. 84: Fractional area coverage of coated and not-coated (U) samples, before and after being exposed to 3700 cycles with all types of brush materials tested. The area scanned was 50 µm × 50 µm in all cases.

7.2.1.6 Quantitative Comparison of Lifetime of Anti-Soiling Coatings Under Various Abrasion tests:

To understand the impact of each factor that degrades anti-soiling coatings, we calculated the cycles to failure for each case. When the contact angle of the coated surface went below 90˚, it was defined as failure. For datasets where we experimentally saw the failure of the coated surface, the exact number of cycles required for failure were interpolated by using a polynomial fit with Adj R^2>0.9. For data sets where we experimentally did not see the failure of the coated surface, the best fit line through the last three points was used for estimating the cycles to failure through extrapolation. Table 11 shows the cycles to failure for each case, discussed in this section. The acceleration factors with respect to the cleaning with microfiber brush (shown in equation 10) were calculated by taking the ratios of the number of cycles at which the coatings fail (contact angle < 90˚). The reference of cleaning with a microfibre brush was chosen because the coated samples showed the highest lifetime when cleaned with this type of brush.

$$Acceleration\ factor\ =\ \frac{Cycles\ to\ failure-using\ microfibre\ brush}{Cycles\ to\ failure\ during\ stressor\ "x"} \quad (10)$$

In Table 11 and Fig. 85, we may observe that coating life decreased by 82 X (average of A, B, C and D) in the presence of dust (dew-dust-dry-clean), compared to only-clean cycles. Coating life decreased by 8 X (average of A, B, C and D) and 10 X (average of A, B, C and D) times in the presence of dew-dry-clean (DDC) cycles and dust-clean (DC) cycles, compared to only-clean cycles. In the presence of dew-dry-clean cycles, fluoropolymer coatings show 3X (average of A, B and D) lower coating life than phenyl silicone coatings (shown in Table 11).

Table 11: Cycles to failure for each case scenario.

	Cycles to failure			
	Coating A	**Coating B**	**Coating C**	**Coating D**
Abrasive agent				
only-clean	13537	5114	1578	5989
dust-clean	574	1324	170	1212
dew-dry-clean	850	1000	340	888
dew-dust-dry-clean	92	101	20	115
Brush material (“only-clean” cycle)				
Brush A	1912	2840	734	3,351
Brush B (Polyester + Nylon mix)	4469	5785	2091	11268
Nylon 6,12	13537	5114	1578	5989
Microfibre	14078	33143	10223	81291
Direction of rotation of brush (“dust-clean” cycle)				
Towards	227	460	44	553
Opposite	385	1464	117	1850
Clockwise	574	1324	170	1212
Horizontal velocity of brush (“only-clean” cycle)				
0.1m/sec	3452	3018	436	3790
0.4 m/sec	13537	5114	1578	5989

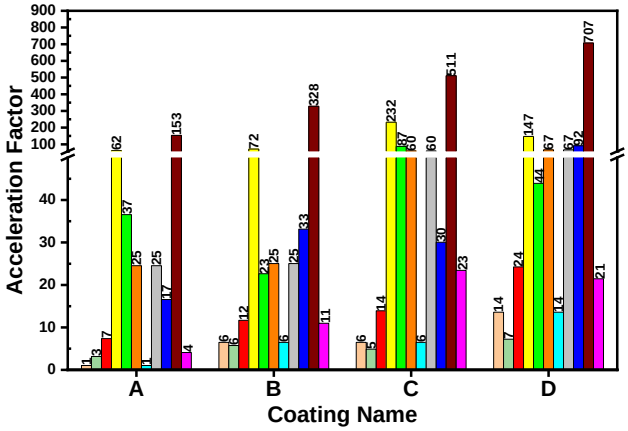

Fig. 85: Acceleration factors (with respect to microfibre brush) by which coating A, B, C and D degrade under various conditions.

Brush A, Nylon 6,12 and microfiber brush show a clear pattern that, increase in hardness caused lower coating life when cleaned with a harder brush material. In terms of the direction of rotation

of brush, coated samples show 3 X (average of A, B, C and D) lower coating life when cleaned with the direction of rotation as “towards the direction of travel”, compared to the other 2 cases. By decreasing the horizontal velocity of brush travel by 4 times, we observe 3 X (average of A, B, C and D) lower coating life when cleaned at 0.1 m/sec, compared to 0.4 m/sec. Phenylsilicone based coatings show 2 times higher failure rates than fluoropolymer-based coatings when cleaned at 0.1 m/sec (compared to 0.4 m/sec).

7.2.2 Effect of Rainfall

7.2.2.1 Acid Immersion Test

To emulate the composition of acidic rain in Mumbai, an acid immersion test was carried out. In this test, all samples were immersed in a pH 6 sulphuric acid solution at room temperature, for which the sulphur concentration was 60 ppm, which is a 20 X acceleration over the rainfall samples collected during field exposure test.

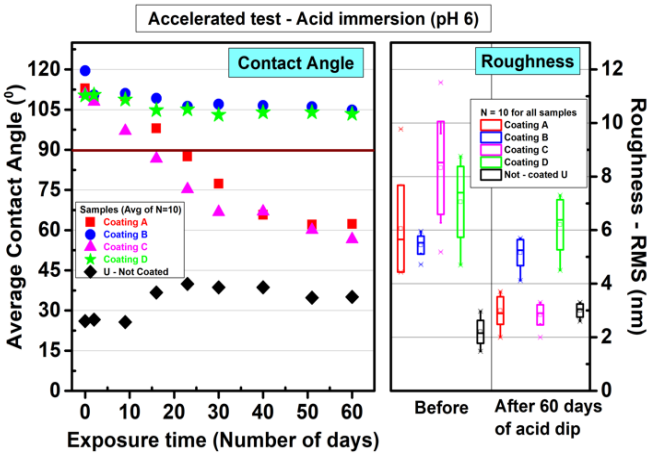

(a)

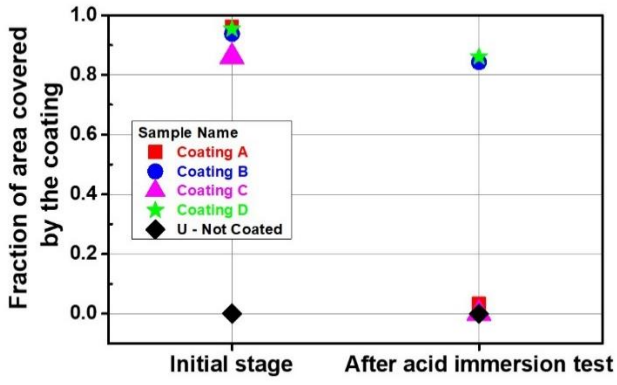

(b)

Fig. 86: (a) Average contact angle and roughness of coated (A, B, C, D) and not-coated (U) glass samples before and after 60 days of acid (pH 6) immersion test. (b) Fractional area coverage of coated (A, B, C, D) and not-coated (U) glass samples before and after 60 days of acid (pH 6) immersion test.

During the acid (pH 6) immersion test, we saw a statistically significant decrease in contact angle for all coated samples after 16 days of acid immersion, Fig. 86. Coatings A and C show linear (Adj R^2=0.9) rates of degradation, which was also seen in field study during the rainy season. Coating C also shows higher rate of initial degradation in the first 30 days of acid immersion, which reduces by a factor of 3 after 30 days of acid immersion. Similar trends for coating C were also seen in field exposure during the rainy season, with higher initial rate of degradation. Field degradation rates of coating C during the rainy season were higher than the acid immersion test, which may be attributed to the concurrent action of several stressors in the field. Coatings B and D show a nonlinear contact angle decrease with time by the acid immersion test. Coating A and C show a statistically significant decrease in roughness before and after 60 days of acid immersion, which correlates well with the decrease in contact angle. This was not seen in coatings B and D. Not-coated sample (U) do not show any change in TM-AFM phase angle (Fig. 86 (b)) after the acid immersion test, which indicates that the increase in contact angle (shown in Fig. 86) is due to the increase in roughness that is likely caused by etching of Na from the glass surface [67]. After being exposed to the acid immersion test, the fractional area coverage is approximately 0% for coatings A, and C. Fractional area coverage for coatings B and D are approximately 84% and 86% (respectively) after being exposed to the acid immersion test. These correlate well with the trends in contact angles measured before and after the acid immersion test.

7.2.2.2 Impact of Raindrops with pH 6 and pH 7 Water

All coated (A, B, C and D) and not-coated samples (U) were exposed to the impact of raindrops with pH 6 and pH 7 water samples. In Fig. 87 (a), we may observe that all coated samples (A, B, C and D), after being exposed to the impact of raindrops with pH 6 water show lower coating life varying from 1 X to 2 X compared to those being exposed to the impact of raindrops with pH 7 water samples. In terms of roll-off angle (Fig. 87 (b)), we observe that all coated samples show a statistically significant change after 1250 mm of precipitation with both pH 6 and pH 7 water samples. After being exposed to 1250 mm of precipitation with pH 6 and pH 7 water, all coated samples show high RoA for Mumbai's location (tilt angle = 19°), which indicates that the coatings won't exhibit any self-cleaning property when exposed in Mumbai. The not-coated samples show a statistically insignificant difference in RoA after 1250 mm of precipitation with both pH 6 and pH 7 water samples. All coated samples show a reduction in the fractional area coverage after

1250 mm of precipitation with both pH 6 and pH 7 water samples (Fig. 87 (c)). Coating C shows complete removal of the coated layer after 1250 mm of precipitation with pH 6 water sample. When exposed to the impact of raindrops with a pH 7 water sample, coating C shows 70% removal of the coated layer after 1250 mm of precipitation. This indicates that greater damage occurred when samples were exposed to acidic rainfall (impact of raindrop + acidic water) than those exposed to the impact of raindrops with pH 7 water samples.

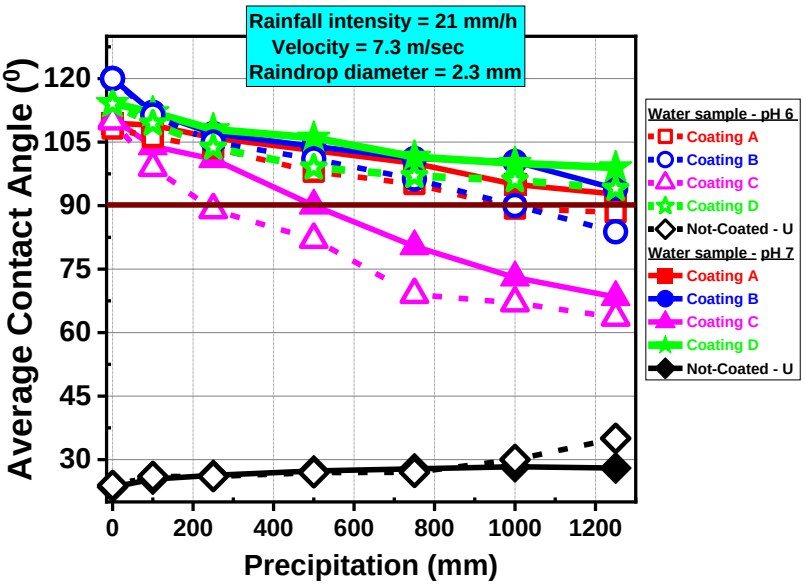

(a)

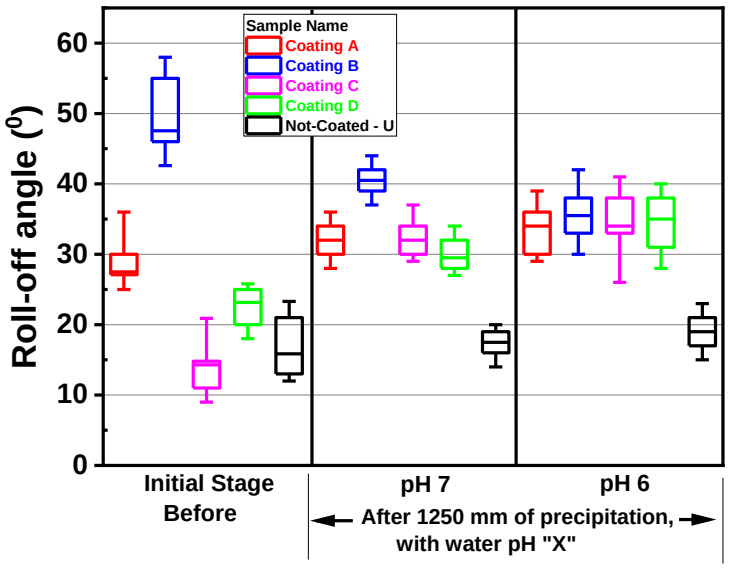

(b)

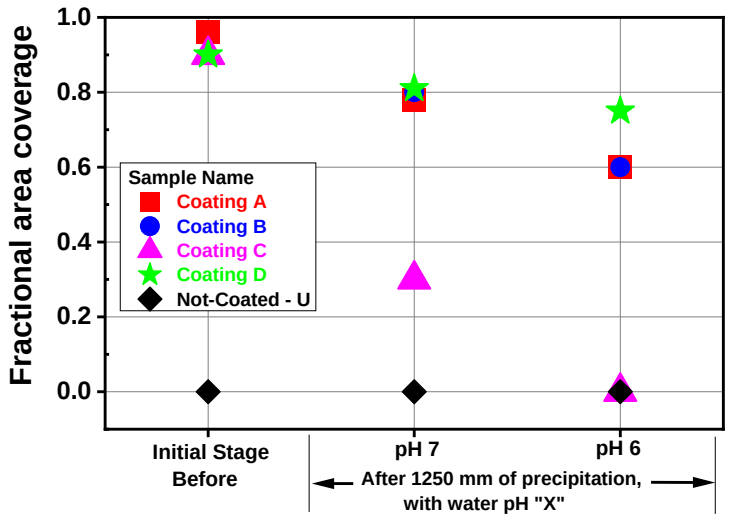

(c)

Fig. 87: Performance of coatings A, B, C, D and not-coated samples U, after being exposed to the impact of raindrops with pH 6 and pH 7 water sample: (a) Contact angle, (b) Roll-off angle and (c) Fractional area coverage.

7.2.3 Effect of UV Radiation

Single wavelength LED source of 365nm UV light was used for this test. As the intensity of light varied with positions, each sample received different dosage of UV exposure. Here the total UV exposure received by the samples was twice the total exposure received in the QUV Accelerated weather tester (used for understanding the impact of combination of UV exposure and condensation). The intensity of UV light falling on each sample is given in Table 12.

Table 12: Intensity of UV light received by coated samples.

Sample	Intensity (W/m^2)
Coating - A	434
Coating - B	820
Coating - C	1004
Coating - D	386

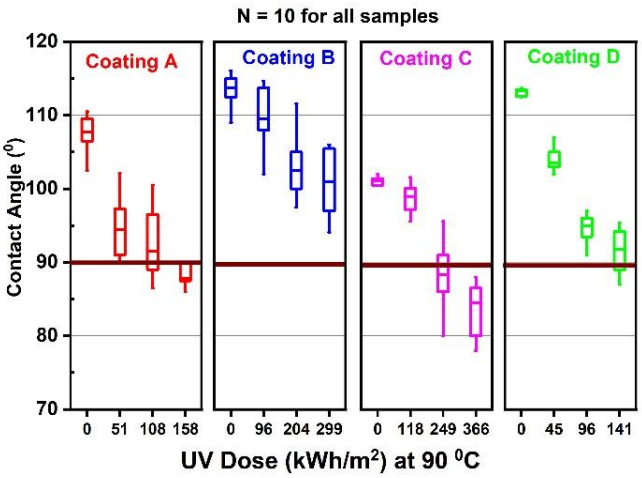

Fig. 88: Contact angle of coated samples with increase in UV dose (single wavelength – 365 nm) at 90 ºC.

In Fig. 88, we observe that UV alone (single wavelength – 365 nm) causes a statistically significant decrease in contact angle. The rate of decrease in contact angle, however, is low. Coating C becomes completely hydrophilic at very high UV dose of 366 kWh/m^2. The transition from hydrophobic to hydrophilic happened at a much lower dose when combination of UV (at 32 kWh/m^2) and condensation (441 h) was present (Fig. 89). Effect of combination of UV and condensation was studied in the QUV-accelerated weather tester, model QUV/basic [75]. In Fig. 89 (a), we observe that coating C shows an approximately 0° phase angle (TM-AFM phase angle) after being exposed to a combination of 61 kWh/m^2 of UV exposure and 846 h of condensation.

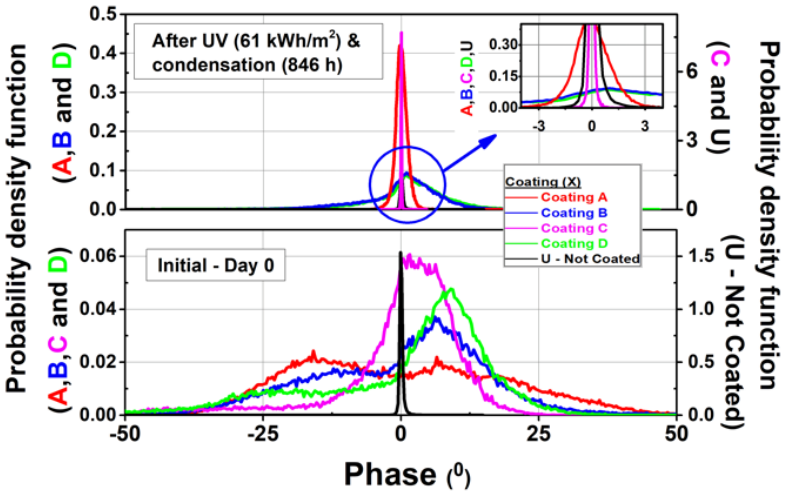

(a)

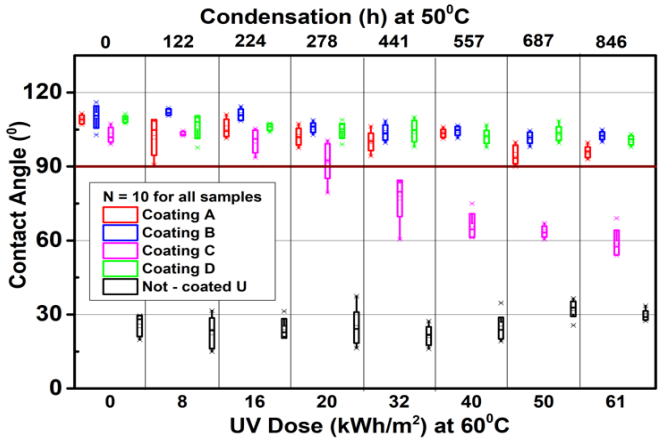

(b)

Fig. 89: (a) Probability density function of TM-AFM phase angle for coated (A, B, C and D) and not-coated sample (U), before and after exposure to UV dose (at 60°C) and condensation hours (at 50°C). (b) Average contact angle and roughness of coated (A, B, C, D) and not-coated (U) glass samples with an increase in UV dose (at 60°C) and condensation hours (at 50°C).

From Fig. 89 (a), we may infer that the surface coverage of the coating material has decreased significantly (from its initial stage) for coating C after being exposed to a combination of 61 kWh/m^2 of UV exposure and 846 h of condensation. After being exposed to 61 kWh/m^2 of UV exposure and 846 h of condensation, the fractional area coverage for coating C is approximately 0 %. The fractional area coverage for coatings A, B and D are approximately 16 %, 77 % and 80 % (respectively) after being exposed to 61 kWh/m^2 of UV exposure and 846 h of condensation. We observe a good correlation between the spread of the TM-AFM phase angle and contact angle measurement before and after the combination of UV exposure and condensation test.

7.2.4 Combination of UV Exposure and Acidic Rainfall

Here, one cycle of the combination of UV exposure and acidic rain refers to 189 mm of precipitation which was followed by 5 kWh/m^2 of UV exposure. In Fig. 90 (a) and Table 13, we may observe that all coated samples show lower coating life when exposed to a combination of 3 stressors (Impact of raindrops + acidic water + UV radiation) compared to samples being exposed to a combination of 2 stressors (Impact of raindrops + acidic water). In terms of RoA (Fig. 90 (b), all coated samples show a statistically significant change when exposed to a combination of 2 and 3 stressors. After being exposed to combination of 3 and 2 stressors, all coated samples show high RoA for Mumbai's location (tilt angle = 19˚), which indicates that the coatings won't exhibit any self-cleaning properties when exposed in Mumbai. When exposed to a combination of 3 stressors, the not-coated samples show a statistically significant increase in RoA, which correlates well with

the increase in contact angle. However, when exposed to a combination of 2 stressors, the not-coated samples show a statistically insignificant change in RoA. Coating C shows complete removal of the coated layer when exposed to a combination of 2 as well as a combination of 3 stressors (Fig. 90 (c)). All coated samples show a decline in the fractional area coverage of the coated layer when exposed to a combination of 2 as well as a combination of 3 stressors.

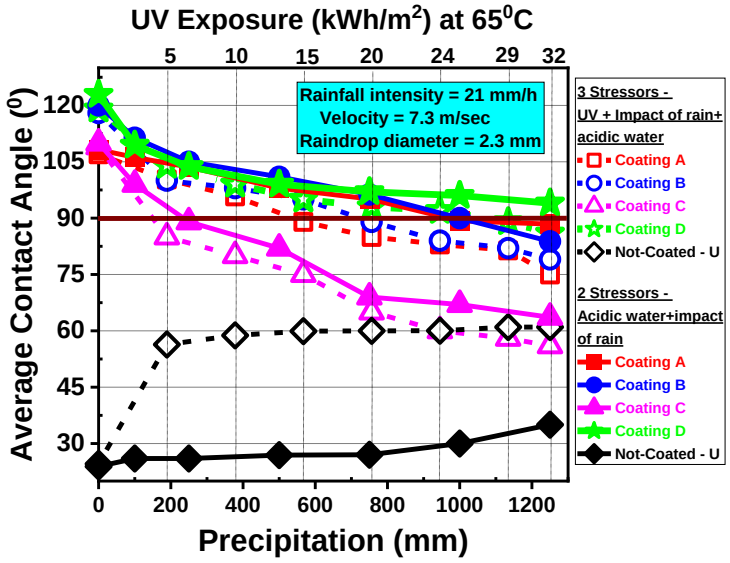

(a)

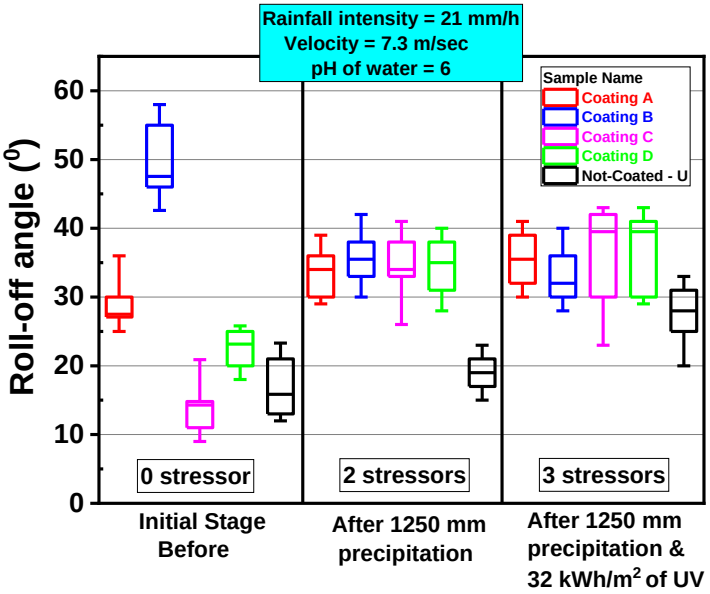

(b)

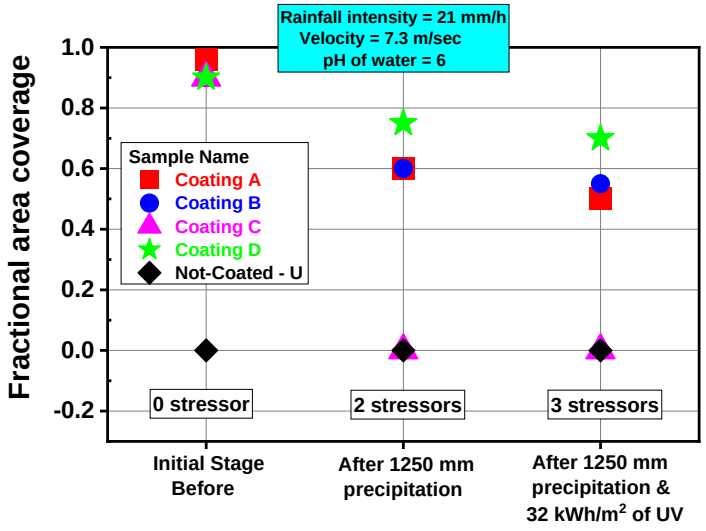

(c)

Fig. 90: Performance of coatings A, B, C, D and not-coated samples U, after being exposed to combination of 3 stressors (Impact of raindrops + acidic water + UV radiation) and 2 stressors (Impact of raindrops + acidic water): (a) Contact angle, (b) Roll-off angle and (c) Fractional area coverage.

7.2.5 Combination of Abrasion, UV radiation and Rainfall

In this section, 1 cycle of the combination of abrasion, UV radiation and acidic rain refers to 189 mm of precipitation which was followed by 1 cycle of the dew-dust-dry-clean abrasion cycle and 5 kWh/m^2 of UV exposure. In Fig. 91 (a), we observe that all coated samples that underwent a combination of 4 stressors (Impact of raindrops + acidic water + UV radiation + abrasion) show lower coating life than the samples that underwent a combination of 3 stressors (Impact of raindrops + acidic water + UV radiation). Table 13 shows the stressor accumulated before the coating failed under different combinations of stressors. The coatings were deemed to have failed when the contact angle of the coated samples went below 90˚. All coated and not-coated samples show a statistically significant change in RoA when exposed to a combination of 4 stressors (Fig. 91 (b). In terms of fractional area coverage, coating C shows complete removal of the coated layer after being exposed to a combination of 4 stressors (Fig. 91, c). All coated samples show a decline in the fractional area coverage after being exposed to a combination of 4 stressors.

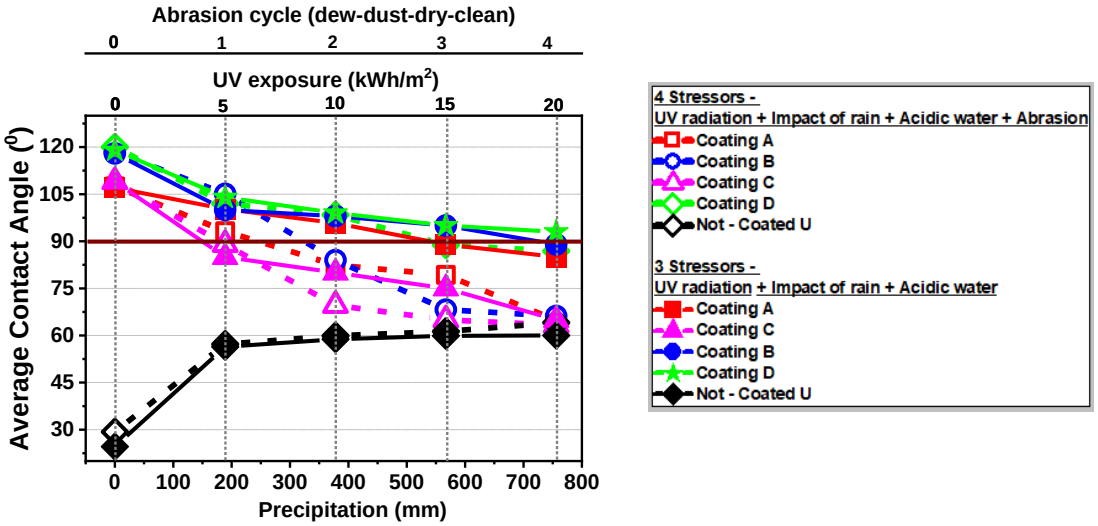

(a)

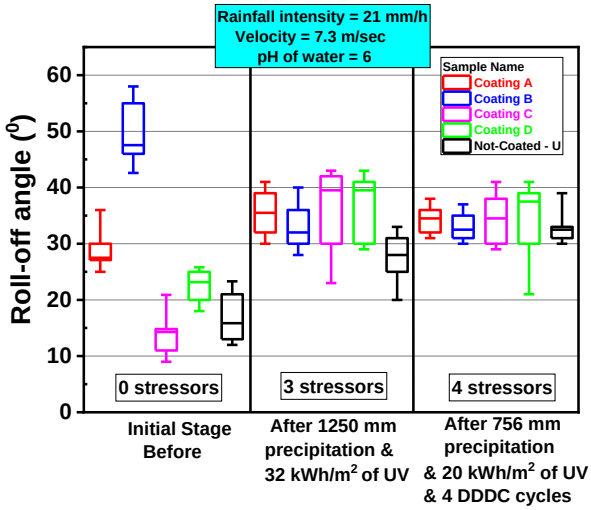

(b)

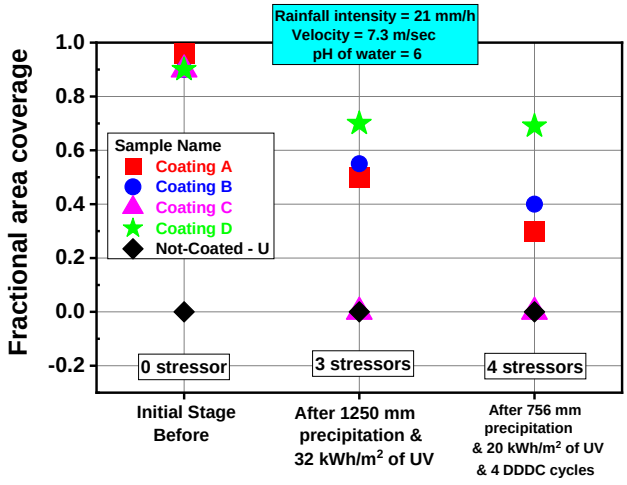

(c)

Fig. 91: Performance of coatings A, B, C, D and not-coated samples U, after being exposed to combination of 4 stressors (Impact of raindrops + acidic water + UV radiation + abrasion) and 3 stressors (Impact of raindrops + acidic water + UV radiation): (a) Contact angle, (b) Roll-off angle and (c) Fractional area coverage.

Table 13: Amount of stressor required for the coated samples (A, B, C and D) to become hydrophilic. *The coating remained hydrophobic till 1250 mm, and we ended the experiment after exposing the samples to 1250 mm of precipitation. The details of the experiment are given in section 7.2.2.2.

Name of sample	Impact of raindrop (pH 7)	Impact of raindrop + acidic water (pH 6)	Impact of raindrop + acidic water (pH 6) + UV	Impact of raindrop + Acidic water (pH 6) + UV + abrasion
Coating A	2000 mm	1000 mm	567 mm + 15 kWh/m^2	378 mm + 10 kWh/m^2 + 2 DDDC cycles
Coating B	2500 mm	1250 mm	756 mm + 19 kWh/m^2	378 mm + 10 kWh/m^2 + 2 DDDC cycles
Coating C	500 mm	250 mm	189 mm + 5 kWh/m^2	189 mm + 5 kWh/m^2 + 1 DDDC cycles
Coating D	3250 mm	*1250 mm +	1134 mm + 29 kWh/m^2	567 mm + 15 kWh/m^2 + 3 DDDC cycles

7.2.6 Quantitative Comparisons

In this section, we quantified the impact of various stressors that degrade anti-soiling coatings during field exposure tests. Time to failure was calculated for indoor accelerated stress tests. Time to failure was noted when the contact angle of the coated samples went below 90˚. For datasets where we experimentally saw the failure of the coated sample, the exact time to failure data was determined by interpolation, using a polynomial fit with Adj R^2>0.9. For data sets where we experimentally did not see the failure of the coated sample, the best fit line through the last three points was used for estimating the time to failure through extrapolation. The time to failure for indoor accelerated stress tests is shown in Table 14. Equation 11 show the acceleration factors for indoor accelerated stress tests. The experimental details of the water immersion test with pH 4 and pH 7 water samples are shown in Appendix I, Fig. A19 and Fig. 20, and the water immersion test at pH 6 in section 7.2.2.1.

$$Acceleration\ factor\ (Indoor)\ =\ \frac{Time\ to\ failure-water\ immersion\ test,with\ pH\ 7}{Time\ to\ failure-with\ "X"\ stresoor} \qquad (11)$$

In Fig. 92, we may observe that, in the indoor accelerated stress tests, the impact of raindrops with pH 7 water showed 33 X higher acceleration factor than the sample being exposed to water immersion/water contact tests with pH 7 water samples. Similar patterns were seen with acidic water; 32 X higher acceleration factor were observed when exposed to the impact of raindrops with pH 6 water, compared to the samples being exposed to only water immersion/water contact tests

with pH 6 water. This indicated that during a rain event, the impact of raindrops causes greater damage than caused by mere contact with water. When the samples are exposed to the impact of raindrops with pH 7 water, phenylsilicone based coatings (coating C) show 5 X lower coating life than fluoropolymer based coating (average of coating A, B and D). Coating life decreased by 2 X (average of coating A, B, C and D) when exposed to acidic rain (Impact of rain with pH 6 water) compared to the impact of raindrop tests with pH 7 water samples. When exposed to water immersion tests with pH 4 water samples, acceleration factor of coated samples increased by 1587 X (average of coating A, B, C and D) compared to samples exposed to water immersion/water contact tests with pH 7 water samples.

Table 14: Time to failure in hours for indoor accelerated stress test.

	Coating A	**Coating B**	**Coating C**	**Coating D**
Indoor accelerated stress test - Failure time at which the samples become hydrophilic (h)				
Water immersion test, pH 7	987	5674	633	7263
Impact of raindrops, pH 7	95	119	24	155
Water immersion test, pH 6	552	3491	384	4208
Impact of raindrops, pH 6	48	60	24	100
Water immersion test, pH 4	1	2	1	5

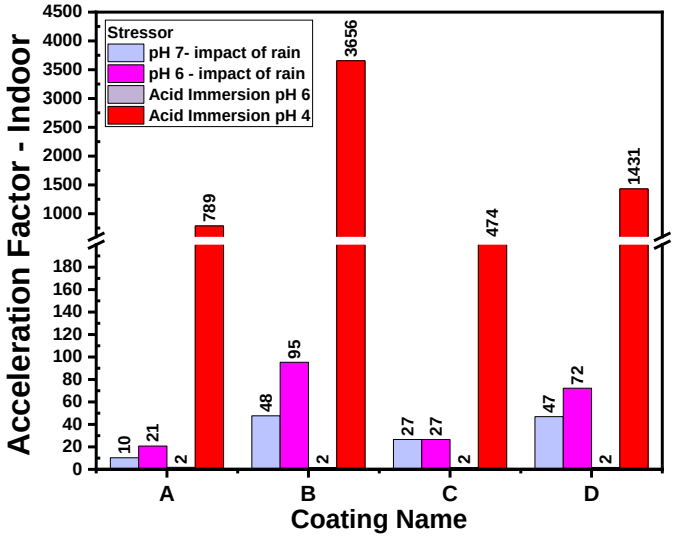

Fig. 92: Acceleration factor for indoor accelerated stress tests.

7.2.7 IEC 61215 Standard Tests

All coated samples were exposed to damp heat, thermal cycling and humidity freeze test based on the IEC 61215 standard [78]. In the damp heat test, samples were exposed to 85℃ and 85% relative humidity for 1000 h. In the thermal cycling test, samples are exposed to -30℃ for 30 minutes, followed by exposure to 85℃ for 30 minutes. This cycle is repeated 200 times. Under the Humidity freeze test, samples were exposed to 85% relative humidity for 20 h for 10 cycles. All tests were done in a small environmental chamber (Make - Heat & control systems, Model - HCS/EC/90L/10/60).

7.2.7.1 Damp Heat Test

In Fig. 93, we may observe that coating C becomes hydrophilic after 211 hours of damp heat test. All other coated samples (A, B and D) remain hydrophobic until 1000 hours. Coated samples B, C and D, show a statistically significant change in roll-off angle before and after 1000 h of the damp heat test (shown in Fig. 94). Coating C also shows a statistically significant decrease in roughness after 1000 h of damp heat test. In terms of fractional area coverage, we may observe that coating C shows complete removal of the coated layer after 1000 h of damp heat test (Fig. 95). The TM-AFM phase angle data correlates well with contact angle, RoA and roughness measurements.

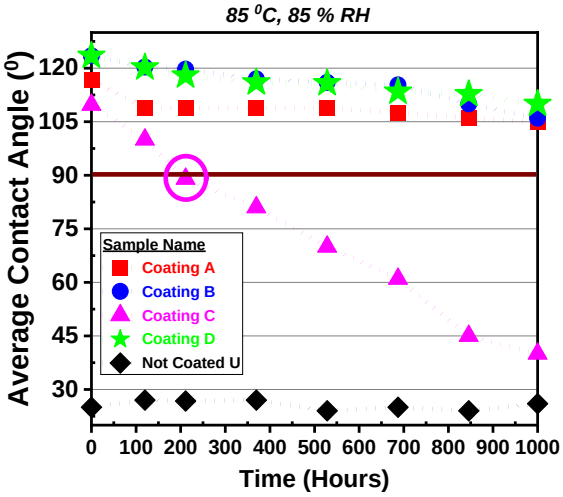

Fig. 93: Average contact angle of the coated (A, B, C, and D) and not-coated (U) samples after being exposed to the damp heat test. The contact angle was measured at 10 locations, and the averages are shown in the graph.

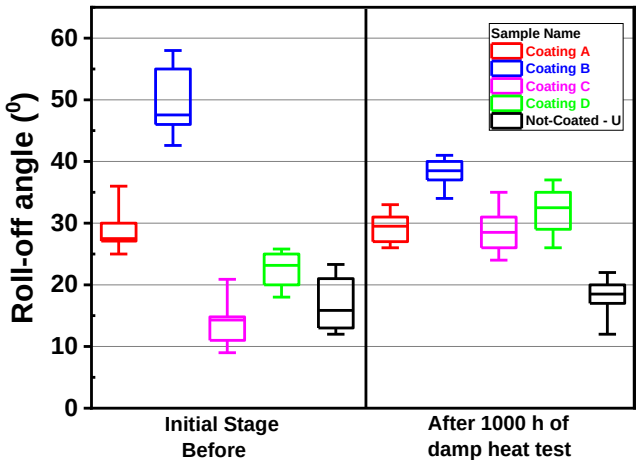

Fig. 94: Roll-off angle of the coated (A, B, C and D) and not-coated (U) samples before and after 1000 h of damp heat test. Each box plot in this graph is based on 10 data points.

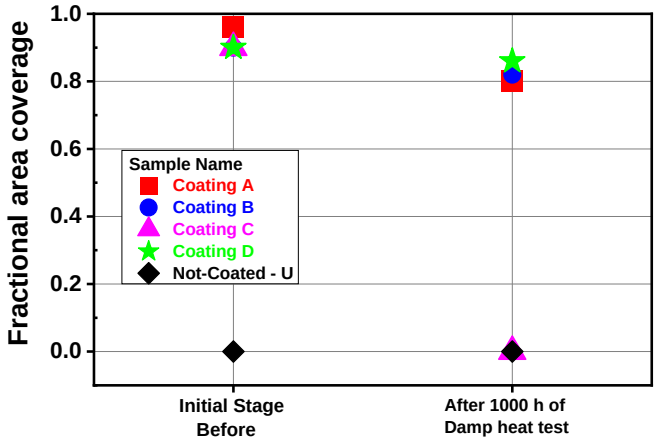

Fig. 95: Fractional area coverage of coated (A, B, C, and D) and not-coated (U) samples, before and after 1000 h of damp heat test. The area scanned was 50 µm × 50 µm in all cases.

7.2.7.2 Thermal Cycling Test

The cycle that was followed for the thermal cycling test is shown in Fig. 96. Due to some constraints in the instrument specification, few parameters were modified. In the IEC 61215 thermal cycling test, samples are exposed to -40℃ for 30 minutes. However, in our study, the samples were exposed to -30℃ for 30 minutes. This was still a representative figure as in most sunbelt countries where soiling is a major concern, temperatures may never go to such low values. We did not apply current equal to the STC peak power current of the modules under test, as the complete study was done on solar glass samples (size 5 cm × 2.5 cm).

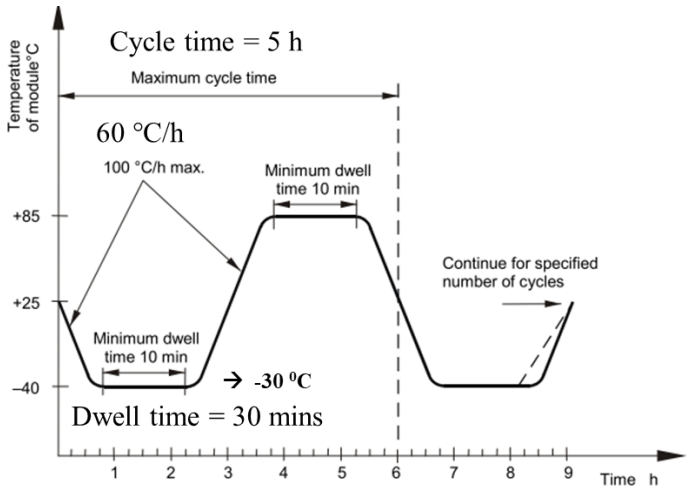

Fig. 96: Schematic diagram of the thermal cycling test [78].

In Fig. 97, we may observe that coating C becomes hydrophilic after 200 cycles of thermal cycling test. All other coated samples (A, B and D) remain hydrophobic until 200 cycles of thermal cycling test.

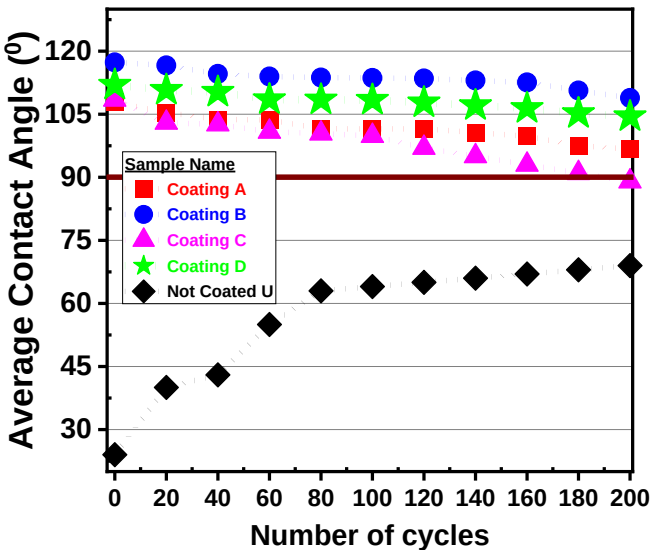

Fig. 97: Average contact angle of the coated (A, B, C, and D) and not-coated (U) samples after being exposed to the thermal cycling test. The contact angle was measured at 10 locations, and the averages are shown in the graph.

Coated sample C and the not-coated samples show a statistically significant change in RoA before and after 200 cycles of thermal cycling test (shown in Fig. 98). Coating C also shows a statistically significant decrease in roughness after 200 cycles of the thermal cycling test. All other coated samples (A, C and D) show a statistically insignificant change in roll-off angle (RoA) and roughness after 200 cycles of thermal cycling test. The not-coated sample shows a statistically significant increase in roughness after 200 cycles of the thermal cycling test, which increases the

contact angle and RoA. In terms of fractional area coverage, we may observe in Fig. 99 coating C shows 30% coating removal after 200 cycles of thermal cycling test.

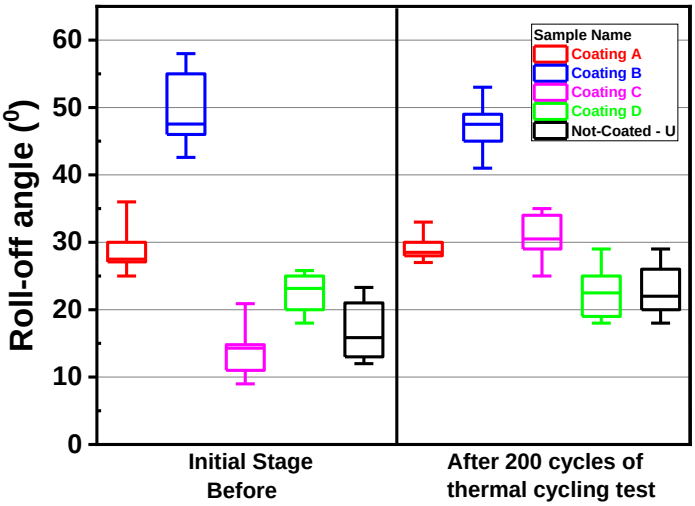

Fig. 98: Roll-off angle of the coated (A, B, C and D) and not-coated (U) samples before and after 200 cycles of thermal cycling test. Each box plot in this graph is based on 10 data points.

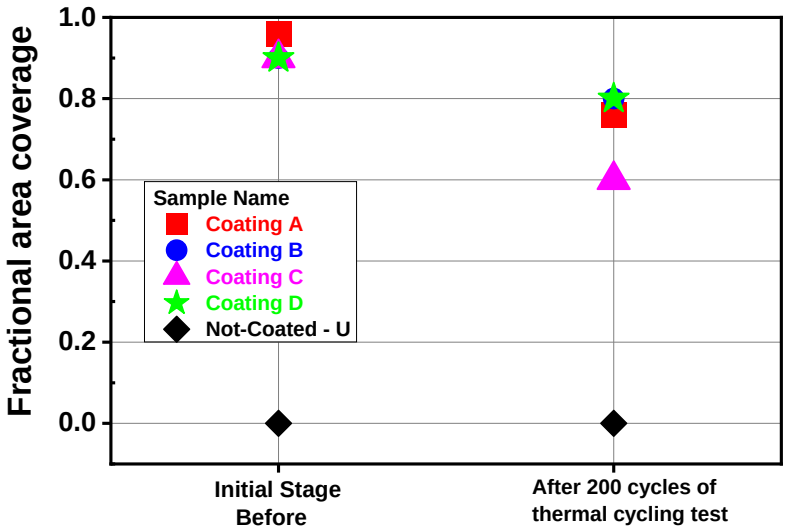

Fig. 99: Fractional area coverage of coated (A, B, C, and D) and not-coated (U) samples, before and after 200 cycles of thermal cycling test. The area scanned was 50 µm × 50 µm in all cases.

7.2.7.3 Humidity Freeze Test

The cycle followed for the humidity freeze test is shown in Fig. 100. Due to some constraints in the instrument specification, specific parameters were modified. In the IEC 61215 Humidify freeze test, samples are exposed to -40℃ for 4 h. However, in our study, the samples were exposed to -

30℃ for 4 h. This was still a representative figure as in most sunbelt countries where soiling is a major concern, temperatures may never go to such low values.

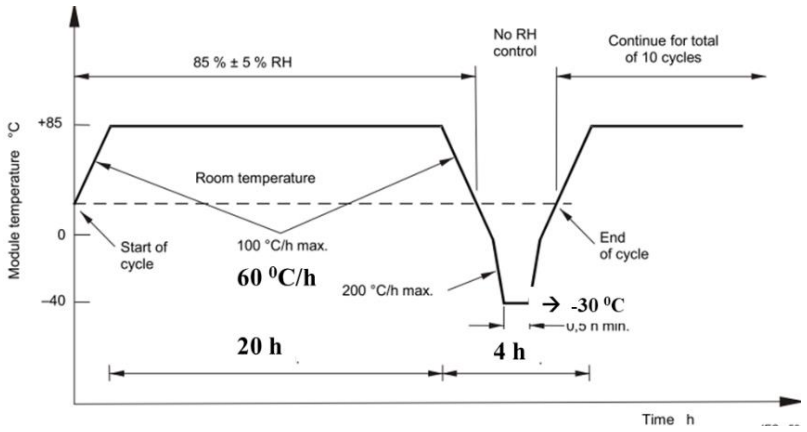

Fig. 100: Schematic diagram of the humidity freeze test [78].

In Fig. 101, we may observe that coating C becomes hydrophilic after 4 cycles of humidity freeze test. All other coated samples (A, B and D) remain hydrophobic until 10 cycles of humidity freeze test. Coated sample C show a statistically significant change in RoA before and after 10 cycles of humidity freeze test (shown in Fig. 102). Coating C also shows a statistically significant decrease in roughness after 10 cycles of humidity freeze test. All other coated samples (A, C and D) show a statistically insignificant change in RoA and roughness after 10 cycles of humidity freeze test. In terms of fractional area coverage, Coating C shows 90% coating removal of the coated layer after 10 cycles of humidity freeze test (Fig. 103).

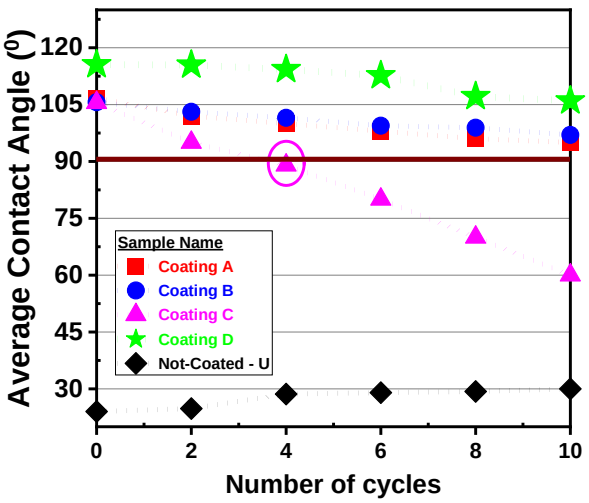

Fig. 101: Average contact angle of the coated (A, B, C, and D) and not-coated (U) samples after being exposed to humidity freeze test. The contact angle was measured at 10 locations, and the averages are shown in the graph.

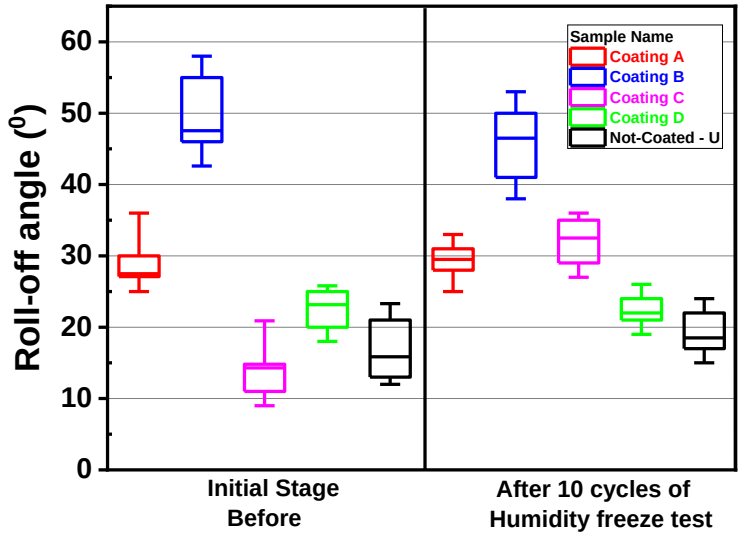

Fig. 102: Roll-off angle of the coated (A, B, C and D) and not-coated (U) samples before and after 10 cycles of humidity freeze test. Each box plot in this graph is based on 10 data points.

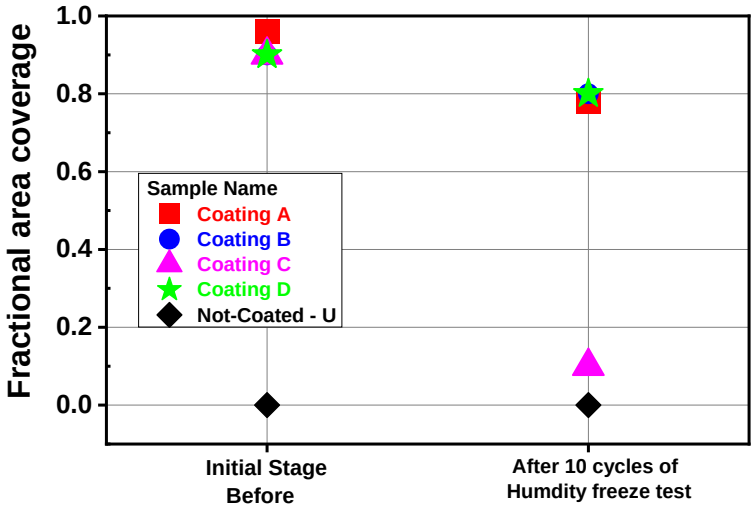

Fig. 103: Fractional area coverage of coated (A, B, C, and D) and not-coated (U) samples, before and after 10 cycles of humidity freeze test. The area scanned was 50 µm × 50 µm in all cases.

7.3 Conclusions

In the previous chapter, it was inferred that rain, abrasion and UV radiation were significant stressors that degraded AS-coating upon field exposure. In this chapter, we analysed the influence of various factors that cause damage due to exposure to rain, UV radiation and abrasion damage. Two accelerated testbeds, named the cleaning cycle simulator and the rainfall simulator, were developed to simulate the damage caused by outdoor abrasion and rainfall.

The key findings from the abrasion study are as follows;

1. The presence of dust (dew-dust-dry-clean) decreased the coating life by 82 X compared to only-clean cycles, acting as the most significant stressor that abrades the coated samples. Coating life decreased by 8 X and 10 X times in the presence of dew-dry-clean (DDC) cycles and dust-clean (DC) cycles, compared to only-clean cycles. In the presence of dew-dry-clean cycles, fluoropolymer coatings show 3X lower coating life than phenylsilicone coatings. It was also seen that coatings degrade faster when exposed to a combination of stressors, representing actual field conditions (dew-dust-dry-clean cycles and dew-dry-clean cycles) than an isolated stressor (only-clean cycles).
2. Brush A, Nylon 6,12 and microfiber brush show a clear pattern that, an increase in hardness caused lower coating life when cleaned with a harder brush material. Microfibre cloth brush causes the least damage to the anti-soiling coatings as it applies the smallest weight on the sample's surface compared to other brush materials. As the weight applied by the Microfibre cloth was the least, it is implied that the hardness of the microfibre brush was also significantly less than the other brush materials (Brush A, Brush B, and Nylon 6, 12).
3. Coated samples show 3 X lower coating life when cleaned with the direction of rotation as "towards the direction of travel" compared to "Opposite to the direction of travel" and "clockwise rotation". This is because, as the brush moves towards the direction of travel, the dust is dragged along with the brush over the samples, which causes severe scratches on the samples due to the combined effect of brush and dust particles.
4. Decreasing the horizontal velocity of brush travel by 4 times, we observe 3 X lower coating life when cleaned at 0.1 m/sec, compared to 0.4 m/sec. Phenylsilicone based coatings show 2 times higher failure rates than fluoropolymer-based coatings when cleaned at 0.1 m/sec (compared to 0.4 m/sec). At a low horizontal velocity of brush travel (0.1 m/sec), a sample comes in contact with a higher number of bristle tufts during each pass per cleaning cycle, causing greater abrasion damage to the coated samples.

The key findings from the study on the effect of rain and combination of stressors are as follows;

1. All coated samples exposed to the impact of raindrops with pH 7 water samples show 33 X lower coating life than those exposed to water immersion/water contact with pH 7 water samples. Similar finding was seen with acidic water, which indicates that during a rain event, the impact of raindrops causes greater damage than water immersion/water contact,

2. All coated samples show lower coating life when exposed to a combination of 4 stressors, followed by a combination of 3 stressors and 2 stressors.

The key findings from accelerated tests based on the IEC 61215 standard are as follows;

1. Damp heat, humidity freeze and the thermal cycling test (based on the IEC 61215 standard) were conducted to compare the results with the other accelerated stress tests (such as abrasion test, impact of rainfall, UV exposure and combination of various stressors).
2. Here we observed that Coating A, B and D pass the damp heat, thermal cycling and humidity freeze test based on the IEC 61215 standard. However, they fail the impact of rain test, abrasion (DDDC) test, and combination of abrasion, UV and rain test, which is more relevant to what the coatings have to endure in outdoor field conditions. This indicates the need for a relevant standard for AS-coating, specific to PV application (Appendix II).
3. Coating C fails (becomes hydrophilic) the tests based on the IEC 61215 standard after undergoing 211 h of damp heat test, 200 cycles of thermal cycling tests and 4 cycles of humidity freeze tests.

Chapter 8 – Lifetime Prediction of AS-Coatings

The previous chapters (6 and 7) show the impact of outdoor and indoor accelerated stress tests, such as thermal cycling, UV exposure, humidity freeze, abrasion, and rainfall tests, on anti-soiling coatings. These durability studies show that abrasion, UV exposure, and rainfall are the significant stressors that degrade anti-soiling coatings. Chapter 6 shows coating life decreased by 21 X when exposed to the rainy season compared to the samples being exposed to the non-rainy season. These durability studies imply that rainfall acts as a significant stressor that degrades such coatings. UV and abrasion were also identified as critical parameters that affect the coating life. This chapter aims to estimate the lifetime of four commercial hydrophobic anti-soiling coatings when subjected to rain and UV exposure.

8.1 Lifetime Prediction of AS-Coatings Considering Rain as a Stressor

Rain has three components of stressors, i.e. water contact, pH of the water and the impact of the raindrops. In this section we aim to estimate the lifetime of four commercial hydrophobic anti-soiling coatings when subjected to rain, considering the pH of the water as a stressor. The experiment was conducted by doing various water immersion tests at variable temperatures and pH; thus, the mechanical impact of raindrops is not considered in this study. The activation energy and the factor of pH dependence (N) was calculated based on the Arrhenius-Modified Peck model [79]. We then used historical weather data of 2 locations and calculated the effective coating life for various water pH values using the Miner's rule [80]. The entire study was conducted on solar glass samples of size 5 cm × 2.5 cm.

8.1.1 Experimental Details

The glass samples were manually spray-coated with fluoropolymer-based coatings A, B and D, and phenylsilicone based coating named C. Details of the sample preparation and sample history is shown in section 4.1.1. The activation energy was calculated based on the Arrhenius-Modified Peck model. 15 samples of each coating type were immersed in pH 6 water solution at 4 different temperatures, 25℃, 45℃, 65℃ and 97℃. Samples were kept in the hot air oven to attain the desired temperature (Fig. 104).

Fig. 104: Photograph of coated samples immersed in pH 6 water solution inside a hot air oven.

Water solutions of variable pH were made using diluted sulphuric acid. Sulphuric acid was used to make acidic water samples, as traces of sulphate are seen in actual rainwater samples collected from the field [69]. Contact angle measurements (Data-Physics Instruments, model OCA 15SEC) were done at intermediate intervals to determine the failure time of each sample. The coating was considered failed when the contact angle fell below 90˚, and the sample's failure time was noted in hours. Failure time (F(t)) data of all samples for each coating type was then fitted to a Weibull distribution; α (time scale parameter) and β (shape parameter) was calculated for each coating type at the four variables. The cumulative density function of a standard Weibull equation is given in equation 12.

$$F(t) = 1 - e^{-\left(\frac{t}{\alpha}\right)^{\beta}} \tag{12}$$

Our data set was assumed to give the exact failure time. Weibull distribution was fitted using the maximum likelihood method [81], [82]. β signifies the failure mechanism. The activation energy for each coating type was calculated using data sets with similar β values (outlier β values were removed) and Adjusted R^2 (used to verify the fit of Weibull distribution) above 0.7. Outliers were identified based on the interquartile range [83].

The pH dependence (N parameter) factor was calculated based on the Arrhenius-Modified Peck model. 15 samples of each type of coating were immersed at pH 7, pH 6, and pH 5 water solution at 45℃. The failure time data was fitted to a Weibull distribution for each coating type to estimate the α and β values. The N factors for each coating type were calculated using data sets with similar β values (outlier β values were removed from the data set) and Adjusted R^2 (used to verify the fit of Weibull distribution) above 0.7.

8.1.2 Results and Discussions

8.1.2.1 Determination of Activation Energy

Weibull distribution fits of the failure time data for each coating type immersed in 25℃, 45℃, 65℃ and 97℃ are shown in Fig. 105, Fig. 106, Fig. 107 and Fig. 108.

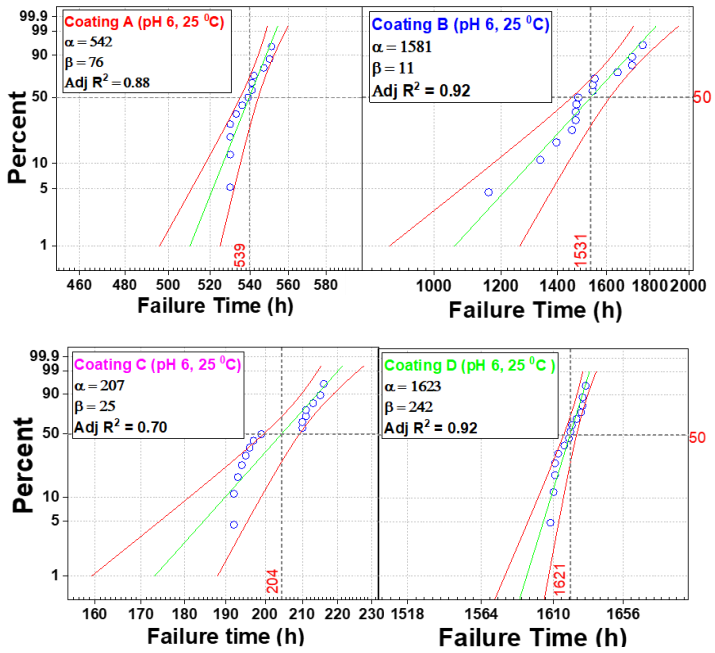

Fig. 105: Weibull distribution fits of the failure time data for coating A, B, C and D, immersed in pH 6 water solution at 25 ℃.

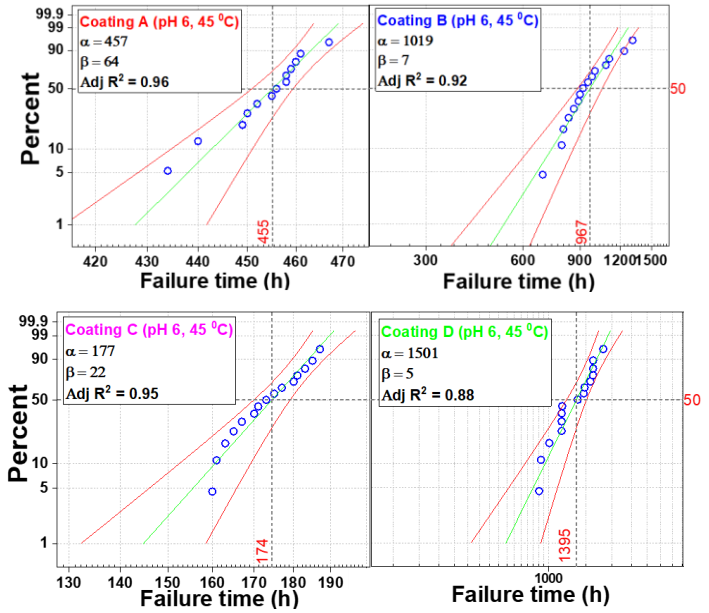

Fig. 106: Weibull distribution fits of the failure time data for coating A, B, C and D, immersed in pH 6 water solution at 45 ℃.

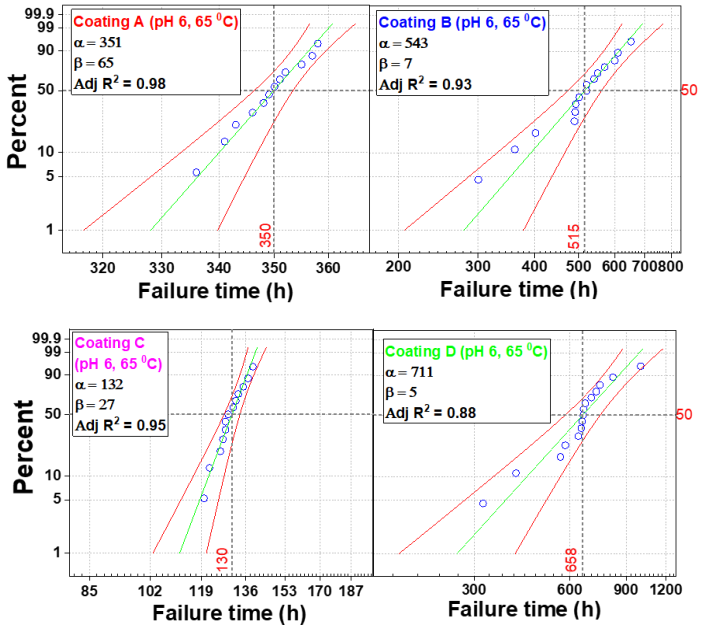

Fig. 107: Weibull distribution fits of the failure time data for coating A, B, C and D, immersed in pH 6 water solution at 65 ℃.

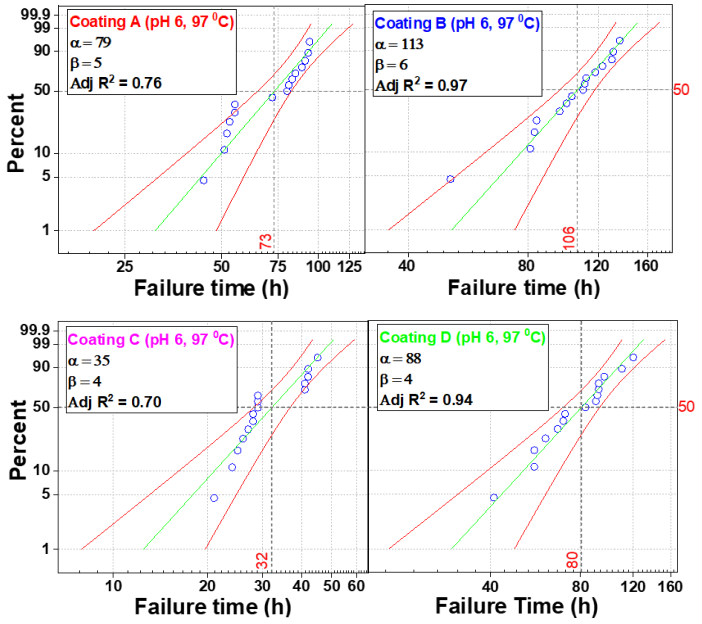

Fig. 108: Weibull distribution fits of the failure time data for coating A, B, C and D, immersed in pH 6 water solution at 97 ℃.

Data sets that had outlier β values were excluded from Table 15. The Arrhenius model [79] used to calculate the activation energy of coatings A, B, C and D is shown in equations 13 and 14.

$$\alpha = \mathrm{A}\, e^{\frac{E_a}{k_B T}} \tag{13}$$

$$\ln(\alpha) = \ln(\mathrm{A}) + \left(\frac{E_a}{k_B \times T}\right) \tag{14}$$

Where α is the life of the coating (h), A is the prefactor, E_a is the activation energy (eV), k_B is the Boltzmann constant (eV K^{-1}), and T is the temperature of the substrate (K). α values from Table 15 was plotted against their respective temperature values (shown in Fig. 109), and the slope of the plot gave the activation energy.

Table 15: Scale (α) and shape (β) parameter of the coated samples immersed in pH 6 water solution at 25 ℃, 45 ℃, 65 ℃ and 97 ℃.

Name	25℃		45℃		65℃		97℃	
	α	***β***	***α***	***β***	***α***	***β***	***α***	***β***
Coating A	542	76	457	64	351	65	-	
Coating B	-		1019	7	543	7	113	6
Coating C	207	25	177	22	132	27	-	
Coating D	-		1501	5	711	5	88	4

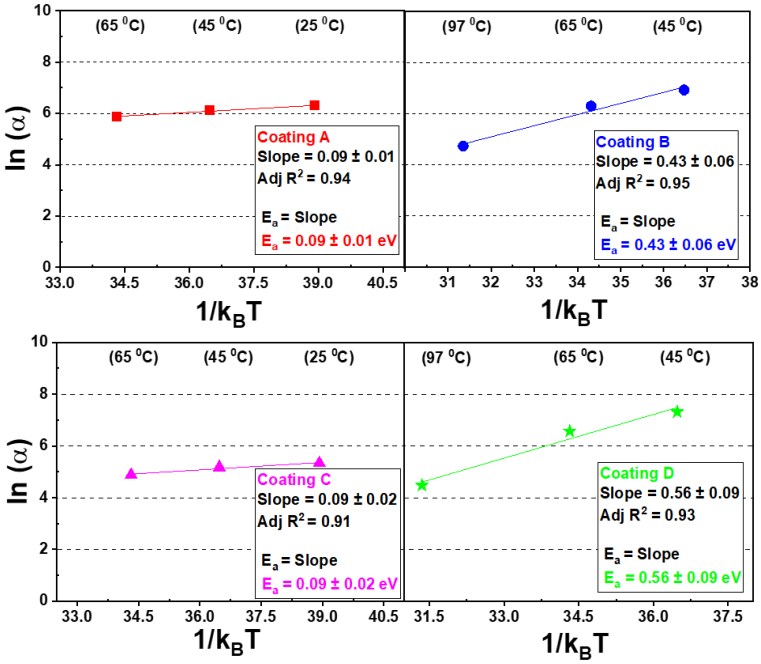

Fig. 109: Activation energy of coating A, B, C and D.

The activation energies of coatings A, B, C and D are 0.09 eV, 0.43 eV, 0.09 eV and 0.56 eV respectively (shown in Fig. 109). All coatings show positive activation energy when subjected to water contact under variable temperatures. This indicates that the life of the coatings decreases with an increase in temperature, as is also evident in Table 15.

8.1.2.2 Estimation of pH Dependence Factor (N)

To understand the dependence of pH on coating life, we used the Arrhenius-modified Pecks model, given in equations 15 and 16.

$$\alpha = \mathrm{A}\ (pH)^{N} e^{\frac{E_a}{k_B T}} \tag{15}$$

$$\ln(\alpha) = \ln(\mathrm{A}) + \mathrm{N}\ln(pH) + \left(\frac{E_a}{k_B T}\right) \tag{16}$$

Where pH is the pH values of the water solution, N is the exponential factor which indicates the pH dependence. The other parameters are as defined in equations (13) & (14). Failure time data of each coating type, immersed in pH 5, pH 6 and pH 7 water solution at 45℃, was then fitted to a Weibull distribution to calculate the α and β values (shown in Fig. 110, Fig. 106 and Fig. 111). Data sets with similar β (outlier β values were removed) were used to calculate the factor N. α and β parameters of each coating type when immersed in pH 7, pH 6, and pH 5 water solution at 45 ℃ is shown in Table 16. Data sets that had outlier β values were excluded from Table 16.

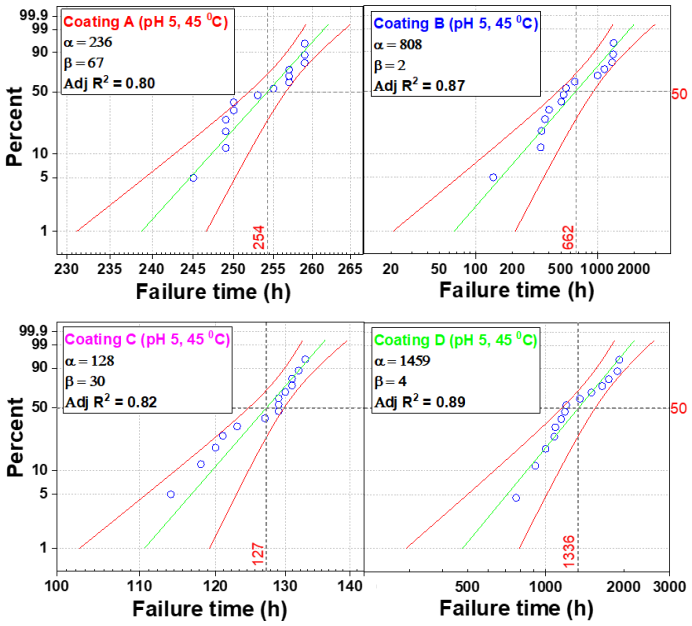

Fig. 110: Weibull distribution fits of the failure time data for coating A, B, C and D, immersed in pH 5 water solution at 45 ℃.

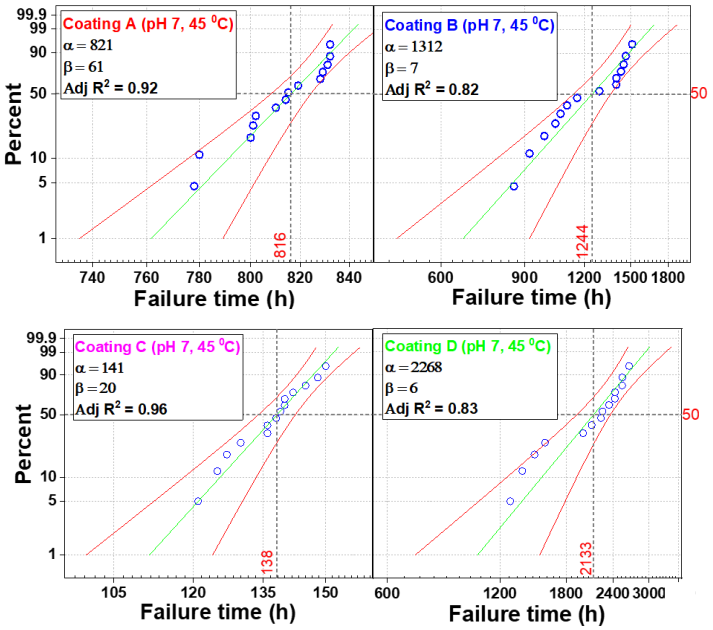

Fig. 111: Weibull distribution fits of the failure time data for coating A, B, C and D, immersed in pH 7 water solution at 45 ℃.

Table 16: Time (α) and shape (β) parameters of the coated sample immersed in pH 5, pH 6 and pH 7 water solution at 45 ℃.

Name	pH 5		pH 6		pH 7	
	α	***β***	***α***	***β***	***α***	***β***
Coating A	236	67	457	64	821	61
Coating B	808	2	1019	7	1312	7
Coating C	128	30	177	22	141	20
Coating D	1459	4	1501	5	2268	6

Following equation 16, α values from Table 16 were plotted against their respective pH values (shown in Fig. 112), and the slope of the plot gave the factor N. The N factor for coating A, B, C and D were estimated as 3.6, 1.4, 0.28, and 1.31, respectively. Higher N values indicate a greater dependence of pH on the coating life.

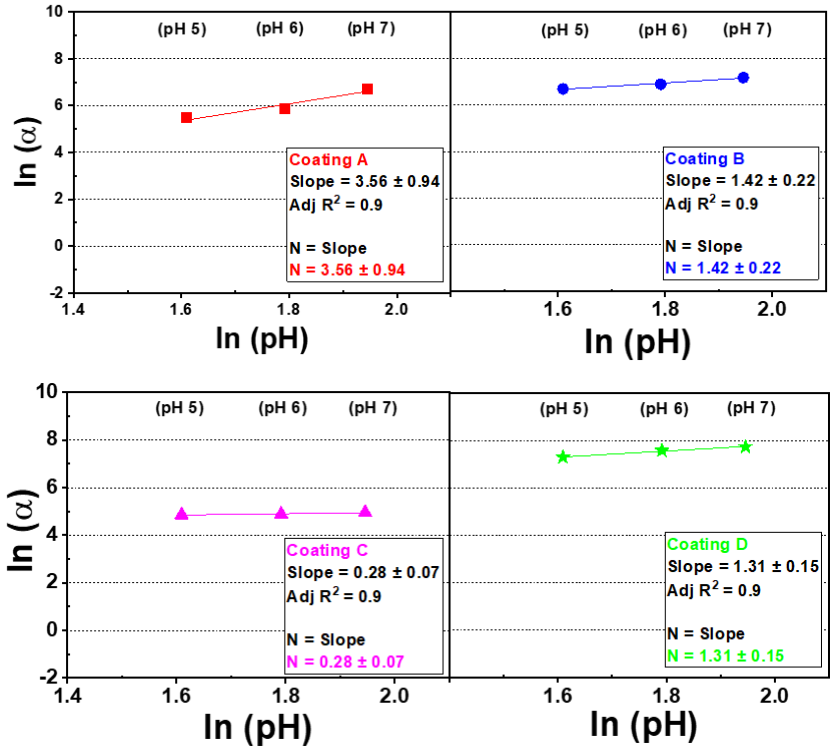

Fig. 112: pH dependence factor (N) for coating A, B, C and D.

In Fig. 112, we may observe that fluoropolymer-based coatings (A, B, and D) show a higher pH dependence factor than phenylsilicone-based coating C. Using Miner's rule, we estimated the lifetime of the coated samples from the activation energy and N values for each coating type.

8.1.2.3 Lifetime Prediction of Coated Samples

The lifetime prediction of the coated samples was performed using the concept of cumulative damage using Miner's rule [80]. According to Miner's rule, the damage is inversely proportional to the value of the time scale parameter (shown in equation 17).

$$\text{Damage} \propto \frac{1}{\alpha_i} \tag{17}$$

$$\text{Damage} = k\,\frac{1}{\alpha_i} \tag{18}$$

Where α (h) is the time scale parameter (assuming Weibull distribution) and k is the proportionality factor. Cumulative damage for 1 year, $D_{1\,year}$, is given by

$$D_{1\ year} = \mathrm{k} \sum_{i=0}^{8760} \frac{1}{\alpha_i} \quad (19)$$

According to Miner's rule, failure occurs when the sum of damage fractions at various stress levels reaches unity, referred to as the damage threshold [84]. Thus, in simple terms, the damage threshold is the cumulative damage at which the coating fails (equation 20); it is the product of the cumulative damage that occurs in 1 year and the number of years at which the coating fails.

$$1 = \mathrm{k} \times \sum_{i=0}^{8760} \frac{1}{\alpha_i} \quad (20)$$

$$\mathrm{k} = \frac{1}{\sum_{i=0}^{8760} \frac{1}{\alpha_i}} \quad (21)$$

$$\text{Number of years at which the coatings fail} = \frac{1}{D_{1\ year}} \quad (22)$$

Where k is the proportionality factor, i.e. the number of years at which the coatings fail, α (h) is the time scale parameter (assuming Weibull distribution) and $D_{1\ year}$ is the cumulative damage that occurred in 1 year. Coating life was calculated for 2 locations, California and Wyoming, United States. Hourly weather data of these 2 locations were taken from National Solar Radiation Database for 2018 [85]. The weather data was fed into the modelled equation 16 to calculate α (h). The substrate temperature was calculated using the Sandia module temperature model [86]. Coating life was calculated for 2 different scenarios. Scenario 1 refers to a condition when the tilt angle of the coated PV module is lower than the roll-off angle. In this case, the raindrops hitting the surface of the coated module would not roll off and sit on the surface of the coated module. For scenario 1, we calculated the rain intensity at which the top surface of the coated module would be completely wet. The total number of droplets required to completely wet the top surface of the sample is shown in equation 25.

$$\text{Area of sample} \times \mathrm{Y} = \text{Volume of raindrop} \times N_{drop} \quad (23)$$

$$\mathrm{L} \times \mathrm{B} \times \mathrm{Y} = \frac{4}{3} \pi r^3 \times N_{drop} \quad (24)$$

$$N_{drop} = \frac{L \times B \times Y}{\frac{4}{3} \pi r^3} \quad (25)$$

Where Y is the rate of rainfall (mm/h), r is the radius of the raindrop, L is the length of the sample, B is the breadth of the sample, and N_{drop} is the total number of droplets required to wet the top surface of the sample in 1 h.

$$N_r \times N_c = N_{drop} \tag{26}$$

$$\frac{L}{2r} \times \frac{B}{2r} = N_{drop} \tag{27}$$

$$\frac{L \times B}{4 \times r^2} = N_{drop} \tag{28}$$

Where, N_r is the total number of raindrops in a row in each sample, N_c is the total number of raindrops in a column in each sample, and 2r is the diameter of the raindrop. Equating equations 25 and 28, we get;

$$\frac{\mathrm{L} \times \mathrm{B} \times \mathrm{Y}}{\frac{4}{3}\pi r^3} = \frac{L \times B}{4 \times r^2} \tag{29}$$

$$\mathrm{Y} = \frac{\pi r}{3} \tag{30}$$

$$Y = 1.04\, r \tag{31}$$

Assuming the radius of the raindrop is equal to 1 mm [87], we conclude that, under scenario 1, the top surface of the sample is entirely wet when the rainfall intensity is greater than 1.04 mm/h (shown in equation 31). Scenario 2 refers to a situation when the tilt angle of the coated PV module is greater than the roll-off angle. Under this condition, the raindrops would roll off the surface of the coated modules; thus, the top surface of the coated sample was assumed to be completely wet when the rainfall intensity was greater than 2.6 mm/h [88]. Coating life was calculated for 3 different pH values and 2 different locations (Fig. 113).

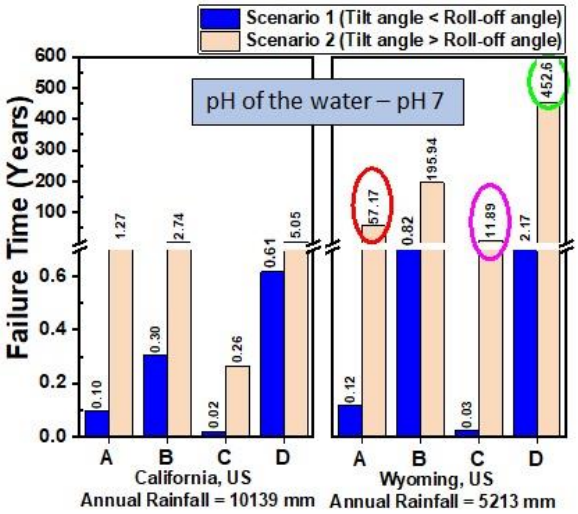

(a)

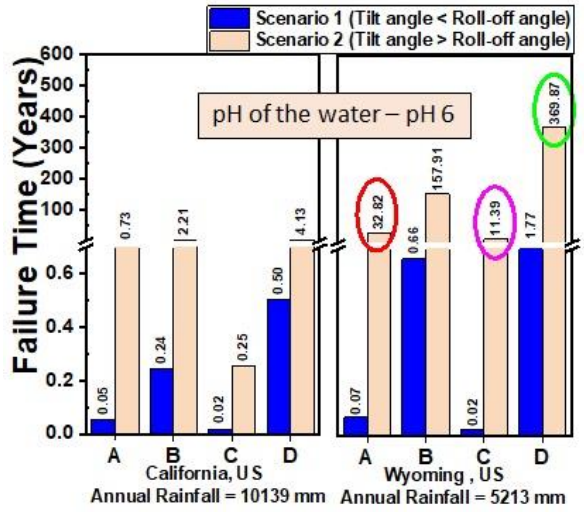

(b)

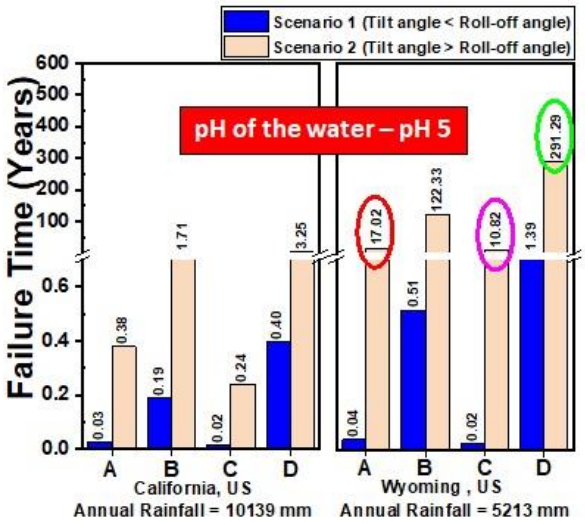

(c)

Fig. 113: Number of years at which the coatings fail, at 2 different locations, when exposed to rain at variable pH values.

In Fig. 113, we may observe that all coated samples show lower coating life when exposed at a tilt angle lower than their respective roll-off angle. Coatings exposed in California, subjected to 2X higher annual precipitation (compared to Wyoming, US), show reduced lifetime varying from 1X to 4X (when exposed at tilt angles less than the roll-off angle), 45X to 90X (when exposed at tilt angles greater than the roll-off angle). Coating C shows the smallest change in its lifetime when exposed to variable pH compared to coatings A, B, and D (Fig. 113), correlated well with the pH dependence factors (Fig. 112). It should also be noted that the predicted lifetime for coatings under water immersion with pH 6 water (in scenario 1) is significantly less than the desired lifetime of

the modules (> 25 years). Also, this is expected to reduce further when the effect of the impact of raindrops is factored in.

8.2 Lifetime Prediction of AS-Coatings Considering UV Radiation as a Stressor

This section estimates the life of 4 commercial hydrophobic anti-soiling coatings, considering UV radiation as a stressor. Other parameters like rain, abrasion and high humidity also play a critical role in coating degradation and are not considered here to allow detailed analysis of the effect of UV. The activation energy was calculated using the Arrhenius model [79]. Weibull distribution was considered for fitting the failure time data. Failure was noted when the contact angle of the coated sample went below 90˚. Weibull distribution was considered for this study as it is a simple empirical model which can explain all 3 segments of the bathtub curve [81], [89]. Using the modelled equation and the historical weather data, we estimated the life of the coated samples at 3 different locations based on the Miner's rule.

8.2.1 Experimental Details

The study was conducted on four types of commercial hydrophobic anti-soiling coatings named A, B, C and D. Details on sample preparation and sample history are shown in section 4.1.1. Coating A, B and D were fluoropolymer based coatings, and coating C was a phenylsilicone based coating. Ten samples of each coating type were exposed to 5 variations of UV intensity and temperature. The samples were kept inside the QUV Xenon chamber. The coated samples were kept at variable heights and positions to achieve the desired UV intensity and temperature. A schematic diagram of the sample positions is shown in Fig. 114. Samples were exposed to following sets of UV intensities and temperature; 75 W/m^2 & 52°C, 73 W/m^2 & 56°C, 89 W/m^2 & 75°C, 71 W/m^2 & 58°C, and 124 W/m^2 & 122°C. Arrhenius model was used to calculate the activation energy [79]. Failure was calculated in terms of UV dose (kWh/m^2). Failure was noted as the UV dose at which the sample's contact angle became less than 90˚. The contact angle was measured using the Data-Physics Instrument, model OCA 15SEC.

The failure data was then fitted to a weibull distribution function. Weibull distribution was fitted with respect to the interval censoring method [90]. Interval censoring was chosen as it was not possible to perform continuous measurements; contact angle was measured at weekly intervals. The weibull distribution fits were based on the maximum likelihood method [89]. α (time scale

parameter) and β (shape parameter) values were calculated via weibull distribution for each coating type exposed to 5 variable UV intensities and temperatures. α was the characteristic life, and β refers to the degradation mechanism [91]. Adjusted R^2 was calculated to verify the fit of the weibull distribution. Data sets with similar β values (outlier β values were removed from the study) and adjusted R^2 above 0.8 were used to calculate the activation energy. The outlier values were identified based on the interquartile range [83].

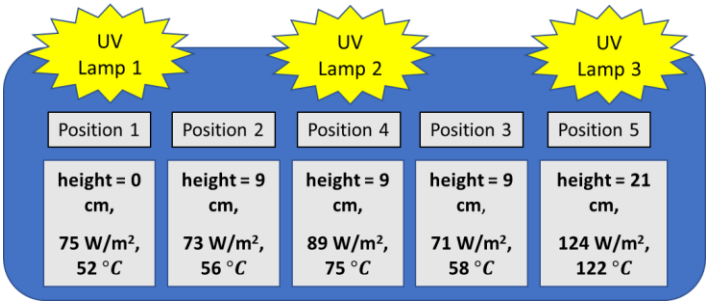

Fig. 114: Schematics representing the sample positions inside the QUV Xenon chamber.

8.2.2 Results and Discussion

8.2.2.1 Determination of Activation Energy:

Weibull distribution fits for each coating type exposed to 5 sets of UV intensities and temperatures are shown in Fig. 115, Fig. 116, Fig. 117, Fig. 118, and Fig. 119.

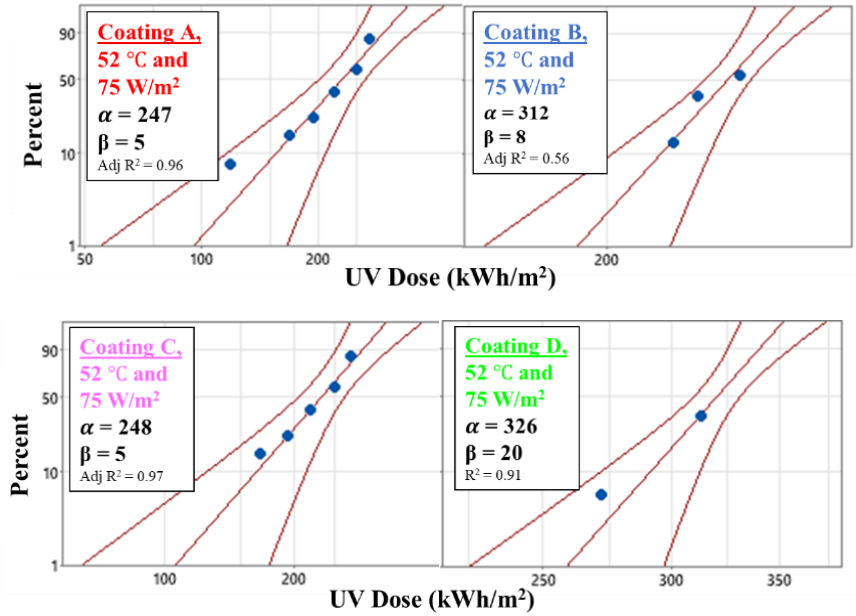

Fig. 115: Weibull distribution fits of coating A, B, C and D, exposed to 75 W/m^2 & 52 °C.

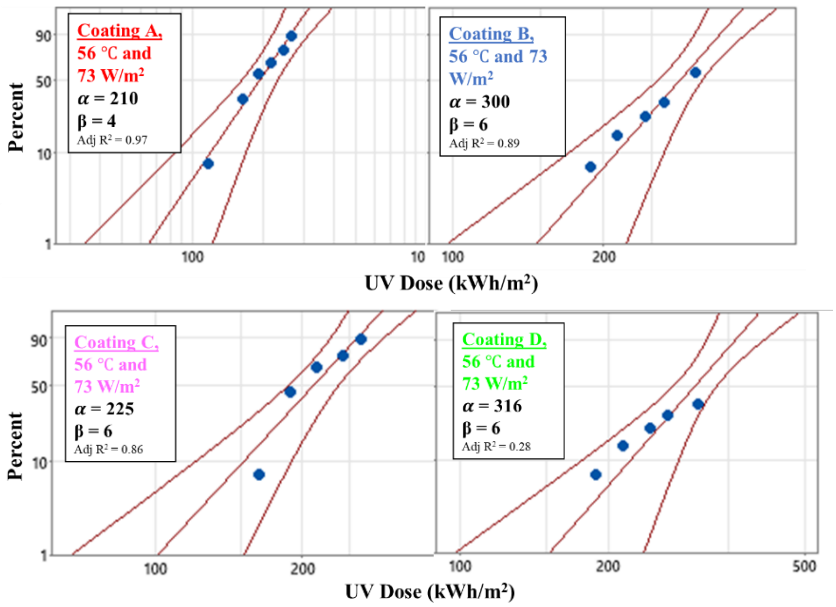

Fig. 116: Weibull distribution fits of coating A, B, C and D, exposed to 73 W/m^2 & 56 °C.

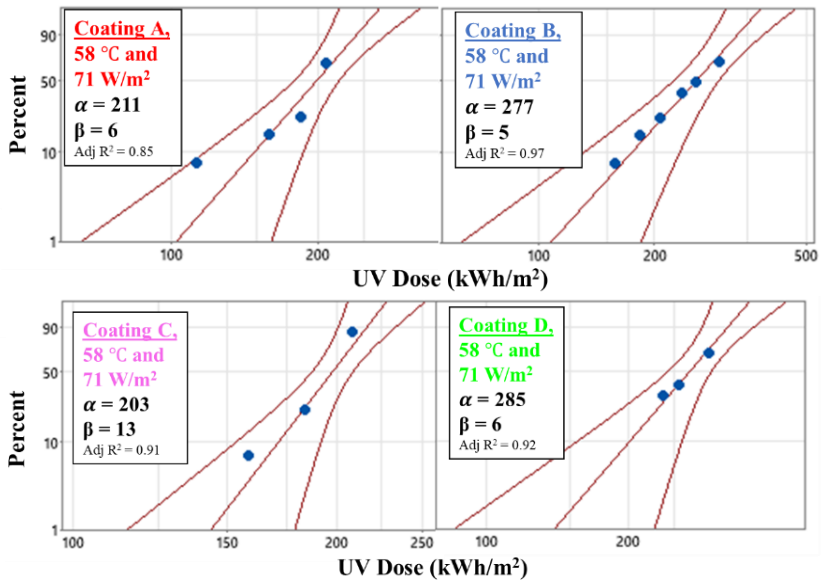

Fig. 117: Weibull distribution fits of coating A, B, C and D, exposed to 71 W/m^2 & 58 °C.

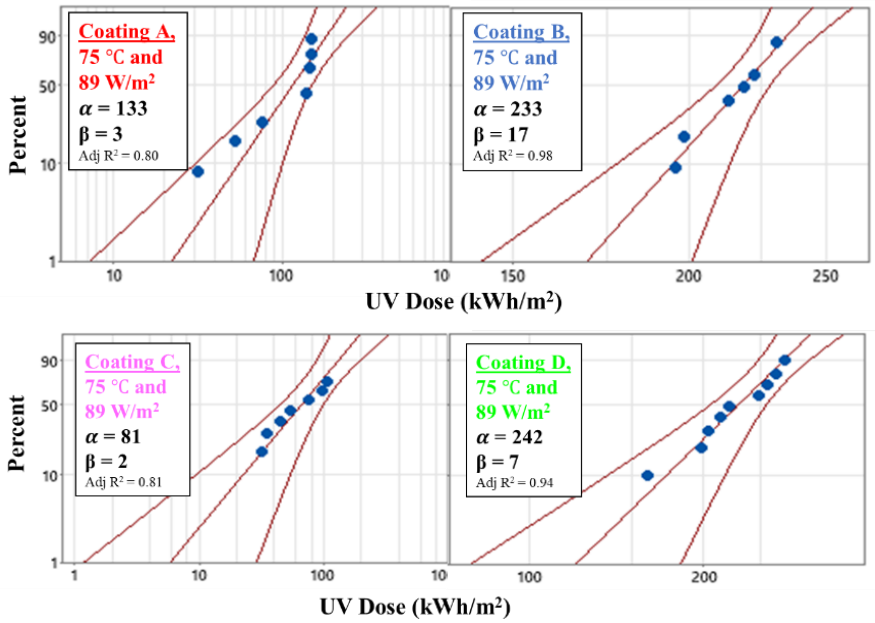

Fig. 118: Weibull distribution fits of coating A, B, C and D, exposed to 89 W/m^2 & 75 °C.

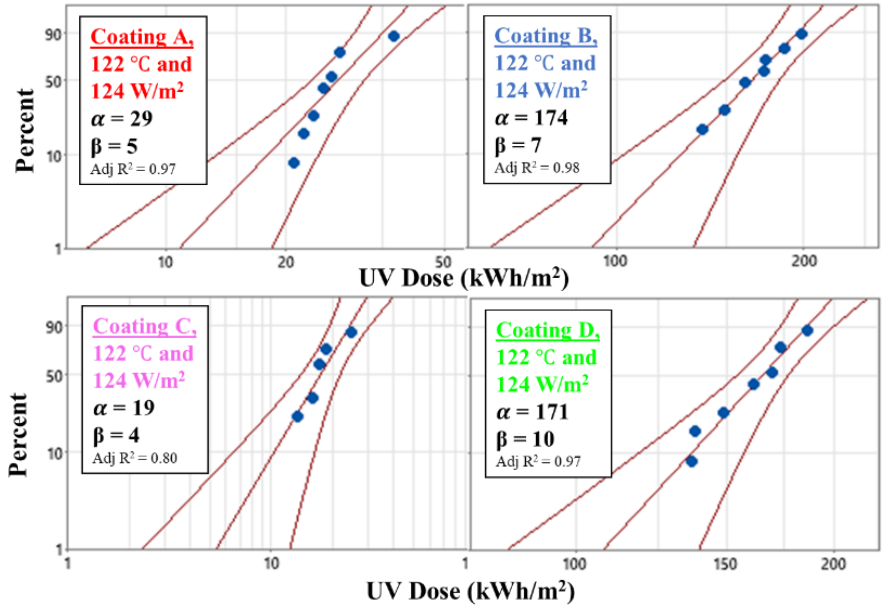

Fig. 119: Weibull distribution fits of coating A, B, C and D, exposed to 124 W/m^2 & 122 °C.

Table 17 shows the α and β values for each coating type. Data sets with outlier β values and adjusted R^2 less than 0.8 were excluded from the analysis and are not shown in Table 17. α values were calculated in terms of UV dose (kWh/m^2) at which the coatings become hydrophilic.

Table 17: Time (α) and shape (β) parameters of the coated samples exposed to variable intensities and temperatures.

Coating Type	52 °C and 75 W/m²		56 °C and 73 W/m²		58 °C and 71 W/m²		75 °C and 89 W/m²		122 °C and 124 W/m²	
	α	β	α	β	α	β	α	β	α	β
A	247	5	210	4	211	6	133	3	29	5
B	-		300	7	277	5	-		174	7
C	248	5	225	6	-		81	2	19	4
D	-		-		286	6	242	7	171	10

α values were then fitted into the Arrhenius model [79] to estimate the activation energy for each coating type. The Arrhenius equation used to calculate the activation energy is shown in equation 33.

$$\alpha = A\, e^{\frac{E_a}{k_B T}} \tag{32}$$

$$\ln(\alpha) = \ln(A) + \left(\frac{E_a}{k_B \times T}\right) \tag{33}$$

Where α is the UV dose (kWh/m^2) at which the coating fails, A is the prefactor, E_a is the activation energy (eV), k_B is the Boltzmann constant (eV K^{-1}), and T is the temperature of the substrate (K). α values from Table 17 were plotted against their respective temperature values, and the slope of the line was equal to the activation energy. Fig. 120 shows the activation energy plots for coating A, B, C, and D.

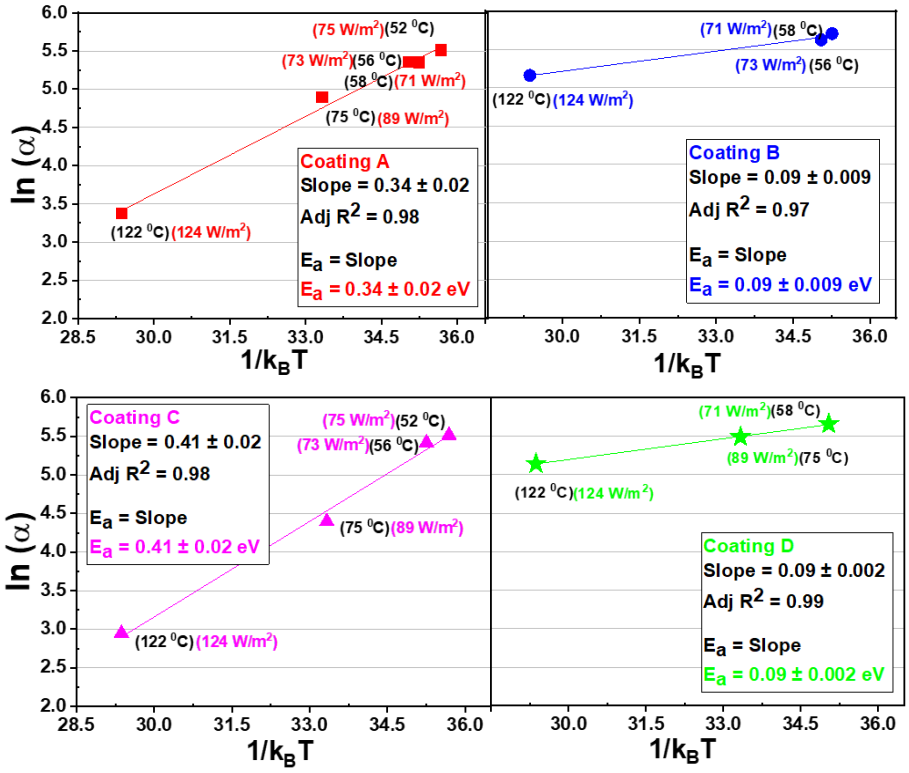

Fig. 120: Activation energy of coating A, B, C and D under UV exposure.

The activation energy of coating A, B, C and D were calculated to be 0.34 eV, 0.09 eV, 0.41 eV and 0.09 eV, respectively. All coatings show positive activation energy, which indicates that the coating life decreases with increased temperature. Coating A and C shows higher activation energy than coating B and D, which correlates well with the percentage of inorganic matter in the coated samples (shown in Fig. 121).

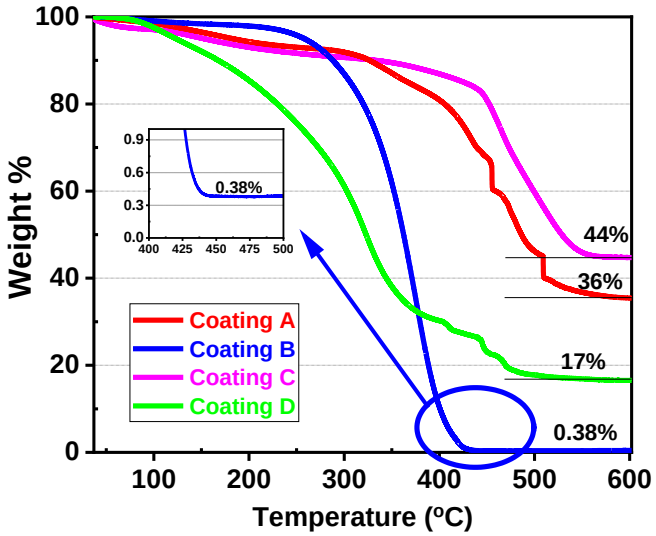

Fig. 121: Thermogravimetric analysis of coating A, B, C and D.

Fig. 121 shows the thermogravimetric analysis of all coated samples. The weight percentage remaining at the end of the heating cycle (in Fig. 121) is the percentage of inorganic matter present in the coated samples. Coating A and C show a higher percentage of inorganic matter, which correlates well with the higher activation energy data shown in Fig. 120. The activation energy and the historical weather data were fed into the modelled equation (equation 33) to estimate the life of the coated samples via Miner's rule [80].

8.2.2.2 Lifetime Prediction of Coated Samples

The life of the coated samples was estimated based on the concept of cumulative damage via the Miner's rule [80]. Miner's rule was implemented as cumulative damage gives more insight when dealing with scenarios involving non-constant values of stressors or when lifetime prediction has to be performed using time series data for a long duration of time. According to the Miner's rule [80], the damage is inversely proportional to the values of the time scale parameter (α, Weibull distribution) and directly proportional to the time spent at the corresponding stressors that result in this time scale parameter (shown in equation 34).

$$\text{Damage} \propto \frac{t_i}{\alpha_i} \tag{34}$$

$$\text{Damage} = k\,\frac{t_i}{\alpha_i} \tag{35}$$

Where α (kWh/m^2) is the time scale parameter (assuming weibull distribution), t is the time spent at the corresponding stressor that results in the time scale parameter, and k is the proportionality factor. Cumulative damage for 1 year is represented as $D_{1\ year}$.

$$D_{1\ year} = k \times \sum_{i=0}^{8760} \frac{u_i}{\alpha_i} \tag{36}$$

Where u_i is the cumulative UV dose (kWh/m^2) at the plane of array received by the sample in 1 year, and α_i is calculated based on equation 33, where T is the module temperature. Module temperature was calculated based on the Sandia module temperature model [86]. Miner's rules state that failure occurs when the sum of damage fractions at various stress levels reaches unity, referred to as the damage threshold [84]. In simple words, the damage threshold is the cumulative UV dosage at which the coatings fail/becomes hydrophilic, shown in equation 37. Damage threshold is the product of the cumulative damage that occurs in 1 year to the number of years at which the coating fails.

$$1 = k \times \sum_{i=0}^{8760} \frac{u_i}{\alpha_i} \tag{37}$$

$$k = \frac{1}{\sum_{i=0}^{8760} \frac{u_i}{\alpha_i}} \tag{38}$$

$$\text{Number of years at which the coatings fail} = \frac{1}{D_{1\,year}} \tag{39}$$

Where k is the proportionality factor, i.e. the number of years at which the coatings fail/coating life, α_i (kWh/m^2) is the time scale parameter (assuming weibull distribution), u_i is the cumulative UV dose (kWh/m^2) at plane of array (UV-POA) received by the sample in 1 year and $D_{1\,year}$ is the cumulative damage that occurred in 1 year. UV-POA was calculated based on the empirical relation between GHI (Global Horizontal Irradiance) and POA (Plane of Array irradiance). Coating life was calculated at 3 different locations, i.e. Maine, Kansas and Mexico, located in the United States. Hourly weather of these 3 locations was taken from National Solar Radiation Database for the year 2018 [85]. Fig. 122 shows the coating life for coating A, B, C and D at 3 different locations. From Fig. 122, we observe that all coated samples show a decline in the coating life when exposed to sites with an increased annual UV dose. All coated samples show reduced coating life varying from 1.6 X to 2.2 X when exposed to a location that receives 1.4 X higher annual UV dose. Coating A and C show higher coating life at all 3 locations, as they contain more inorganic content (Fig. 121, Fig. 122) and thus show higher activation energy than coating B and D. When exposed to a site that receives 1.9 X higher annual UV dose, all coated samples show a decline in coating life varying from 1.7 X to 3 X.

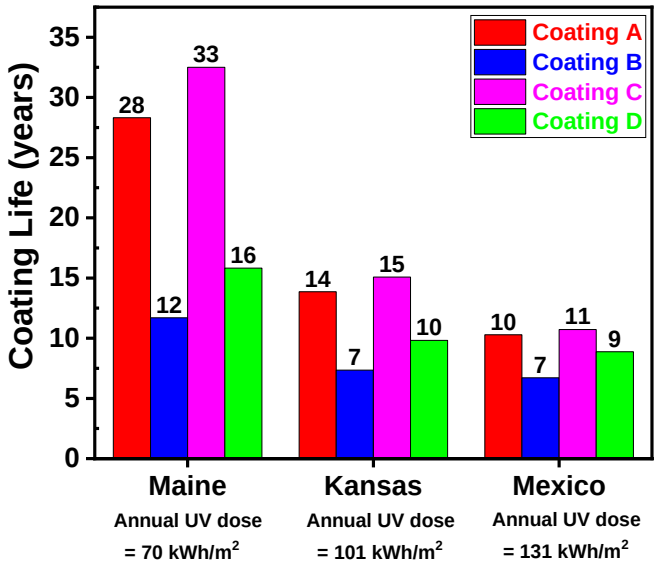

Fig. 122: Coating life at 3 different locations when exposed to UV radiation.

8.3 Conclusions

In this chapter, we estimated the lifetime of AS-coatings when exposed to rain and UV radiation.

8.3.1 Lifetime Prediction of AS-Coatings Considering Rain as a Stressor

Rain has 3 components of stressors; impact of raindrops, water contact and water pH. In this study, the samples were subjected to water immersion tests; thus, the impact of raindrops hitting the surface of the sample was not accounted for in this study. The activation energy of 4 commercial hydrophobic anti-soiling coatings (A, B, C and D) was calculated to be 0.09 eV, 0.43 eV, 0.09 eV and 0.56 eV, respectively. Positive activation energy indicate that coating life decreased with an increase in temperature. The activation energy and the pH dependence factor (N) were calculated assuming an Arrhenius-modified Pecks model. The factor N for coating A, B, C and D was 3.6, 1.4, 0.28 and 1.31, respectively. Higher values of N indicated a higher dependence of pH on coating life. Fluoropolymer based coating showed higher values of N than phenylsilicone based coatings. Based on the modelled equation, we estimated the coating life at 2 different locations and 3 variable pH using the Miner's rule. All coatings showed lower coating life under varying pH when exposed at a tilt angle lower than their respective roll-off angle. Coatings exposed to sites with 2X higher annual precipitation show reduced lifetimes varying from 1X to 4X (when exposed at tilt angles less than the roll-off angle), 45X to 90X (when exposed at tilt angles greater than the roll-off angle).

8.3.2 Lifetime Prediction of AS-Coatings Considering UV Radiation as a Stressor

This work estimates the life of 4 commercial hydrophobic anti-soiling coatings (A, B, C and D) when subjected to UV radiation. The activation energy was calculated based on the Arrhenius model. The activation energy of coating A, B, C and D was estimated to be 0.34 eV, 0.09 eV, 0.41 eV and 0.09 eV, respectively, assuming Weibull distribution. All coatings show positive activation energy, which indicates that the life of the coated samples decreased with an increase in temperature. Coatings with higher organic content (B and D) showed lower activation energy and coating life. The activation energy and the historical weather data were fed into the modelled equation to estimate the coating life at 3 different locations based on the Miner's rule. All coated samples show a decline in coating life when exposed to sites that receive a higher annual UV dose. All coated samples show reduced lifetimes varying from 1.6 X to 2.2 X when exposed to a site

that receives 1.4 X higher annual UV dose. When exposed to a location that receives 1.9 X higher annual UV dose, all coated samples show a decline in coating life, varying from 1.7 X to 3 X. This study shows that no coating would work on all climatic zone. Thus the PV plant developers and researchers can use this database to estimate the coating life at different locations, which can help us in mapping locations best suited for a specific coating type. This will help the users to choose the coatings best suited for their specific weather conditions. This work can also be used as a starting point for modelling the effect of combination of stressors.

Chapter 9 - Conclusions and Future works

Making energy sources assessable, reliable, sustainable and affordable to everyone is an urgent need of this century [92], [93]. As a sunbelt country, India has rapidly integrated solar energy into its energy grid [94]. Harsh climatic conditions in India pose a big challenge to the economic viability of the solar energy sector [83]. In India, loss in power/energy caused only due to soiling can go up to 1%/day if the module glass is not cleaned; a financial loss of 1 billion euros/annum was estimated for 2023 [1]. This shows the urgent need for a cost-effective dust mitigation strategy. This thesis discusses two cost-effective dust mitigation strategies (1) Vertically Mounted Bifacial Modules and (2) Anti-soiling Coating. The key findings from our work are summarized below. Based on the research reported in previous chapters, we have identified various aspects of soiling of PV modules that need further exhaustive research. These are listed in section 9.2.

9.1 Conclusions

9.1.1 Vertically Mounted Bifacial Module

Based on our experiments, it can be concluded that (i) vertical mounting of bifacial modules could mitigate the soiling losses and hence regular cleaning of panels can be avoided. (ii) bifacial modules mounted at the latitude angle have lower soiling loss compared to fixed-tilt monofacial modules (mounted at latitude tilt angle) and hence may require less frequent cleaning (iii) For BF = 90%, vertically mounted bifacial modules produce lower energy compared to latitude mounted bifacial modules, to begin with, in the high soiling conditions prevailing in Mumbai, the latitude mounted bifacial panels would produce lower energy (compared to vertically mounted bifacial modules) after 3 weeks, if they are not cleaned in the meanwhile (iv) vertically mounted modules with high bifaciality factor (of 90%) runs at lower temperature than latitude mounted modules, with potential improvements in the performance ratio and long term reliability (v) by combing vertically mounted bifacial modules and latitude mounted bifacial modules, increase in the duration of peak power generation is approximately 80%. These results were obtained in Mumbai. We anticipate that several of these conclusions would be applicable to many other geographical locations with high irradiance and soiling rates.

9.1.2 Anti-soiling Coatings

Anti-Soiling coatings are nano or microlayer coatings, which reduce the settlement of dust on the surface of the PV module, and are extensively investigated as a mitigation strategy. Even though AS-coatings may require water or air to clean the surface, the amount of water required and the frequency of cleaning runs may be significantly reduced. As the coating is applied on the outer surface of the PV module, the durability of these coatings is essential. Until now, there are no standards to test the reliability of such coatings (considering all environmental stressors). This study evaluates the reliability of 4 commercial hydrophobic AS-coating (A, B, C, and D) under a warm and humid climate zone. The not-coated sample is referred to as U. Various outdoor durability tests followed by numerous accelerated stress tests were performed. The findings of the correlation study between the outdoor and indoor accelerated stress tests were then used to model the life of AS-coatings considering UV radiation and rainfall as a stressor. Two accelerated testbeds, named the cleaning cycle simulator and the rainfall simulator, were developed to simulate the damage caused by outdoor abrasion and rain. Coatings A, B, and D were fluoropolymer-based coatings, and coating C was a Phenylsilicone based coating. A new non-destructive characterization method was established to estimate the surface coverage of the coated area via TM-AFM phase imaging using tapping mode atomic force microscopy. The reliability evaluation of AS-coatings is divided into 4 parts; (1) Cleaning efficacy, (2) Outdoor durability, (3) Indoor Accelerated stress tests and (4) Lifetime prediction of AS-coatings. The key conclusions are given below.

(1) Cleaning efficacy - Coated samples show lower soiling loss than not-coated samples in both controlled environments and field exposure. This indicates that anti-soiling coating can mitigate soiling. We also observed that roll-off angle depends on the surface of the solar glass, which vary upon dust deposition (under field condition). During field exposure study, we saw a significant reduction in the cleaning efficacy (for Coating D) after 2nd manual cleaning, indicating abrasion caused by the cleaning tool. The ranking in cleaning efficacy for coated samples B, C, and D during field exposure correlate well with the ranking of roll-off angle measurements with dust deposition, implying roll-off angle as an important measure for the evaluation of anti-soiling coatings.

(2) Outdoor durability tests – Coating life of all coated samples decreased by 21 X (average of acceleration factors of coating A, B, C and D) when exposed to rainy season compared to

the samples that were exposed to the non-rainy season. During the rainy season, phenylsilicone based coating (C) shows 7 X lower coating life than fluoropolymer based coatings (average of A, B, and D).

(3) Accelerated stress tests – We tested the influence of factors which impact the damage caused by various environmental stressors like abrasion, rain and UV radiation.

a. Rainfall - All coated samples exposed to the impact of raindrops with pH 7 water samples show 33 X lower coating life than those exposed to water immersion/water contact with pH 7 water samples. Similar finding was seen with acidic water, which indicates that during a rain event, the impact of raindrops causes greater damage than mere water immersion/water contact.

b. Abrasion - The presence of dust (dew-dust-dry-clean) decreases the coating life by 82 X compared to only-clean cycles, acting as the most significant stressor that abrades the coated samples. Brush A, Nylon 6,12 and microfiber brush show a clear pattern that, increase in hardness caused lower coating life when cleaned with a harder brush material. Microfibre cloth brush causes the least damage to the anti-soiling coatings as it applies the smallest weight on the sample's surface compared to other brush materials. Coated samples show 3 X lower coating life when cleaned with the direction of rotation as "towards the direction of travel" compared to "opposite to the direction of travel" and "clockwise rotation". This is because, as the brush moves towards the direction of travel, the dust is dragged along with the brush over the samples, which causes severe scratches on the samples due to the combined effect of brush and dust particles. Decreasing the horizontal velocity of brush travel by four times, we observe 3 X lower coating life when cleaned at 0.1 m/sec, compared to 0.4 m/sec. At a low horizontal velocity of brush travel (0.1 m/sec), a sample comes in contact with a higher number of bristle tufts during each pass per cleaning cycle, causing greater abrasion damage to the coated samples.

c. UV radiation - The combination of UV exposure and condensation was studied in the indoor stress test, which showed a statistically significant reduction in the contact angle with an increase in the dosage of UV and condensation. The rate of decrease in contact angle was highest for coating C, making it hydrophilic at 32 kWh/m^2 of UV dose and 441 hours of condensation. However, in indoor stress tests

with individual stressors (UV exposure), very high stress levels (366 kWh/m^2) are required to produce similar degradation. All coated samples show lower coating life when exposed to a combination of 4 stressors (UV radiation + abrasion + impact of raindrop + water pH), followed by a combination of 3 stressors (UV radiation + impact of raindrop + water pH) and two stressors (impact of raindrop + water pH).

d. Lifetime prediction of AS-coatings – From the understanding gained by the outdoor and indoor accelerated stress tests, we modelled an empirical equation to predict the life of coatings under 2 different stressors.

(1) Considering rain as the stressor – Rain has 3 components of stressors, i.e. water contact, pH of the water and the impact of the raindrops. This work aims to estimate the lifetime of 4 commercial hydrophobic anti-soiling coatings when subjected to rain, considering the pH of the water as a stressor. The activation energy of 4 commercial hydrophobic anti-soiling coatings (A, B, C and D) was calculated as 0.09 eV, 0.43 eV, 0.09 eV and 0.56 eV, respectively. Positive activation energies indicate that the coating life decreased with an increase in temperature. The activation energy and pH dependence factor (N) were calculated assuming an Arrhenius-modified Pecks model. The factor N for coating A, B, C and D was 3.6, 1.4, 0.28 and 1.31, respectively. Higher values of N indicated a higher dependence of pH on coating life. Fluoropolymer based coating showed higher values of N than phenylsilicone based coatings. Based on the modelled equation, we estimated the coating life at 2 different locations and 3 variable pH using the Miner's rule. All coatings showed lower coating life under varying pH when exposed at a tilt angle lower than their respective roll-off angle.

(2) Considering UV radiation as the stressor – We estimated the life of 4 commercial hydrophobic anti-soiling coatings (A, B, C and D) when subjected to UV radiation. The activation energy was calculated based on the Arrhenius model. The activation energy of coatings A, B, C and D was estimated as 0.34 eV, 0.09 eV, 0.41 eV and 0.09 eV, respectively, assuming Weibull distribution. All coatings show positive activation energy, which indicates that the life of the coated samples decreased with an increase in temperature. Coatings with higher organic content (B and D) showed lower activation energy and coating life. The activation energy and the historical weather data were fed into

the modelled equation to estimate the coating life at 3 different locations based on the Miner's rule. All coated samples show a decline in coating life when exposed to sites that receive a higher annual UV dose. All coated samples show reduced lifetimes varying from 1.6 X to 2.2 X when exposed to a site that receives 1.4 X higher annual UV dose. When exposed to a location that receives 1.9 X higher annual UV dose, all coated samples show a decline in coating life, varying from 1.7 X to 3 X.

This study indicated that no coating would be durable in all climatic zones. Thus this database can be used by PV plant developers, investors and researchers to estimate the coating life at different locations, which can help us map locations best suited for a specific coating type.

9.2 Future works

We have shown that soiling can be mitigated by vertically mounting the bifacial module. The future directions that emerge from this study are given below:

a) We have compared the energy generation and module temperature between monofacial and bifacial modules. These results need to be examined for other PV technologies like thin films and tracker based systems with annual and seasonal optimum tilt angles for various geographies.
b) Vertical mounting of PV modules may require care in the design of the power plant layout to minimize the effect of shadowing between adjacent modules. A comparison study, focussing on the land use ratio, can be estimated for various landscapes.
c) This dust mitigation strategy may also be used by trackers where the modules can be tilted to 90^0 after sunset. However, vertically mounted structures may experience high wind loading, which would require a change in the structural design and the mounting materials.

In the AS-coating domain, we have shown a detailed study on the durability of AS-coating via various outdoor and indoor accelerated stress tests relevant to warm and humid climate zones. The future directions that emerge from this study are given below:

a. To study the effect of low or sub-zero temperatures, which can help us predict the life of coatings in colder climates. In colder climates, water ingress in the coated layers can lead to freezing and unfreezing of the water inside the coated layer, which may significantly affect the coating life [32]. A detailed study on stressors that degrade AS-coating in colder climates will help develop new durable coatings for colder climates.

b. To study the reliability of anti-soiling coatings under arid (hot and dusty) and other climatic conditions – This would include a detailed series of indoor and outdoor accelerated stress tests. Such research will help map the life of AS-coatings under different climate zones.
c. Degradation study of hybrid coatings (anti-soiling + anti-reflective coatings).
d. Effect of water quality used for cleaning the PV modules on AS-coatings – The type of water used for cleaning the PV modules may react with the coatings and can leave permanent residue, creating cementation [95] like effects. This can be further explored to optimize the type of water suitable for cleaning PV modules.
e. To study the ecological impacts of anti-soiling coatings - Researching the ecological effects of anti-soiling coatings is crucial because coatings that contain harmful components like fluorine can lead to respiratory and flu-like symptoms when inhaled, causing damage to the lungs [96]. Therefore, it is necessary to investigate the environmental impact of new anti-soiling coatings, particularly those that contain hazardous substances. This investigation will ensure that the coatings do not have adverse effects on humans and the environment when they dissolve in water during cleaning or rain events.
f. Correlation of coating uniformity to the durability of AS-coating under different stressors – The most common deposition technique used in the AS-coating industry is via spray coating technology. This technology can lead to non-uniform deposition, depending on the spray head or technique type (automated/manual). Non-uniform coating deposition may result in higher degradation rates [32]. A detailed study on this will help us understand the importance of uniformity of the coated layer at the initial stage and how it impacts the long-term durability of AS-coatings.
g. This thesis shows a lifetime prediction study of AS-coatings considering rain and UV radiation as a stressor. This can be taken forward, and a similar study can be done by considering abrasion and water impact as a stressor. Such a database can also be used as a starting point for modelling the effect of combination of stressors to precisely predict coating life at different locations for different coating types.

Appendix

I. Supplementary data for Indoor Accelerated Stress Tests (Used in Section 7.2)

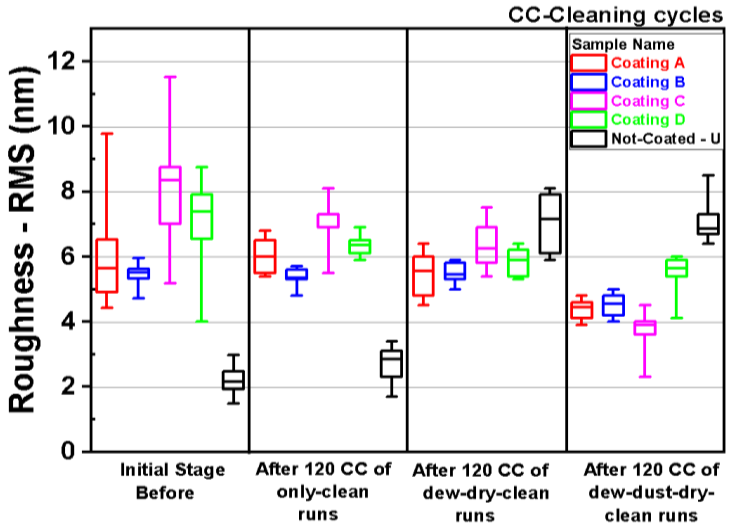

Fig. A1: Roughness of the coated (A, B, C and D) and not-coated (U) samples before and after being exposed to 120 runs of dew-dust-dry-clean cycles, dew-dry-clean cycle and only-clean cycle. Each box plot in this graph is based on10 data points.

In Fig. A1, we observe that all coated samples (A, B, C and D) show a statistically significant decrease in roughness after 120 dew-dust-dry-clean cycles. However, after 120 dew-dry-clean and only-clean cycles, the change in roughness when compared to initial state is insignificant for all coated samples (A, B, C and D). This shows that samples that underwent dew-dust-dry-clean cycles show greater abrasion damage. The not-coated samples (U) show a statistically significant increase in roughness after 120 runs of dew-dry-clean and dew-dust-dry-clean cycles.

.

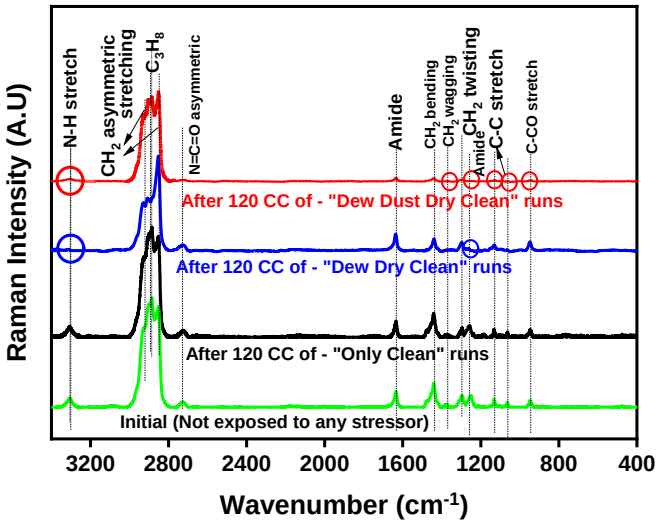

Fig. A2: Raman spectra of the brush bristles tips before and after 120 runs of dew-dust-dry-clean cycles, dew-dry-clean cycles and only-clean cycles. The missing peaks for "After 120 CC of dew-dust-dry-clean cycles" and "After 120 CC of dew-dry-clean cycle" are encircled in the graph.

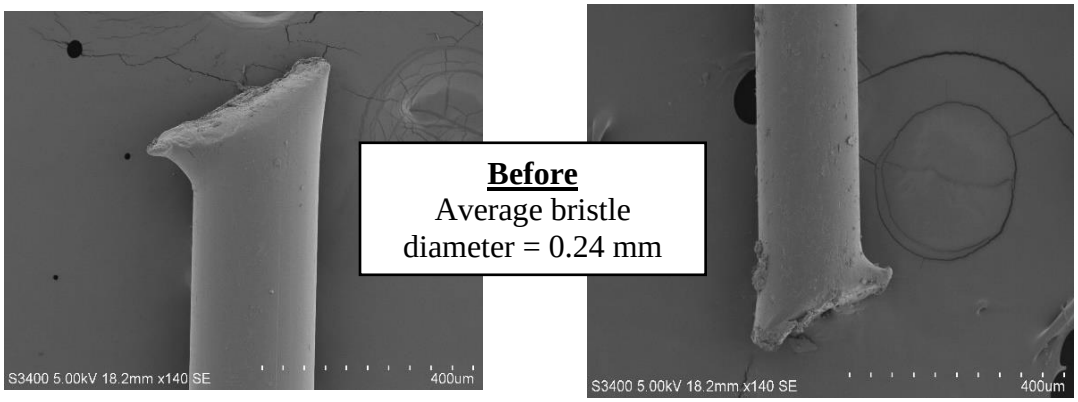

(a)

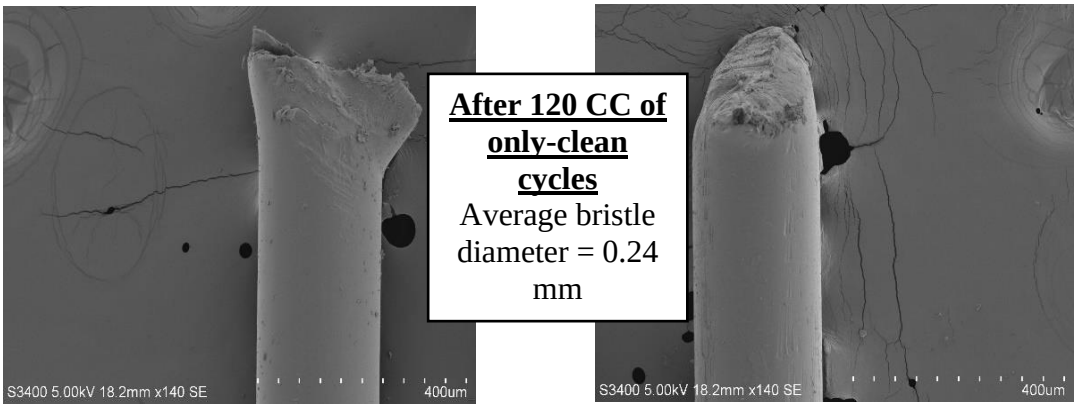

(b)

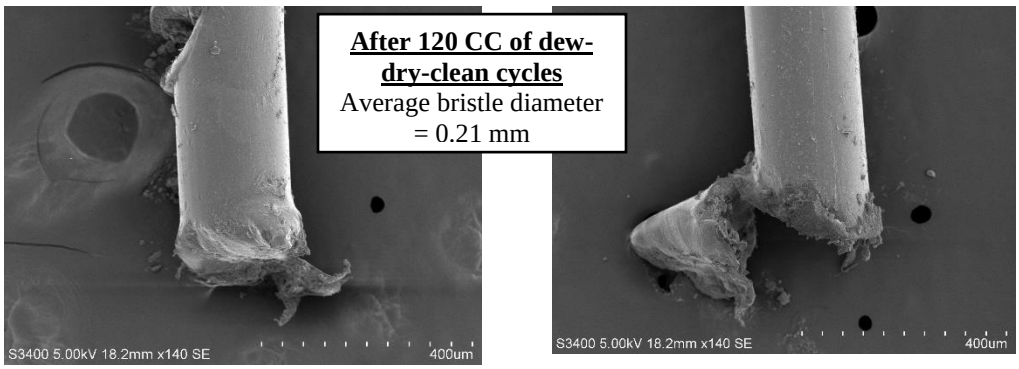

(c)

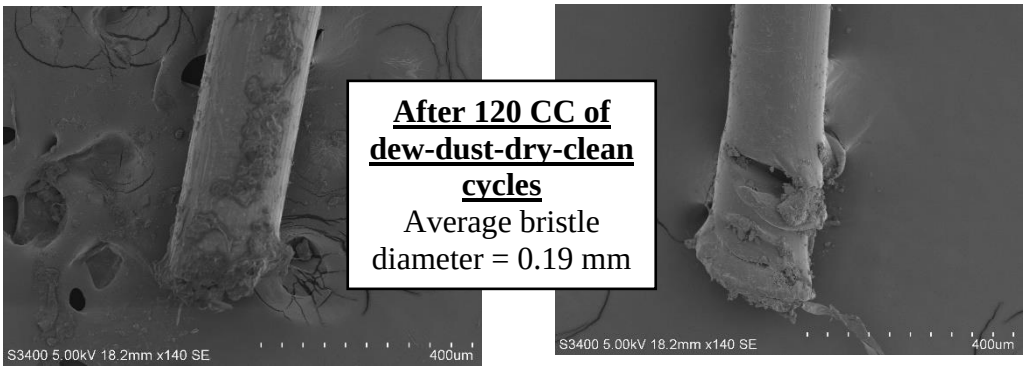

(d)

Fig. A3: Scanning electron micrographs (SEM) of the brush bristles tips (a) before abrasion, (b) after 120 CC of only-clean cycles, (c) after 120 CC of dew-dry-clean cycles and (d) after 120 CC of dew-dust-dry-clean cycles. "CC" stands for cleaning cycles. To compare the dimensions of before and after abrasion tests, an average of 5 brush bristles was taken.

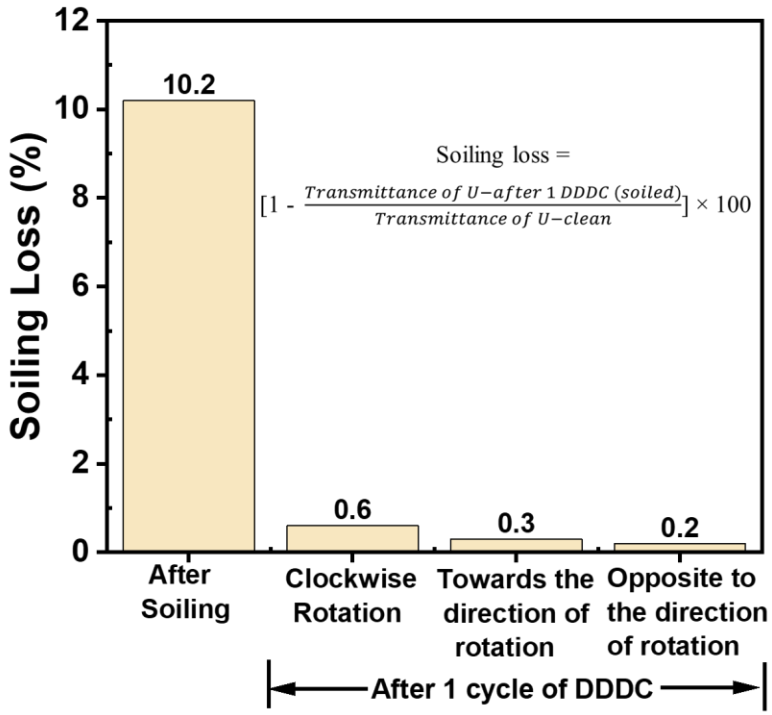

Fig. A4: Soiling loss of not-coated (U) sample before and after 1 dew-dust-dry-clean cycle (DDDC). Cleaning efficacy is calculated in terms of soiling loss, high soiling loss after 1 DDDC refers to low cleaning efficacy.

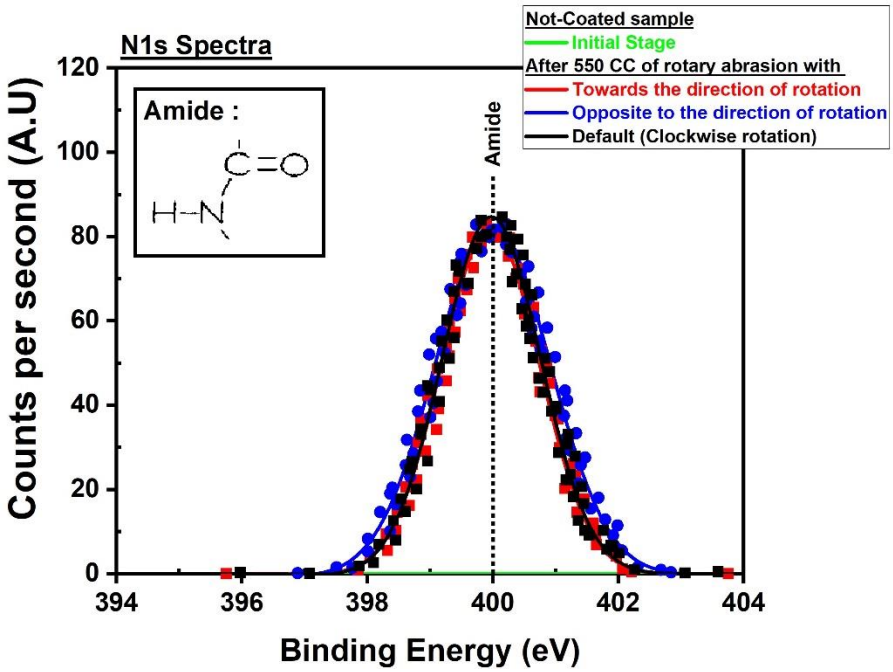

Fig. A5: N1s XPS-narrow scan of the not-coated sample before and after 550 cycles of rotary abrasion with the direction of rotation of brush as "towards the direction of travel", "opposite to the direction of travel", and "clockwise". (symbols represent the experimental data; solid lines represent the data points after smoothening done via Savitzky-Golay method [77]). "CC" refers to cleaning cycles.

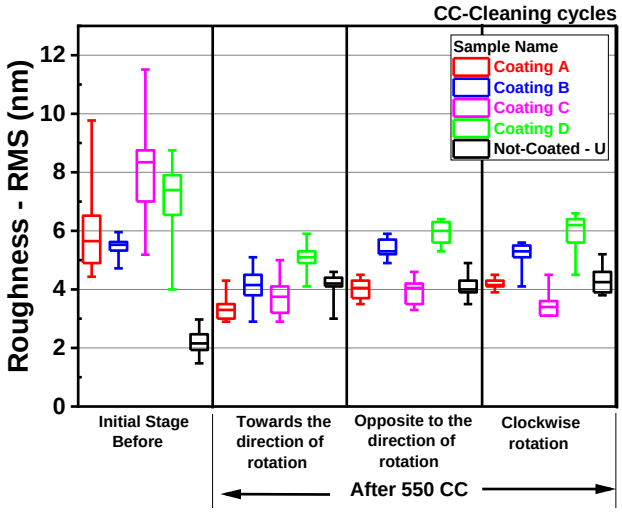

Fig A6: Roughness of coated (A, B, C and D) and not-coated (U) samples before and after 550 cycles of rotary abrasion when the direction of rotation of the brush is "towards the direction of travel", "opposite to the direction of travel" and "clockwise ". Each box plot in this graph is based on 10 data points.

In Fig. A6, all coated samples (A, B, C and D) show a statistically significant decrease in roughness after 550 cycles of rotary abrasion with the direction of rotation as "towards the direction of travel". Coated samples A and C show a statistically significant decrease in roughness after 550 cycles of rotary abrasion, irrespective of the direction of travel. This shows that coated samples that underwent rotary abrasion with the direction of rotation as "towards the direction of travel" show greater abrasion damage. The not-coated sample shows a statistically significant increase in roughness after 550 cycles of rotary abrasion, irrespective of the direction of travel.

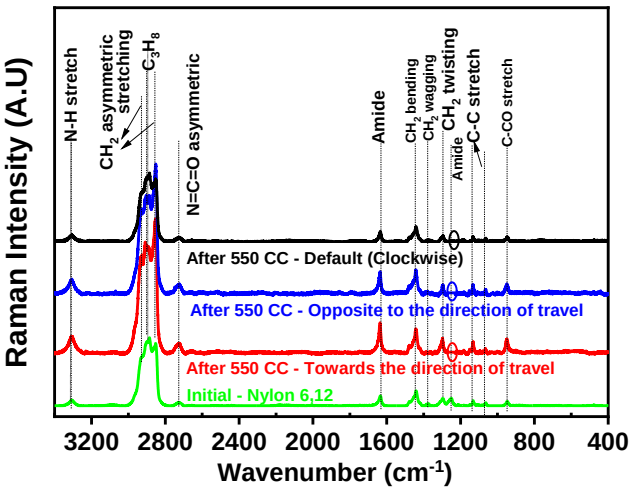

Fig. A7: Raman spectra of the brush bristles tips before and after 550 cycles of rotary abrasion when the direction of rotation of the brush is "towards the direction of travel", "opposite to the direction of travel", and "clockwise". The missing peaks for after 550 cycles of rotary abrasion when the direction of rotation of the brush is "towards the direction of travel", "opposite to the direction of travel", and "clockwise rotation" are encircled in the graph.

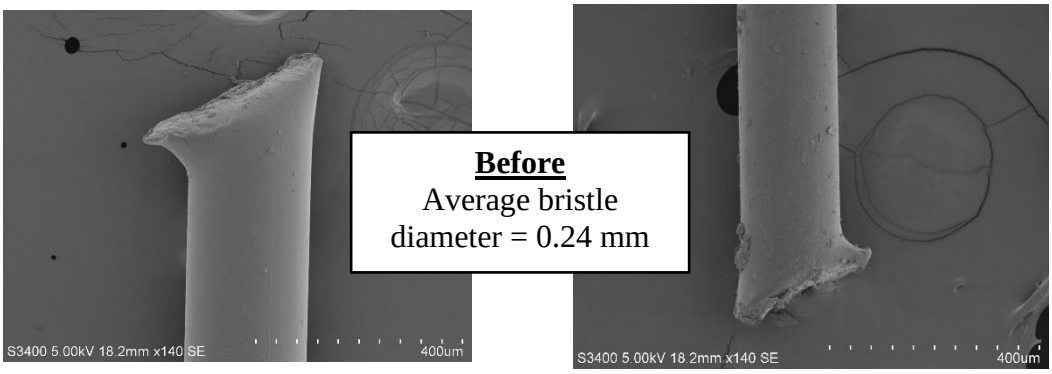
S3400 5.00kV 18.2mm x140 SE
400um
Before
Average bristle diameter = 0.24 mm
S3400 5.00kV 18.2mm x140 SE
400um

(a)

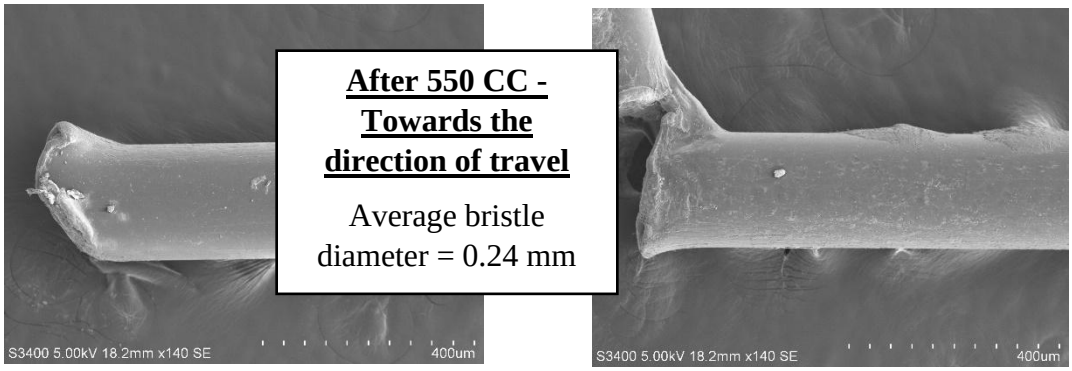
S3400 5.00kV 18.2mm x140 SE
400um
After 550 CC - Towards the direction of travel
Average bristle diameter = 0.24 mm
S3400 5.00kV 18.2mm x140 SE
400um

(b)

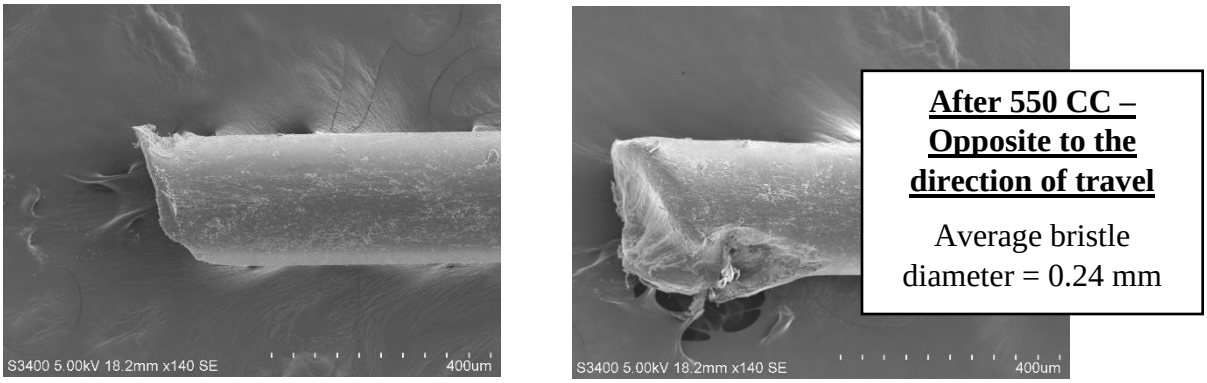
S3400 5.00kV 18.2mm x140 SE
400um
S3400 5.00kV 18.2mm x140 SE
400um
After 550 CC – Opposite to the direction of travel
Average bristle diameter = 0.24 mm

(c)

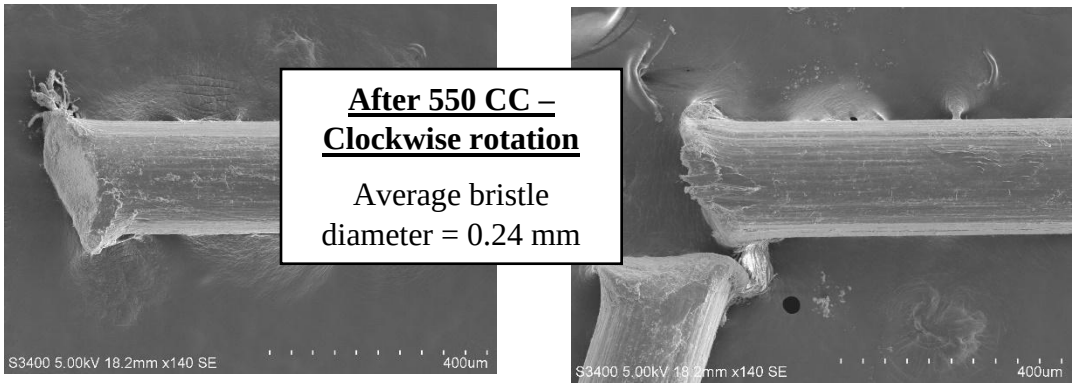

(d)

Fig. A8: Scanning electron micrographs (SEM) of the brush bristles (a) before abrasion tests, and after 550 cycles of rotary abrasion with the direction of rotation of the brush as (b) towards the direction of travel, (c) opposite to the direction of travel and (d) clockwise. "CC" stands for cleaning cycles. To compare the dimensions of before and after abrasion tests, an average of 5 brush bristles was taken.

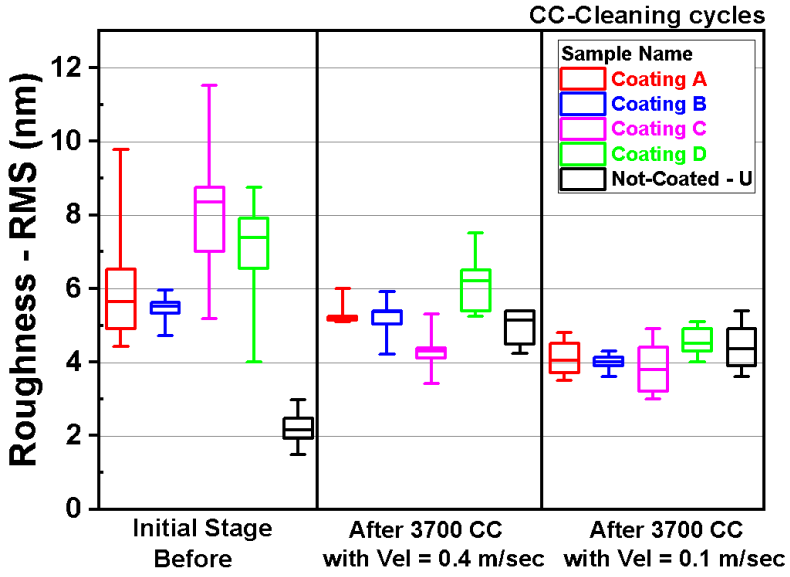

Fig. A9: Roughness of the coated (A, B, C and D) and not-coated (U) samples before and after 3700 cycles of rotary abrasion, cleaned at two different horizontal velocities of brush travel (1) 0.4 m/sec and (2) 0.1 m/sec. Each box plot in this graph is based on 10 data points.

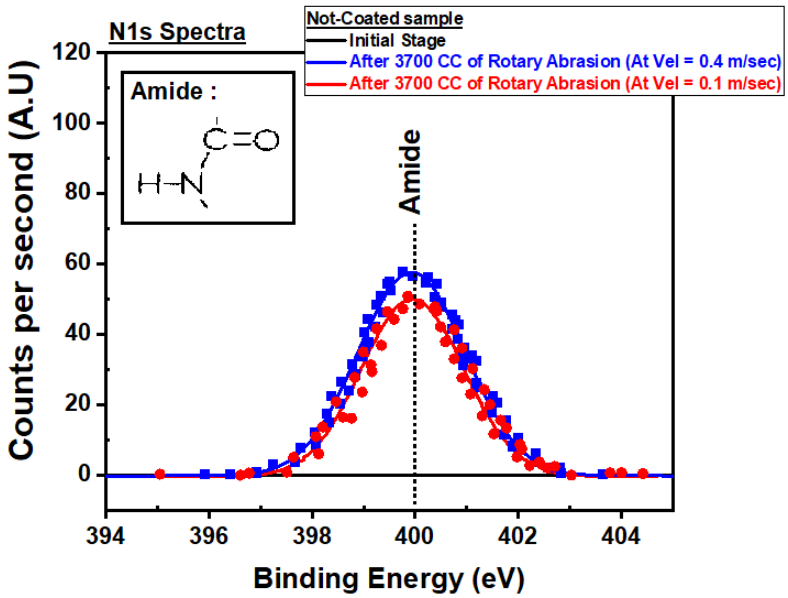

Fig. A10: N1s XPS-narrow scan of the not-coated sample before and after 3700 cycles of rotary abrasion, cleaned at two different horizontal velocities of brush travel (1) 0.4 m/sec and (2) 0.1 m/sec. (symbols represent the experimental data; solid lines represent the data points after smoothening done via Savitzky-Golay method [77]). "CC" refers to cleaning cycles.

All coated samples (A, B, C and D) show a statistically significant decrease in roughness after 3700 cycles of rotary abrasion when cleaned at a velocity of 0.1 m/sec (shown in Fig. A9). Coating C shows a statistically significant decrease in roughness after 3700 cycles of rotary abrasion when cleaned at a velocity of 0.4 m/sec and 0.1 m/sec. This shows that all coated samples show greater abrasion damage after being cleaned at a velocity of 0.1 m/sec. Not Coated show a statistically significant increase in roughness after 3700 cycles of rotary abrasion when cleaned at a velocity of 0.4 m/sec and 0.1 m/sec.

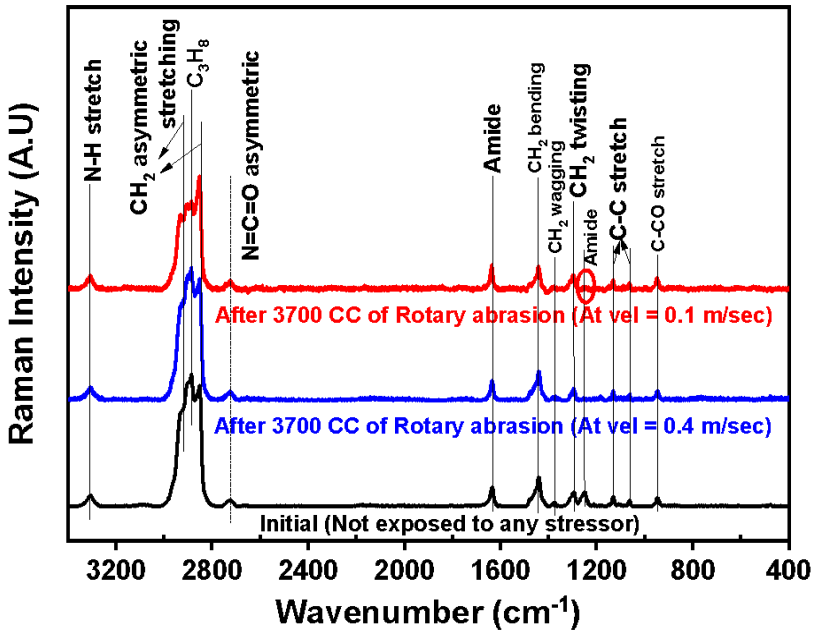

Fig. A11: Raman spectra of the brush bristles tips before and after 3700 cycles after 3700 cycles of rotary abrasion cleaned at two different horizontal velocities of brush travel (1) 0.4 m/sec and (2) 0.1 m/sec. The missing peaks for "After 3700 CC of rotary abrasion at velocity 0.1 m/sec" are encircled in the graph.

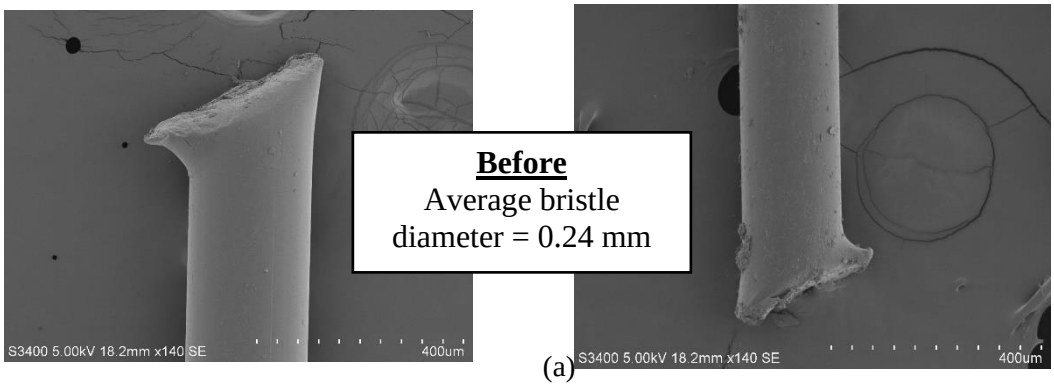

(a)

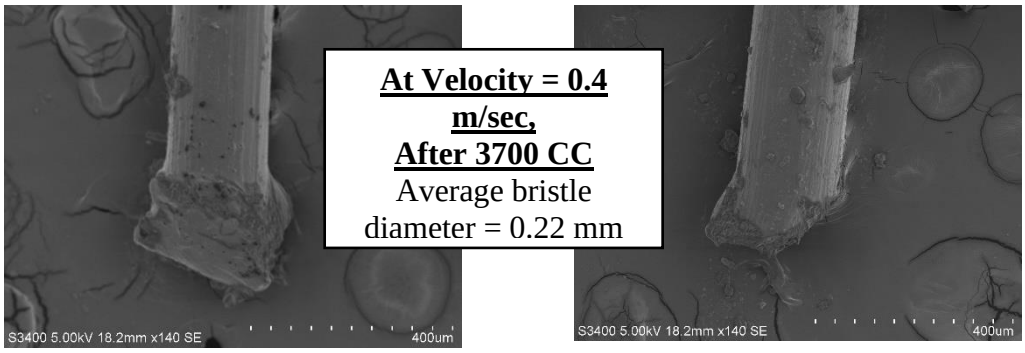

(b)

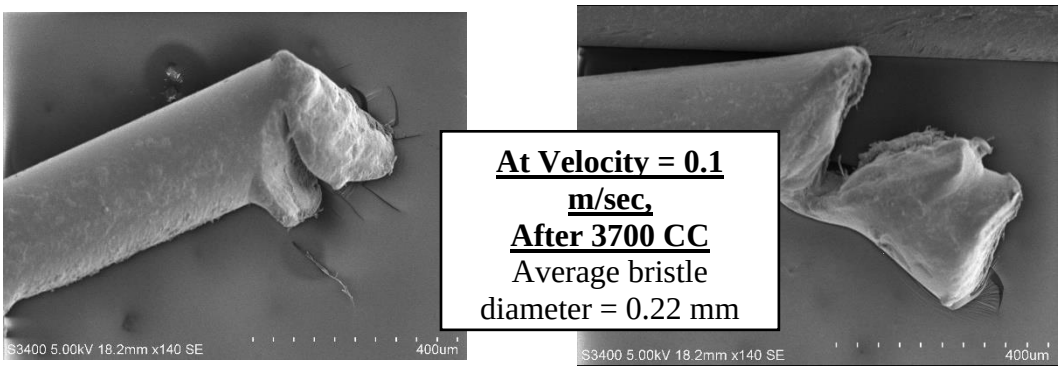

(c)

Fig. A12: Scanning electron micrographs (SEM) of the brush bristles (a) before abrasion tests and after 3700 cycles of rotary abrasion cleaned at two different horizontal velocities of brush travel (b) 0.4 m/sec and (c) 0.1 m/sec. "CC" stands for cleaning cycles. To compare the dimensions of before and after abrasion tests, an average of 5 brush bristles was taken.

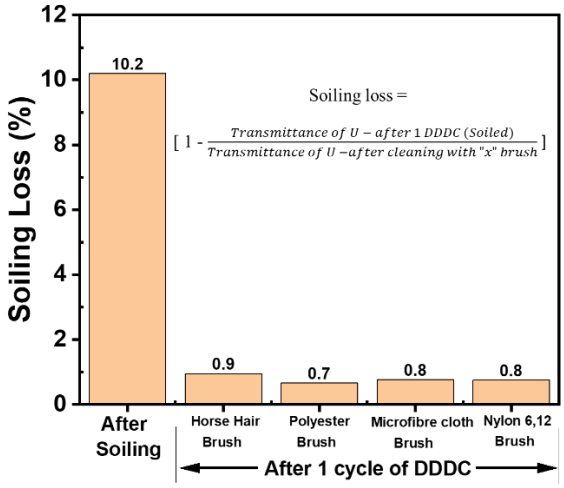

Fig. A13: Soiling loss of not-coated (U) sample before and after 1 dew-dust-dry-clean cycle (DDDC), after being cleaned via Microfibre cloth brush, Nylon 6,12 brush, Brush B, and Brush A. Cleaning efficacy is calculated in terms of soiling loss, high soiling loss after 1 DDDC refers to low cleaning efficacy.

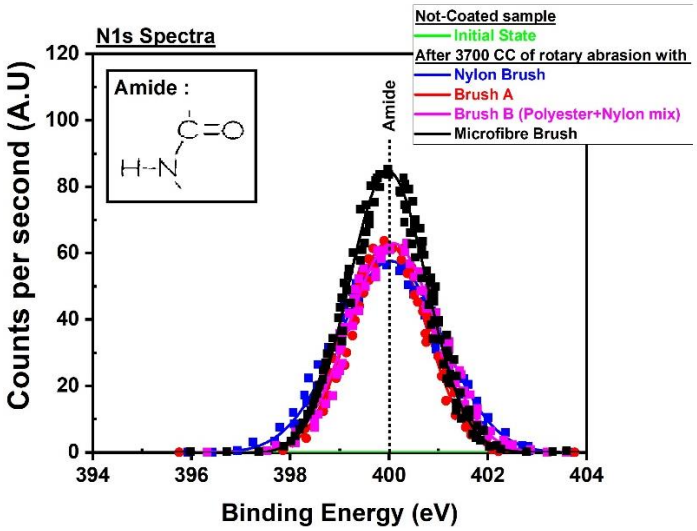

Fig. A14: N1s XPS-narrow scan of the not-coated sample before and after exposure to 3700 cycles with Brush A, Nylon 6,12, Brush B (Polyester + Nylon mix), and a Microfibre cloth brush (symbols represent the experimental data; solid lines represent the data points after smoothening done via Savitzky-Golay method [77]). "CC" refers to cleaning cycles.

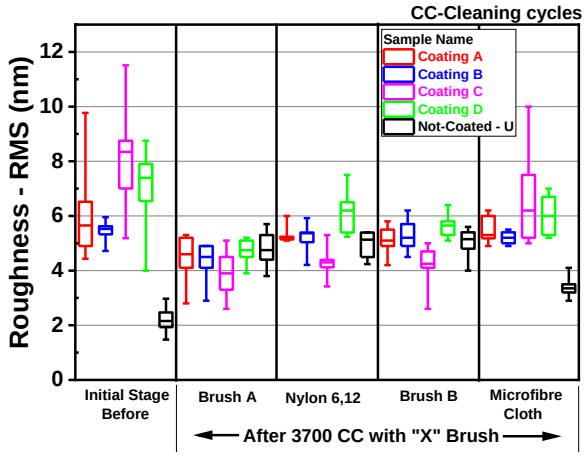

Fig. A15: Roughness of the coated (A, B, C and D) and not-coated (U) samples before and after being exposed to 3700 cycles with Brush A, Nylon 6,12, Brush B and Microfiber cloth brush. Each box plot in this graph is based on 10 data points.

All coated samples (A, B, C and D) show a statistically significant decrease in roughness after 3700 cycles of rotary abrasion with Brush A (shown in Fig. A15). Coating C shows a statistically significant decrease in roughness after 3700 cycles of rotary abrasion with Brush A, Nylon 6,12 and Brush B. This shows that all coated samples which underwent rotary abrasion via Brush A show greater abrasion damage than the other brush materials. Not-coated sample shows a statistically significant increase in roughness after 3700 cycles of rotary abrasion with Brush A, Nylon 6,12, Brush B and Microfiber cloth brush.

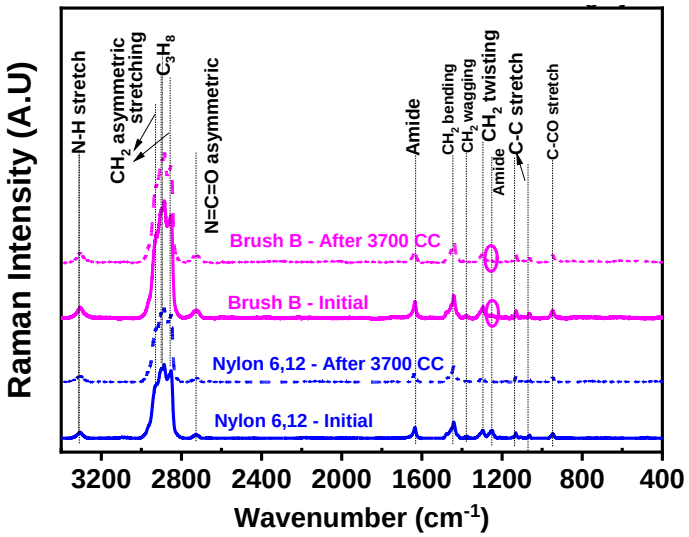

Fig. A16: Raman spectra of the brush bristles tips before and after being exposed to 3700 cycles with Brush A, Nylon 6,12 and Brush B (Polyester + Nylon mix).

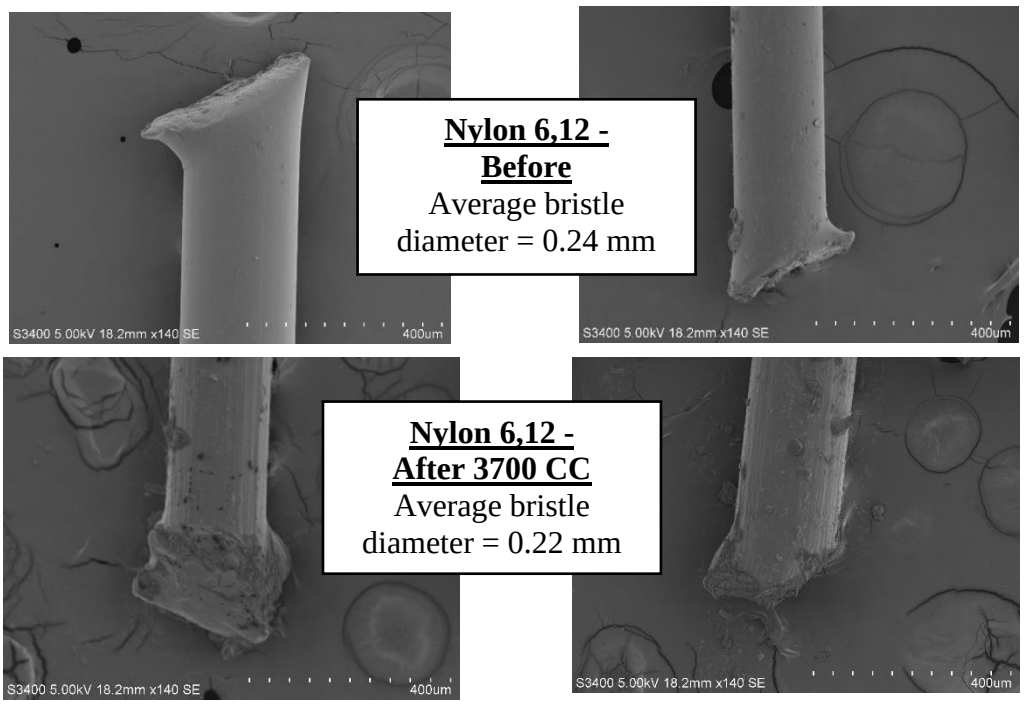

(a)

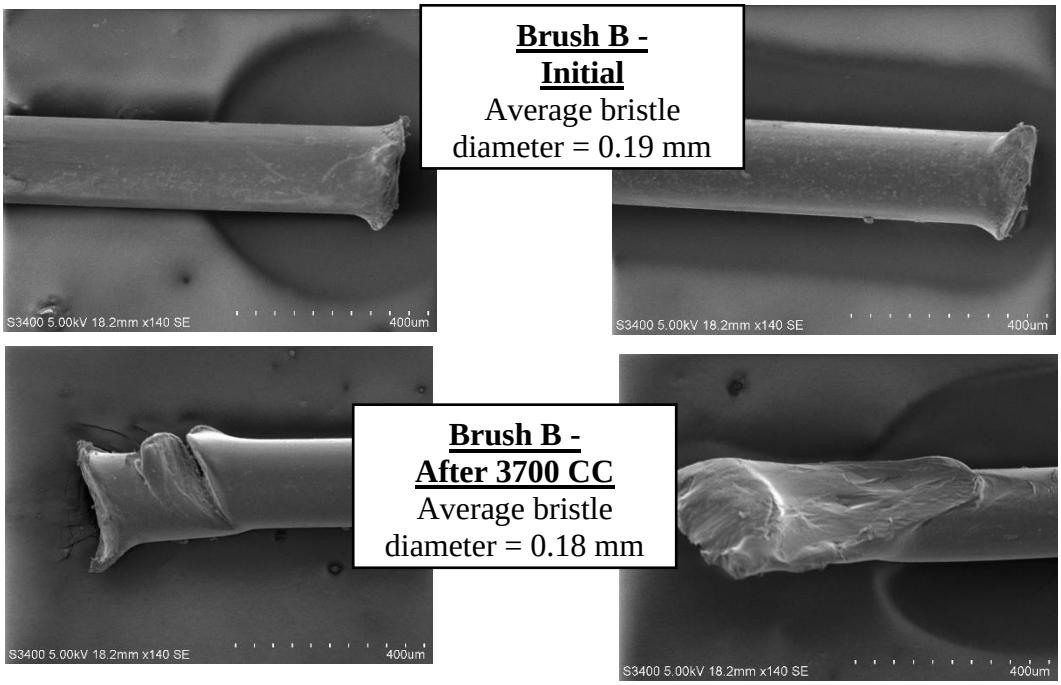

(b)

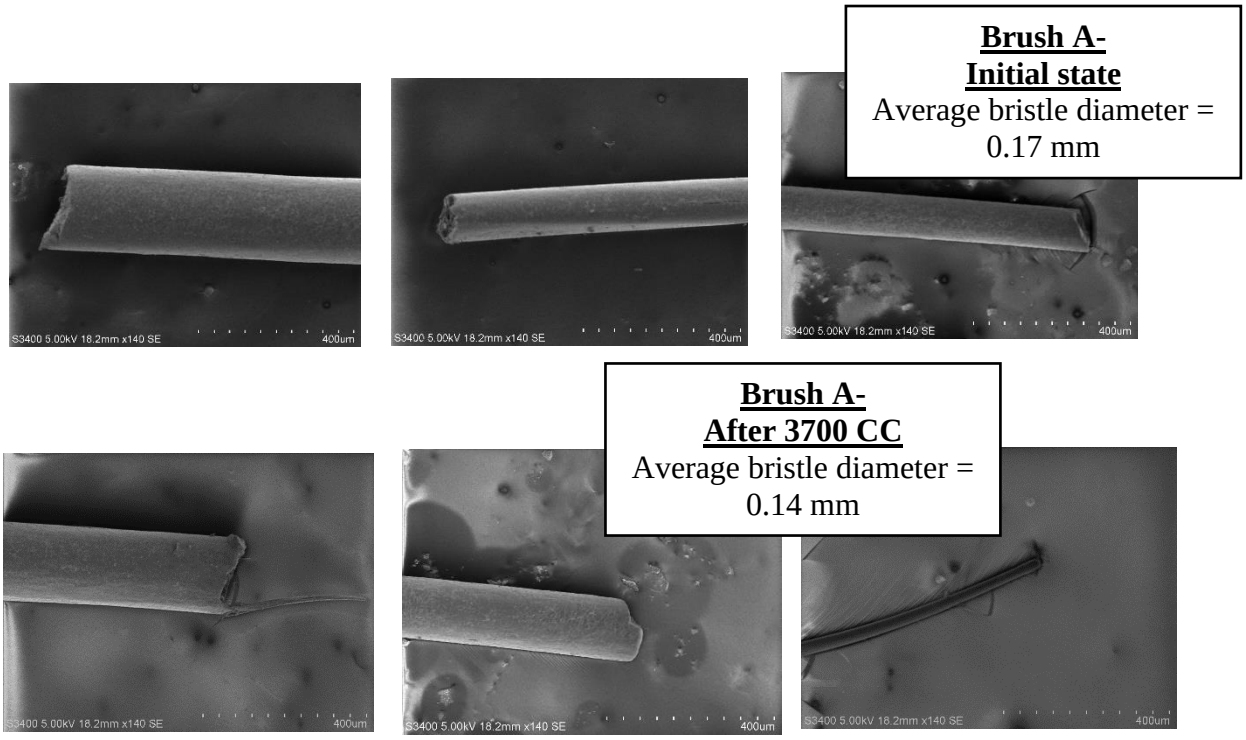

(c)

Fig. A17: Scanning electron micrographs (SEM) of the brush bristles (a) before abrasion tests and after exposure to 3700 cycles with Nylon 6,12 brush, (b) before abrasion tests and after exposure to 3700 cycles with Brush B and (c) before abrasion tests and after exposure to 3700 cycles with Brush A. "CC" stands for cleaning cycles. To compare the dimensions of before and after abrasion tests, an average of 5 brush bristles was taken.

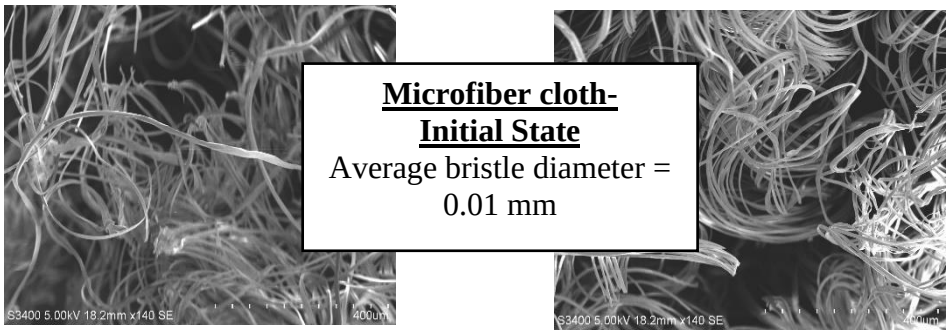

Fig. A18: Brush bristles of the Microfiber cloth brush at its initial state (Since the fibres are approximately 10 µm in diameter, it was impossible to identify the exact location after 3700 cycles). "CC" stands for cleaning cycles. The average diameter of 5 brush bristles is shown in Fig.

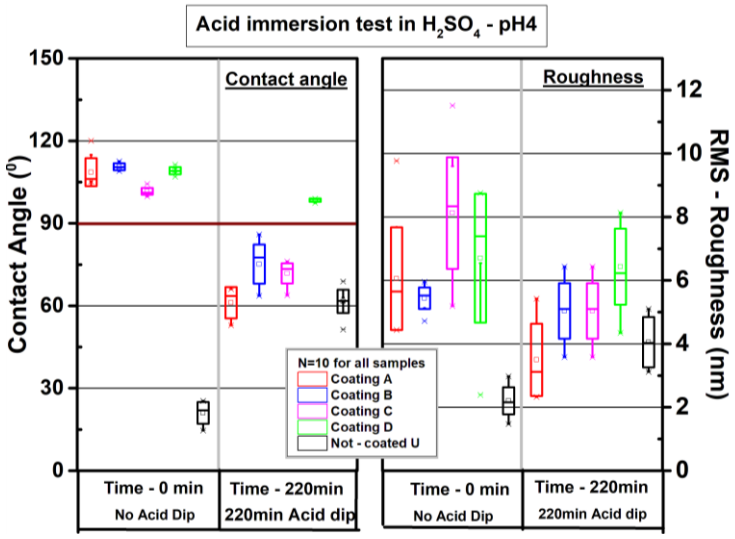

Fig. A19: Contact angle (left) and RMS roughness (right) of coated and not-coated glass samples before and after 220 min of acid immersion.

To emulate the composition of acid rain in Mumbai, dilute H_2SO_4 with pH4 was used [69]. All samples were immersed in the acid solution for 220 min at room temperature. A statistically significant decrease in contact angle was observed for all the coatings (Fig. A19). Roughness also showed a statistically significant decrease for all coated samples except coating B and D. Not-coated samples also showed a difference in roughness after acid immersion. This is likely due to etching of Na from the glass surface [66].

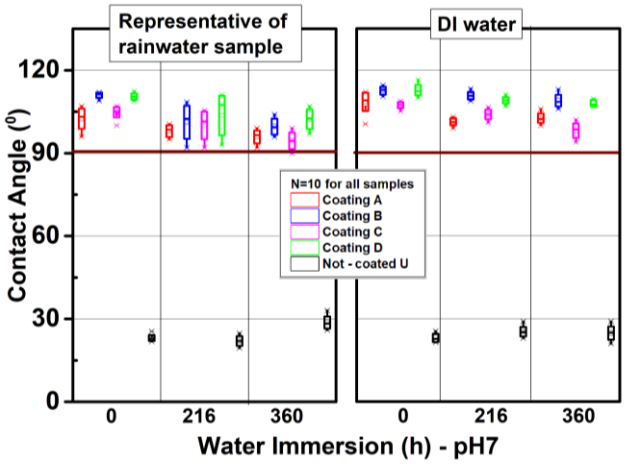

Fig. A20: Contact angle of coated and not coated samples with an increase in water immersion time (pH 7 water and DI water) at 50ºC.

Water Immersion test was done to understand the effect of water contact on coated samples at module operating temperature [72]. This was a more severe test than condensation, where streams of water flow through the sample at 50℃. This may also emulate the effect of rainfall at pH -7. However, it will not take into account the pressure/abrasion caused by the force of water hitting the surface. Water immersion test was done with two water sources. The water source representative of the rainwater had pH 7, and elemental composition was similar to the rainwater sample collected in IIT - Bombay described in section 7.1.2) and DI water. Here coated and not-coated samples were immersed in water and kept at hot air oven at 50℃.

In Fig. A20, we observe that the water immersion test (representative of rainwater sample in IIT - Bombay and DI water) show a statistically significant decrease in contact angle; however, the rate of change in contact angle is considerably small. All coated samples are hydrophobic after 360 hours of water immersion.

II. A Proposal for Test Procedure for Evaluation of Anti-Soiling Coatings

The learning from chapter 4 to chapter 8 was used to develop a proposal for the test procedure for the evaluation of AS-coatings. This test procedure can act as a baseline for testing the commercially available AS-coatings and will also facilitate the development of new durable coatings. The industry associates can use this test procedure to check the reliability of anti-soiling coatings with minimum time and resources.

(1) Scope and Objective

This testing procedure lays down requirements for the long-term reliability of anti-soiling coatings under field conditions. These tests are only relevant for anti-soiling coatings, which are applied to the PV glass (outermost front surface of the PV module). This test procedure is not a universal testing document. This test sequence is established on the timelines, testing equipment and total duration mentioned in chapters 4, 6, 7 and 8. The test sequences mentioned in this Appendix II are based on the data and resources used for our sample set (4 different hydrophobic ASC).

These test sequences aim to determine the characteristic property of the coatings and show with a minimum cost and time that the coating can withstand exposure to different stressors/climates mentioned in the testing sequence. This testing sequence will not give information about the lifetime of the coatings, as it depends on environmental factors and operating conditions.

(2) Sampling

The procedure for pre-cleaning the solar glass coupons/PV module and applying anti-soiling coating must be done per the manufacturer's instruction manual.

Small glass coupons - For every individual sample, the measurements must be performed at least at ten different locations before and after each test sequence. The locations should be marked to ensure that the before and after measurements are performed exactly at the same location. This is for creating a statistically significant data set. The glass coupons must be at least 2.5 cm × 2.5 cm in size. (The size requirement is built on the characterization tools available in IIT Bombay and NCPRE).

(3) Marking

Each sample should be marked with a serial number with detailed traceable information. The serial number should have the following information in code/complete name and numbers.

1. Type of the AS-Coating (material type).
2. Name of the AS-Coating.
3. Deposition technique of AS-Coating.
4. Date of manufacturing of AS-Coating.
5. The characterization location should be marked at the backside of each solar glass sample.

(4) Pass Criteria

Note: The pass criteria used in this test procedure are taken from the work done in chapters 4, 5, 6, 7 and 8 on the degradation of anti-soiling coatings.

Samples will be judged to have passed the test sequence if the coated samples show a statistically insignificant change in the characteristic property (contact angle, roll-off angle transmittance and reflectance) before and after the test sequence. The detailed pass criteria for each test are mentioned in their respective sections. The non-parametric Wilcoxon signed-rank test will be used for testing the statistical significance [52].

If the coated samples change their wetting property (i.e. hydrophobic to hydrophilic or hydrophilic to hydrophobic) after any test sequence, it will be considered as fail.

Roll-off angle is only relevant for hydrophobic coatings. If the roll-off angle is less than the tilt angle after the test sequence, it will be considered as pass.

Wilcoxon Signed rank test [52] – The Wilcoxon signed-rank test is used to identify if the difference between samples before and after the experiment is statistically significant. p-values obtained by the Wilcoxon signed-rank test, < 0.05, were considered to be statistically significant, with a confidence interval of 95%.

(5) Summary of Test Procedures

Following is the summary of the test procedures. The summary only provides critical test methodologies. A detailed description of all test sequences is provided in Appendix II (6).

Important Note: The timelines, testing equipment and total duration mentioned here are based on the data and resources used for our sample set (4 different hydrophobic ASC).

Test	Title	Test Condition
(I)	Rain test (Two-part test)	Part 1 – Mechanical impact of rainfall test (pH 7 water sample) Samples are exposed to rainfall simulator (pH of water – 7) with a rainfall intensity of 21 mm/h. The velocity of droplets hitting the sample surface is 7.3 m/s. The test will be conducted till 2000 mm of precipitation. Part 2 - Mechanical impact of acidic rainfall (pH 6 water sample) Samples are exposed to rainfall simulator with acidic water (pH 6, Diluted with Sulphuric acid), rainfall intensity of 21 mm/h. The velocity of droplets hitting the surface is 7.3 m/s. The test will be conducted till 2000 mm of precipitation. For Part 1 and 2 - To study the rate of degradation, at least 10 measurement intervals of contact angle, roll-off angle, transmittance and reflectance are to be done throughout the complete experiment.
(II)	Abrasion test (Two-part test)	Part 1 – This emulates 25 years of cleaning cycles, emulating a low/zero-soiling location. Cleaning cycles of to and fro motion is run on clean coated and not coated sample. Each cleaning cycle consists of cooling (Substrate temperature = 21 ^{0}C, Relative humidity = 52% and Air temperature = 30 ^{0}C) for 3 mins, followed by heating for 3 mins (Substrate temperature is 65 ^{0}C) and then cleaning (one set of to and fro motion) at 25 ^{0}C. (Cooling + heating + cleaning) × 1300 cycles Part 2 – This emulates 25 years of cleaning cycles, emulating a high soiling location. Cleaning is done after 2 weeks of soiling. The soiling rate of the area is assumed to be 0.4 %/day.

		Cleaning cycles of to and fro motion is run on dust deposited sample. Each cleaning cycle consists of cooling (Substrate temperature = 21 ^{0}C, Relative humidity = 52% and Air temperature = 30 ^{0}C) for 3 mins, followed by dry dust deposition of 0.2 mg/cm^2 (~two weeks of dust deposition in Mumbai), followed by heating for 3 mins (Substrate temperature is 65 ^{0}C) and then cleaning (one set of to and fro motion) at 25 ^{0}C. (Cooling + dust deposition + heating + cleaning) × 650 cycles For Part 1 and 2 – To study the rate of degradation, at least 10 intermediate measurements of contact angle, roll-off angle, transmittance, and reflectance are to be done throughout the complete experiment.
(III)	Combination of UV, rain and abrasion test (Optional - Due to the high cost of testing samples in UV chamber)	The samples are exposed to a combination of cleaning cycles, UV exposure and rainfall – The test is to be followed sequentially. 1. Samples are exposed to cleaning cycles. Each cleaning cycle consists of cooling (Substrate temperature = 21 ^{0}C, Relative humidity = 52% and Air temperature = 30 ^{0}C) for 3 mins, followed by dry dust deposition of 0.2 mg/cm^2 (~ two weeks of dust deposition in Mumbai), followed by heating for 3 mins (Substrate temperature is 65 ^{0}C) and then cleaning (one set of to and fro motion) at 25 ^{0}C. (Cooling + dust deposition + heating + cleaning) × 650 cycles 2. Samples are exposed to acidic (pH 6) rainfall, with a rainfall intensity of 21 mm/h for 1 h. The velocity of water droplets hitting the surface is 7.2 m/s. 3. The samples are then exposed to UV exposure (UV 365 nm) at 65 ^{0}C, with a total dose of 5 kWh/m^2. The intensity of the UV radiation was fixed at 203 W/m^2 [Abrasion + Rain + UV exposure] × 10 cycle

		To study the degradation rate, at least 10 intermediate measurements of contact angle, roll-off angle, transmittance, and reflectance are to be done throughout the experiment.

(6) Test Procedure

Important Note: The timelines, testing equipment and total duration mentioned here are based on the data and resources used for our sample set (4 different hydrophobic ASC).

(A) Rain Test

Purpose – To verify that the anti-soiling coating can withstand a rainfall event of 2000 mm of precipitation. This test can be done only on small solar glass samples/mini modules (Minimum size – 2.5 cm × 2.5 cm).

Apparatus –

Rain simulator (built In-house at NCPRE, IIT Bombay), Contact angle measurement tool (Make and Model - Data Physics OCA 15SEC, accuracy ± 0.1°), Roll-off angle set up (build in-house at NCPRE – IIT Bombay, accuracy $\pm 1^0$), Transmittance and reflectance (UV-Vis-NIR Spectrometer - Lambda 950)

Procedure

(A.I) Mechanical impact of rainfall test, pH 7 water sample

1. Clean the bare solar glass samples with IPA (Isopropyl alcohol) to remove contamination.
2. Apply the anti-soiling coating to the not-coated samples according to the application manual of the product (given by the manufacturer). For comparisons, also take a not-coated sample for the complete test sequence. After the coating application process is complete, take a visual image with a DSLR camera of the coated and not coated samples under proper lighting to ensure that no white residue is formed.
3. Measure the transmittance and reflectance (at 3 locations within each sample) of the coated and not-coated samples.

4. Measure contact angle and roll-off angle at ten areas in each sample. Mark the areas where the measurements are done. Ensure that all other characterizations are done on the marked area.

5. Expose the samples in rainfall simulator with a rainfall intensity of 21 mm/h. The velocity of droplets hitting the surface should be 7.3 m/s. The water used in the rainfall simulator should be pH 7. The rainfall parameters are representative of actual field conditions [68], [69].

6. Measure the contact angle, roll-off angle, transmittance (at three locations) and reflectance (at three locations) at ten areas of all samples after every 6 hrs (126 mm of precipitation) of exposure. The location of the measurement should be the same as in Appendix II (A.I), point 4.

Before characterization (contact angle, transmittance, reflectance, and roll-off angle), the samples must be cleaned with DI water and lint-free cloth to remove all contaminations**.**

Pass criteria:

- After the completion of the experiment, if the coated samples show the same wetting (hydrophobic or hydrophilic) property as its initial (before exposure) stage, then the coated sample would pass the test sequence.
- After completing the test sequence, If the sample shows lower transmittance and higher reflectance than the not-coated samples, the coated samples would be considered as a failure.
- After completing the test sequence, If the roll-off angle of the sample is higher than the tilt angle of the required location, the coated sample would be considered as a fail.

Passing this test sequence indicate that the coated sample can withstand the exposure to the mechanical impact of rainfall of 2000 mm of precipitation (pH 7) under room temperature.

(A.II) Mechanical impact of acidic rainfall, pH 6 water sample

1. Follow steps 1 to 4 of Appendix II (A.I) on not-coated samples.

2. Expose the samples in rainfall simulator with a rainfall intensity of 21 mm/h. The velocity of the water droplet hitting the surface is 7.3 m/s. In this test, the water used in the rainfall simulator should be pH 6. Diluted sulphuric acid should be used to make the water acidic.

3. Measure the contact angle, roll-off angle, transmittance (at three locations) and reflectance (at three locations) at ten areas of all samples after every 6 hrs (126 mm of precipitation) of exposure. The location of the measurement should be the same as in Appendix II (A.I), point 4.

Before characterization (contact angle, transmittance, reflectance and roll off-angle), the samples must be cleaned with DI water and lint-free cloth to remove all contaminations**.**

Pass criteria:

Follow the pass criteria given in Appendix II (A.I).

Passing this test sequence indicate that the coated sample can withstand the mechanical impact of rainfall of 2000 mm of precipitation (when the rainwater is of pH 6) at room temperature.

(B) Abrasion Test

Purpose – To verify that the coated samples can withstand abrasion damage caused by frequent cleaning for 25 years. This test can be done only on small solar glass samples of size 2.5 cm × 2.5 cm (minimum size).

Apparatus –

Cleaning cycle simulation (build In-house at NCPRE, IITB), Nylon 6,12 rotary brush, Contact angle measurement tool (Make and Model - Data Physics OCA 15SEC, accuracy ± 0.1 °), Roll-off angle set up (build in-house at NCPRE – IIT Bombay, accuracy $\pm 1^0$), Transmittance and reflectance (*UV*-*Vis*-NIR Spectrometer - Lambda 950).

Procedure

(B.I) Abrasion test without dust deposition cycles - emulating a low soiling location.

1. Follow steps 1 to 4 of Appendix II (A.I) on not-coated samples.

2. Run cleaning cycles of to and fro (scrubbing in forward and reverse direction) motion on all samples.

3. Each cleaning cycle must consist of cooling (Substrate temperature = 21 ^{0}C) for 1 min, followed by heating for 1 min (Substrate temperature is 65^{0}C) and then cleaning (one set of to and fro motion).

4. After every 100 cleaning cycles, measure the contact angle, roughness, transmittance (at 3 locations), reflectance (at three locations) and roll-off angle at ten areas of all samples. The location of the measurement should be the same as in Appendix II (A.I), point 4.

Before characterization (contact angle, transmittance, reflectance and roll off-angle), the samples must be cleaned with DI water and lint-free cloth to remove all contaminations**.**

Pass criteria:

Follow the pass criteria given in Appendix II (A.I).

By doing this test, we can analyse the number of cycles the coated sample can withstand when exposed to a low-soiling location.

(B.II) Abrasion test with dust deposition cycles - emulating a high soiling location

1. Follow steps 1 to 4 of Appendix II (A.I) on not-coated samples.

2. Run cleaning cycles of to and fro motion on all dust deposited samples.

3. Each cleaning cycle consists of cooling (Substrate temperature = 21^{0}C) for 1 min, followed by dry dust deposition [51] of 0.2 mg/cm^2 (two weeks of dust deposition in Mumbai), followed by heating for 1 min (Substrate temperature is 65 ^{0}C) and then cleaning (one set of to and fro motion).

4. After every 50 cleaning cycles, measure the contact angle, roughness, transmittance (at 3 locations), reflectance (at 3 locations) and roll-off angle at 10 areas of all samples. The measurement's location should be the same as in Appendix II (A.I), point 4.

Before characterization (contact angle, transmittance, reflectance and roll off-angle), the samples must be cleaned with DI water and lint-free cloth to remove all contaminations**.**

Pass criteria:

Follow the pass criteria given in Appendix II (A.I).

By doing this test, we can analyse the number of cycles the coated sample can withstand when exposed to a high soiling location.

(C) Combination of UV, Rain and Abrasion Tests

Purpose – To verify that the coated sample can withstand a combination of exposure to UV radiation, rain and abrasion. In outdoor conditions, stressors act concurrently. By analysing the combination of significant stressors, we can understand the degradation rates under worst-case scenarios relevant to field conditions.

Apparatus –

Cleaning cycle simulation (built In-house at IITB), Rain simulator (built In-house at IITB), Weighing machine, Contact angle measurement tool (Make and Model - Data Physics OCA 15SEC, accuracy ± 0.1°), Roll-off angle set up (build in house at NCPRE – IIT Bombay, accuracy $\pm 1^0$), UV chamber (Average UV intensity - 203 W/m^2, at 365nm wavelength), Transmittance and reflectance (UV-Vis-NIR Spectrometer - Lambda 950).

Procedure

1. Follow steps 1 to 4 of Appendix II (A.I) on not-coated samples.
2. Expose all samples to cleaning cycles. Each cleaning cycle consists of cooling (Substrate temperature = 21^0C) for 1 min, followed by dry dust deposition [51] of 0.2 mg/cm^2 (two weeks of dust deposition in Mumbai), followed by heating for 1 min (Substrate temperature is 65 ^{0}C) and then cleaning (one set of to and fro motion).
3. Then expose the samples to an acidic (pH 6) rainfall (in a rainfall simulator) with a rainfall intensity of 21 mm/h for 9 h (189 mm of precipitation). The velocity of droplets hitting the surface is 7.3 m/s. The water used in the rainfall simulator should be of pH 6 (dilute solution of H_2SO_4).
4. Expose the samples to UV radiation at 65^0C for 24 h (equivalent to UV dose of 5 kWh/m^2).
5. Measure the contact angle, roughness, transmittance (at 3 locations), reflectance (at 3 locations) and the roll-off angle at 10 areas of all samples. The measurement's location should be the same as Appendix II (A.I), point 4.

6. Repeat steps 2 to 5 (from C, Procedure) in cycles for 10 times.

Before characterization (contact angle, transmittance, reflectance and roll off-angle), the samples must be cleaned with DI water and lint-free cloth to remove all contaminations**.**

Pass criteria:

Follow the pass criteria given in Appendix II (A.I).

By doing this test, we can analyse the number of cycles the coated sample can withstand exposure to combination of UV, rain, and abrasion.

(7) Test Report

a) A test report shall be prepared containing the following minimum information:

b) Title of the report

c) Name and address of the test laboratory and location where the tests were carried out

d) Unique identification of the report

e) Name and address of the client

f) Description and identification of the item tested, including the specimen size

g) Date of receipt of test item and date(s) of the test

h) Characterization details and condition of the test item, including sample orientation,

i) Equipment details (Make and model), method (if applicable) and abrasive used

j) The severity of exposure (including the mass of dust, test duration, or number of test cycles)

k) Specimen history (e.g., before or after testing in a sequence, if applicable)

l) Reference to sampling procedure, where relevant

m) Any deviations from, additions to, or exclusions from, the test method and any other information relevant to a specific test

n) Measurements, examinations, and derived results supported by tables, graphs, sketches and photographs as appropriate

o) Signature and title, or equivalent identification of the persons accepting responsibility for the content of the report, and the date of issue

p) Where relevant, a statement to the effect that the results relate only to the items tested;

A statement that the report shall not be reproduced except in full without the written approval of the laboratory.

Publications

Journal Publications Related to this Thesis Work

1. **Sonali Bhaduri**, Sudhanshu Mallick, Narendra Shiradkar, and Anil Kottantharayil, Characterization of reliability of anti-soiling coatings using tapping mode-AFM phase imaging, *Journal of Renewable and Sustainable Energy*, vol. 13, pp 023702, 2021. DOI: 10.1063/5.0039255

2. **Sonali Bhaduri** and Anil Kottantharayil, "Mitigation of Soiling by Vertical Mounting of Bifacial Modules," *IEEE J. Photovoltaics*, vol. 9, no. 1, pp. 240–244, 2019. DOI: 10.1109/JPHOTOV.2018.2872555.

3. **Sonali Bhaduri**, Ajeesh Alath, Sudhanshu Mallick, Narendra S Shiradkar and Anil Kottantharayil, "Identification of Stressors Leading to Degradation of Antisoiling Coating in Warm and Humid Climate Zones," *IEEE J. Photovoltaics*, vol. 10, no. 1, pp. 166–172, 2020. DOI: 10.1109/JPHOTOV.2019.2946709.

4. **Sonali Bhaduri**, Makrand Farkade, Rohan Bajhal, Sudhanshu Mallick, Narendra Shiradkar and Anil Kottantharayil, Abrasion Resistance of Spray Coated Anti-Soiling Coatings During Waterless Cleaning of PV Modules, under review in *Materials Today Communications*, 2022.

5. **Sonali Bhaduri**, Rohan Bajhal, Makrand Farkade, Sudhanshu Mallick, Narendra Shiradkar and Anil Kottantharayil, Factors influencing the effect of abrasion damage upon the performance of anti-soiling coatings, to be submitted *Materials Chemistry and Physics*, 2023.

6. **Sonali Bhaduri**, Sudhanshu Mallick, Anil Kottantharayil and Narendra Shiradkar, Lifetime prediction of anti-soiling coatings undergoing degradation due to rain, to be submitted to *Progress in Photovoltaics*, 2022.

7. **Sonali Bhaduri**, Sudhanshu Mallick, Anil Kottantharayil and Narendra Shiradkar, Lifetime prediction of anti-soiling coatings undergoing degradation due to UV radiation, to be submitted to *Progress in Photovoltaics*, 2022.

8. **Sonali Bhaduri**, Sudhanshu Mallick, Narendra Shiradkar and Anil Kottantharayil, Understanding multiple stressors which degrade anti-soiling coatings: combined effect of rain, abrasion and UV radiation, under review, *IEEE J. Photovoltaics*, 2023.

Conference Proceedings Related to this Thesis Work

Year - 2021

1. **Sonali Bhaduri**, Makrand Farkade, Rohan Bajhal, Sudhanshu Mallick, Narendra Shiradkar and Anil Kottantharayil, Impact of different brush designs in robotic cleaning on the degradation of anti-soiling coatings. *2021 IEEE 48th Photovoltaic Specialists Conference (PVSC)*, pp. 2434-2438, 2021. DOI: 10.1109/PVSC43889.2021.9519046.

Year - 2020

2. **Sonali Bhaduri**, Rohan Bajhal, Sudhanshu Mallick, Narendra Shiradkar and Anil Kottantharayil, "Degradation of anti-soiling coatings : mechanical impact of rainfall." *47th IEEE Photovolt. Spec. Conf.*, 2020. DOI: 10.1109/PVSC45281.2020.9300414.

3. **Sonali Bhaduri**, Makrand Farkade, Rohan Bajhal, Lawrence L. Kazmerski, Sudhanshu Mallick, Narendra Shiradkar and Anil Kottantharayil1, "Cleaning efficacy of anti-soiling coatings," *47th IEEE Photovolt. Spec. Conf.*, 2020. DOI: 10.1109/PVSC45281.2020.9300697.

Year - 2019

4. **Sonali Bhaduri**, Ajeesh Alath, Sudhanshu Mallick, Narendra S Shiradkar and Anil Kottantharayil, "Identification of stressors leading to degradation of anti-soiling coating in warm and humid climate zones," presented in *46th IEEE Photovoltaic Specialist Conference*, Chicago, 2019.

5. Lloyd Fernandes, **Sonali Bhaduri**, Ajeesh Alath, Narendra S Shiradkar, and Anil Kottantharayil, "Artificial dust deposition chamber for investigation of soiling loss on photovoltaic modules," *46th IEEE Photovoltaic Specialist Conference*, Chicago, 2019. **DOI:** 10.1109/PVSC40753.2019.8981343.

6. Suellen C. Silva Costa, Antonia Sonia A.C. Diniz, Tulio Duarte, **Sonali Bhaduri**, Vinicius Camatta Santana, and Lawrence L. Kazmerski, "Performance of Soiled PV Module Technologies: Behavior Based on Controverted Parameters," *46th IEEE Photovolt. Spec. Conf.*, Chicago, 2019. **DOI:** 10.1109/PVSC40753.2019.8980675

Year - 2018

7. **Sonali Bhaduri** and Anil Kottantharayil, "Mitigation of Soiling by Vertical Mounting of Bifacial Modules," at *7th edition of the World Conference on Photovoltaic Energy Conversion*, Hawaii, 2018.

Year - 2017

8. **Sonali Bhaduri**, Sachin. Zachariah, L. L. Kazmerski, Balasubramaniam. Kavaipatti and Anil Kottantharayil, "Soiling loss on PV modules at two locations in India studied using a water based artificial soiling method," *44th IEEE Photovoltaic Specialists Conference*, Washington DC, 2017. **DOI:** 10.1109/PVSC.2017.8366289.

Journal Publications Not Related to this Thesis Work

1. Shashwata Chattopadhyay, Rajiv Dubey, **Sonali Bhaduri**, Sachin Zachariah, Hemant Kumar Singh, Chetan Singh Solanki, Anil Kottantharayil, Narendra Shiradkar, Brij M. Arora, K. L. Narasimhan, and Juzer Vasi., "Correlating Infrared Thermography With Electrical Degradation of PV Modules Inspected in All-India Survey of Photovoltaic Module Reliability 2016," *IEEE J. Photovoltaics*, 2018. DOI: 10.1109/JPHOTOV.2018.2859780.

2. Yogeswara Rao Golive, Sachin Zachariah, Rajiv Dubey, Shashwata Chattopadhyay**, Sonali Bhaduri**, Hemant K. Singh, Birinchi Bora, Sanjay Kumar, A.K. Tripathi, Anil Kottantharayil, Juzer Vasi, and Narendra Shiradkar., "Analysis of Field Degradation Rates Observed in All-India Survey of Photovoltaic Module Reliability 2018," *IEEE J. Photovoltaics*, vol. PP, pp. 560–567, 2019. DOI: 10.1109/JPHOTOV.2019.2954777.

Conference Proceedings Not Related to this Thesis Work

Year 2020

1. Yogeswara Rao Golive, Sachin Zachariah, **Sonali Bhaduri**, Rajiv Dubey, Shashwata Chattopadhyay, Hemant K. Singh, Anil Kottantharayil, Narendra Shiradkar, and Juzer Vasi, "Analysis and Failure Modes of Highly Degraded PV Modules Inspected during the 2018 All India Survey of PV Module Reliability," presented in "*4th IEEE Electron Devices Technology & Manufacturing Conference (EDTM)"*, Penang, Malaysia, 2020. **DOI:** 10.1109/EDTM47692.2020.9117930

Year 2019

2. **Sonali Bhaduri**, Sachin Zachariah, Yogeswara Rao Golive, Shashwata Chattopadhyay, Rajiv Dubey, Ritesh Ingle, Ali Asger Khattab, Hemant Kumar Singh, Sudhanshu Mallick, Anil Kottantharayil, Juzer Vasi and Narendra Shiradkar, "Correlating the Hot Spots and Power Degradation seen in crystalline silicon modules in All India Survey of PV Module Reliability 2018," 46*th IEEE Photovoltaic Specialist Conference*, Chicago, 2019. **DOI:** 10.1109/PVSC40753.2019.8980514.

3. Sachin Zachariah, Rajiv Dubey, Golive Yogeswara Rao, **Sonali Bhaduri**, Shashwata Chattopadhyay, Chetan Singh Solanki, Anil Kottantharayil, Brij M. Arora, K.L. Narasimhan, Hemant Kumar Singh, Juzer Vasi and Narendra Shiradkar., "Electroluminescence Study of over 700 Fielded PV Modules in All India Survey 2018," *46th IEEE Photovoltaic Specialist Conference*, Chicago, 2019. **DOI:** 10.1109/PVSC40753.2019.8981208.

Year 2018

5. Sweta Priyadarshi, **Sonali Bhaduri** and Narendra Shiradkar, "IoT Based, Inexpensive System for Large Scale, Wireless, Remote Temperature Monitoring of Photovoltaic Modules, "*7th World Conf. Photovolt. Energy Conversion, WCPEC 2018 - A Jt. Conf. 45th IEEE PVSC, 28th PVSEC 34th EU PVSEC*, Hawaii, 2018. **DOI:** 10.1109/PVSC.2018.8547354.

6. Rajiv Dubey, Shashwata Chattopadhyay, Sachin Zachariah, Vivek Kuthanazhi, Sugguna Rambabu, **Sonali Bhaduri**, Hemant K. Singh, Anil Kottantharayil, Brij M. Arora, K.L. Narasimhan, Narendra Shiradkar, Birinchi Bora, O.S. Sastry, Juzer Vasi, "Investigation of Poor Performing PV Modules Observed in All-India Survey of PV Module Reliability**,**" at *7th edition of the World Conference on Photovoltaic Energy Conversion*, Hawaii, 2018. DOI: 10.1109/PVSC.2018.8548000.

Year 2017

7. **Sonali Bhaduri**, Shashwata Chattopadhyay, Rajiv Dubey, Sachin Zachariah, Vivek Kuthanazhi, Chetan Singh Solanki, Anil Kottantharayil, Brij M. Arora, K.L. Narasimhan, Juzer Vasi, "Correlating Infra-red Thermography with Electrical Degradation of Modules Inspected in All India Survey of Photovoltaic Module Reliability" at *NREL/SNL/BNL PV Reliability workshop, 2017*, Lakewood, Colorado, USA. (**Poster – First prize**)

8. Rajiv Dubey, Sachin Zachariah, Shashwata Chattopadhyay, Vivek Kuthanazhi, **Sonali Bhaduri**, Hemant K. Singh, Archana Sinha, Chetan S. Solanki, Anil Kottantharayil, Brij M. Arora, K. L. Narasimhan, Juzer Vasi, Birinchi Bora, Rajesh Kumar, O.S. Sastry, "Performance of Field-Aged PV Modules in India: Results from the 2016 All India Survey of PV Module Reliability", *44th IEEE Photovoltaic Speclist conf*., Washington DC,2017. **DOI:** 10.1109/PVSC.2017.8366143.

Reports:

1. Yogeswara Rao Golive, Sachin Zachariah, **Sonali Bhaduri**, Rajiv Dubey, Shashwata Chattopadhyay, Pratik Joshi, Nilesh Kusher, Arpit Nandi, Amey Chindarkar, Devan P Vasudevan, Pratik Mundle, Sugguna Rambabu, Ajeesh MV, Ritesh Ingle, Ali Asger Khattab, Hemant Kumar Singh, Brij Mohan Arora, K. L. Narasimhan, Anil Kottantharayil, Juzer Vasi and Narendra Shiradkar, "All-India survey of photovoltaic module reliability: 2018", National Centre for Photovoltaic Research and Education (NCPRE), IIT Bombay & National Institute of Solar Energy (NISE), Gurugram, March-May 2018. (Report)
2. Shashwata Chattopadhyay, Rajiv Dubey, Vivek Kuthanazhi, Sachin Zachariah, **Sonali Bhaduri**, Chiranjibi Mahapatra, Sugguna Rambabu, Firoz Ansari, Amey Chindarkar, Archana Sinha, Hemant Kumar Singh, Narendra Shiradkar, Brij Mohan Arora, Anil Kottantharayil, K. L. Narasimhan, Sanjeev Sabnis and Juzer Vasi, "All-India survey of photovoltaic module reliability: 2016", National Centre for Photovoltaic Research and Education (NCPRE), IIT Bombay & National Institute of Solar Energy (NISE), Gurugram, March-May 2016. (Report)

Workshop Presentations

1. **Sonali Bhaduri**, Reliability of anti-soiling coatings, presented at *2nd Indo-UK PV Soiling workshop*, 2022.
2. **Sonali Bhaduri**, Soiling Loss and Mitigation Techniques, presented at *NCPRE – NTPC Workshop*, 2021.
3. **Sonali Bhaduri** and Anil Kottantharayil, "Vertical Mounted of Bifacial Modules for Zero soiling loss, presented at *2017 International Soiling Workshop*, 2017.
4. **Sonali. Bhaduri**, L. L. Kazmerski, and Anil Kottantharayil, "Cementation of soil on PV modules during 10 years of exposure in Mumbai", presented at *2017 International Soiling Workshop*, 2017.

References

[1] K. Ilse *et al.*, "Techno-Economic Assessment of Soiling Losses and Mitigation Strategies for Solar Power Generation," *Joule*, vol. 3, no. 10, pp. 1–19, 2019, doi: 10.1016/j.joule.2019.08.019.

[2] M. Gostein, B. Littmann, J. R. Caron, and L. Dunn, "Comparing PV power plant soiling measurements extracted from PV module irradiance and power measurements," *2013 IEEE 39th Photovolt. Spec. Conf.*, no. 1, pp. 3004–3009, 2013, doi: 10.1109/PVSC.2013.6745094.

[3] M. Gostein, T. Duster, and C. Thuman, "Accurately measuring PV soiling losses with soiling station employing module power measurements," *2015 IEEE 42nd Photovolt. Spec. Conf. PVSC 2015*, pp. 8–11, 2015, doi: 10.1109/PVSC.2015.7355993.

[4] M. Gostein, B. Bourne, and B. Stueve, "Field Testing of Mars ™ Soiling Sensor," *Int. Photovolt. Qual. Assur. Task Force webinar*, 2019.

[5] Kipp and Zonen, "DustIQ novel soiling measurement technology-," *Int. Photovolt. Qual. Assur. Task Force webinar*, no. February, 2018.

[6] Sonali Bhaduri, Sachin Zachariah, Lawrence L. Kazmerski, Balasubramaniam Kavaipatti,and Anil Kottantharayil, "Soiling loss on PV modules at two locations in India studied using a water based artificial soiling method," in *2017 IEEE 44th Photovoltaic Specialist Conference (PVSC)*, 2017, pp. 2799–2803. doi: 10.1109/PVSC.2017.8366289.

[7] L. L. Kazmerski *et al.*, "Fundamental studies of adhesion of dust to PV module surfaces: Chemical and physical relationships at the microscale," *IEEE J. Photovoltaics*, vol. 6, no. 3, pp. 719–729, 2016, doi: 10.1109/JPHOTOV.2016.2528409.

[8] M. R. Maghami, H. Hizam, C. Gomes, M. A. Radzi, M. I. Rezadad, and S. Hajighorbani, "Power loss due to soiling on solar panel: A review," *Renew. Sustain. Energy Rev.*, vol. 59, pp. 1307–1316, 2016, doi: 10.1016/j.rser.2016.01.044.

[9] J. Cano, "Photovoltaic Modules: Effect of Tilt Angle on Soiling," *A Thesis Present. Partial Fulfillment Requir. Degree Master Sci. Technol.*, no. July, pp. 1–65, 2011, [Online]. Available: https://core.ac.uk/download/pdf/79560086.pdf

[10] A. K. Yadav and S. S. Chandel, "Tilt angle optimization to maximize incident solar radiation: A review," *Renew. Sustain. Energy Rev.*, vol. 23, pp. 503–513, 2013, doi: 10.1016/j.rser.2013.02.027.

[11] M. K. Kim, K. O. Abdulkadir, J. Liu, J. H. Choi, and H. Wen, "Optimal design strategy of a solar reflector combining photovoltaic panels to improve electricity output: A case study in Calgary, Canada," *Sustain.*, vol. 13, no. 11, 2021, doi: 10.3390/su13116115.

[12] S. Guo, T. M. Walsh, and M. Peters, "Vertically mounted bifacial photovoltaic modules: A global analysis," *Energy*, vol. 61, pp. 447–454, 2013, doi: 10.1016/j.energy.2013.08.040.

[13] N. Nuraje, W. S. Khan, Y. Lei, M. Ceylan, and R. Asmatulu, "Superhydrophobic electrospun nanofibers," *J. Mater. Chem. A*, vol. 1, no. 6, pp. 1929–1946, 2013, doi: 10.1039/c2ta00189f.

[14] J. Zhang, W. Wang, S. Zhou, H. Yang, and C. Chen, "Transparent dust removal coatings for solar cell on mars and its Anti-dust mechanism," *Prog. Org. Coatings*, vol. 134, no. May, pp. 312–322, 2019, doi: 10.1016/j.porgcoat.2019.05.028.

[15] W. Glaubitt and P. Löbmann, "Anti-soiling effect of porous SiO2 coatings prepared by sol-gel processing," *J. Sol-Gel Sci. Technol.*, vol. 59, no. 2, pp. 239–244, 2011, doi: 10.1007/s10971-011-2489-5.

[16] M. Kim *et al.*, "Antireflective , self-cleaning and protective film by continuous sputtering of a plasma polymer on inorganic multilayer for perovskite solar cells application," *Sol. Energy Mater. Sol. Cells*, vol. 191, no. November 2018, pp. 55–61, 2019, doi: 10.1016/j.solmat.2018.10.020.

[17] Sarah Toth, Matthew Muller, David C. Miller, Helio Moutinho, Bobby To, Leonardo Micheli, Jeffrey Linger, Chaiwat Engtrakul, Asher Einhorn, Lin Simpson, "Soiling and cleaning-Initial observations from 5-year photovoltaic glasscoating durability study," *Sol. Energy Mater. Sol. Cells*, vol. 185, pp. 375–384, 2018, doi: https://doi.org/10.1016/j.solmat.2018.05.039.

[18] A. Einhorn *et al.*, "Evaluation of Soiling and Potential Mitigation Approaches on Photovoltaic Glass," *IEEE J. Photovoltaics*, vol. 9, no. 1, pp. 233–239, 2019, [Online]. Available:

https://ieeexplore.ieee.org/ielaam/5503869/8585410/8529245-aam.pdf

[19] B. Strauss, F. Lisco, F. Bukhari, J. M. Walls, and K. L. Barth, "Novel Hydrophobic Coatings for Soiling Mitigation in the PV Industry : Durability and Anti-Soiling Demonstrations,", *2019 IEEE 46th Photovoltaic Specialists Conference (PVSC)*, 2019. doi: 10.1109/PVSC40753.2019.8981166.

[20] M. Piliougine *et al.*, "Comparative analysis of energy produced by photovoltaic modules with anti-soiling coated surface in arid climates," *Appl. Energy*, 2013, doi: 10.1016/j.apenergy.2013.01.048.

[21] T. Hirohata, Y. Ota, and K. Nishioka, "Effect of Anti-Soiling Coating on Performance of Fresnel Lens for Concentrator Photovoltaic Module," *Appl. Mech. Mater.*, vol. 372, pp. 575–578, 2013, doi: 10.4028/www.scientific.net/AMM.372.575.

[22] X. F. Yang, C. Vang, D. E. Tallman, G. P. Bierwagen, S. G. Croll, and S. Rohlik, "Weathering degradation of a polyurethane coating," *Polym. Degrad. Stab.*, vol. 74, no. 2, pp. 341–351, 2001, doi: 10.1016/S0141-3910(01)00166-5.

[23] I. Nayshevsky, Q. F. Xu, G. Barahman, and A. M. Lyons, "Fluoropolymer coatings for solar cover glass: Anti-soiling mechanisms in the presence of dew," *Sol. Energy Mater. Sol. Cells*, no. October, p. 110281, 2019, doi: 10.1016/j.solmat.2019.110281.

[24] Z. Song, J. Liu, and H. Yang, "Air pollution and soiling implications for solar photovoltaic power generation: A comprehensive review," *Appl. Energy*, vol. 298, no. March, p. 117247, 2021, doi: 10.1016/j.apenergy.2021.117247.

[25] I. M. Peters, C. Brabec, T. Buonassisi, J. Hauch, and A. M. Nobre, "The Impact of COVID-19-Related Measures on the Solar Resource in Areas with High Levels of Air Pollution," *Joule*, vol. 4, no. 8, pp. 1681–1687, 2020, doi: 10.1016/j.joule.2020.06.009.

[26] E. G. Geetanjanli Patil Choori, CEO and Founder, "Overview of Robotic Module Cleaning & Inspection System Webinar," *Int. Photovolt. Qual. Assur. Task Force webinar*, no. March, 2018.

[27] N. M. Kumar, K. Sudhakar, M. Samykano, and S. Sukumaran, "Dust cleaning robots (DCR) for BIPV and BAPV solar power plants-A conceptual framework and research challenges," *Procedia Comput. Sci.*, vol. 133, pp. 746–754, 2018, doi: 10.1016/j.procs.2018.07.123.

[28] K. K. Ilse, B. W. Figgis, V. Naumann, C. Hagendorf, and J. Bagdahn, "Fundamentals of soiling processes on photovoltaic modules," *Renew. Sustain. Energy Rev.*, vol. 98, no. September, pp. 239–254, 2018, doi: 10.1016/j.rser.2018.09.015.

[29] S. Bhaduri, S. Chattopadhyay, S. Zachariah, C. S. Solanki, and A. Kottantharayil, "Evaluation of increase in the Energy yield of PV modules by inverting the panels during the Non – Sunshine hours," *26th International Photovoltaic Science and Engineering Conferenc*e, Singapore, 2016. [Online]. Available: https://www.eqmagpro.com/wp-content/uploads/2019/04/Sonali_Evaluation-of-increase-in-the-Energy-yield-of-PV-modules.pdf

[30] C. Deline, S. Macalpine, B. Marion, F. Toor, A. Asgharzadeh, and J. S. Stein, "Assessment of Bifacial Photovoltaic Module Power Rating Methodologies-Inside and Out," *IEEE J. Photovoltaics*, vol. 7, no. 2, 2017, doi: 10.1109/JPHOTOV.2017.2650565.

[31] G. Whyman, E. Bormashenko, and T. Stein, "The rigorous derivation of Young, Cassie-Baxter and Wenzel equations and the analysis of the contact angle hysteresis phenomenon," *Chem. Phys. Lett.*, vol. 450, no. 4–6, pp. 355–359, 2008, doi: 10.1016/j.cplett.2007.11.033.

[32] G. C. Oehler *et al.*, "Testing the Durability of Anti-Soiling Coatings for Solar Cover Glass by Outdoor Exposure in Denmark," *Energies*, vol. 13, no. 2, 2020, doi: 10.3390/en13020299.

[33] C. R. Crick and I. P. Parkin, "Preparation and characterisation of super-hydrophobic surfaces," *Chem. - A Eur. J.*, vol. 16, no. 12, pp. 3568–3588, 2010, doi: 10.1002/chem.200903335.

[34] Q.F. Xu, Y. Zhao, E. Kujan, J.C. Liu and A.M. Lyons, "An Anti-Reflective and Anti-Soiling Coating for Photovoltaic Panels," in *TechConnect Briefs*, 2015, pp. 624–627. [Online]. Available: https://briefs.techconnect.org/wp-content/volumes/TCB2015v1/pdf/413.pdf

[35] M. Sun *et al.*, "Influence of cuticle nanostructuring on the wetting behaviour/states on cicada wings," *PLoS One*, vol. 7, no. 4, 2012, doi: 10.1371/journal.pone.0035056.

[36] N. A. Patankar, "Mimicking the lotus effect: Influence of double roughness structures and slender pillars," *Langmuir*, vol. 20, no. 19, pp. 8209–8213, 2004, doi: 10.1021/la048629t.

[37] C. E. Cansoy, H. Y. Erbil, O. Akar, and T. Akin, "Effect of pattern size and geometry on the use of Cassie-Baxter equation for superhydrophobic surfaces," *Colloids Surfaces A Physicochem. Eng. Asp.*, vol. 386, no. 1–3, pp. 116–124, 2011, doi: 10.1016/j.colsurfa.2011.07.005.

[38] A. R. Parker and C. R. Lawrence, "Water capture by a desert beetle," *Nature*, vol. 414, no. 6859, pp. 33–34, 2001, doi: 10.1038/35102108.

[39] Kenan Isbilir, Fabiana Lisco, Gerald Womack, Ali Abbas and John Michael Walls, "Testing of an Anti-Soiling Coating for PV Module Cover Glass," *2018 IEEE 7th World Conf. Photovolt. Energy Convers. (A Jt. Conf. 45th IEEE PVSC, 28th PVSEC 34th EU PVSEC)*, pp. 3–5, 2018, doi: 10.1109/PVSC.2018.8547272.

[40] P. Tummers, "Outdoor Modelling of Anti-Soiling Coatings Performance for PV Applications," *Int. PV Qual. Assur. Task Force webinar*, 2018.

[41] M. Zahid *et al.*, "Outdoor performance of anti-soiling coatings in various climates of Saudi Arabia," *Sol. Energy Mater. Sol. Cells*, vol. 235, no. June 2021, p. 111470, 2022, doi: 10.1016/j.solmat.2021.111470.

[42] D. Goossens, "Wind tunnel protocol to study the effects of anti-soiling and anti-reflective coatings on deposition, removal, and accumulation of dust on photovoltaic surfaces and consequences for optical transmittance," *Sol. Energy*, vol. 163, pp. 131–139, 2018, doi: https://doi.org/10.1016/j.solener.2018.01.088.

[43] I. Nayshevsky, Q. Xu, J. M. Newkirk, D. Furhang, D. C. Miller, and A. M. Lyons, "Self-Cleaning Hybrid Hydrophobic – Hydrophilic Surfaces : Durability and Effect of Artificial Soilant Particle Type," *IEEE J. Photovoltaics*, vol. 10, no. 2, pp. 577–584, 2020, doi: 10.1109/JPHOTOV.2019.2955559.

[44] I. Nayshevsky, Q. Xu, and A. M. Lyons, "Hydrophobic-Hydrophilic Surfaces Exhibiting Dropwise Condensation for Anti-Soiling Applications," *IEEE J. Photovoltaics*, vol. 9, no. 1, pp. 302–307, 2019, doi: 10.1109/JPHOTOV.2018.2882636.

[45] S. F. Bukhari *et al.*, "Development of a Hydrophobic , Anti-soiling coating for PV Module Cover Glass," 2020. doi: 10.1109/PVSC40753.2019.8981377.

[46] J. M. Newkirk *et al.*, "Artificial linear brush abrasion of coatings for photovoltaic module first-surfaces," *Sol. Energy Mater. Sol. Cells*, vol. 219, no. September 2020, p. 110757, 2021, doi: 10.1016/j.solmat.2020.110757.

[47] S. Chattopadhyay *et al.*, "Visual degradation in field-aged crystalline silicon PV modules in India and correlation with electrical degradation," *IEEE J. Photovoltaics*, vol. 4, no. 6, pp. 1470–1476, 2014, doi: 10.1109/JPHOTOV.2014.2356717.

[48] R. J. Isaifan *et al.*, "Improved Self-cleaning Properties of an Efficient and Easy to Scale up TiO2 Thin Films Prepared by Adsorptive Self-Assembly," *Sci. Rep.*, vol. 7, no. 1, pp. 1–9, 2017, doi: 10.1038/s41598-017-07826-0.

[49] J Jiale Yong, Qing Yang, Feng Chen, Dongshi Zhang, Guangqing Du, Hao Bian, Jinhai Si and Xun Hou, "Bioinspired superhydrophobic surfaces with directional Adhesion," *RSC Adv*, vol. 4, no. January, 2014, doi: 10.1039/c3ra46929h.

[50] Yasuaki Tokudome, Kenji Okada, Atsushi Nakahira, and Masahide Takahashi, "Thermally-induced Switchable and Reversible Water Adhesion: Photopatternable Titanate Nanostructures Fabricated on Soft Substrates," *R. Soc. Chem.*, no. November, 2013, doi: 10.1039/C3TA13536E.

[51] Lloyd Fernandes, Sonali Bhaduri, Ajeesh Alath , Narendra S Shiradkar, and Anil Kottantharayil, "Artificial dust deposition chamber for investigation of soiling loss on photovoltaic modules," in *46th IEEE Photovoltaic Specialists Conference*, 2019, pp. 2–4. [Online]. Available: https://ieeexplore.ieee.org/abstract/document/8981343

[52] B. Rosner, R. J. Glynn, and M. T. Lee, "The Wilcoxon Signed Rank Test for Paired Comparisons of Clustered Data," *Biometrics*, vol. 62, no. 1, pp. 185–192, 2006, doi: 10.1111/j.1541-0420.2005.00389.x.

[53] Fabiana Lisco, Farwah Bukhari, Sona Ulicná, Kenan Isbilir, Kurt L. Barth, Alan Taylor and John M. Walls, "Degradation of Hydrophobic, Anti-Soiling Coatings for Solar Module Cover Glass," *Energies*, vol. 13, no. 15, 2020, doi: https://doi.org/10.3390/en13153811.

[54] I. Schmitz, M. Schreiner, G. Friedbacher, and M. Grasserbauer, "Phase imaging as an extension to tapping mode AFM for the identification of material properties on humidity-sensitive surfaces," *Appl. Surf. Sci.*, vol. 115, no. 2, pp. 190–198, 1997, doi: 10.1016/S0169-4332(97)80204-8.

[55] R. Dong and L. E. Yu, "Investigation of suflace changes of nanoparticles using TM-AFM phase imaging," *Environ. Sci. Technol.*, vol. 37, no. 12, pp. 2813–2819, 2003, doi: 10.1021/es034071k.

[56] H. Liu, S. Fu, J. Y. Zhu, H. Li, and H. Zhan, “Visualization of enzymatic hydrolysis of cellulose using AFM phase imaging,” *Enzyme Microb. Technol.*, vol. 45, no. 4, pp. 274–281, 2009, doi: 10.1016/j.enzmictec.2009.06.009.

[57] Z. Ye and X. Zhao, “Phase imaging atomic force microscopy in the characterization of biomaterials,” *J. Microsc.*, vol. 238, no. 1, pp. 27–35, 2010, doi: 10.1111/j.1365-2818.2009.03282.x.

[58] G. K. H. Pang, K. Z. Baba-Kishi, and A. Patel, “Topographic and phase-contrast imaging in atomic force microscopy,” *Ultramicroscopy*, vol. 81, no. 2, pp. 35–40, 2000, doi: 10.1016/S0304-3991(99)00164-3.

[59] X. Chen, M. C. Davies, C. J. Roberts, S. J. B. Tendler, P. M. Williams, and N. A. Burnham, “Optimizing phase imaging via dynamic force curves,” *Surf. Sci.*, vol. 460, no. 1–3, pp. 292–300, 2000, doi: 10.1016/S0039-6028(00)00574-4.

[60] T. R. Albrecht, P. Grütter, D. Horne, and D. Rugar, “Frequency modulation detection using high-Q cantilevers for enhanced force microscope sensitivity,” *Journal of Applied Physics*, vol. 69, no. 2. pp. 668–673, 1991. doi: 10.1063/1.347347.

[61] S. N. Magonov, V. Elings, and M. H. Whangbo, “Phase imaging and stiffness in tapping-mode atomic force microscopy,” *Surface Science*, vol. 375, no. 2–3. 1997. doi: 10.1016/S0039-6028(96)01591-9.

[62] M. H. Whangbo, “Tip-sample force interactions and surface stiffness in scanning probe microscopy,” *Surf. Sci*, vol. 429, pp. 178–185, 1997.

[63] L. Wang, “Role of damping in phase imaging in tapping mode atomic force microscopy,” *Surf. Sci.*, vol. 429, no. 1, pp. 178–185, 1999, doi: 10.1016/S0039-6028(99)00368-4.

[64] R. Hillenbrand, M. Stark, and R. Guckenberger, “Higher-harmonics generation in tapping- mode atomic-force microscopy : Insights into the tip – sample interaction,” *Appl. Phys. Lett*, vol. 76, no. 3478, 2000, doi: https://doi.org/10.1063/1.126683.

[65] “Weather data for year 2020, Website - https://www.accuweather.com for Pin 400076.”

[66] H. K. Jang *et al*, “Effects of chemical etching with sulfuric acid on glass surface,” *J. Vac. Sci. Technol.*, vol. Volume 18, no. Issue 2, 2000, doi: 10.1116/1.582200.

[67] H. K. Jang *et al.*, “Effects of chemical etching with nitric acid on glass surfaces,” *Journal of Vacuum Science & Technology*, vol. 267, no. 2001, 2003, doi: 10.1116/1.1333087.

[68] R. Sequeira, “Monsoonal deposition of sea salt and air pollutants over Bombay,” *Tellus*, vol. 28, no. 3, 1975, doi: https://doi.org/10.3402/tellusa.v28i3.10291.

[69] P. Prathibha, P. Kothai, I. V. Saradhi, G. G. Pandit, and V. D. Puranik, “Chemical characterization of precipitation at a coastal site in Trombay, Mumbai, India,” *Environ. Monit. Assess.*, vol. 168, no. 1–4, pp. 45–53, 2010, doi: 10.1007/s10661-009-1090-7.

[70] J. J. John, “Characterization of Soiling Loss on Photovoltaic Modules , and Development of a Novel Cleaning System,”, *PhD Thesis*, IIT Bombay, 2015. [Online]. Available: https://www.ee.iitb.ac.in/~anilkg/Jim-thesis.pdf

[71] N. S. Bhairamadgi *et al.*, “Hydrolytic and Thermal Stability of Organic Monolayers on Various Inorganic Substrates,” *ACS Appl. Mater. Interfaces Res. Artic.*, 2014, doi: 10.1021/la500533f.

[72] Denis V. Okhrimenko, Akin Budi, Marcel Ceccato, Marité Cárdenas, Dorte B. Johansson, Dorthe Lybye, Klaus Bechgaard, Martin P. Andersson, and Susan L. S. Stipp, “Hydrolytic Stability of 3 - Aminopropylsilane Coupling Agent on Silica and Silicate Surfaces at Elevated Temperatures,” *ACS Appl. Mater. Interfaces*, vol. 9, pp. 8344−8353, 2017, doi: 10.1021/acsami.6b14343.

[73] M. A. Serio, F. G. Carollo, and V. Ferro, “Raindrop size distribution and terminal velocity for rainfall erosivity studies. A review,” *J. Hydrol.*, vol. 576, no. June, pp. 210–228, 2019, doi: 10.1016/j.jhydrol.2019.06.040.

[74] D. R. Dourte, C. W. Fraisse, and W. L. Bartels, “Exploring changes in rainfall intensity and seasonal variability in the Southeastern U.S.: Stakeholder engagement, observations, and adaptation,” *Clim. Risk Manag.*, vol. 7, pp. 11–19, 2015, doi: 10.1016/j.crm.2015.02.001.

[75] “Website of Q-Lab Corporation – QUV accelerated weathering tester, accessed on 2nd June 2019. URL : https://www.q-lab.com/products/quv-weathering-tester/quv.”

[76] D. C. Miller *et al.*, “The Abrasion of Photovoltaic Glass : A Comparison of the Effects of Natural and Artificial Aging,” *IEEE J. Photovoltaics*, vol. 10, no. 1, pp. 173–180, 2020, doi: 10.1109/JPHOTOV.2019.2947029.

[77] W. H. Press and S. A. Teukolsky, "Savitzky-Golay Smoothing Filters," *Comput. Phys.*, vol. 4, no. 6, p. 669, 1990, doi: 10.1063/1.4822961.

[78] I. E. Commission, *IEC 61215-1:2016 : Terrestrial photovoltaic (PV) modules - Design qualification and type approval*. 1990.

[79] E. Bumiller and C. Hillman, "A Review of Models for Time-to-Failure Due to Metallic Migration Mechanisms," *White Pap. DfR Solut.*, no. January, 2006, [Online]. Available: http://www.dfrsolutions.com/uploads/white-papers/Time-to-Failure_Metallic_Migration.pdf

[80] T. Shimokawa and S. Tanaka, "A statistical consideration of Miner's rule," *Int. J. Fatigue*, vol. 2, no. 4, pp. 165–170, 1980, doi: 10.1016/0142-1123(80)90044-4.

[81] Edilson M. Assis, Ernesto P. Borges and Silvio A.B. Vieira de Melo, "Generalized q-Weibull model and the bathtub curve," *Int. J. Qual. Reliab. Manag.*, vol. 30, no. 7, pp. 720–736, 2013, doi: 10.1108/IJQRM-Oct-2011-0143.

[82] N. R. Farnum and P. Booth, "Uniqueness of maximum likelihood estimators of the 2-parameter weibull distribution," *IEEE Trans. Reliab.*, vol. 46, no. 4, pp. 523–525, 1997, doi: 10.1109/24.693786.

[83] Shashwata Chattopadhyay, Rajiv Dubey, Vivek Kuthanazhi, Sachin Zachariah, Sonali Bhaduri, Chiranjibi Mahapatra, Sugguna Rambabu, Firoz Ansari, Amey Chindarkar, Archana Sinha, Hemant Kumar Singh, Narendra Shiradkar, Brij Mohan Arora, Anil Kottantharayil, K. L. Narasimhan, Sanjeev Sabnis and Juzer Vasi, "All-India Survey of Photovoltaic Module Reliability : 2016 All-India Survey of Photovoltaic Module Reliability : 2016," 2017. [Online]. Available: https://www.researchgate.net/publication/322386040_All-India_Survey_of_Photovoltaic_Module_Reliability_2016

[84] A. Risitano, D. Corallo, and G. Risitano, "Cumulative damage by Miner's rule and by energetic analysis," *SDHM Struct. Durab. Heal. Monit.*, vol. 8, no. 2, pp. 91–109, 2012, [Online]. Available: https://file.techscience.com/files/sdhm/2012/v8n2/sdhm.2012.008.091.pdf

[85] National Solar Radiation Database (NSRDB) Data Download (Point), Year 2018, Last accessed on 29th March 2022. Available: https://nsrdb.nrel.gov."

[86] Sandia Model for Module operating temperature, Access date: 31st March 2022. Available: https://pvpmc.sandia.gov/modeling-steps/2-dc-module-iv/module-temperature/sandia-module-temperature-model/."

[87] S. Lavanya, N. V. P. Kirankumar, S. Aneesh, K. V. Subrahmanyam, and S. Sijikumar, "Seasonal variation of raindrop size distribution over a coastal station Thumba: A quantitative analysis," *Atmos. Res.*, vol. 229, no. June, pp. 86–99, 2019, doi: 10.1016/j.atmosres.2019.06.004.

[88] S. Barthiban, B. J. Lloyd, and M. Maier, "Sanitary Hazards and Microbial Quality of Open Dug Wells in the Maldives Islands," *J. Water Resour. Prot.*, vol. 04, no. 07, pp. 474–486, 2012, doi: 10.4236/jwarp.2012.47055.

[89] M. Xie and C. D. Lai, "Reliability analysis using an additive Weibull model with bathtub-shaped failure rate function," *Reliab. Eng. Syst. Saf.*, vol. 52, no. 1, pp. 87–93, 1996, doi: 10.1016/0951-8320(95)00149-2.

[90] B. R. Radke, "A demonstration of interval-censored survival analysis," *Prev. Vet. Med.*, vol. 59, no. 4, pp. 241–256, 2003, doi: 10.1016/S0167-5877(03)00103-X.

[91] Horst Rinne, *The Weibull distribution: a handbook. Chapman and Hall/CRC*. 2008. [Online]. Available: https://www.routledge.com/The-Weibull-Distribution-A-Handbook/Rinne/p/book/9780367577469

[92] J. Lemons, "The urgent need for universities to comprehensively address global climate change across disciplines and programs," *Environ. Manage.*, vol. 48, no. 3, pp. 379–391, 2011, doi: 10.1007/s00267-011-9699-z.

[93] UN, "The 17 Sustainable Development Goals," Last accessed on 05th February 2023. Available: https://sdgs.un.org/goals

[94] P. Behuria, "The politics of late late development in renewable energy sectors: Dependency and contradictory tensions in India's National Solar Mission," *World Dev.*, vol. 126, p. 104726, 2020, doi: 10.1016/j.worlddev.2019.104726.

[95] T. Sarver, A. Al-Qaraghuli, and L. L. Kazmerski, "A comprehensive review of the impact of dust on the use of solar energy: History, investigations, results, literature, and mitigation approaches," *Renew. Sustain. Energy Rev.*, vol. 22, pp. 698–733, 2013, doi: 10.1016/j.rser.2012.12.065.

[96] Hays HL, Spiller H. Fluoropolymer-associated illness. Clin Toxicol (Phila). 2014 Sep-Oct;52(8):848-55. doi: 10.3109/15563650.2014.946610. PMID: 25200453.